SOLAR FLUX EMERGENCE
A THREE-DIMENSIONAL NUMERICAL STUDY

Michelle Joanne Murray

A Thesis Submitted for the Degree of PhD
at the
University of St Andrews

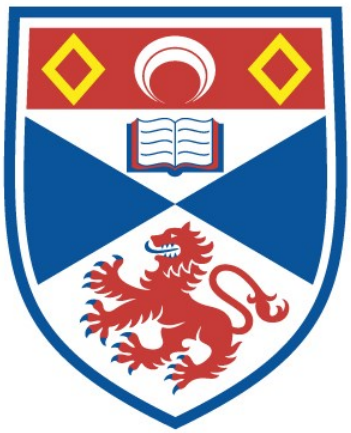

2008

SOLAR FLUX EMERGENCE

A Three-Dimensional Numerical Study

Michelle Joanne Murray

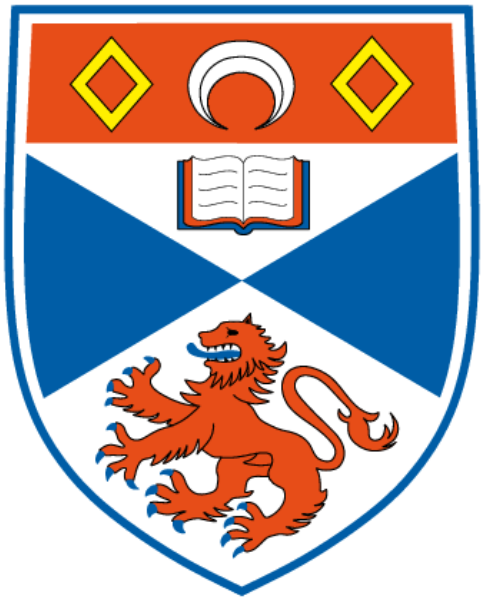

Thesis submitted for the degree of Doctor of Philosophy
of the University of St Andrews

27 August 2007

Abstract

Flux is continually emerging on the Sun, making its way from the solar interior up into the atmosphere. Emergence occurs on small-scales in the quiet Sun where magnetic fragments emerge, interact and cancel and on large-scales in active regions where magnetic fields emerge and concentrate to form sunspots. This thesis has been concerned with the large-scale emergence process and in particular the results from previous solar flux emergence modelling endeavours.

Modelling uses numerical methods to evolve a domain representing simplified layers of the Sun's atmosphere, within which the subsurface layer contains magnetic flux. The flux is initialised such that it will rises towards the surface at the start of the simulation. Once the flux reaches the solar surface, it can only emerge into the atmosphere if a magnetic buoyancy instability occurs, after which it expands rapidly both vertically and horizontally.

The aim of this thesis is to test the robustness of these general findings from simulations to date upon the seed magnetic field. More explicitly, we have used three-dimensional numerical simulations to investigate how variations in the subsurface magnetic field modify the emergence process and the resulting atmospheric field. We initially consider a simple constant twist flux tube for the seed field and vary the tube's magnetic field strength and degree of twist. Additionally, we have examined the effects of using non-constant twist flux tubes as the seed field by choosing two different profiles for the twist that are functions of the tube's radius. Finally, we have investigated the effects of increasing the complexity of the seed field by positioning two flux tubes below the solar surface and testing two different configurations for the tubes. In both cases, the magnetic fields of the two tubes are such that, once the tubes come into contact with each other, reconnection occurs and a combined flux system is formed.

From our investigations, we conclude that the general emergence results given by previous simulations are robust. However, for constant twist tubes with low field strength and twist, the buoyancy instability fails to be launched when the tubes reach the photosphere and they remain trapped in the low atmosphere. Similarly, when the non-constant twist profile results in a low tension force throughout the tube, we find that the buoyancy instability is not initialised.

Declaration

I, Michelle Joanne Murray, hereby certify that this thesis, which is approximately 78,000 words in length, has been written by me, that it is the record of work carried out by me and that it has not been submitted in any previous application for a higher degree.

Name: Michelle Joanne Murray **Signature:**..... **Date:** .....

I was admitted as a research student in September 2004 and as a candidate for the degree of Doctor of Philosophy in September 2005; the higher study for which this is a record was carried out in the University of St Andrews between 2004 and 2007.

Name: Michelle Joanne Murray **Signature:**..... **Date:** .....

I hereby certify that the candidate has fulfilled the conditions of the Resolution and Regulations appropriate for the degree of Doctor of Philosophy in the University of St Andrews and that the candidate is qualified to submit this thesis in application for that degree.

Name: Alan Hood **Signature:**..... **Date:** .....

In submitting this thesis to the University of St Andrews I understand that I am giving permission for it to be made available for use in accordance with the regulations of the University Library for the time being in force, subject to any copyright vested in the work not being affected thereby. I also understand that the title and abstract will be published, and that a copy of the work may be made and supplied to any bona fide library or research worker, that my thesis will be electronically accessible for personal or research use, and that the library has the right to migrate my thesis into new electronic forms as required to ensure continued access to the thesis. I have obtained any third-party copyright permissions that may be required in order to allow such access and migration.

Name: Michelle Joanne Murray **Signature:**..... **Date:** .....

Acknowledgements

I would like to thank my supervisor, Professor Alan Hood of the University of St Andrews (UK), for his guidance and support over the past three years. His endless enthusiasm and patience have been key in enabling me to produce an interesting and worthy thesis.

I would like to thank Professor Fernando Moreno-Insertis of the Institúto de Astrofísica de Canarias (Tenerife, Spain), Dr Klaus Galsgaard of the Niels Bohr Institute for Astronomy, Physics and Geophysics (Denmark) and Dr Vasilis Archontis of the University of St Andrews for accepting me into their established research group, teaching me about the field of numerical emergence simulations and contributing to one of the papers published from this work.

I would also like to thank the staff and PhD students of the Solar and Magnetospheric Theory Group at the University of St Andrews for useful scientific and technical discussions.

This work has been undertaken with the financial assistance of the Particle Physics and Astronomy Research Council (PPARC). The computational analysis for this work was carried out on the joint SRIF and PPARC funded UKMHD Linux cluster, Copson, at the University of St Andrews.

Abbreviations

2D:	Two-dimensional
2.5D:	Two-and-a-half-dimensional
3D:	Three-dimensional
AFS:	Arch Filament System
CFL:	Courant-Friedrichs-Lewy (condition)
CME:	Coronal Mass Ejection
EIT:	Extreme-ultraviolet Imaging Telescope
EUV:	Extreme Ultraviolet
IMS:	Iterative Multistep (method)
MDI:	Michelson Doppler Imager
MHD:	Magnetohydrodynamics
MPI:	Message Passing Interface
SOHO:	Solar and Heliospheric Observatory
SUMER:	Solar Ultraviolet Measurements of Emitted Radiation
TFTM:	Thin Flux Tube Model
TRACE	Transition Region and Coronal Explorer

Contents

Contents

Chapter 1

Introduction

The scientific research comprising this thesis considers solar flux emergence through the use of three-dimensional computational simulations. In this chapter, we will provide the motivation for studying flux emergence and any necessary background information. In section 1.1 we introduce basic details about the Sun, with particular emphasis placed upon features relating to flux emergence. The computational experiments we have performed study the Sun on a macro-scale and, therefore, use the magnetohydrodynamic (MHD) approximation. This approximation and its associated equations will be discussed in section 1.2.

As will be seen in section 1.1, flux tubes play an important role in flux emergence on the Sun and we will consider the features and properties of flux tubes in section 1.3. Multiple analytical studies and computational simulations have been performed in order to understand the rise of flux tubes through the solar interior. From these, many important characteristics of subsurface flux tubes have been discovered, which give direction as to the initialisation of flux in emergence simulations. Finally, in section 1.4, we will draw together all of the introductory information and present the aim of this thesis.

1.1 The Sun

The Sun is one of billions of stars in the Milky Way galaxy. Its proximity to the Earth makes the Sun the most studied star in the universe. By studying the Sun we not only learn about the Sun itself, but about possible processes occurring on other stars. In a wider context, the Sun provides a living laboratory for learning about plasmas, heliosismology techniques, and large-scale energy events.

The Sun is a spectral type G2 star and is approximately 4.5×10^9 years old. The radius of the

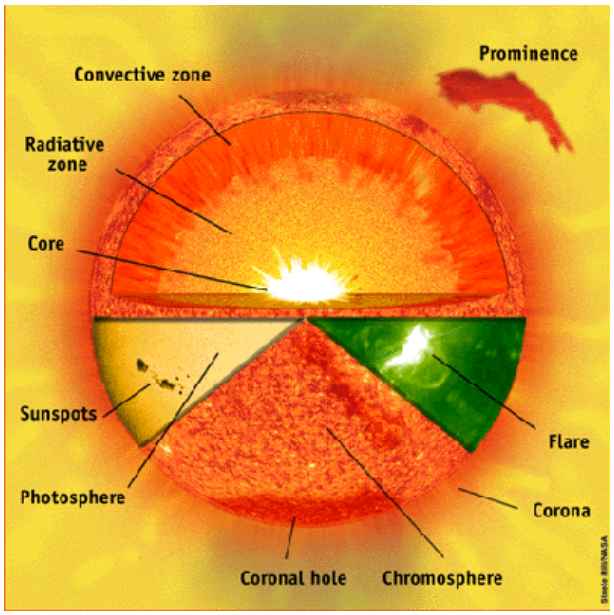

Figure 1.1: Schematic diagram of the Sun's layers. The northern hemisphere identifies the three solar interior layers (core, radiative zone and convection zone) while the southern hemisphere illustrates the atmospheric layers (photosphere, chromosphere and corona). Photo courtesy SOHO consortium. SOHO is a project of international cooperation between the European Space Agency (ESA) and the U.S. National Aeronautics and Space Administration (NASA).

Sun, the distance from its centre to the top of its interior, is $696,000$ km. The atmosphere could be thought of extending out to approximately $10\ R_\odot$, where $R_\odot$ is one solar radius, since coronal streamers can extend up to this height. However, in reality it is not possible to determine the exact end of the Sun's atmosphere since the solar wind carries the Sun's material far out into the solar system.

The interior of the Sun is classified into three domains: the core, the radiative zone, and the convection zone, as shown in figure 1.1. The core extends to $0.25\ R_\odot$ and is the region where nuclear processes occur. The radiative zone is the largest interior domain and lies above the core. It is here that energy and heat are transported away from the core through radiative transfer. The outer most layer of the interior is the convection zone, which occupies the region from $0.86\ R_\odot$ to the interior's boundary. As its name suggests, the plasma in this region is subject to convective motions. The motions arise because the temperature gradient in the convection zone is too great for the plasma to remain in equilibrium and a convective instability sets in.

The solar atmosphere comprises four layers: the photosphere, the chromosphere, the transition region, and the corona. Each of these regions is distinguished by its temperature profile. The photosphere is the layer of the atmosphere lying above the visible solar surface, where the temperature falls with distance from the solar surface. The overall height of the photosphere is approximately 300 km. In contrast, the overlying chromospheric region is characterised by increasing tempera-

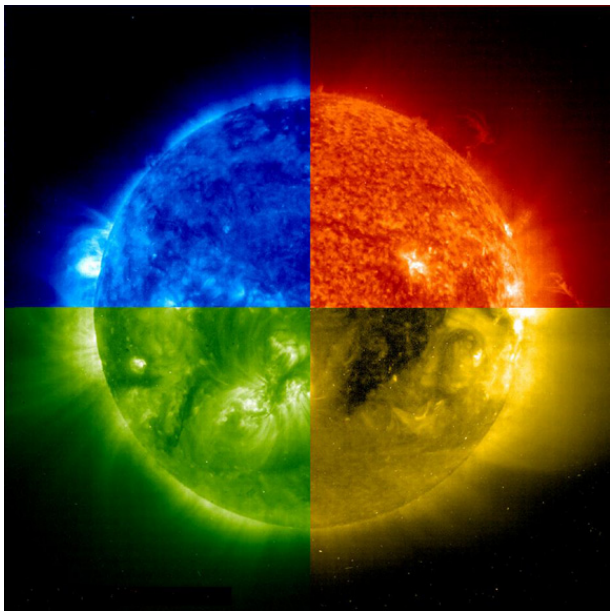

Figure 1.2: An "EIT colour wheel", showing images in the four filters of EIT. Anticlockwise from upper right: HeII 304Å $(\sim 80,000\ \mathrm{K})$, FeIX/X 171Å $(1\ \mathrm{MK})$, FeXII 195Å $(1.5\ \mathrm{MK})$, FeXIV 284Å $(2\ \mathrm{MK})$. Photo courtesy SOHO consortium.

ture with height. At a height of approximately $2300\ \mathrm{km}$, the temperature rapidly increases from $5000\ \mathrm{K}$ to $1\ \mathrm{MK}$ over a height of $500\ \mathrm{km}$. This layer is the transition region, above which lies the million degree corona that extends for many solar radii. The reasons for the corona maintaining such a high temperature are still under debate but prime candidates for the heating mechanism include waves and reconnection. The different temperatures for each region mean that observational images can single out each region by using specific filters. Figure 1.2 illustrates the differences between four filters from the EIT instrument upon SOHO. The increasing temperature of each filter isolates a region higher in the atmosphere.

Events and changes on the Sun occur over differing time periods, from a couple of seconds to years. The overall temperament of the Sun changes on a twenty-two year cycle. This cycle is comprised of two consecutive eleven year cycles, during which the flux at the poles builds such that it finally causes the magnetic direction associated with the polar field to reverse. The reversal of the polar field polarity signifies the start of the next eleven year cycle. During each eleven year cycle, dynamical activity on the Sun shows a general trend of increase and decrease. The start of the cycle is characterised by few visible features on the Sun's surface and this stage is termed solar minimum. Over the course of approximately five years these features increase in number until solar maximum, when the Sun is at its most active. The activity and visible features decrease in number again over a further five years until solar minimum is reached in the eleventh year. Figure 1.3 shows the increase in the number of atmospheric magnetic fields as the cycle moves to solar maximum.

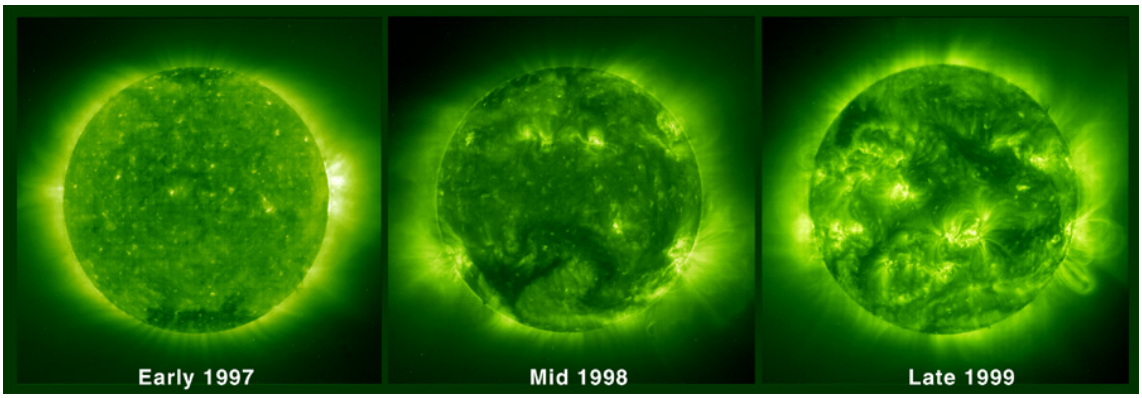

Figure 1.3: Three EIT images taken in 195Å that show an increasing complexity of the magnetic corona as solar maximum is approached. Photo courtesy SOHO consortium.

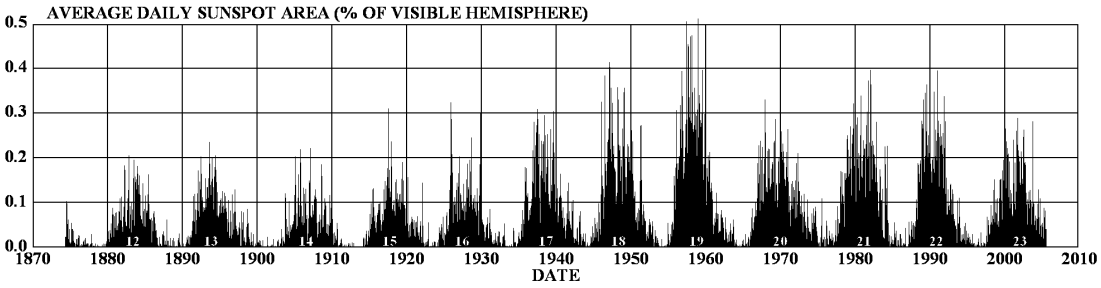

Figure 1.4: The average daily sunspot area as a percentage of the observed hemisphere over time. This gives a guide as to the average number of sunspots, hence the eleven year cycle clearly stands out. Image courtesy NASA.

One of the most visible features on the Sun's surface are sunspots. Although, as explained above, there is a significant variation in their number during the solar cycle. This variation is shown in figure 1.4, where the eleven year cycle can clearly be identified. Figure 1.5 shows the visible surface of the Sun with a number of sunspots visible near solar maximum. Sunspots were first observed with the naked eye by one of the pupils of Aristotle, Theophrastus. Sunspots were systematically charted by the Chinese in 23 B.C. though they had little understanding of what they were actually seeing. The Aztecs are also believed to have seen the dark spots on the Sun since their story of creation has a pock-marked god sacrificing himself to become the Sun. It was not until the seventeenth century that sunspots could finally be studied in greater detail with the invention of the telescope. Though Galileo Galilei of Italy is perhaps the most renowned sunspot discoverer of 1610, there is some debate over which European was the first to identify sunspots with the aid of telescopes. Other contenders are Christopher Schiener of Germany, Johannes Fabricius of Holland, and Thomas Herriot of England. Each discoverer made drawings of the changing sunspot shapes by hand, watching them cross the visible surface of the sun.

During these early discovery days, sunspots were thought to have been planets or moons orbiting the Sun or dark clouds in the Sun's atmosphere. We now know sunspots to be sites of extremely

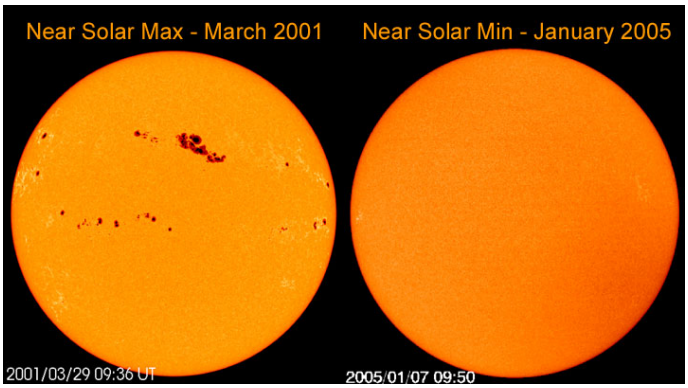

Figure 1.5: Michelson Doppler Imager (MDI) continuum images of the Sun showing how the number of sunspots varies over the course of a sunspot cycle. The image on the left, with many sunspots, was taken near solar maximum in March 2001. The righthand image, in which no spots are evident, was taken near solar minimum in January 2005. Photo courtesy SOHO consortium.

strong magnetic field. Figure 1.6(a) shows the fine detail of a sunspot pair. The central darker region of each sunspot is the umbra and this is surrounded by the brighter, filamentary penumbra. For standard sunspots, the umbra has a diameter of $10,000 - 20,000$ km and the strongest field in the sunspot is found here. The umbral magnetic field is vertical and has a strength of $2,000 - 3,000$ G, as illustrated in the schematic diagram in figure 1.6(b). In the penumbra, the magnetic field lies parallel to the photospheric plane soon after it passes through the surface. Each of the strands in the filamentary structure can be $5,000 - 7,000$ km long and $300 - 400$ km wide.

Fifty-three percent of sunspots appear in bi-polar pairs (Priest 1982) and the formation of a sunspot usually happens over a period of days. Magnetic flux first appears at the photosphere in the centre of a supergranular cell in the form of a small flux tube (see Zwaan (1985), Meyer et al. (1974) and references therein). The emerged flux tube forms an arcade structure or arch filament system (AFS) above the photosphere. Supergranular convection pushes the feet of the flux tube towards opposing boundaries of the cell over a period of $4 - 5$ hours. The continuing emergence of flux tubes in the centre of the cell and the cell's convection lead to concentrations of tubes' feet forming at the cell boundaries and, eventually, pores appear. These are characterised by locations on the photosphere that are cooler and, hence, darker than the surrounding material. If flux continues to accumulate at the pores then, over the space of a few days, these pores develop into spots. Once formed, the motion of the spots continues as they move away from each other to a distance of $\sim 150,000$ km, which is five times longer than the diameter of a supergranular cell. Most sunspots disappear as rapidly as they form, over a period of a couple of days, but some larger spots experience a slower rate of decay over a few months.

The magnetic field we observe in the solar atmosphere originates from within the interior of the Sun. Magnetic field is continually recycled within the interior through dynamo action. Strong toroidal flux ropes are generated in the tachocline from a diffuse magnetic field. The tachocline

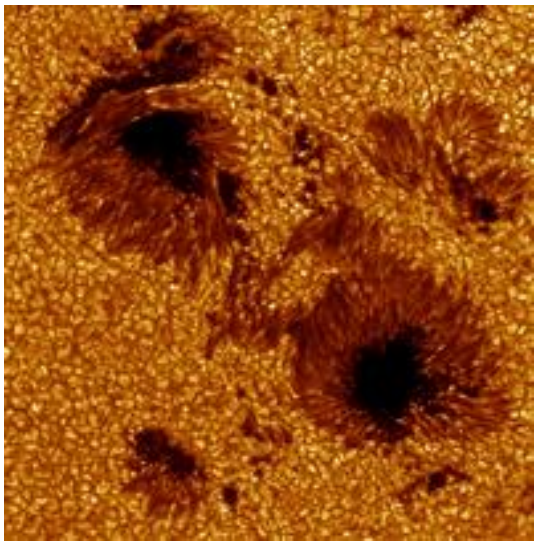

(a) Close up of a sunspot pair from 14^{th} August 2003 captured using the Swedish $1\ \text{m}$ Solar Telescope situated on the island of La Palma. Photo courtesy Royal Swedish Academy of Sciences and the observers Göran Scharmer and Kai Langhans.

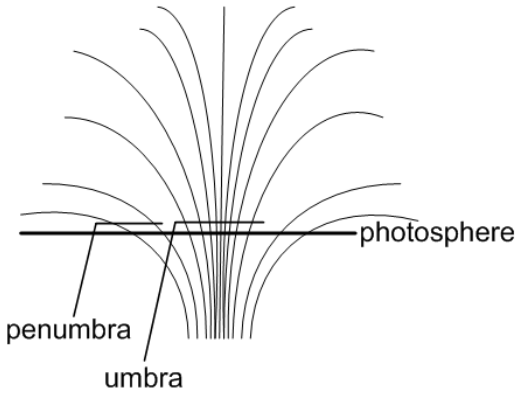

(b) Schematic illustration of the magnetic field associated with a sunspot. The inner umbral field is vertical while the outer penumbral field lies parallel to the photosphere.

Figure 1.6: (a) Observation and (b) schematic illustration of sunspots.

lies between the uniformly and differentially rotating radiative and convective zones, respectively. The shear motions associated with the change in rotational regimes across the tachocline act to amplify the diffuse magnetic field and structure it into toroidal tubes. Once the field strength exceeds 10^5 G, undular instabilities lead to the formation of loops in the tubes, which then rise up to the surface on the time-scale of months. Turbulence and instabilities within the convection zone can deform these tubes, halting their rise and returning the magnetic field to the tachocline. For loops that rise uninhibited, their intersection with the photosphere results in the formation of large- and small-scale flux emergence.

Figure 1.7 demonstrates the dynamic evolution of a typical large-scale flux emergence event. In line with the observations of Kurokawa and Kawai (1993), the first indicators of the event are upwardly directed surges of cool plasma, indicated by the arrow in figure 1.7(a). These are initiated in the region where the flux will shortly emerge. The emerging loops initially lie close to the photosphere, as highlighted by the arrow in figure 1.7(b). Over time, these loops expand into the atmosphere, both vertically and horizontally. As seen in figure 1.7(d), after 24 hours the AFS formed by the loops has adopted a fan shape but, at the footpoints of the loops in the photosphere, the sunspots will still be underdeveloped and are only a collection of pores. Over the course of a further day or two, these pores will develop into complete sunspots with umbras and penumbras. If the emergence is occurring near an existing active region, the topology and geometry of the new system may be affected. Through some type of reconnection mechanism, links can quickly

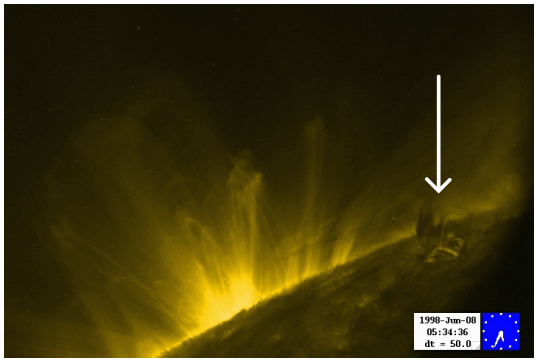

(a) $t = 0$: Upsurges of $\sim 10^3$ K during the early stages of flux emergence.

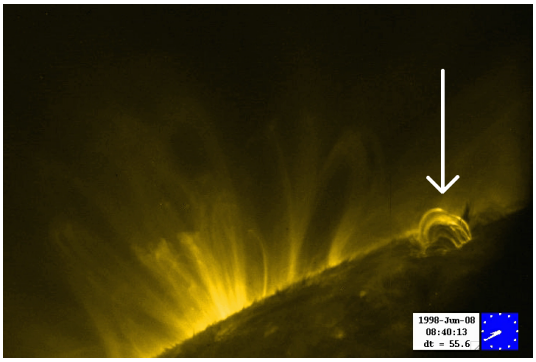

(b) $t = 3$ hours: Bright loops at the site of the newly emerging flux.

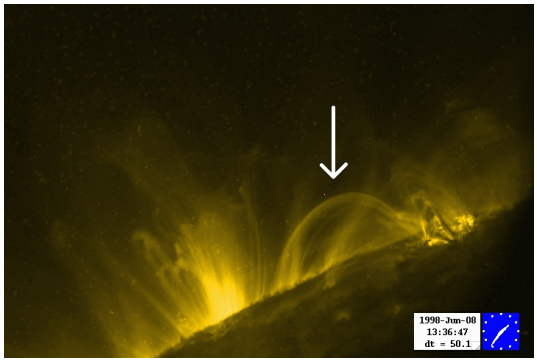

(c) $t = 8$ hours: Loops link the new emerging region with the existing active region.

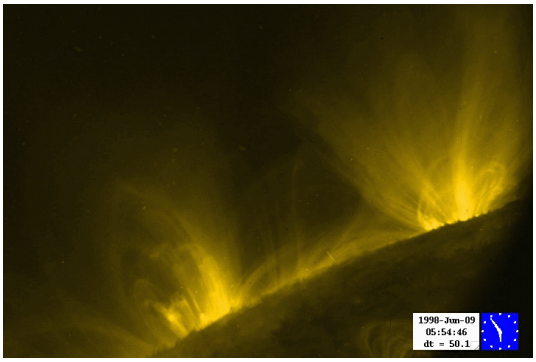

(d) $t = 24$ hours: Expansion of the new magnetic system into the atmosphere. Fieldlines appear to have adopted a fan shape.

Figure 1.7: Flux emergence event on 8^{th} June 1998, viewed at the solar limb. At the left-hand side of the images an active region is already in existence and, to the right, a new active region emerges. Event captured by the Transition Region and Coronal Explorer (TRACE) in 171Å. TRACE is a mission of the Stanford-Lockheed Institute for Space Research and is a NASA Small Explorer Mission. Movie and extracted images courtesy Nasa TRACE Mission.

be established that connect the two flux systems. In figure 1.7(c), some of these linking loops that have one footpoint in each active region are indicated by the arrow. A quantitative description of flux emergence will be considered in chapter 2, where comparisons between previous simulations and observations will be made.

The emerged magnetic field promotes coupling between the various atmospheric layers. For example, plasma motions at the photospheric level can propagate along fieldlines and have an effect in the corona. Flux emergence can also have a greater impact on the surrounding region by destabilising existing structures. This can have large-scale dynamical consequences such as initiating coronal mass ejections (CMEs) or flares.

1.2 The MHD Equations

In order to understand the effects induced by flux emergence, it is necessary to have an in depth knowledge of the physics of the driving event. Hence, the study of flux emergence has become increasingly important for improving our understanding of events such as CMEs. Analytically modelling multiple layers of the Sun is extremely complex and, without massive simplifications, impossible. Numerical simulations provide a practical tool for investigating flux emergence. Although simplifications are still necessary, the models are far closer to reality than can be achieved with analytical techniques and are, therefore, worth pursuing.

Everything in the universe is made from electrons, protons and neutrons. Thus, models wishing to provide a complete picture would be required to consider each species individually and their interaction with each other. Studies at this micro-scale use particle orbit theory. However, this is very challenging and only manageable for small-scale problems. As an alternative, we consider magnetohydrodynamics (MHD). This provides a macroscopic description and enables us to consider larger-scale scenarios.

The MHD equations are a combination of the governing equations of fluid dynamics and Maxwell's equations, describing the evolution of electric and magnetic fields. They are, therefore, particularly well suited to describing plasmas, which are ionised gases and, hence, receptive to electromagnetic fields.

The equations are:

Mass Continuity:

$$\frac{\partial \rho}{\partial t} + \nabla \cdot (\rho \mathbf{v}) = 0, \tag{1.1}$$

Momentum:

$$\rho \frac{\partial \mathbf{v}}{\partial t} + \rho \left(\mathbf{v} \cdot \nabla \right) \mathbf{v} = -\nabla p + \rho \mathbf{g} + \mathbf{J} \times \mathbf{B}, \tag{1.2}$$

Energy:

$$\frac{\partial p}{\partial t} + \mathbf{v} \cdot \nabla p = -\gamma p \nabla \cdot \mathbf{v} + \frac{1}{\sigma} |\mathbf{J}|^2, \tag{1.3}$$

Faraday's Law:

$$\frac{\partial \mathbf{B}}{\partial t} = -\nabla \times \mathbf{E}, \tag{1.4}$$

Ideal Gas Law:

$$p = \frac{\rho \tilde{R} T}{\tilde{\mu}}, \tag{1.5}$$

Ampére's Law:

$$\mu \mathbf{J} = \nabla \times \mathbf{B}, \tag{1.6}$$

Ohm's Law:

$$\mathbf{E} = -\mathbf{v} \times \mathbf{B} + \frac{1}{\sigma}\mathbf{J}, \tag{1.7}$$

Solenoidal Condition:

$$\nabla \cdot \mathbf{B} = 0, \tag{1.8}$$

These equations involve density ρ, velocity $\mathbf{v}$, gas pressure p, acceleration due to gravity $\mathbf{g}$, electric current density $\mathbf{J}$, the magnetic field $\mathbf{B}$, electrical resistivity $1/\sigma$, the electric field $\mathbf{E}$, temperature T, the gas constant $\tilde{R}$, mean atomic weight $\tilde{\mu}$ (the average mass per particle in units of mass per proton), magnetic permeability μ, and the ratio of specific heats, which is usually taken as $\gamma = 5/3$. The equation of motion used here ignores any explicit viscous terms.

In solar MHD, it is more common to work with $\mathbf{B}$ and $\mathbf{v}$. Thus, Faraday's law (1.4) is rewritten as

$$\frac{\partial \mathbf{B}}{\partial t} = \nabla \times (\mathbf{v} \times \mathbf{B}) + \eta \nabla^2 \mathbf{B}, \tag{1.9}$$

where $\mathbf{E}$ and $\mathbf{J}$ have been eliminated using Ampére's law (1.6) and Ohm's law (1.7) and $\eta = 1/\mu\sigma$ is the magnetic diffusivity. This equation is often just referred to as the induction equation.

There are several assumptions made prior to arriving at these equations, which must continue to be adhered to when using them. The assumptions are as follows:

- The equations are written in an inertial frame of reference.
- The equations refer to a single fluid in a state of quasi-neutrality. Under quasi-neutrality, $n_+ - n_- \ll n$, where n_+ and n_- are the number densities of positive and negative ions per unit volume and n is the total number density.
- The characteristic time-scale is greater than internal plasma time-scales, such as the ion gyro period and the collision time. Thus, the plasma can be assumed to be in thermodynamic equilibrium with distribution functions close to Maxwellian.

- The characteristic length-scale is greater than internal plasma lengths, such as the ion gyro-radius and the mean free path length, thus the plasma can be treated as collision dominated.

- The plasma velocities, sound speed and Alfvén speed are all assumed to be much smaller than the speed of light and, therefore, relativistic effects can be neglected. This allows the displacement current in Ampere's law, $\frac{1}{c^2}\frac{\partial \mathbf{E}}{\partial t}$, to be neglected and is frequently called the MHD approximation.

- $\tilde{\mu}$ is considered to be uniform.

1.3 Flux Tubes

As discussed in section 1.1, flux tubes are an integral part of flux emergence. It is widely agreed that sunspot pairs are the product of toroidal flux ropes that have risen through the convection zone and erupted into the atmosphere. However, observations of sunspots identify that they are actually a collection of many smaller flux tubes. The individual research projects undertaken in this thesis aim to emulate the largescale structure of sunspots. Therefore, our simulations use a single flux tube to achieve a basic active region. In this section, we will consider the definition of a flux tube and its properties. We will also give details about well used flux tube models, such as Gold-Hoyle and the Thin Flux Tube Model (TFTM).

1.3.1 Definition of a Flux Tube

A magnetic flux tube is made up of multiple field lines so we first define a magnetic fieldline. If the magnetic field in a domain is given by **B**, then a magnetic fieldline is a line whose tangent at any point on that line is in the direction of **B**. If the field **B** is known then solving

$$dy/dx = B_y/B_x, \tag{1.10}$$

for x and y in two dimensions, or

$$dx/B_x = dy/B_y = dz/B_z, \tag{1.11}$$

for x, y, and z in three dimensions, will give the equations of the fieldlines for that magnetic field.

A flux tube is the volume enclosed by the set of fieldlines, in which every fieldline intersects the same simple closed curve. The total flux belonging to the tube, F, is measured by the amount of

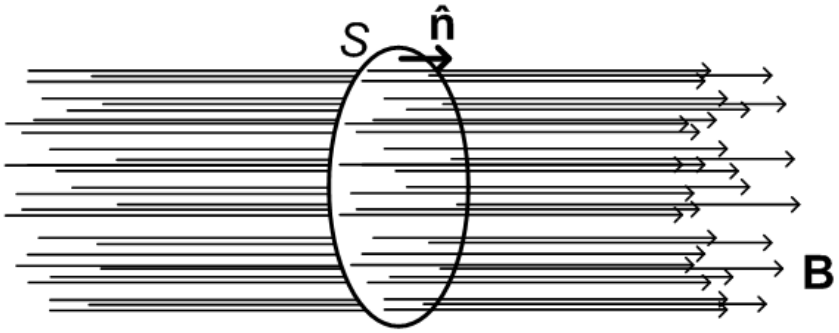

Figure 1.8: Schematic illustration of the total flux of a tube. The magnetic field of the tube is given by **B** and S is the surface whose periphery encompasses all of the tube's fieldlines.

tube flux crossing a surface, S,

$$F = \int_S \mathbf{B} \cdot \mathbf{dS}, \tag{1.12}$$

where dS is directed normal to that surface, as shown in figure 1.8.

1.3.2 Properties of a Flux Tube

1. **The total flux of a tube remains constant along its length.** Consider measuring the flux over the surface S enclosing the volume V. The normal to the surface is directed away from the volume. We can simplify the surface by splitting it into three sections: two end surfaces, S_1 and S_2, and one curved rectangular surface that defines the radial edge of the tube and whose normal vector is perpendicular to the magnetic field, S_3. We have thus defined a section of a flux tube. The surface decomposition is illustrated in figure 1.9.

   Rewriting (1.12) in terms of the three surfaces yields

   $$\int_S \mathbf{B} \cdot \mathbf{dS} = \int_{S_1} \mathbf{B} \cdot \mathbf{dS} + \int_{S_2} \mathbf{B} \cdot \mathbf{dS} + \int_{S_3} \mathbf{B} \cdot \mathbf{dS}. \tag{1.13}$$

   By applying the divergence theorem to the left-hand side we have

   $$\int_S \mathbf{B} \cdot \mathbf{dS} = \int_V \nabla \cdot \mathbf{B}\, dV = 0. \tag{1.14}$$

   Using this result and the fact that the third integral on the right-hand side of (1.13) is zero, by definition of the surface S_3, we find that (1.13) reduces to

   $$0 = \int_{S_1} \mathbf{B} \cdot \mathbf{dS} + \int_{S_2} \mathbf{B} \cdot \mathbf{dS}, \tag{1.15}$$

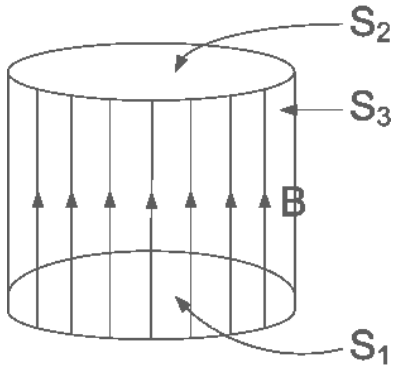

Figure 1.9: Decomposition of a flux tube's surface, S, into three separate surfaces: $S1$, $S2$ and $S3$.

and in turn

$$-\int_{S_1} \mathbf{B} \cdot \mathbf{dS} = \int_{S_2} \mathbf{B} \cdot \mathbf{dS}. \tag{1.16}$$

The right-hand side integral of (1.16) tells us the total flux of the tube at the location of surface S_2 and we will assume this to be equal to F. Inserting this information into (1.16) and rearranging gives

$$\int_{S_1} \mathbf{B} \cdot \mathbf{dS} = -F. \tag{1.17}$$

The normal to the surface S_1 is in the opposite direction to the field and, therefore, the total flux of the tube will be given as negative when evaluating this integral. Thus, the total flux of the tube at the location of surface S_1 will actually be F. We have now shown that the total flux of the tube at the locations of the two surfaces is the same and this can be proved for any two locations along the tube's length, thus the total flux of this tube is constant along its length. Given that the flux tube we chose to consider was arbitrary, the initial statement holds for all flux tubes.

2. **The mean field of a flux tube increases (decreases) when the tube narrows (widens).** Property 1 tells us that the strength, F, of a flux tube is constant along the length of the tube. The strength is measured by integrating the flux through a surface, S, perpendicular to the direction of the field, **B**. We will let the area of S that contains flux from the tube, and hence the cross-sectional area of the tube, be A. The mean field of the tube, $\bar{B}$, is the average field strength per unit area of the tube's cross-section, thus we have

$$F = \bar{B}A. \tag{1.18}$$

We can see that by increasing the cross-sectional area of the tube (i.e. making the tube

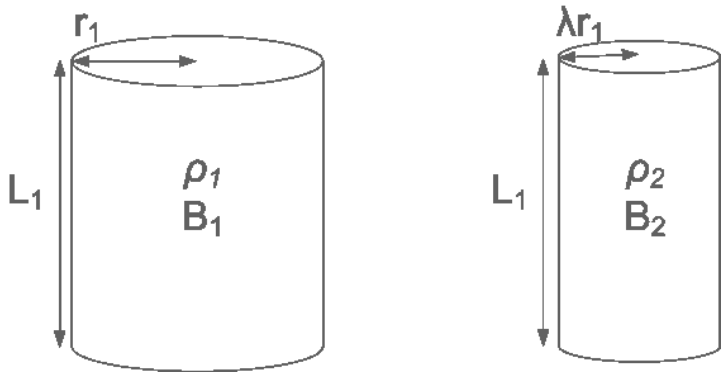

Figure 1.10: The left-hand side flux tube undergoes a transverse compression to become the right-hand side tube.

wider) the mean field of the tube must decrease to ensure F remains constant. Similarly, if the mean field strength increases then the cross-sectional area of the tube must decrease and, thus, the tube becomes narrower.

3. **Transverse compression of a flux tube increases the mean field and density in the same proportion.** Consider a flux tube which under goes a transverse compression such that the length of the flux tube, L_1, remains unchanged, as shown in figure 1.10. The radius of the flux tube changes from r_1 to λr_1, where $\lambda < 1$. The density in the tube is initially uniform at ρ_1 and it changes to ρ_2, remaining uniform. The mean field of the tube changes from $\bar{B}_1$ to $\bar{B}_2$ during the compression.

   By mass conservation

$$\rho_1 \left(\pi {r_1}^2 L_1\right) = \rho_2 \left(\pi \lambda^2 {r_1}^2 L_1\right), \tag{1.19}$$

   and rearranging gives

$$\rho_2 = \rho_1/\lambda^2. \tag{1.20}$$

   Similarly, by magnetic flux conservation

$$\bar{B}_1 \left(\pi {r_1}^2\right) = \bar{B}_2 \left(\pi \lambda^2 {r_1}^2\right), \tag{1.21}$$

   giving

$$\bar{B}_2 = \bar{B}_1/\lambda^2. \tag{1.22}$$

   Thus transverse compression of the tube has resulted in both the density and the mean field changing by $1/\lambda^2$, and increasing since $\lambda < 1$.

4. **Extension of a flux tube without compression increases the tube's field strength.** We consider the same initial flux tube as in property 3. However, this time the tube is elongated so the length changes from L_1 to $\lambda^* L_1$, where $\lambda^* > 1$, and the radius changes from r_1 to αr_1. Again, the density is uniform pre- and post-extension and changes from ρ_1 to ρ_2 and the mean field changes from $\bar{B}_1$ to $\bar{B}_2$. Mass conservation shows that

$$\rho_2 = \rho_1 / \left(\lambda^* \alpha^2\right), \tag{1.23}$$

and because the tube experiences no compression $\lambda^* \alpha^2 = 1$. Given that $\lambda^* > 1$, we must have $\alpha^2 < 1$. Thus, if the material in the tube is not compressed when the tube becomes stretched in length, the tube's radius must shrink. The mean field of the elongated tube is

$$\bar{B}_2 = \bar{B}_1 / \alpha^2, \tag{1.24}$$

by magnetic flux conservation. Since $\alpha^2 < 1$ we can see that lengthening causes the mean field of the tube to increase.

1.3.3 Gold-Hoyle Flux Tube

In flux tube simulations, the most used magnetic field definition for the flux tube is the Gold-Hoyle tube. The magnetic field of the Gold-Hoyle flux tube was originally given by an explicit set of equations, whose constants could be varied. Over time, the equations prescribing the Gold-Hoyle tube have been generalised and now encompass a larger set of magnetic profiles. Before giving the generalised definition of the Gold-Hoyle tube, we consider the origin of the explicit equations.

The paper by Gold and Hoyle (1960) considers the origins of solar flares. Prior to a flare taking place, large amounts of energy must build-up and be stored in the chromosphere. This build-up must occur over a prolonged period of time since a rapid motion and storage would produce visible effects. Observations of flares in Hα frequently show them aligned along pre-existing filamentary patterns. The filaments are described by the authors as being bundles of magnetic fieldlines that arch into the atmosphere and whose footpoints pass through the photospheric surface.

The authors aimed to answer the two main questions surrounding flares at the time, namely the following:

1. How can the large amount of energy dispersed in a flare be stored in the chromosphere?
2. What process invokes the sudden release of energy and, thus, the flare?

If a magnetic field is to persist for a prolonged period of time while the energy builds, it should

be mostly force-free. The energy stored in the field will be due to currents travelling along the magnetic fieldlines and these currents can be generated by turbulent motions in the photosphere.

The authors use the following assumptions to allow them to determine the structure of a force-free twisted filament or flux tube:

- the curvature of the axis of the filament is sufficiently small over a short distance such that it can be neglected;
- all points along a fieldline are the same distance from the axis;
- all fieldlines have the same number of turns per unit length of the axis;
- the field is independent of the azimuthal coordinate about the axis and the distance coordinate in the axial direction, thus the field is only a function of radius.

We consider this problem in a cylindrical coordinate system, (r, θ, z), where the axis of the flux tube is aligned with the z direction. The above assumptions result in the field having no radial component and being independent of θ and z in the azimuthal and axial components. Thus, the form of the field is given by $\mathbf{B} = (0, B_\theta(r), B_z(r))$. This prescribes a magnetic field where all of the fieldlines rotate about the axis of the tube. The rate of rotation of the fieldlines is defined as the twist of the tube, Φ, and measures the radian angle through which the fieldlines rotate over one axial unit in length. The twist is given by

$$\Phi = \frac{d\theta}{r\, dz} \equiv \frac{B_\theta}{r\, B_z}, \tag{1.25}$$

where B_θ and B_z are the magnetic field components in the θ and z directions, respectively. Defining ν as the number of turns of a fieldline per axial unit length gives

$$\Phi = 2\pi\nu. \tag{1.26}$$

We define the variable ϕ as the angle that a fieldline makes with the plane normal to the axis, as shown in figure 1.11. Decomposing the magnetic fieldline in figure 1.11 into its individual magnetic components and applying simple trigonometry yields

$$\cot\phi = \frac{B_\theta}{B_z}. \tag{1.27}$$

Substituting (1.26) and (1.27) into (1.25) gives

$$\cot\phi = 2\pi\nu r. \tag{1.28}$$

This result will be used shortly.

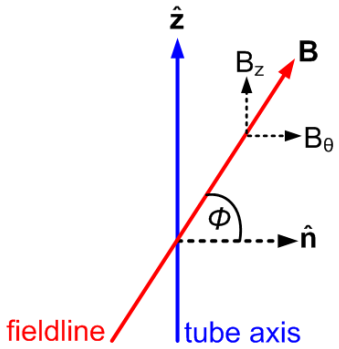

Figure 1.11: Schematic diagram identifying the angle ϕ between the normal to the axis, $\hat{\mathbf{n}}$, and a given fieldline.

We now return our attention to finding a force-free magnetic field, $\mathbf{B}$. This field arises when the following is satisfied:

$$(\nabla \times \mathbf{B}) \times \mathbf{B} = 0. \tag{1.29}$$

In cylindrical coordinates, with the above assumptions, this yields

$$0 = \left(B_\theta \frac{1}{r} \frac{d}{dr} (r B_\theta) + B_z \frac{d}{dr} (B_z) \right) \hat{\mathbf{r}}, \tag{1.30}$$

where both the azimuthal and axial components of (1.29) are zero. With $B_\theta = B \cos\phi$ and $B_z = B \sin\phi$, (1.30) reduces to

$$\frac{d}{dr} (\log B) = \frac{-\cos^2 \phi}{r}. \tag{1.31}$$

Redefining (1.28) in terms of $\sin\phi$ and $\cos\phi$ gives

$$\sin\phi = 1/\sqrt{1 + 4\pi^2\nu^2 r^2}, \tag{1.32}$$

$$\cos\phi = 2\pi\nu r/\sqrt{1 + 4\pi^2\nu^2 r^2}. \tag{1.33}$$

Substituting (1.33) into (1.31) and integrating the result yields

$$B = A/\sqrt{1 + 4\pi^2\nu^2 r^2}, \tag{1.34}$$

where A is a constant of integration.

The flux tube is considered to have a radius a, thus $\mathbf{B} = 0$ for $r > a$. The flux in the tube, F, can be measured by calculating the axial flux passing through the plane normal to the axial direction

such that

$$F = 2\pi \int_{r=0}^{a} B_z r dr. \tag{1.35}$$

Using (1.32) and (1.34), (1.35) can be simplified to

$$F = 2\pi \int_{r=0}^{a} \frac{Ar}{1 + 4\pi^2\nu^2 r^2} dr. \tag{1.36}$$

Integrating (1.36) and rearranging for A gives

$$A = \frac{qF}{\pi a^2 \log(1+q)}, \tag{1.37}$$

where $q = 4\pi^2\nu^2 a^2 = \Phi^2 a^2$. The constant of integration can now be removed from the formulation for B, (1.34), and thus

$$B_z = B\sin\phi = \frac{qF}{\pi a^2 \log(1+q)} \frac{1}{1 + qr^2/a^2}, \tag{1.38}$$

$$B_\theta = B\cos\phi = \frac{qF}{\pi a^2 \log(1+q)} \frac{2\pi\nu r}{1 + qr^2/a^2}. \tag{1.39}$$

More simply written, these become

$$B_z = \frac{B_0}{1 + \Phi^2 r^2}, \tag{1.40}$$

$$B_\theta = \Phi r B_z. \tag{1.41}$$

These magnetic field components, together with $B_r = 0$, define the original Gold-Hoyle flux tube.

At the axis, $B_\theta = 0$ so the field is purely in the axial direction. Although it was stated that the tube would have a radius of a and that there would be no field at larger radii, the field prescribed by (1.40) and (1.41) does not satisfy this. For $r \to \infty$, B reduces to zero as $1/r$ as does B_θ, whilst B_z decays as $1/r^2$ making the field mainly azimuthal at large radii.

One of the initial assumptions used by Gold and Hoyle was that all field lines have the same number of turns about the axis per unit distance in the axial direction. For the field profile defined by (1.40) and (1.41), the twist is $2\pi\nu$. Thus, to satisfy the assumption ν must be a constant and, from (1.28), ϕ varies with r. Figure 1.12 illustrates the profile of the function $\phi(r)$ for $\upsilon = 0.1$. As the radial distance from the axis increases, the fieldlines turn away from the axial direction and towards the direction of the normal to the axis.

Today, a Gold-Hoyle flux tube is given by any **B** describing a set of nonlinear force-free fields representing a uniformly twisted, cylindrical, flux tube. The field found by Gold and Hoyle (1960)

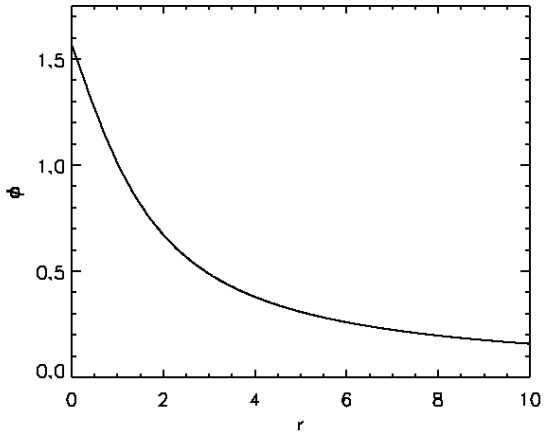

Figure 1.12: For a constant value of $\upsilon = 0.1$, ϕ decreases from an angle of $\pi/2$ to approximately parallel to the normal to the axis, $\hat{\mathbf{n}}$, as the distance from the axis increases.

is just one solution. Emerging flux simulations that do not use Gold-Hoyle flux tubes still consider uniformly twisting tubes. However, they do not require the tube to be force-free and this generates a much larger set of field definitions to choose from. Constant and non-constant twist tubes will be considered further in chapters 5 and 6, respectively.

1.3.4 Thin Flux Tube Model

As discussed in section 1.1, toroidal flux tubes are believed to be created deep in the solar interior through dynamo action and under buoyancy rise towards the surface, erupting through the photosphere to form sunspots. There have been many studies of tubes rising through the convection zone and, from these, the Thin Flux Tube Model (TFTM) has been developed. The TFTM describes the motion of tubes that are following an arbitrary path. It was initially derived by Spruit (1981) for an untwisted flux tube and extended by Longcope and Klapper (1997) for twisted flux tubes.

The main assumption of the TFTM is that the flux tube being considered is thin. To be thin, the radius of the tube, r_0, must be negligible in comparison to the local pressure scale height of the surrounding fluid and any scales of variation along the tube. Since the sound crossing time of the tube is considered to be smaller than other dynamic time scales, it is also assumed that pressure balance is instantly maintained between the tube and the external fluid. Thus, we have

$$p + B^2/2\mu = p_e, \tag{1.42}$$

where p and p_e are the gas pressure inside and outside of the tube, respectively.

The TFTM is valid when considering flux tubes in the base of the convection zone, since the local pressure scale height is very large there. However, the pressure scale height is much smaller near to the photospheric surface and, thus, the model is no longer valid in the upper layer of the convection zone or the atmosphere. The TFTM is, therefore, of limited use in flux emergence simulations but during the early phases of experiments it can provide useful insight.

The equations comprising the TFTM are derived under the MHD approximation. We begin with the equation of motion (a rewritten form of (1.2))

$$\rho\frac{D\mathbf{v}}{Dt} = -\nabla\left(p + \frac{B^2}{2\mu}\right) + \frac{1}{\mu}\left(\mathbf{B}\cdot\nabla\right)\mathbf{B} + \rho\mathbf{g}, \tag{1.43}$$

where $\mathbf{v}$, $\mathbf{B}$, and ρ are the velocity, magnetic field and density of the tube, respectively.

We use a local cylindrical coordinate system (r, θ, l) along the tube. Since the flux tube we are considering is thin, B_r is negligible. We initially consider an untwisted flux tube, thus $B_\theta = 0$. Hence, the magnetic field of the tube is $\mathbf{B} = B(r, \theta, l)\boldsymbol{l}$, assuming that $\nabla \cdot \mathbf{B} = 0$ is satisfied. Evaluating the tension force acting on the tube yields

$$\left(\mathbf{B}\cdot\nabla\right)\mathbf{B} = B\frac{\partial}{\partial l}\left(B\boldsymbol{l}\right) = \frac{1}{2}\boldsymbol{l}\frac{\partial B^2}{\partial l} + B^2\frac{\partial \boldsymbol{l}}{\partial l}, \tag{1.44}$$

where the rightmost partial derivative gives the curvature of the path of the tube. This vector is perpendicular to $\boldsymbol{l}$ and is rewritten as $\mathbf{k}$. Hence, the perpendicular component of the tension force is

$$\left[\left(\mathbf{B}\cdot\nabla\right)\mathbf{B}\right]_\perp = B^2\mathbf{k}. \tag{1.45}$$

Substituting (1.44) and (1.45) into (1.43) gives

$$\rho\frac{D\mathbf{v}}{Dt} = -\nabla\left(p + \frac{B^2}{2\mu}\right) + \frac{1}{2\mu}\boldsymbol{l}\frac{\partial B^2}{\partial l} + \frac{1}{\mu}B^2\mathbf{k} + \rho\mathbf{g}. \tag{1.46}$$

If we assume the surrounding fluid is in hydrostatic equilibrium then

$$\nabla p_e = \rho_e\mathbf{g}, \tag{1.47}$$

where ρ_e is the density of the external fluid. Taking the gradient of (1.42) and using the hydrostatic equilibrium result (1.47) gives

$$\nabla\left(p + B^2/2\mu\right) = \rho_e\mathbf{g}. \tag{1.48}$$

Inserting this into (1.46) we have the simple TFTM equation of motion

$$\rho\frac{D\mathbf{v}}{Dt} = \frac{1}{2\mu}\boldsymbol{l}\frac{\partial B^2}{\partial l} + \frac{1}{\mu}B^2\mathbf{k} + (\rho - \rho_e)\,\mathbf{g}. \tag{1.49}$$

Longcope and Klapper (1997) considered weakly twisted tubes for which $|\Phi r_0| \ll 1$. They found that (1.49) adequately describes the motion of the twisted tube. For more strongly twisted tubes ($\Phi r_0 \sim 2\pi$), the axis of the tube can develop writhe and, thus, (1.49) no longer provides a correct motion description for the tube.

The derivation by Spruit (1981) also includes an enhanced inertia term in the equation of motion (1.49). This term accounts for the back-reaction of the fluid to the motion of the flux tube. This effect is significant during the impulsive acceleration phases of the tube. The correct treatment of the fluid's back-reaction is yet to be agreed upon in existing literature. Since these impulsive phases occur rarely in thin flux tube simulations, the enhanced inertia term is usually ignored.

As a flux tube rises a wake develops behind the tube. Pressure differences are created between the rising tube and the external fluid and, thus, a drag force acts on the tube. The drag force, F_D, is derived from studies of incompressible flows past a rigid cylinder and takes the form (Batchelor 1967; Caligari et al. 1995)

$$F_D = -C_D\frac{\rho_e|\mathbf{v}_\perp|\mathbf{v}_\perp}{\pi r_0}. \tag{1.50}$$

$\mathbf{v}_\perp$ is the perpendicular part of the tube's relative velocity with respect to the external fluid and C_D is the drag coefficient. The drag term is approximately $\mathrm{O}\,(1)$ (Caligari et al. 1995; Emonet and Moreno-Insertis 1998). This term is added to the TFTM equation of motion (1.49) to give

$$\rho\frac{D\mathbf{v}}{Dt} = \frac{1}{2\mu}\boldsymbol{l}\frac{\partial B^2}{\partial l} + \frac{1}{\mu}B^2\mathbf{k} + (\rho - \rho_e)\,\mathbf{g} + F_D. \tag{1.51}$$

Studies of thin flux tubes rising through the Sun's rotating interior included additional terms in (1.51) to account for the effects of the Coriolis force and differential rotation on the motion of the tube. These simulations have successfully reproduced Joy's law of active region tilt, where the leading spot lies closer to the equatorial line than the following spot (D'Silva and Choudhuri 1993; Caligari et al. 1995; Fan and Fisher 1996). However, as we will see in chapter 2, emerging flux simulations are limited to the upper layers of the convection zone and, thus, do not consider a rotating frame of reference. Hence, we will not expand upon these rotational terms further.

To completely describe the evolution of a thin untwisted flux tube, the TFTM equation of motion must be used in conjunction with mass continuity, energy, induction and ideal gas equations. In the absence of resistivity, the MHD mass continuity (1.1) and induction (1.9) equations can be

combined to give the Walén equation (Caligari et al. 1995)

$$\frac{D}{Dt}\left(\frac{\mathbf{B}}{\rho}\right) = \left(\frac{\mathbf{B}}{\rho}\cdot\nabla\right)\mathbf{v}. \tag{1.52}$$

The definition of the tube's magnetic field reduces (1.52) to

$$\frac{D}{Dt}\left(\frac{B}{\rho}\right)\boldsymbol{l} + \frac{B}{\rho}\frac{D\boldsymbol{l}}{Dt} = \frac{B}{\rho}\frac{\partial\mathbf{v}}{\partial l}, \tag{1.53}$$

and multiplying this by $\boldsymbol{l}$ gives

$$\frac{D}{Dt}\left(\frac{B}{\rho}\right) + \frac{B}{\rho}\boldsymbol{l}\cdot\frac{D\boldsymbol{l}}{Dt} = \frac{B}{\rho}\boldsymbol{l}\cdot\frac{\partial\mathbf{v}}{\partial l}. \tag{1.54}$$

Following the derivation of the TFTM equation of motion, the second term on the left-hand side of (1.54) simplifies to $\frac{B}{\rho}\boldsymbol{l}\cdot\mathbf{k}$ and the definition of $\mathbf{k}$ means this term is zero. Using the expansion

$$\frac{\partial}{\partial l}(\mathbf{v}\cdot\boldsymbol{l}) = \frac{\partial\mathbf{v}}{\partial l}\cdot\boldsymbol{l} + \mathbf{v}\cdot\frac{\partial\boldsymbol{l}}{\partial l} = \frac{\partial\mathbf{v}}{\partial l}\cdot\boldsymbol{l} + \mathbf{v}\cdot\mathbf{k}, \tag{1.55}$$

(1.54) reduces to

$$\frac{D}{Dt}\left(\frac{B}{\rho}\right) = \frac{B}{\rho}\left(\frac{\partial}{\partial l}(\mathbf{v}\cdot\boldsymbol{l}) - \mathbf{v}\cdot\mathbf{k}\right). \tag{1.56}$$

This equation describes the evolution of the flux tube's magnetic field and replaces the MHD induction and mass continuity equations.

Fan and Fisher (1996) derived the following energy equation for the TFTM:

$$\frac{1}{\rho}\frac{D\rho}{Dt} = \frac{1}{\gamma\rho}\frac{Dp}{Dt} - \frac{\nabla_{ad}}{p}\frac{DQ}{Dt}, \tag{1.57}$$

where $\nabla_{ad} = (\partial \ln T/\partial \ln p)_l$ and DQ/Dt corresponds to the rate of heating of the flux tube from non-adiabatic sources, such as radiative diffusion.

To summarise, the equations comprising the TFTM are (1.51), (1.56), (1.57) and the standard ideal gas law (1.5).

1.3.5 Buoyant Flux Tubes

The TFTM describes the general motion of a thin flux tube and is most appropriate for tubes in the convection zone. However, it does not give any insight as to why a flux tube embedded in the base of the convection zone will begin to rise in the first place. Analytical work by Parker (1955)

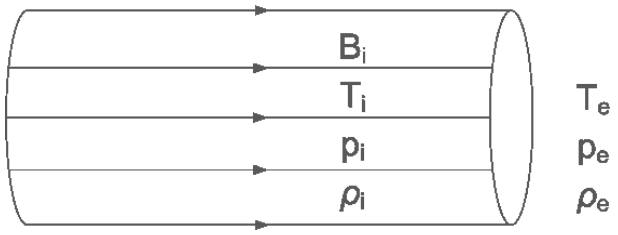

Figure 1.13: A section of a horizontal, untwisted magnetic flux tube lying in an unmagnetised ambient fluid. The gas pressure, temperature and density of the plasma in the tube are p_i, ρ_i and T_i, respectively. Similarly, the gas pressure, temperature and density of the ambient fluid are p_e, ρ_e and T_e. The magnitude of the flux tube's field is given by B_i.

gives the conditions under which a flux tube will be buoyant and rise through the solar interior.

Parker (1955) considered a horizontal, untwisted flux tube lying in the solar convection zone, as shown in figure 1.13. At a height z the external temperature is T_e, the external gas pressure is p_e, the internal gas pressure is p_i and the flux tube has a magnetic field strength B_i. We assume that

- the tube is in thermal equilibrium with its surroundings and, thus, $T_i = T_e$ (for simplicity we will drop the subscript from the temperature variable);

- there is lateral pressure balance between the tube and the environment such that

$$p_e = p_i + {B_i}^2/2\mu. \tag{1.58}$$

Eliminating the gas pressures from (1.58), using the ideal gas law, yields

$$(\rho_e - \rho_i)\, RT = {B_i}^2/2\mu. \tag{1.59}$$

Given that the right-hand side is greater than zero, we must have $\rho_e > \rho_i$. Hence, the tube is lighter than the ambient plasma and feels a buoyancy force of $(\rho_e - \rho_i)\, g$ per unit volume. The buoyancy force will cause the tube to start rising.

If only a section of the tube satisfies the given assumptions, only that part of the tube will begin to rise. This can lead to the tube becoming curved and, therefore, it will experience a restoring downwards tension force. The resulting tension force is dependent upon the length over which the tube is buoyant. If a segment of length L is buoyant, the tension force will be ${B_i}^2/\mu L$. Buoyancy will be the dominant force if

$$(\rho_e - \rho_i)\, g > {B_i}^2/\mu L. \tag{1.60}$$

Substituting (1.60) into (1.59) we find that the tube will continue to rise under buoyancy if

$$L > 2RT/g. \tag{1.61}$$

The pressure scale height is defined as

$$\Lambda(z) = \frac{p(z)}{\rho(z)\, g} = \frac{RT(z)}{g}, \tag{1.62}$$

and is the vertical distance over which the pressure falls by a factor of e. Thus, we can reformulate the criterion for buoyancy (1.61) in terms of the pressure scale height to give

$$L > 2\Lambda. \tag{1.63}$$

This tells us that, if the buoyant segment of the tube is longer than twice the local scale height, the segment will overcome the restoring tension force and rise.

As stated in section1.3.4, the pressure scale height decreases as the distance from the base of the convection zone increases. In the case of simulations, flux tubes initialised deeper in the convection zone will require a larger axial length to be buoyant if they are to rise uninhibited by the restoring tension force. In reality, the buoyant region of the tube in emergence simulations is always much greater in length than 2Λ.

1.4 Aim of Thesis

In this thesis, we will be presenting results from numerical simulations of emerging flux. Our aim is to test the robustness of findings from simulations to date upon the seed magnetic field. More explicitly, we will be investigating how variations in the subsurface magnetic field initialisation modify the emergence process and the resulting atmospheric field.

In chapter 2, we will discuss our present understanding of flux emergence events. Our knowledge comes from results of simulations and observations. In section 1.1, we gave a qualitative description of observed flux emergence events but the observational discussion in chapter 2 will take a quantitative approach. At the end of this chapter, we will identify the areas where result robustness has not been checked. Individual chapter objectives have been formulated from some of the identified areas.

In chapter 3, we will present the numerical code we will be using to carry out the simulations. The code solves the three-dimensional MHD equations discussed in section 1.2 and has been used for a number of studies, including previous flux emergence simulations.

1.4 Aim of Thesis

In chapter 4, we will consider the hydrostatic equilibrium of the ambient fluid in our simulation domain. The atmospheric stratification used in our simulations has been used in other flux emergence simulations but its numerical implementation does not result in a perfectly static environment. In this chapter, we will look for a better analytical stratification, which will result in fewer numerical errors when implemented.

In our experiments, the seed magnetic field will take the form of one or more twisted flux tubes. In section 1.3, we introduced the definitions of a flux tube's magnetic field strength and twist. We have chosen to test four areas of the magnetic flux initialisation for robustness. These are as follows:

Chapter 5: Magnetic field strength and twist of a constant twist flux tube;

Chapter 6: Constant versus non-constant twist of a flux tube;

Chapter 7: Increased complexity of the seed field through the use of two flux tubes.

Each of these chapters will describe the particular simulation model being used, present the results from the simulations and conclude by considering what the results tell us about the robustness of results from previous simulations.

Finally, in chapter 8 we will summaries the findings of chapters 4, 5, 6 and 7 in the context of result robustness. We will also present ideas for future flux emergence work.

Chapter 2

Simulations & Observations

The birth, growth and decay of solar active regions is a continual process. In section 1.1, we discussed the development of sunspots, the most visual element of newly emerging flux. It is widely believed that bundles of flux in the form of buoyant toroidal flux tubes rise through the solar interior and erupt into the atmosphere, with sunspots marking the location of each tube's intersection with the photosphere. Once into the atmosphere, observations show that the newly emerged flux expands to form an AFS.

Many simulations have been carried out with the aim of understanding flux emergence. Of specific interest to this thesis, are those that consider largescale, localised flux emergence and the subsequent atmospheric expansion process. By "localised" we mean that they mostly consider the emergence of a single active region and do not simulate global flux emergence. Additionally, these simulations ignore meridional flow and differential rotation since their modelling domains start in the upper layers of the convection zone.

Simulations of localised emergence mainly consist of a stratified domain representing the solar interior and one or more atmospheric layers. Magnetic flux is initialised either in the form of a sheet or a tube within the solar interior. Through imposed velocities or non-equilibrium with the environment, the flux rises through the solar interior and, depending upon whether certain conditions are met, emerges into the atmosphere.

In this chapter, we will discuss the results of previous flux emergence simulations. Figure 2.1 categories the experimental papers discussed in this chapter according to their basic setup. To determine how well these simulations recreate the solar flux emergence process it is necessary to compare their results with observations of flux emergence. Hence, where possible, we will consider the simulation results alongside measurements from observations.

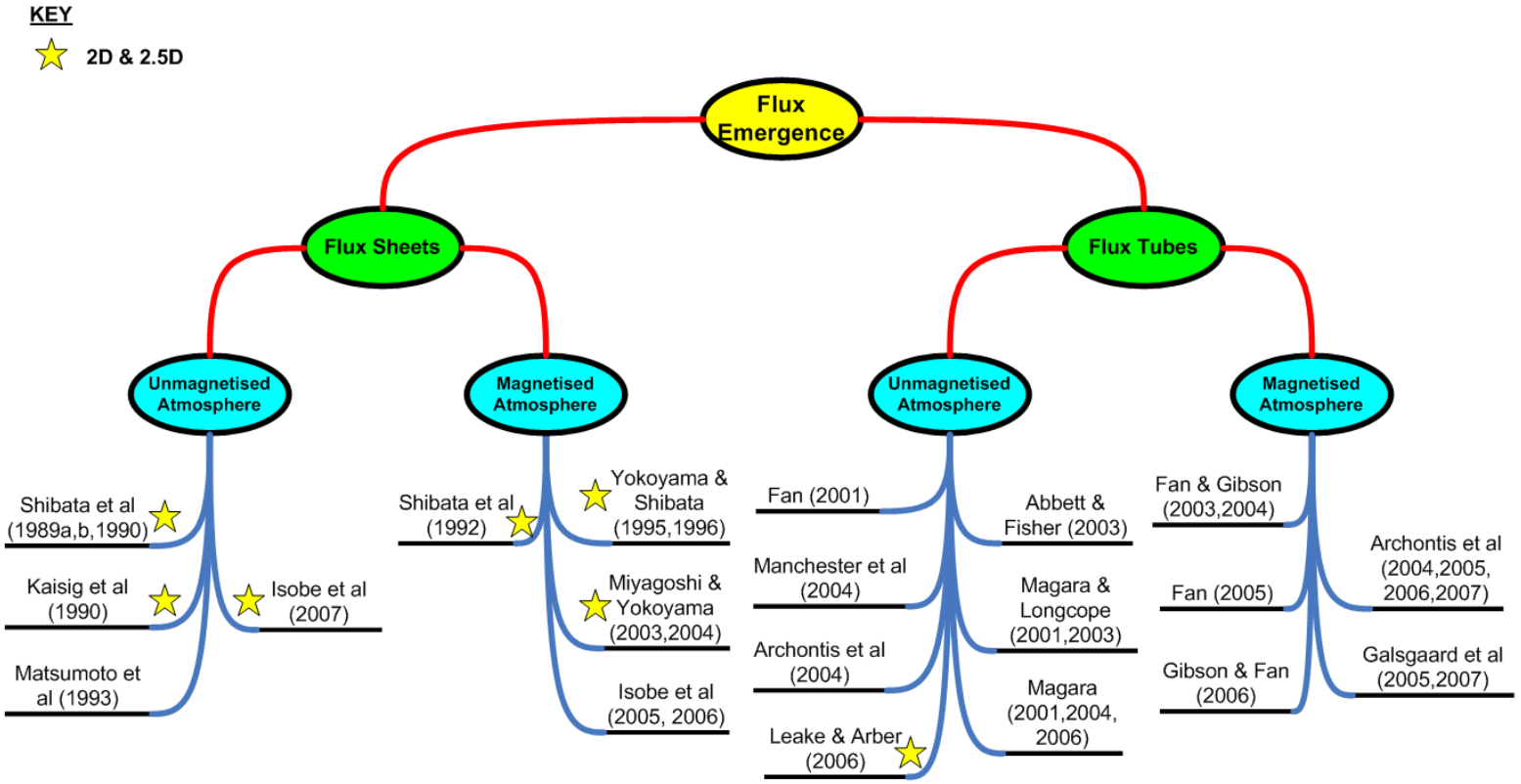

Figure 2.1: Tree diagram identifying the basic experiment setup of the simulation papers discussed in this chapter. The papers containing 2D and 2.5D simulations are indicated by a yellow star. All of the remaining papers carry out 3D experiments.

We note that, with the exception of Leake and Arber (2006), all simulations have been performed under the MHD approximation, whereby the atmosphere of the Sun is represented by a fully ionised plasma consisting of electrons and ions only. For the main part, the Sun is at temperatures where the gas is fully ionised and only in cooler regions, say the chromosphere, should partial ionisation be taken into consideration. The flux emergence simulations discussed in this chapter model the Sun's interior and multiple layers of the Sun's atmosphere. It is, therefore, simpler to model all regions as being fully ionised and this is why the MHD approximation is used in the majority of experiments.

This chapter is laid out as follows: In section 2.1 we will consider mainly early experiments, which simulated the emergence of horizontal flux sheets. Section 2.2 presents the results from two-dimensional (2D) and three-dimensional (3D) simulations of emerging flux tubes. In section 2.3 we will discuss the effects when emerging flux expands into an atmosphere that contains a pre-existing flux system. Finally, section 2.4 will summarise the general findings of the papers and identify areas of the simulations where variations in the seed magnetic field may affect the results.

2.1 Emerging Flux Sheets

These experiments considered a uniform horizontal flux sheet, placed in the lowest layer of the simulation domain. In the early experiments, the domain consisted of two stratified layers: a cool photosphere or chromosphere and a hot corona. It was not until later experiments that the sheet was initialised in a convectively unstable solar interior, with two overlying atmospheric regions. Regardless of where the sheet is initialised, an instability must occur before dense magnetic flux can be transported into the upper atmosphere.

A uniform flux sheet is force-free and, within the simulations discussed here, is chosen to be in pressure and density equilibrium with the surrounding plasma. In order to perturb the system, a vertical velocity must be imposed on the flux sheet. Shibata et al. (1989a) impose a sinodal vertical velocity, with wavenumber parallel to the magnetic field, and this causes the flux sheet to take on an undulating characteristic. Gravity allows downflows of plasma along the magnetic loops, resulting in rarefied apices and dense valleys. Since k is parallel to $\mathbf{B}$, the draining drives the nonlinear Parker instability or magnetic buoyancy instability. The concave sets of loops expand both horizontally and vertically but a central set become dominant, expanding to a much greater degree than the other sets of loops.

During the initial emergence stage, strong downflows of $\sim 1 - 3\ \mathrm{km\ s^{-1}}$ occur. Observations of emerging flux also reveal strong downflows of $1 - 2\ \mathrm{km\ s^{-1}}$ near pores in the photosphere during the initial emergence stage (Brants 1985).

2.1 Emerging Flux Sheets

The rise of the loops through the photosphere occurs with velocity ≤ 1.4 km s^{-1} (Shibata et al. 1989b), coinciding with observations giving a velocity of < 1 km (Kawaguchi and Kitai 1976; Brants 1985). The rise of the loops is described as having a self-similar pattern of emergence in that the velocity of the loops increases linearly with height, first under an exponential time dependence and then with a power law time dependence (Shibata et al. 1989b). Once the loops reach a height of 4000 km their rise velocity has increased to $10 - 15$ km s^{-1}, similar to observed values (Kawaguchi and Kitai 1976; Bruzek 1964, 1969; Chou and Zirin 1988). During the self-similar expansion phase, the density and field strength have power law distributions $\rho \propto z^{-4}$ and $B_x \propto z^{-1}$ respectively, where z is the height measured from the base of the flux sheet and the field is initially in the x-direction.

The background gas pressure falls sharply with height in the photosphere but less steeply in the corona. As the loops expand vertically through the photosphere their magnetic pressure continually exceeds the local gas pressure and they experience an acceleration with higher altitude. Once the loops reach the corona the difference is smaller and the greater curvature of the loops gives a significant oppositely acting tension force, thus the loops decelerate. The acceleration stage of the loops is estimated to have a duration of $10 - 20$ mins but this will be dependent upon the height of the corona in the simulation (Shibata et al. 1989b).

The expansion process continues to generate downflows along the loops. For example, loops at a height of 4000 km experience downflows with velocities of $30 - 50$ km s^{-1} (Shibata et al. 1989a,b) and these values are consistent with observations (Bruzek 1964, 1969; Chou and Zirin 1988). For loops with a height greater than 2000 km, the downflows exceed the local sound speed and produce shock waves near the footpoints of the loops. Shibata et al. (1989b) find both fast and intermediate shocks. For an intermediate shock, the magnetic field component parallel to the shock plane reverses direction across the shock. For the fast (slow) shock, the field strength increases (decreases) across the shock but both a decrease and an increase are possible for an intermediate shock.

Kinetic energy flux carried by the downflows is converted to thermal energy at the footpoints of the loops by the shock waves there. Shibata et al. (1989b) suggest that the kinetic energy prior to conversion could amount to 6×10^6 ergs cm^{-2} s^{-1} and, therefore, partly explain chromospheric heating in bright plages of emerging flux regions.

There is a decrease in magnetic and gravitational energies of $\sim 4 \times 10^9$ ergs cm^{-2} s^{-1} each within the computational domain as the loops freely expand and try to reach a lower magnetic energy state. The corresponding increase in energy occurs as a slight increase in the kinetic energy but mainly a rise in the thermal energy through compressional and shock heating. It is believed by Shibata et al. (1989b) that the release rate of the magnetic energy is sufficient to explain enhanced activities within emerging flux regions. When the rising loops were constrained by an overlying

parallel magnetic field it is expected that there will be a reduction in magnetic energy released by expansion.

Increasing the wavelength of the initial velocity perturbation causes the following (Shibata et al. 1989a):

- a decrease in the curvature of the expanding loops and, therefore, a decrease in the deceleration of the loops when they reach the corona;
- an increase in the velocity of the downflows.

Alternatively, perturbing just a small section of the field will cause neighbouring parts of the field to suffer from the Parker instability, though onset will be slightly later and therefore loops in the initially affected region will dominate the expansion and suppress the rise of loops in other Parker unstable regions (Shibata et al. 1989a).

Horizontal shearing motions, applied at the photosphere in a perpendicular direction to the magnetic field, are also found to initiate the Parker instability (Kaisig et al. 1990). Expansion into the atmosphere occurs in the same manner as observed in the "imposed velocity" simulations discussed above. Increasing the distance over which the shearing motion is imposed results in the lose of self-similarity during the expansion. The loops retain the same horizontal size during their expansion, rising into the atmosphere with a approximately constant velocity. No shockwaves are produced at the loop footpoints. Together these findings indicate that, under long-wavelength perturbations, the magnetic flux sheet expands into the atmosphere through a series of hydrostatic equilibria.

The 3D study by Matsumoto et al. (1993) varies the initial velocity imposed on the flux sheet such that the wavenumber is still parallel to the magnetic field but varies in intensity in the perpendicular horizontal direction. The evolution of the sets of loops in the regions of maximum velocity intensity occurs in the same manner as discussed above. However, for the sets of loops where the vertical velocity intensity is smaller, the onset of the buoyancy instability is delayed. The material between emerging loops is compressed during their horizontal expansion and, thus, dense filaments are formed parallel to the magnetic field. These may correspond to arch filament systems recorded in observations (Bruzek 1967).

The simulations of Shibata et al. (1989a,b) and Matsumoto et al. (1993) initialised the flux sheet in the photosphere, a region that is stable against convective motions. However, the flux of active regions originates from below the photosphere, in the convection zone. This deeper region, as the name suggests, is convectively unstable. The modified setups of Shibata et al. (1990) and Kaisig et al. (1990) aimed to take this into account by placing the flux sheet in a convectively unstable layer, above which lies a stable photospheric layer and then a hotter coronal layer. Alone, this

change makes very little difference to the emergence process. The initial velocity perturbation brings the flux to the photosphere and allows the conditions for the Parker instability to develop and, thus, emergence ensues. Kaisig et al. (1990) also considered a flux sheet in the photosphere with a convective region lying below. The convective motions transported some of the flux down into the convection zone and acted to push other parts of the sheet higher into the photosphere. The flux sheet again becomes subject to a magnetic buoyancy instability and expansion ensues.

Shibata et al. (1990) add a photospheric radiative cooling effect to their model, whereby positive thermal perturbations decay by radiation on the timescale $0.05H/c_s \exp\left((z-3H)^2/2H^2\right)$, with the photospheric scale height $H = 200$ km and sound speed $c_s = 10$ km s^{-1}. Now, the initial downflows along the rising loops trigger convective collapse of the vertical parts of the flux tube in the photosphere. This creates long-lived downflows and an increased field intensity there. The emerging flux initially had a strength of ~ 600 G but through the convective collapse this becomes amplified to ~ 1000 G in the vertical sections over a period of 14 mins.

The inclusion of cooling also results in the horizontal expansion near the photosphere being constrained and the vertical rise velocity of loops in the chromosphere being slightly smaller. The constrained horizontal expansion is due to the large converging flow towards the vertical flux regions. The results from the cooling cases do not fit well with observations though. The downflow speeds in the photosphere are too large by a factor greater than two and the size of the emerging flux region produced is too small by a factor of approximately three. The authors contribute these deviations to the unrealistic convection zone model and the low spatial resolution of observations. Once the flux reaches the corona, horizontal expansion resumes and after 27 mins there is little difference in the volume of the corona containing emerged flux between the cooling and non-cooling cases.

During the simulations discussed above, the sets of emerging loops come into contact with each other as they expand horizontally in the atmosphere. Neutral sheets form at the interface between neighbouring loops but no reconnection is ever reported. Although no resistivity is explicitly included in the simulations by Shibata et al. (1989a) and Shibata et al. (1990), the experiments of Shibata et al. (1989b) do include it in a uniform manner. The simulations of Isobe et al. (2007) explicitly consider the reconnection between sets of emerging flux loops. The horizontal domain is much larger than in previous simulations and the initialising random vertical velocity applied to the flux sheet creates many more undulations. As before, draining instigates the Parker instability and the sets of loops emerge into the low atmosphere, expanding horizontally and vertically as shown in figure 2.2. Reconnection occurs in the valleys between neighbouring sets of loops and this allows originally dipped parts of the flux sheet to emerge into the atmosphere, figure 2.2 (c). The tension force acting on reconnected fieldlines causes upflows comparable to the local Alfvén speed and the temperature of the reconnection outflow is enhanced in comparison to the surrounding plasma. These results fit with observations of Ellerman Bombs.

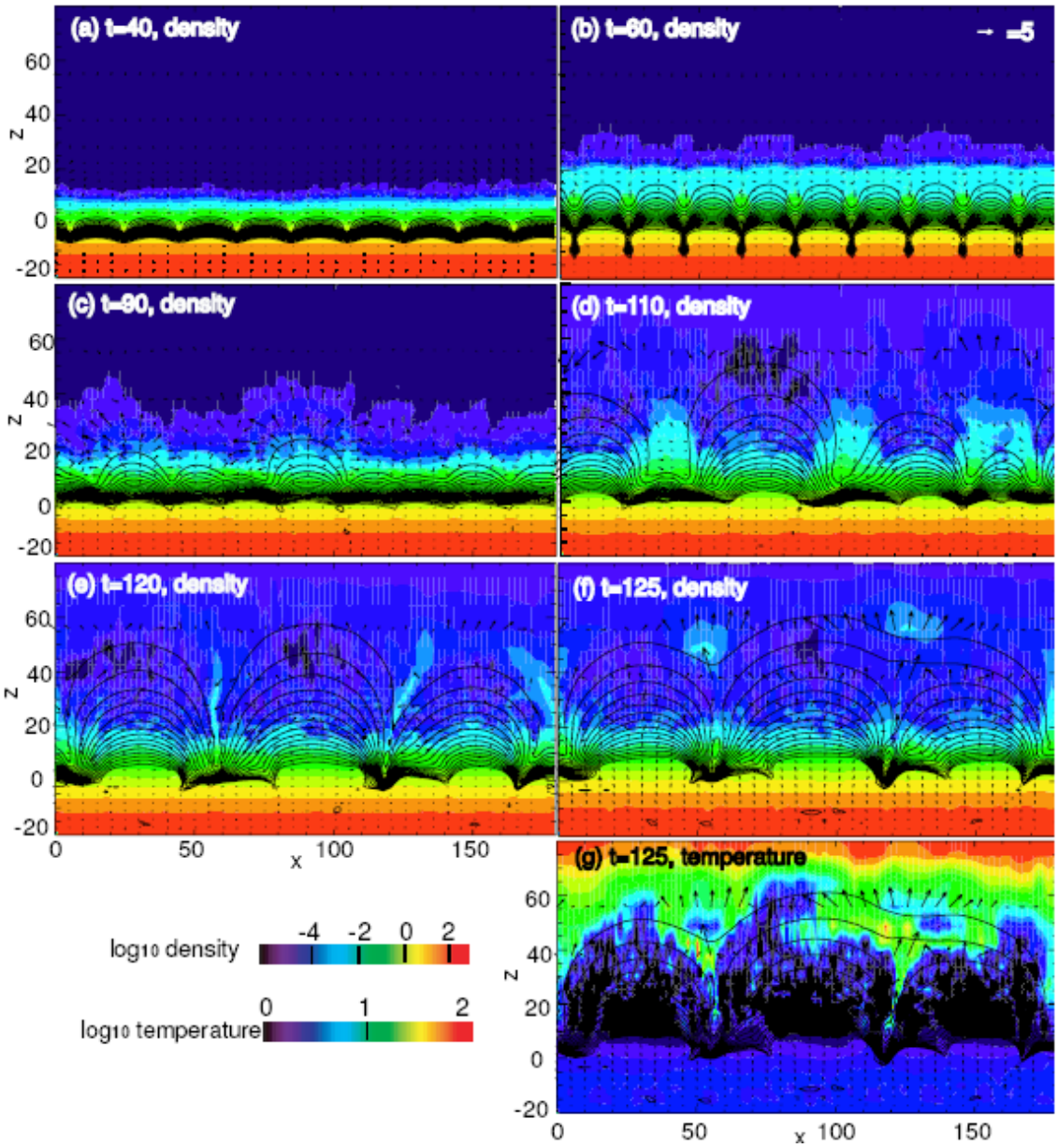

Figure 2.2: Reconnection between sets of emerging magnetic loops results in both cold and hot ejections of plasma. Fieldlines are given in black and the colour map in images a-f gives density and in image g gives temperature. This graph is Fig.1 from Isobe et al. (2007).

Post-reconnection, the flux sheet undergoes the Parker instability for a second time but now only some sets of loops develop into large Ω-shaped loops. Again, mass drains along these loops and dense material accumulates at the valleys between sets of loops. Horizontal expansion of the rising loops causes the accumulated material to be compressed and, thus, it forms elongated structures of cold dense plasma between the sets of loops, figure 2.2 (e). Once these large loops come into contact with each other, reconnection occurs and the cold plasma is ejected into the atmosphere followed by hot reconnection jets, figure 2.2 (g). The cold and hot ejections may be observed as Hα and X-ray jets, respectively. This reconnection occurs higher in the atmosphere than the first reconnection events and may be the cause of observed transition region explosive events. The successive bouts of reconnection allow the whole of the flux sheet to emerge into the atmosphere, forming one very large loop with a width of $\sim 30\ \mathrm{Mm}$.

2.2 Emerging Flux Tubes

Convective motions are likely to fashion the subsurface magnetic field into random bundles of twisted fieldlines. Although flux sheet simulations provide an insight into magnetic buoyancy instabilities and the expansion of emerged flux into the atmosphere, it is important to consider how these results would vary if bundles of flux replaced the horizontal flux sheet.

The simulations in this section represent the subsurface bundle of flux by a twisted flux tube. The magnetic field of the flux tube is very ordered in comparison to a random bundle of fieldlines. However, the twist of the tube's field brings new aspects to the experiments since plasma can drain into concave portions of fieldlines rather than just along fieldlines, towards the tube's footpoints.

The flux tube is initialised in the solar interior but, for the simulations discussed within this section, this region is chosen to be marginally stable to the convective instability.

There are several options for the initialisation of a flux tube within the convection zone.

- **Thermal Equilibrium** The flux tube is defined such that the magnetic forces in the tube do not balance each other. The gas pressure in the tube is chosen such that its gradient, together with the magnetic forces, results in force balance. The temperature in the tube is chosen to match the external plasma and, therefore, the density in the tube must vary from that of the environment. The direction of the gas pressure gradient in the tube will determine whether the tube is buoyant or overdense compared with the background plasma and, hence, whether the tube will rise or sink when the simulation begins.

- **Mechanical Equilibrium** The flux tube is chosen to be force free, such that the magnetic forces balance. If the density and pressure inside the tube are chosen to match the external

stratification, the tube is in mechanical equilibrium. Hence, any initial motion in the simulation domain must come from outwith the flux tube. A vertical velocity is usually imposed on the tube to force it to rise towards the surface. (If the pressure is chosen to vary from the external stratification, it is possible to make the tube buoyant by setting the systems in thermal balance.)

- **Equal Entropy** The flux tube is not required to be force-free. The total pressure in the tube is set equal to the background pressure, thus the gas pressure in the tube, p_i, can be determined. The density in the tube, ρ_i, is then calculated by satisfying $p_i/{\rho_i}^{\gamma} = C$. Given that the density and gas pressure in the tube are known, the temperature inside the tube can also be calculated. The flux tube has an element of buoyancy but is not in thermal equilibrium, thus this method can be thought of as falling midway between thermal and mechanical equilibrium.

Below the surface of the Sun, where $\beta > 1$, flux tubes cannot be assumed to be force-free and, therefore, mechanical equilibrium is often ruled out for flux tube initialisation. Thermal equilibrium is the easiest state to prescribe and is, therefore, the most readily used.

Within this section we will consider first 2D simulations, of which there have been few studies, and secondly fully 3D simulations.

2.2.1 Two-Dimensional (2D & 2.5D)

This section considers 2D and 2.5D experiments. In 2D simulations, the coordinate system has two directions and, correspondingly, vectors have only two directions. In 2.5D simulations, the coordinate system and associated vectors have three directions but the partial derivatives with respect to one of the coordinates, y say, are chosen to be always zero. This effectively reduces the coordinate system to 2D since all quantities are uniform in the y direction. It is standard to align the axis of the tube with the "uniform" coordinate.

Magara (2001) places a Gold-Hoyle flux tube in the upper layers of the convection zone, above which lies a photosphere and corona. The flux tube has a defined radius at r_t and, beyond this, an external field reduces to zero at large radii. The gas pressure inside the tube is reduced below the corresponding external gas pressure but the tube is chosen to remain in thermal equilibrium with the environment. Thus, at the beginning of the simulation, the flux tube is buoyant and wants to rise. The dynamical evolution of the tube is classified into four distinct phases. The first phase sees the gradual increase in the rise velocity of the tube, which can be explained by a rigid cylinder model. The tube front takes ~ 25 min to rise from a depth of 1200 km to the photosphere. The background density in the photosphere falls off very quickly with height and, thus, the tube is severely overdense compared with the new surroundings. The subadiabatic

characteristic of the photosphere prevents the overdense tube rising under its established velocity. Hence the tube begins to decelerate when it comes into proximity of the photosphere, entering the second evolution phase. The top of the tube flattens since it cannot proceed in the photosphere but tube plasma, with high velocity, is still rising below it. Rising tube plasma becomes deflected sideways and, thus, the flattened region increases in area with time. The magnetic field in the flattened region lies parallel to the photospheric plane.

Magara (2001) states that the flattened surface becomes subject to the Rayleigh-Taylor instability, whereby heavier photospheric plasma is lying on top of a magnetic layer with lighter plasma. This instability enables the magnetic field to emerge into the atmosphere, where it begins to expand since the background gas pressure is weaker than the magnetic pressure of the tube. The post emergence expansion allows the draining of plasma from the expanding layers and, therefore, decreases the downward magnetic pressure on lower layers. These lower layers are then free to rise into the atmosphere under the Parker instability, as described in section 2.1. Analogous to a shock tube problem, an excess magnetic pressure exists below the tube front and, hence there is a driver for the expansion in the atmosphere, which occurs in a 2D manner. The advancement into the atmosphere and the subsequent second acceleration of the tube front comprise the third and fourth phases respectively.

Emergence becomes suppressed before the entire magnetic field of the tube has advanced into the photosphere and, thus, some field remains trapped within the convection zone. In particular the axis of the tube does not advance beyond the upper layers of the convection zone. This occurs because the Parker instability shuts off when the wavelength of the undulating field, λ, becomes smaller than some critical wavelength, λ_{cr}. For $\beta \sim 1$, the instability is suppressed when

$$\lambda < \lambda_{cr} \sim 10\Lambda, \tag{2.1}$$

where Λ is the local pressure scale height. A smaller undulation is associated with a stronger tension force and, thus, for smaller wavelengths it becomes possible to turn off the instability. Magara (2001) finds that fieldlines closer to the tube axis, and trying to emerge at a later time, have a smaller undulation wavelength so remain trapped in the photosphere. Proposals for lifting the axis into the atmosphere include allowing draining of material in the direction of the axis by moving to 3D simulations and increasing the strength of the external field. The study by Krall et al. (1998) found that a strong vertical ambient field can reduce the expansion and fragmentation of a flux tube rising through the atmosphere. Increasing the external field may have the same effect on the subsurface flux tube but this will not help the axis drain or increase the undulation wavelength of the axis and, therefore, is unlikely to solve the problem.

Of the field that does emerge, the first fieldlines have a direction almost transverse to the neutral line, while later emerging fieldlines are sheared. This fits with the observations reported by

Kurokawa (1987) and Schmieder et al. (1996). The changing orientation of the fieldlines is as a direct result of the twist of the fieldlines about the tube's axis and will be discussed in more detail in section 2.2.2. The photospheric field has a strength of 600 G but observations give individual magnetic elements having strength of over 1 kG in a typical sunspot's umbra (Solanki 2003). These simulations do not include the physics for radiative cooling but the results of flux sheet emergence simulations by Shibata et al. (1990) have shown that this cooling can increase the field strength to observed values.

Simultaneously decreasing the twist and field strength of the tube, results in the flux tube having approximately the same rise within the convection zone, where the plasma-β is large and magnetic forces are dominated by the fluid forces. However, once into the atmosphere the tube rises and expands more slowly since its magnetic pressure is weaker and cannot drive the expansion at the same pace. Similarly, modifying the radius and twist of the tube only causes variations once the tube reaches the top of the convection zone. The tube with the smallest radius and largest twist does not expand into the atmosphere although the wavelength of its outer field does contravene (2.1). In this case the magnetic pressure of the field does not exceed the surrounding gas pressure. Hence, the field lacks a vertical driver and, therefore, cannot make a strong expansion.

The 2.5D simulations of Leake and Arber (2006) include a Newton cooling term in the adiabatic energy equation, which forces the temperature to relax to some predefined value whenever and wherever it deviates. This term models the effects of thermal conduction, radiative transfer and coronal heating without worrying about the small-scale physics of each individual mechanism. The timescale over which the forcing takes place reflects the local cooling and heating mechanisms and, therefore, is chosen to be a function of density. Practically instantaneous heat transfer results in the magnetic buoyancy instability occurring more quickly, once the rising magnetic field reaches the photosphere. This is considered further in section 2.2.2. As the magnetic field emerges into the atmosphere it is heated to its original temperature rather than being allowed to cool as it expands adiabatically. This retains a more realistic atmosphere during the simulation. However, since flux emerges into the atmosphere at an earlier time the buoyancy instability also quenches earlier.

Leake and Arber (2006) also take into account the partial ionisation of the Sun's chromosphere by including Cowling resistivity ($\frac{1}{\sigma_c}$) in addition to Coulomb resistivity($\frac{1}{\sigma}$). Cowling resistivity gives a measure of the diffusion of the magnetic field due to collisions of ions and electrons with neutrals and acts perpendicular to the field. Coulomb resistivity only considers collisions between ions and electrons and acts on the current parallel to the magnetic field. In the standard MHD induction and energy equations, $\frac{1}{\sigma}\mathbf{J}$ and $\frac{1}{\sigma}\mathbf{J}^2$ are replaced by $\frac{1}{\sigma}\mathbf{J}_{\parallel}+\frac{1}{\sigma_c}\mathbf{J}_{\perp}$ and $\frac{1}{\sigma}{\mathbf{J}_{\parallel}}^2+\frac{1}{\sigma_c}{\mathbf{J}_{\perp}}^2$ respectively. $\frac{1}{\sigma_c}$ must be recalculated after every iteration of the simulation from an estimation of the fraction of neutrals, itself derived from the plasma variables ρ, T and $\mathbf{B}$. The inclusion of the diffusion layer in the chromosphere results in the magnetic field emerging into the atmosphere at a faster rate. Fieldlines reach greater heights in the corona and the magnetic field is more diffuse. More importantly,

the field emerging into the corona is force free, with all cross-field currents dissipated by ion-neutral collisions when the magnetic field passes through the chromosphere. This is concurrent with observations of coronal magnetic fields that suggest them to be predominantly force free (Metcalf et al. 1995; Georgoulis and Labonte 2004). From observations, it is estimated that the field becomes force free when it reaches a height of $\sim 400 - 1000$ km above the photosphere. However, the simulation results yield a height of ~ 2000 km but this discrepancy may be as a result of the simulation not being fully 3D.

In these simulations, the flux tube must rise as a whole due to the reduced dimensionality of the experiment. This prevents draining of material from any portion of the tube's axis and may be the reason why the axis does not emerge into the atmosphere (Magara 2001). Additionally, the magnetic buoyancy instability occurs along the whole length of the tube and, therefore, there is no possibility of forming distinct sunspots. Solutions to these limitations are addressed in the next section, in which we consider 3D simulations. Finally, it is important to note that 2D models have a tendency to build enhanced flows due to the lack of the extra degrees of freedom associated with three dimensions (Dorch 2007).

2.2.2 Three-Dimensional (3D)

Here we consider fully 3D simulations, whose coordinate system and vectors have three directions. There is no imposed uniform direction in these experiments and this enables the simulations to be initialised such that only selected portions of the flux tube will rise. This should facilitate draining of material from sections of the tube and, since the tube is not rising as a whole, should produce an active region which more closely resembles sunspots. We consider two different initialisations for the flux tube: thermal equilibrium and mechanical equilibrium.

Thermal Equilibrium

As discussed in section 2.2, a tube in thermal equilibrium will be more buoyant than its surroundings and will, therefore, rise. In the simulations considered in this section, the tube is driven towards the surface due to a buoyancy force.

The first 3D simulation of an emerging flux tube was carried out by Fan (2001). The tube has a uniform twist profile and, through the balance of radial gas pressure gradients with radial magnetic forces, it is buoyant along its length. To encourage the formation of an Ω-shaped loop the temperature of the plasma is decreased in the ends of the tube setting them in density equilibrium with their surroundings. The buoyant portion of the tube rises and, as in the 2D simulations, both the front and axis of the tube experience a deceleration in their vertical velocity when the tube enters

the photosphere due to the stable stratification of the isothermal atmosphere. The front of the tube then undergoes a magnetic buoyancy instability which enables it to expand into the unmagnetised atmosphere but the axis remains constrained in the lower photosphere.

Fan (2001) observes that as the tube emerges from the solar interior, the horizontal magnetic field appears to undergo a rotation at the photospheric boundary, in line with the 2.5D results of Magara (2001). The apparent rotation occurs because the tube's field is twisted and each orientation observed can be attributed to a different part of the tube crossing the boundary. When the top of the tube passes through the photospheric plane, the horizontal field is concentrated in a bipolar region with a north-south orientation. By the time of the arrival of the axis at the photosphere, the horizontal field is practically parallel to the polarity inversion line. As the field below the axis passes through the photosphere, the orientation moves away from parallel to a south-north direction. Comparisons to the potential field expected from extrapolations of the photospheric boundary field reveal the atmospheric field to be far from potential (Abbett and Fisher 2003).

The 2D and 2.5D simulations of emerging flux tubes, see the tubes rising as a whole. Therefore, there is no possibility for the formation of a realistic bipolar region, whereby a limited region of the tube intersects the photosphere and the tube's feet remain deep in the convection zone. Hence, the simulation by Fan (2001) identifies some interesting photospheric features that could not occur previously due to the limited dimensions of the experiments. Horizontal shearing motions in the photospheric plane are found to arise naturally when a magnetic field with components parallel to the tube's axis expands into a stratified atmosphere. These motions cause opposite field polarities to move parallel to the neutral line in opposite directions. Thus, the magnetic field becomes concentrated in east and west locations near the edge of the ellipse of fieldlines that have risen into the photosphere. At these two concentrations, the field is vertical and the axis of the tube intersects the interface between the solar interior and the photosphere. The upper part of the tube expands extensively in the corona while the lower part of the tube remains highly compressed in and below the photosphere. A large vertical gradient occurs in the axial component of the field and this results in a magnetic tension force within the emerging tube that drives the shearing motions (Manchester et al. 2004). Observations by Strous et al. (1996) corroborate the results of Fan (2001), finding a shear velocity pattern that concentrates the photospheric field in east and west corners. Observations with SUMER reveal significant velocity shear in active region loops expanding high into the transition region (Chae et al. 2000).

The flux tube chosen by Fan (2001) is left-hand twisted and is more commonly found in the northern hemisphere of the Sun. According to Joy's law we would expect there to be a tilt angle between the east and west intensity spots, with the leading west spot being further south than the following east spot. Although Fan (2001) does see a tilt between the two spots, the reverse of Joy's law is actually observed. The cause of the tilt in the simulations is due to the twisted nature of the magnetic field lines. The author concludes that the lack of Coriolis force in the model prevents

the correct tilt from being achieved.

As the loops emerge into the atmosphere, the plasma associated with the field experiences rapid cooling due to adiabatic expansion. The plasma then flows away from apicies and down the loops as a result of trying to reach hydrostatic equilibrium along the field line. Some of the downflowing plasma collects in the valleys of still rising, concave fieldlines but where the flux tube is more vertical, in the east and west spots, faster downflows of $\sim 20\,\mathrm{km\,s^{-1}}$ are seen. As in the flux sheet simulations by Shibata et al. (1989b), this speed is greater than the local sound speed and shock fronts develop just above the photosphere.

The study by Archontis et al. (2004) uses the initial conditions of Fan (2001). They find that the advance of the buoyantly rising tube is to some extent counteracted by a drag force, which is exerted on the tube by the surrounding solar interior medium. Additionally, the axial field strength of the flux tube diminishes during its rise following the law of magnetic flux conservation

$$B_y\left(z\right) = B_y\left(z_0\right)\rho\left(z\right)/\rho\left(z_0\right), \tag{2.2}$$

where z_0 is the initial height of the tube's axis, B_y is axial field strength and ρ is density. Although all components of the magnetic field decrease during the tube's rise, compression at the front of the tube results in a slower decrease in the azimuthal component. Thus, by the time the tube reaches the photosphere, the pitch of the fieldlines at the front of the tube has increased away from the axial direction.

Some observations of active regions give values of 600 G for the rising magnetic field close to the photosphere and, thus, a plasma-β of 4 for the mass elements reaching the photosphere. These values are approximately reproduced by the simulation of Archontis et al. (2004) for a tube with axial field strength of 3.77 kG at an initial depth of 1700 km.

Archontis et al. (2004) find that the onset of the magnetic buoyancy instability observed by Fan (2001) is precisely given by the following criterion (Newcomb 1961; Yu 1965; Thomas and Nye 1975; Acheson 1979)

$$-H_p\frac{\partial}{\partial z}\left(\log B\right) > -\frac{\gamma\beta\delta}{2} + \tilde{k_\parallel}^2\left(1+\frac{\tilde{k_\perp}^2}{\tilde{k_z}^2}\right), \tag{2.3}$$

with the pressure scale height, H_p, the ratio of specific heats, γ, the plasma-β and perturbations with wavevector $\mathbf{k}$ (where $\tilde{k_\parallel}$ and $\tilde{k_\perp}$ are the horizontal components parallel and perpendicular to the magnetic field and $\tilde{k_z}$ is the vertical component). The superadiabatic excess, δ is given by $\delta = \nabla - \nabla_{ad}$, where ∇ is the actual logarithmic temperature gradient in the equilibrium stratification and ∇_{ad} is its adiabatic value. This criterion describes the instability when perturbations bend the fieldlines and satisfying it allows over-dense material to be transported into the upper atmosphere.

The criterion describes the competition between the destabilising gradient in the magnetic field and the convectively stable temperature gradient. Once the magnetic field reaches the photosphere, the temperature gradient varies very little. Therefore, the magnetic pressure must build up in the tube's uppermost field so that the plasma-β falls and the stabilising temperature gradient becomes less important, thus satisfying the criterion and allowing emergence. The righthand wave term of (2.3) indicates that if fieldlines become too bent, the tension force will additionally prevent the field from emerging. The inclusion of Newton cooling results in the stabilising effect of the convectively stable temperature gradient being lost and, therefore, the onset of a magnetic buoyancy instability occurs on a faster timescale (Leake and Arber 2006).

Once emergence is underway, expansion is seen to occur in a runaway fashion both in the horizontal and vertical directions (Archontis et al. 2004). Horizontal growth occurs at a slightly faster rate since in the vertical direction gravity acts to slow growth. In line with the results of Fan (2001), Archontis et al. (2004) measures strong vertical downflows of $\sim 14\ \mathrm{km\ s^{-1}}$ in the transition region and $\sim 24\ \mathrm{km\ s^{-1}}$ in the low corona. Observations of developing active regions give line of sight velocities of these orders (Brekke et al. 1997; Chae et al. 2000).

The expansion in the atmosphere causes the gas pressure and density of the tube's plasma to fall below that of the surrounding stratification. In the absence of any coronal heating mechanism or radiative transfer, the plasma remains cooler than its surroundings. The density of the plasma is 100 times greater than that of the pre-existing atmosphere at the front of the expanding volume. However, as in the flux sheet and 2.5D flux tube simulations, the high magnetic pressure gradient driving upwards prevents emergence from halting.

The photospheric signatures of the emerging flux tube reported by Fan (2001), discussed above, are reproduced by the simulations of Archontis et al. (2004). Post-emergence, isosurfaces of current reveal an **S** shaped current concentration lying in the lower photosphere along the tube's axial direction. Fieldlines wrapping around this current concentration indicate that the twist of the tube has been converted to writhe during the simulation. The development of writhe of the tube's axis is also seen by Fan (2001).

On a side note, a separate but related interesting feature has been observed in the buoyant tube experiments. The background stratification is chosen to be in hydrostatic equilibrium initially. At the start of the experiments the sudden upwards motion of the tube launches a compression wave towards the atmosphere (Archontis et al. 2004). The wave has small amplitude in the convection zone, but the steep temperature gradient in the photosphere causes the wave to grow in amplitude and steeped to form a shock wave. Within the isothermal photosphere, the post-shock speed closely follows an exponential law since the background density decreases exponentially with height. However, the overlying transition region is characterised by a steep temperature gradient and, therefore, the sound speed also increases sharply with height. Thus, the post-shock speed

increases at a slower rate before finally decreasing through the corona.

Manchester et al. (2004) choose to reduce the length over which the tube is buoyant and increase the flux in the tube, which results in a dramatic evolution of the magnetic field post-emergence. Largescale shearing flows pull the left and right sides of the emerged tube's field in opposite directions, parallel to the direction of the tube's axis. Thus, the expanding magnetic field becomes almost parallel with the neutral line. The fieldlines located above the tube's axis bulge upwards and have a large vertical displacement over a short horizontal distance and, as a result of the shearing motions, the core of the emerged region erupts upwards. This results in horizontal compression of the expanded volume, the subsequent development of a current sheet and ensuing reconnection. The reconnection occurs above the original axis of the tube and results in a secondary O-point developing in the erupting volume. Eventually, the original axis is lost when it is drawn into the growing current sheet at the base of the now, reforming tube.

Fieldlines of the erupting rope have no valleys, completing less than a full rotation in the corona, and, therefore, have little mass containment capability. Manchester et al. (2004) find the acceleration of the tube's new axis is driven by magnetic pressure but eventually the tube approaches a nearly force-free configuration. It is unlikely that the newly formed flux rope will be able to escape the corona without the aid of a further driving force. One possible driver could be procured from increasing the twist of the magnetic field and, thus, inducing a kink instability. Given the smaller buoyant tube region, it is unsurprising that the resulting active region is also smaller, with the sunspots situated closer together. The buoyant section bends more sharply and has fewer fieldline turns so the tube drains more efficiently than in the case of Fan (2001). Thus, it rises slightly higher into the photosphere prior to the onset of the magnetic buoyancy instability and the photospheric line of sight magnetic field develops a quadrupolar pattern.

Mechanical Equilibrium

As discussed at the beginning of section 2.2, employing a fluid velocity provides an alternative mechanism to buoyancy for driving the magnetic tube towards the surface. Magara and Longcope (2001) and Magara and Longcope (2003) modify the initialisation of the flux tube in the earlier 2.5D simulation by Magara (2001) by choosing the tube to be in mechanical equilibrium with the surrounding system. In Magara and Longcope (2001), the imposed velocity drives the middle of the tube upwards and the ends downwards for a period of ~ 3 min. The variation in the driving mechanism has little effect on the overall evolution of the flux tube. The tube rises towards the photosphere and emerges into the atmosphere, forming the classic magnetic bipole structure on the photospheric plane. Since the feet of the tube were driven downwards, the atmospheric unsigned flux reaches a maximum value once the axis crosses the photosphere. As in the simulation by Fan (2001), the opposing polarity regions separate and rotate towards a more axial direction. Surface

flows are initially transverse to the neutral line but this becomes more parallel as time continues. Thus, the distance between the positive and negative line of sight field concentrations increases with time. Magara and Longcope (2001) find a strong draining downflow of -2 km s^{-1} near the footpoints of the loops, which is inline with the emerging flux sheet results of Shibata et al. (1989b). As the field expands into the atmosphere, its density reduces due to both expansion and draining.

Again, the main upward driving force acting on the emerging loops is magnetic pressure but the draining of plasma from the crest of the field reduces the gravitational force opposing to the magnetic pressure and, thus, additionally helps lift the field. This lifting adds further draining and this continual feedback cycle gives continual acceleration. The portion of fieldlines under the axis rise through the convection zone but their velocity decreases to zero before they reach the photosphere because plasma is draining into their concave portions. Hence, these fieldlines become trapped below the surface. These results from Magara and Longcope (2001) and Magara and Longcope (2003) fit well with those of Fan (2001).

However, in these mechanical equilibrium simulations, the axis of the tube also emerges into the atmosphere but fails to for all thermal equilibrium experiments. The dynamics of the rising axis found by Magara and Longcope (2003) reveal a complicated time evolution. The axial field line is much flatter when it passes through the photosphere and draining is also reduced. The magnetic pressure associated with this fieldline is smaller than the surrounding gas pressure and so it cannot expand vertically. A dip develops in the centre of this fieldline as mass collects. The consequential vertical compression of the field in the dipped location increases the vertical magnetic pressure gradient there, while the dipped nature of the fieldlines increases the vertical tension force. Eventually, the upward magnetic forces become larger than the downward gravitational force and the fieldline starts to expand. Magara and Longcope (2003) develop a simplified model for curved fieldlines and demonstrate that the evolution of a fieldline is dependent upon the ratio of its height to footpoint distance. Fieldlines close to the axis have a large footpoint separation and are classified as undulating. Providing the magnetic forces are strong enough to support the concave portion of the fieldline against gravity, it will gradually rise and eventually reach a position where the magnetic forces are dominant and the fieldlines can expand.

The outer and inner fieldlines of a flux tube adopt different geometries during and post- emergence (Magara 2004). The outer fieldlines expand freely in all three dimensions, keeping a fan shape and constant curvature. However, the inner fieldlines are surrounded by tightly twisting adjacent fieldlines particularly at their footpoints. This confinement prevents lateral expansion but allows for vertical expansion, giving a consequential increase in curvature of the fieldlines. A model derived by Magara (2004) indicates that these fieldlines will reach force-free equilibrium within a certain risen height. If the quasi-static inner fieldlines were heated, such that they became illuminated, they could be likened to actual observed coronal loops.

Once the fieldlines have expanded into the atmosphere they take on both forward and inverse **S** geometries when viewed from above. The outer fieldlines expand to form a potential-like arcade but the set of inner fieldlines, although emerged, remain constrained in an **S** structure and have high current concentrations at their footpoints (Fan 2001; Magara and Longcope 2001, 2003; Magara 2004). Magara and Longcope (2003) believe that this points towards the inner fieldlines being related to sigmoid structures seen in X-ray observations taken by Yohkoh. These sigmoid structures will be discussed in greater detail in section 2.3.1.

Magara and Longcope (2003) find a quadrupolar structure develops on that photospheric plane. This is not seen by Magara and Longcope (2001) and the authors attribute this to a variation in the driving velocity. When the feet of the tube are not driven downwards, the legs of the emerging flux tube become more inclined to the photosphere, thus giving a quadrupolar pattern.

During the process of flux emergence, energy and helicity are injected into the atmosphere through motions (Magara and Longcope 2003). While the photospheric polarity region is expanding, this injection is from emergence motions. Once the emergence saturates, the bipolar region begins to deform and fragment due to shearing motions and these motions become the dominant injection mode.

2.3 Effects of a Magnetised Atmosphere

We now consider the effects of including magnetic fields in the atmosphere. These atmospheric fields overlie the emergence location of the subsurface flux sheet or tube. Thus, upon emergence and expansion of the initially subsurface flux, the two fields will be forced to interact in some manner. The interaction of emerging flux with an overlying field has been used to explain observational results of X-ray bright points, flares and CMEs.

For atmospheric magnetic fields, simulations to date have considered potential arcades and horizontal or oblique magnetic fields. As we will see, in some cases reconnection between the emerging magnetic field and the atmospheric field is possible. For the simulations discussed in this section, the strength of the atmospheric field is chosen such that the coronal plasma-β is between 8×10^{-2} and 6×10^{-2}. This gives values of order 10 G for the strength of the pre-existing coronal field.

2.3.1 Potential Arcades

Studies of flux tubes emerging into potential arcade magnetic fields have been used to study the development of photospheric sigmoidal structures. Soft X-ray images of active regions frequently

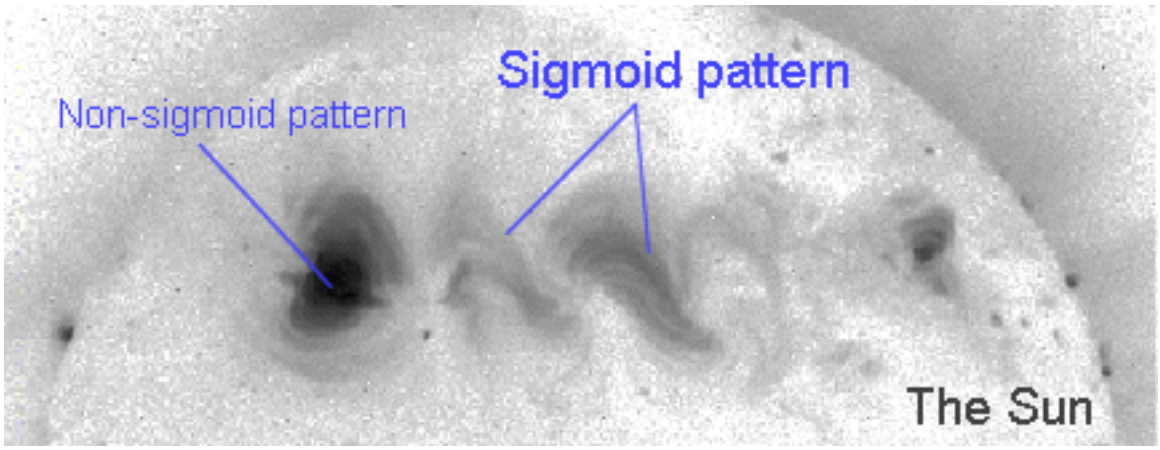

Figure 2.3: The northern hemisphere of the Sun, with two sigmoids (15 May 1998, 10:47 UT). Photo taken by Yohkoh's Soft X-Ray Telescope (SXT). SXT was prepared by the Lockheed Palo Alto Research Laboratory, the National Astronomical Observatory of Japan, and the University of Tokyo with the support of NASA and ISAS.

show forward and inverse **S** shaped morphology, referred to as "X-ray sigmoids". In the northern (southern) hemisphere these sigmoids preferentially show an inverse (forward) **S** shape, as shown in figure 2.3. Sigmoidal brightenings are thought to correspond to sites of enhanced magnetic energy dissipation as a result of the formation of intense current sheets (Titov and Démoulin 1999). Observationally, transient brightenings and sharpening of X-ray sigmoids have been found during the onset of eruptive flares and CMEs (Sterling and Hudson 1997). An overlying arcade can confine an emerging field, allowing the later to build up twist and free magnetic energy. Given some trigger, such as the kink instability, this magnetic energy can be suddenly released, resulting in the emerged field taking on a new, stretched and partially open state, such as during a CME.

A series of papers have studied the evolution of half of a toroidal, left-hand twisted flux tube that is transported kinematically into an domain representing the Sun's atmosphere, through the domain's bottom boundary (Fan and Gibson 2003, 2004; Gibson et al. 2004). The atmosphere contains a pre-existing magnetic arcade directed in the same direction as the poloidal component of the field at the top of the tube. Hence, no reconnection is expected to occur between the emerging tube and the atmospheric field. The fieldlines of the tube uniformly twist about the axis through a radian angle of $0.1 \times 2\pi$ per unit length along the axis. Given that the axis itself is curved, this results in each fieldline winding about the axis $1.875 \times 2\pi$ times over the length of the semicircle. Once half of the toroidal tube has been transported into the domain, the rise of the tube is stopped and the fieldlines become anchored to the boundary. These simulations are interested in the development of the coronal magnetic field formed as a result of an emerging twisted flux tube and, therefore, do not aim to simulate a more realistic flux emergence event by including a convection zone.

The velocity used to transport the twisted tube into the domain is highly sub-Alfvénic and, therefore, the evolution of the emerging magnetic field occurs quasi-statically. The emerging field

expands and displaces the atmospheric arcade. Once a significant portion of the tube has entered the domain, the tube becomes subject to a kink instability. As a result, the tube experiences acceleration in its vertical rise and substantial writhing of its axis. Given the left-handed sense of twist of the fieldlines about the axis, conservation of helicity is satisfied by the writhing of the axis also being left-handed.

The onset of the kink instability occurs when the number of twists of the fieldlines about the axis between the two boundary points reaches ~ 1.5 (Fan and Gibson 2003). This value is larger than that found by Hood and Priest (1981), who conducted stability analysis on a line-tied, uniformly twisted, cylindrical tube and found the tube becomes unstable when fieldlines twist more than 1.25 times between the tube end points. If driving of the tube is stopped (and the domain boundaries fixed) before the twist reaches the critical level obtained by Hood and Priest (1981), the tube does not undergo the kink instability and settles into an equilibrium. In the cases where the kink instability does occur, the flux tube does not reach a new equilibrium before it moves out of the top of the domain.

As discussed in section 2.2.2, Magara and Longcope (2003) find that the inner tube fieldlines adopt an **S** structure once they have emerged. The current concentrations at the footpoints of these sheared inner fieldlines provide a possible explanation for X-ray sigmoids, given some illuminating mechanism (Magara and Longcope 2003; Manchester et al. 2004). Fan and Gibson (2003) find both forward and inverse **S** structures for their left-handed writhe fieldlines, when viewed from above, depending upon whether individual fieldlines are upward protruding or dipped. They conclude that fieldlines geometry alone cannot explain X-ray sigmoids. However, the kink instability deforms the tube, pushing the legs together and creating a sharp gradient in the vertically directed magnetic field. A highly concentrated current sheet forms between the tube's legs, along the neutral line of the vertical field component, in the form of an inverse **S** shape. The current sheet is extended by the misalignment of the flux rope with the arcade field. This inverse **S** sigmoid shape would be expected in the northern hemisphere (Rust and Kumar 1996), where left-hand twisted tubes are predominant over right-handed ones (Pevtsov et al. 1995). Thus, the results of these simulations are consistent with observations.

Two subsequent papers by Fan (2005) and Gibson and Fan (2006) investigate the process of CME onset by changing to a spherical geometry. A cartesian geometry, with vertically conducting wall side boundaries, prevents CMEs since the energy needed to stretch the field to infinity is infinite. Other than a change in coordinate system, the setup of the simulations is the same as that of the earlier potential arcade papers. A twisted toroidal field is driven through the lower boundary of a domain that contains a potential arcade. The writhing initiated by the kink instability causes the apex of the tube to rotate through 90^{o}. Viewed from above, the fieldlines wrapping over the top of the tube now lie perpendicular to the arcade field. The forces exerted on the ambient field by the emerging flux are now localised and it is easier for the flux rope to part the arcade field and

erupt outwards. In the absence of the kink instability, the force on the ambient arcade would have affected a larger proportion of its fieldlines and most of the field would have need to be opened up for the emerging field to escape.

In the pre-eruption state, dense material is trapped in the concave sections of the tube's twisted fieldlines. Fan (2005) likens the flux rope to a prominence field in an equilibrium state, with dense material supported by the dipped fieldlines. At the onset of the eruption the prominence field accelerates at $\sim 450\ \mathrm{km\ s^{-1}}$. The lower part of the prominence evolves into a cross-legged structure, due to the kink instability, while the top part of the field rotates. These qualitative findings fit will observations of several CME events, whereby a flux rope appears to undergo a kink instability before expanding radially away from the Sun's surface (Williams et al. 2005).

The eruption of the flux rope allows for dense material trapped in the twisted fieldlines to be transported upwards. During the loss of equilibrium, a significant amount of magnetic energy is released. The development of the **S** shaped current concentration, previous discussed, results in reconnection and the further release of magnetic energy. Reconnection occurs in the centre of the separatrix surface, delineated by the current sheet, where the tube's legs have been pushed together due to the kink instability. This reconnection splits the flux tube in two, with effectively a stretched tube that is propagating away from the surface and a second low lying tube.

2.3.2 Horizontal Fields

There have been a multitude of studies that consider the emergence of flux into an atmosphere with a horizontal coronal field. Simulation have used flux sheets and flux tubes for the subsurface magnetic field and have initiated the rise of the subsurface flux through both buoyancy and imposed velocities. However, within the atmosphere they all include space-filling, straight, horizontal magnetic fields. Of the simulations discussed within this section, most are 2D (or 2.5D) and consider emerging flux sheets. Only a handful of the simulations have been carried out in 3D with an emerging flux tube (Archontis et al. 2004, 2005, 2006; Galsgaard et al. 2005).

The initial evolution of an emerging flux system is unaffected by the inclusion of an atmospheric field. Emergence occurs in the same manner and on the same timescales in cases with and without an atmospheric field (Shibata et al. 1989b, 1992; Archontis et al. 2004, 2005). However, once the emerging field reaches the ambient field, its evolution begins to deviate. When the emerging field reaches the magnetised atmosphere, it either has to push the overlying field out of the way or reconnect with the ambient field in order to open up a volume into which it can expand. The type of interaction between the two flux systems will depend upon their orientation to each other at the time of first contact.

We now consider three different types of magnetic field orientation of the two flux systems: par-

allel, antiparallel, and intermediary orientations.

Parallel Orientation

No reconnection will occur if the field components of the horizontal field have the same sign as the horizontal components comprising the emerging magnetic field. In this case, the atmospheric field is pushed upwards or "dented". In the 3D simulation by Galsgaard et al. (2005), the emerging field is formed from a centrally buoyant magnetic flux tube. The atmospheric field is pushed upwards into a dome shape by the expanding tube plasma. Yet, it is energetically favourable for the deformed horizontal field to slide down the plasma hill and, thus, its fieldlines end up passing around the emerging field at a nearly constant height. Additionally, Shibata et al. (1989b) find that the rising loops of their flux sheet decelerate when they come into contact with the overlying field. Simulations of rising flux tubes in the convection zone also show that the inclusion of a parallel horizontal field causes the tubes to deceleration. This is as a result of the horizontal field's downward acting tension force, which increases as the layer becomes increasingly dented (Dorch 2007). We conjecture that modifying the relative strength of the atmospheric field to the emerging field will accelerate the increase in the downward tension force and, therefore, directly affect the amount by which the horizontal field is deformed and the deceleration felt by the emerging flux. The restrictions of two dimensions prevents the horizontal field from "sliding" in the study by Shibata et al. (1989b). Hence, a continuous distribution of magnetic field forms that is approximately current free.

Antiparallel Orientation

When an antiparallel field overlies the rising magnetic loops of a flux sheet, a neutral sheet (or current sheet) forms between the two flux systems, which is characterised by enhanced density and gas pressure (Shibata et al. 1989b). For the 3D emerging flux tube of Galsgaard et al. (2005), the current concentration has a dome structure with the curvature matching that of the emerging flux dome. Over time the current surface concentrates into a narrow and curved sheet, arching over the summit of the emerging plasma. The magnitude of the current increases and eventually reconnection starts, occurring all along the current arch. The magnetic reconnection causes the temperature in the current sheet to increase by an order of magnitude and may explain the occurrence of compact flares or X-ray bright points (Shibata et al. 1992).

There have been reports of both deceleration (Yokoyama and Shibata 1996; Miyagoshi and Yokoyama 2004) and no deceleration (Shibata et al. 1989b) of the rising loops when they come into contact with an antiparallel ambient field. There are two factors that can cause the rising loops to decelerate, when in the absence of the atmospheric field they would have continued to accelerate:

- **Strength of the ambient field:** As for parallel flux systems, a downward tension force acts on the ambient field when it becomes dented by the emerging flux system. The strength of the ambient field will determine the size of the tension force and, therefore, the amount of deceleration experienced by the emerging plasma. A significantly weak overlying field may not cause any deceleration of the rising loops at all.

- **Starting height of the ambient field:** The emerging field will be decelerated when its magnetic pressure becomes comparable to the total pressure at the bottom of the ambient field. Overlying fields are chosen to start at different heights in different simulations, some starting in the chromosphere and others in the corona. Consequently, the gas pressure at the bottom of the ambient field will also vary between simulations. Ambient fields starting in the chromosphere could stand a better chance of decelerating the emerging field than a coronal field, since the latter will have a significantly lower gas pressure.

Neither of these factors have been tested, so the above conjectures are unconfirmed. Regardless of any variation in the change of speed of the rising loops, the coronal field does not feel a significant acceleration force. Study of the current sheet reveals a sharp decrease in the vertical velocity of the sheet. The magnetic fieldlines from the two flux systems reconnect at a rate comparable to the vertical velocity of the emerging field (Archontis et al. 2004, 2005).

In the current sheet, the plasma and fieldlines are accelerated by the gas pressure gradient formed along reconnected field lines between the high gas pressure corona and the low gas pressure emerging flux (Shibata et al. 1989b). Upon exiting the current sheet, the plasma is slowed when it collides with the ambient field. The plasma is still travelling faster than the fast mode speed and a fast shock forms. The pressure excess in the post-shock region acts to again accelerate the plasma along atmospheric fieldlines creating high velocity, hot plasma jets. The jets form all along the edges of the current sheet and, in the case of a curved current sheet, take on the characteristic curve of that sheet (Archontis et al. 2005). The jets occur with temperatures of up to 6×10^6 K and velocities of 100 km s^{-1}, with little reduction in velocity away from the current sheet (Shibata et al. 1992; Yokoyama and Shibata 1995; Galsgaard et al. 2005). The reconnection jets will, therefore, be seen over very large distances in the corona. The inclusion of anisotropic heat conduction results in a second type of jet existing around the reconnection region (Miyagoshi and Yokoyama 2003, 2004). Thermal energy generated during the reconnection process is transported along magnetic fieldlines to the chromosphere through heat conduction. In turn, this causes the "evaporation" of dense chromospheric material on neighbouring and already reconnected fieldlines, sending jets into the atmosphere. In contrast to the low density reconnection jets, these slow evaporation jets have high densities in comparison to their coronal surroundings. Gas pressure in the evaporation jet flow is balanced by the total pressure of the surrounding medium and gives an estimated temperature of the jet material as 6.7×10^6 K. The higher emission measure of the evaporation jets makes them more observable and these are probably the coronal X-ray jets

emanating from emerging flux regions observed by Yohkoh.

Archontis et al. (2004) find an **X** structured vorticity pattern situated about the reconnection region, a telltale sign that reconnection is occurring. Additionally, the reconnection between the two flux systems creates plasma heating in the reconnection region through Joule or magnetic dissipation. Temperatures can reach close to 10^7 K and this fits with plasma temperatures from observations of fast energy release events, e.g. flares.

As time progresses, the current sheet moves upwards pushed by the rising plasma of the emerging field. In the simulation by Archontis et al. (2005), the atmospheric field begins in the transition region and fills the corona. The first reconnection occurs between the emerging flux and the transition region magnetic field. Measurements at the top of the current sheet identify all of the transition region flux as having undergone reconnection once the density entering the current sheet returns to coronal values. There is a corresponding change in temperature as the hotter coronal material starts to reconnect.

Observations of newly emerging active regions identify a long buildup phase during which very little new flux connects to a pre-existing region (Longcope et al. 2005). This is followed by a burst of activity in which a significant amount of flux transfers from the new region to the existing region. This is not reproduced by any of the simulations discussed, where most of the activity occurs immediately after the emergence of the subsurface field. There are several simple reasons for these differences. In the observations, the pre-existing atmospheric field is an active region situated quite some distance from the newly emerging flux. Hence, the field of the new region must expand significantly before it feels any impinging effects of the existing field resulting in a delay between emergence and onset of reconnection. In the simulations, the temperature in the current sheet during the early reconnection phase reflects transition region values and is accordingly relatively low. The temperatures measured by EUV instruments are only recorded at later times in the simulations and, thus, the onset of reconnection in observations may be wrongly estimated.

Plasmoids are observed forming in the current sheet, through the development of the tearing mode instability (Shibata et al. 1992; Yokoyama and Shibata 1995, 1996; Archontis et al. 2005, 2006). The current sheet develops several X-line (X-point in 2D) reconnection locations across its width, between which magnetic O-lines, or plasmoids, develop and grow with time. In some cases, plasmoids have been found to coalesce with each other due to a coalescence instability (Shibata et al. 1992; Yokoyama and Shibata 1995, 1996). Asymmetry of the reconnection rate between successive X-points may lead to an imbalance in the tension force, resulting in the plasmoid being pushed sideways in the current sheet and eventually ejected. Archontis et al. (2006) find the ejection of a plasmoid occurs over a period of ~ 90 s. Plasmoids formed when the current sheet is in the transition region will be accelerated from the sheet with a velocity of $15\ \mathrm{km\ s^{-1}}$. However,

as the current sheet rises into the corona, the Alfvén speed increases and the velocity of ejected plasmoids increases to $150\ \mathrm{km\ s^{-1}}$. Similarly, for plasmoids created in the corona rather than the transition region, their density will be lower while their temperature will be higher ($\approx 10^4$ K when formed in the transition region and $\approx 10^5 - 10^6$ K when formed in the corona). Between the time of formation and ejection, the plasmoids move up in height with the current sheet they are contained within. Thus, by the time of their ejection, plasmoids contain significantly cooler and denser plasma than the surrounding environment. Hence, their ejection could perhaps be observed as Hα or Hβ surges.

Plasmoid creation and ejection are continual processes during reconnection. The degree to which the fieldlines of the plasmoid wind tightly around the central O-line is determined by the alignment of the two reconnecting flux systems. In the case of practically antiparallel fields, the plasmoid will resemble a tightly wound solenoid. This is because the horizontal field component aligned with the length of the current sheet becomes significantly small after reconnection and, thus, the direction of the field is dominated by the remaining field components. As the flux systems become increasingly less antiparallel, this horizontal component increases in size and the fieldlines in the plasmoid become less tightly wound (Shibata et al. 1992; Archontis et al. 2006). Archontis et al. (2006) also comment that, in line with the evolution of the current sheet, the shape of the plasmoids becomes increasingly arched over time.

The development of plasmoids affects the rate of reconnection between the two flux systems (Yokoyama and Shibata 1996). As plasmoids develop, the X-lines become more rarefied (decrease in gas density). This in turn increases the anomalous resistivity and, therefore, increases the reconnection rate. A second increase in the reconnection rate occurs when the plasmoid is ejected from the current sheet, causing the latter to collapse. This generates a large converging flow into the neutral point and, thus, reconnection is enhanced again. Plasmoid formation has been shown to be robust and independent of the resistivity model employed in a simulation, providing the resolution is high enough to resolve small structures (Archontis et al. 2007).

In both the 3D and 2D cases, the reconnection process begins with the fieldlines on the outer edge of the emerging flux and proceeds towards the inner fieldlines. Archontis et al. (2004) likened this type of reconnection to peeling off the layers of an onion and described the tube as being turned inside out by the interaction with the atmospheric field. The emerging field must have a larger amount of flux than the field it is reconnecting with if the former is to maintain its integrity and not become completely reconnected to the horizontal field. In the 3D simulations, there is a high level of asymmetry in the two ends of the current sheet due to the varying strengths of the reconnecting magnetic field components of each individual system. The reconnection point is consistently located to one side of the current sheet, an effect not seen in simpler 2D models.

Usually, in the simulations of emerging flux sheets, the direction of the magnetic field of the sheet

is initially chosen to be uniform with depth. Thus, when reconnecting with an ambient field post-emergence, the fieldlines from the sheet all have the same characteristics. If reconnection occurs for the first fieldlines of the sheet then, providing the flux of the atmospheric system does not run out, reconnection will occur for all of the later emerging fieldlines of the sheet.

For a uniformly twisted, emerging flux tube this is not the case. The pitch of the tube's fieldlines varies with depth and, although the outer fieldlines may be ideally orientated for reconnection, the fieldlines will become less suitably aligned with the atmospheric field as the axis of the tube is approached. Thus, as discussed by Archontis et al. (2005), the properties of reconnection gradually change with time. For perfectly aligned outer layers of the tube, the field distribution across the current sheet has a tangential discontinuity. This is characterised by no variation in field direction but a decrease in field strength from both edges of the current sheet towards a common null point/line in the centre of the sheet, which separates the field from each individual flux system. Later, when the fieldlines in the two systems are not perfectly antiparallel, the field distribution changes to a rotational discontinuity. Reconnection cannot fully annihilate the horizontal components of the fields in the current sheet. Instead, the field strength decreases slightly across the current sheet but, since the field direction rotates rather than flips, there is no null point. Since the field strength decreases across the current sheet for both a tangential and rotational discontinuity, the plasma-β increases within the current sheet for all cases of reconnection. As the orientation of the emerging field becomes increasingly parallel to that of the atmospheric field, reconnection becomes less efficient and there is less associated heating.

Through the tracking of individual fieldlines, Archontis et al. (2005) identify that while a fieldline passes through the current sheet, or diffusion region, it is no longer frozen to the plasma and changes connectivity continuously. However, upon exiting the diffusion region, the fieldline becomes frozen to the plasma again. In addition to this, a single fieldline may undergo reconnection in different positions along its length as a result of the initial twist of the fieldline about the tube's axis. Through multiple reconnections it is possible for the atmospheric fieldlines to dive under the photosphere and surface on the opposite side of the tube, heading back up into the corona. This is described by the authors as creating "a photospheric pocket of coronal fieldlines". At the end of the simulation by Archontis et al. (2005), 75% of the initial tube flux has become connected to the atmospheric field and 60% of the initial axial flux has emerged into the atmosphere. However, the axis remains trapped at the lower boundary of the photosphere within the time of the simulation. Although the rising emerging field does not decelerate when it reaches the horizontal field, it feels less acceleration than in the case of no atmospheric field. Thus, the emerging flux is transported into the atmosphere more slowly in the presence of an ambient field.

Intermediary Orientations

There have been several investigates into how orientating the horizontal field at arbitrary angles to the emerging field changes the reconnection process (Yokoyama and Shibata 1996; Galsgaard et al. 2005, 2007). Reconnection can be delayed in the case when the field orientations are nearly parallel but in the case of nearly antiparallel fields it is easily initiated. The current sheet between the two flux systems continues to adopts an arch shape passing through the summit of the emerging plasma hill. The vertical midplane of the arch (y-z or x-z plane) varies as the angle between the two systems varies. The approximate angle of the current sheet, ϕ, to the x-z plane is given by

$$\cos\phi = \left(\mathbf{B}_{cor} \cdot \mathbf{B}_t\right) / |\mathbf{B}_{cor}||\mathbf{B}_t|, \tag{2.4}$$

where $\mathbf{B}_{cor}$ and $\mathbf{B}_t$ are the magnetic fields in the corona and at the summit of the emerging region, respectively.

Moving away from antiparallel orientations, results in the reduction of the antiparallel component of the overlying field to the emerging flux and a corresponding increase in the perpendicular component. This increase reduces the compressibility of the plasma and, therefore reduces the rate of reconnection (Yokoyama and Shibata 1996). Depending upon the exact orientation of the horizontal field, it is possible to observe higher velocity outflow jets from the current sheet than in the purely antiparallel case, i.e. close to $200\ \mathrm{km\ s^{-1}}$ for a 45^{o} angle. Observations of X-ray jets report velocities of $10 - 1000\ \mathrm{km\ s^{-1}}$ with an average value of $200\ \mathrm{km\ s^{-1}}$ (Shimojo et al. 1996). In the simulations, the jets are always found to be aligned with the direction of the atmospheric magnetic field.

The vertical acceleration experienced by the expanding field does not depend on the structure of the atmospheric field. Hence, the tube reaches similar heights over the same time period, independent of the orientation of the atmospheric field (Galsgaard et al. 2007). However, reconnection alters the horizontal forces acting on the tube's field and, thus, less horizontal expansion is seen in the cases where reconnection is readily induced.

The orientation of the coronal field also changes the shape of the plasmoids formed in the current sheet. As the field alignment moves away from antiparallel, the plasmoid cross-section becomes more circular (Yokoyama and Shibata 1996).

2.3.3 Oblique Fields

All atmospheric fields will have emerged from the solar interior at some point in their lifetime. It is highly likely that these fields will, therefore, have their footpoints passing through the interior atmosphere interface. Horizontal fields represent the cases where the footpoints of the atmospheric

field are separated by large distances and can, therefore, be ignored. In this section, we consider atmospheric fields that have a non-zero angle of inclination to the horizontal plane. In these cases, the atmospheric field passes from the interior into the atmosphere within the numerical domain.

The 2.5D study by Yokoyama and Shibata (1995) considers the emergence of a horizontal flux sheet from the top of the convection zone. The overlying two temperature atmosphere contains a uniform field at an angle of 135° to the initial orientation of the flux sheet. Upon contact, a current sheet forms between the two flux systems and, although the current sheet is centred over the top of the emerging loops, reconnection ensues at a location slightly to the side of the exact emerging loops' top, though still within the current sheet. Reconnection occurs in the same manner as in the case of a horizontal field, with a tearing instability in the current sheet resulting in plasmoid formation, coalescence and ejection.

Plasma is heated to X-ray temperatures $(4 - 10\ \mathrm{MK})$ at the reconnection location, through Joule dissipation. Post-reconnection, the tension force acting on the reconnected fieldlines causes them to straighten and, thus, a pair of hot jets are created. The velocity of the jets reaches $\sim 100\ \mathrm{km\ s^{-1}}$ and, while one jet is ejected upwards aligned with the oblique field, the second jet is directed downwards and collides with the loops at the side of the emerging system. Here the second jet is compressed and hot loops are formed. This may account for observations of bright points away from the footpoint of X-ray jets.

During the process of straightening, the reconnected fieldlines exhibit a whip-like motion. This accelerates dense, cool plasma from the chromosphere into the atmosphere at a velocity of several tens of kilometres per second. Again, the cool jet ($\approx 10^4$ K) is aligned with the oblique field and could, in fact, be observed as an Hα surge. Observations have found that $10 - 20\%$ of X-ray jets are accompanied by Hα surges (Shimojo et al. 1996). However, since reconnection would heat any cold plasma to X-ray temperatures it was widely believed that the two observables must have been consequences of separate mechanisms. This simulation by Yokoyama and Shibata (1995) produces side by side X-ray jets and Hα surges as byproducts of reconnection. The spatial offset predicted by their results has been observed by Canfield et al. (1996).

Changing the inclination of the ambient field, such that the angle formed between it and the horizontal emerging field is 45°, gives significantly different results (Yokoyama and Shibata 1996). In this case, the field at the top of the emerging loops is orientated in a direction similar to that of the oblique field. The current sheet now forms at the side of the emerging flux loops and, since it is not strongly compressed, reconnection occurs at a slower pace. Hot and cool jets do not form in this simulation.

A purely vertical ambient field does allow for reconnection with an emerging flux system. Hot, vertical jets are seen but cool jets are not. The confinement of reconnected fieldlines by the surrounding vertical field prevents the dramatic release of any existing fieldline tension and, therefore,

no whip-like motion can occur to accelerate the chromospheric material (Yokoyama and Shibata 1996).

Extension of this simulation to 3D identifies that a Rayleigh-Taylor instability occurs at the top of the emerging flux system (Isobe et al. 2005, 2006). The plasma at the top of the flux system is dense, having been brought up from the convection zone. Although draining does occur along the expanding magnetic loops, it is more effective for inner loops whose curvature is smaller and effective gravity larger. Hence, denser loops overlie lighter loops and a dense layer is formed in the atmosphere. These effects are seen in 2.5D experiments but the move to three dimensions introduces numerical noise of the order of 10^{-8} in the initial conditions. This results in variations in density in the previously invariant direction (for the 2.5D studies). The variations grows non-linearly and, once the dense layer has formed, allows the Rayleigh-Taylor instability to set in. The sinking plasma forms mushroom-like structures and, thus, the magnetic field adopts a filamentary form. The dense filaments are of length ~ 9000 km and width ~ 1500 km, which are consistent with typical observed values of Hα arch filament systems (AFS) (Bruzek 1967). The width of the filaments may be determined by the fragmentation of the emerging flux prior to emergence. However, finer filamentary structures of < 1000 km have been observed in high resolution images. It is possible that the largest structure of the AFS is determined while the field is still below the photosphere and that the finer structures are as a result of the Rayleigh-Taylor instability occurring once the flux has emerged into the atmosphere (Isobe et al. 2006).

Current sheets are created at the top of the emerging flux system due to the Rayleigh-Taylor instability and their dissipation heats the plasma at the edge of the dense filaments. Neighbouring hot and cold loops have been observed by TRACE, as shown in figure 2.4, thus the filamentary structure developed by the magnetic field during the simulations is inline with the observations. It is important to note that the dense plasma sheet, Rayleigh-Taylor instability, and resulting filamentary structure to the emerging field are independent of the atmospheric magnetic field and will still occur in its absence.

The interchange of the magnetic field, due to the Rayleigh-Taylor instability, results in intermittent reconnection between the emerging and oblique flux systems. Thus, many distinctive narrow outflow jets are identified.

Archontis et al. (2007) produce their oblique atmospheric field through a "consistent" 2.5D model. Rather than imposing a coronal field from the start of the simulation, they allow one flux tube to emerge into the atmosphere and expand substantially. A second flux tube is initially placed to the side of and slightly deeper than the first tube and, being less buoyant, takes longer to rise through the solar interior before emerging into the atmosphere. By the time the second tube does emerge, the expanded field of the first tube has formed a non-uniform (in strength and direction), oblique atmospheric field lying above the photospheric emergence point of the second tube. At the point

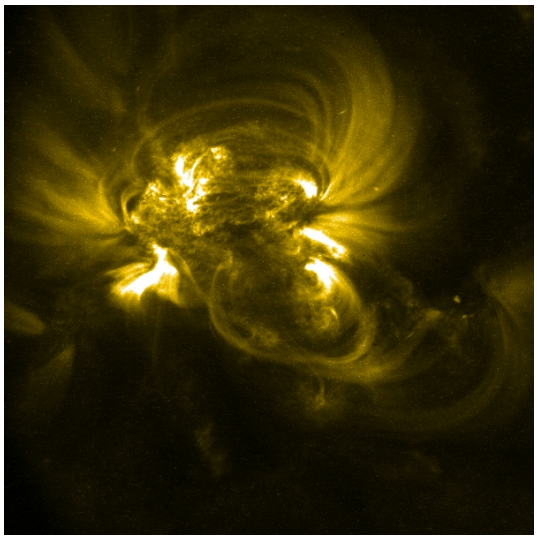

Figure 2.4: The loops associated with an active region on 1st July 2006, captured by TRACE in 171Å. Hot bright loops and cooler dark loops rise up into the atmosphere next to each other. Photo courtesy NASA TRACE mission.

of contact, the magnetic fields of the two flux tubes are differently orientated and a thin current sheet develops. The sheet delineates the emerged portion of the second tube and, therefore, takes on an arch shape. Prior to reconnection commencing, the highest point of the current arch reaches $2.4\ \mathrm{Mm}$ into the corona and the photospheric footpoints of the arch are separated by a distance of $3.4\ \mathrm{Mm}$.

Plasmoids develop in the current sheet and, over time, grow exponentially in size, which indicates that their development is via the linear mode of the tearing instability. The most intense part of the current sheet develops in one of the legs of the arch, where the two tubes try to expand into each other. The largest plasmoid is created here and, once it is vertically ejected, the reconnection rate in this part of the current arch increases again, though the current arch itself disbands. The most intense part of the current sheet survives since horizontal inflows of flux are maintained by the horizontal expansion of the tubes. Pairs of slow shocks form at the ends of the current sheet and, together with the fast reconnection rate, indicate Petschek-type reconnection at work.

Once a significant number of fieldlines have been reconnected, four domains with differing connectivity can be discerned as shown in figure 2.5. Two domains (A and B) consist of fieldlines that have not yet reconnected and, thus, belong to their original flux systems. Two domains (C and D) consist of fieldlines that have reconnected and have one footpoint in each tube. Of the latter two domains, D is a low lying arcade below the intense current sheet and C is a high rising arcade lying above the current sheet that encompasses both A and B. Accelerated reconnection outflows from the ends of the current sheet collide with both the low and high lying arcades, resulting in the plasma becoming compressed and heated. In the low arcade, the temperature increases to $2.5\ \mathrm{MK}$

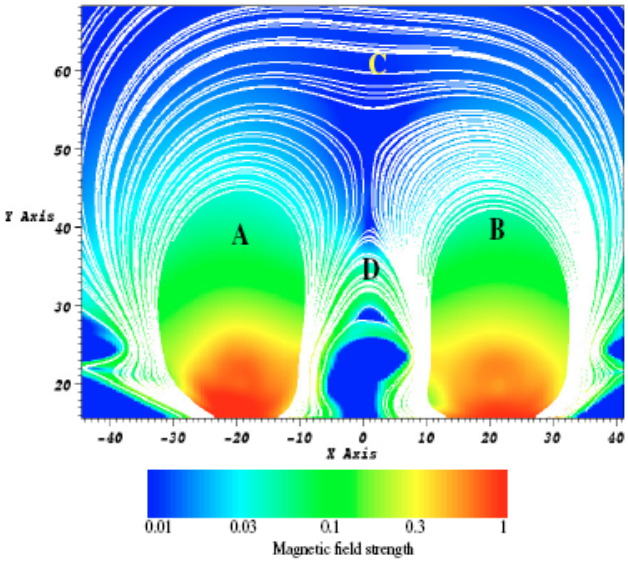

Figure 2.5: Four atmospheric domains of distinct topology result from the emergence of two flux tubes and their subsequent reconnection with each other. This graph is Fig.13 from Archontis et al. (2007).

and this may account for compact flares or arcade flares associated with emerging flux. At the collision point with the high arcade, a fast shock forms and the plasma is accelerated along the seperatricies between regions A and C and regions B and C. The temperature of the accelerated plasma increases to 3 MK and this enhancement along the top of the emerging flux system may be observed as loop brightening. After the ejection of the plasmoids, the current sheet collapses into an X-point and the magnetic field approaches a potential state.

2.4 Summary

In this chapter we have presented results from previous simulations of largescale, localised flux emergence. These simulations have varied in their dimensionality (2D, 2.5D and 3D) and their initialisation of the pre-emergence magnetic flux system (sheets and tubes). In some cases the subsurface flux has been driven upwards by an imposed vertical velocity, whilst in others the flux has risen as a result of its own buoyancy.

Regardless of these variations, the results from all of the simulations are very similar. The force used to drive the flux towards the surface has no knock-on effect. Whether the chosen force would actually occur naturally is a separate issue. In all cases, the flux system must undergo a magnetic buoyancy instability before it can emerge into the atmosphere. Post-emergence, excess magnetic pressure drives the expansion of the flux into the upper atmosphere.

However, flux emergence is fundamentally a three dimensional process. Although much informa-

tion and insight can be gained from 2D simulations, 3D experiments are essential for understanding the effects produced by magnetic shear and magnetic twist of flux tubes. Additionally, only with three dimensions is it possible to reproduce anything corresponding to distinct sunspots.

Only the 3D, velocity driven, flux tube simulations have managed to achieve emergence of the original axis of the tube. It does not seem likely that the driver itself is responsible for this event. Important factors are likely to be the distance over which the driver is applied and the strength and twist of the tube. This is an important area of study for the future if realistic sunspots are to be achieved.

The results from the simulations discussed within this chapter do correspond with observations. However, it should not, therefore, be assumed that they provide a correct model for any observations. In most simulations, the energy equation is adiabatic and lacks heating terms, other than dissipation. Heating terms are important for achieving the correct thermodynamic description of a system. Simulations lacking these heating terms are likely to describe the correct dynamical evolution of the magnetic field. However, temperature profiles will not be described accurately and, therefore, so neither will the objects that are observable. Comparison with observations should, therefore, be made carefully.

The research in this thesis will be based upon the 3D flux tube simulations described in section 2.2.2. The previous flux tube simulations have used parameter values within the following ranges:

- $3.7 - 7.8\ \mathrm{kG}$ for the field strength at the tube's axis;
- $300 - 900\ \mathrm{km}$ for the radius of the tube;
- $0.4 - 0.5$ for the twist of the tube.

A study has never been carried out which considers how varying just one of these parameters at a time alters the emergence of flux. There has been a study into the length over which the flux tube is made buoyant and, as we have seen, this produced exceedingly different results (Manchester et al. 2004). It is, therefore, important to perform a parameter investigation for the field strength, radius and twist of the tube in case any of these should yield wildly different results from the general emergence results. In chapter 5, we will perform simulations in which we will vary the field strength and twist of the flux tube.

Additionally, all of the flux tube simulations consider constant twist flux tubes. There is nothing to suggest that the toroidal tubes produced by dynamo action should have approximately constant twist. In chapter 6, we will investigate whether non-constant twist alters the emergence process.

The use of a flux sheet or tube as the seed magnetic field gives a very organised setup prior to emer-

gence. The lack of convective motions in existing simulations means the magnetic field maintains some degree of organisation during the experiment. Post-emergence, the fieldlines retain some of their original tube characteristics and the atmospheric loops are ordered. In chapter 7, we will increase the complexity of the seed magnetic field by forcing two flux tubes to interact with each other in the solar interior. Given that flux subsequently emerges, we will look for variations in the resulting atmospheric magnetic field. This setup is expected to provide a more complex field without the challenge of having to implement convection.

All of the flux tube models place the magnetic field in the "convection zone" but only Magara (2001) actually has a superadiabatic temperature profile in this region and, thus, the potential for convective motions. In the flux sheet simulations by Kaisig et al. (1990), convective motions dragged some flux at the photospheric level down into the convection zone while propelling other flux further into the photosphere. Although Shibata et al. (1990) found that convection alone made little difference to flux that would have emerged in the absence of convection, it would be interesting to see if convective motions could help flux tube material to emerge in cases when it has reached the photosphere but failed to undergo a buoyancy instability. We shall not be investigating this area in the thesis.

For each of the areas considered further, we aim to determining the robustness of simulation results to date and will highlight any apparent differences in the results.

2.4 Summary

Chapter 3

The Numerical Code – `Diffin3d`

In chapters 4, 5, 6 and 7, we will be discussing results that have been produced using numerical simulations. All of these simulations have been carried out using a code developed by Nordlund and Galsgaard (1997), which will be discussed in this chapter. To date this code remains unnamed and, therefore, for clarity within this thesis it will be referred to as `Diffin3d`.

`Diffin3d` is a 3D code which solves the MHD equations using a finite difference approach. In section 1.2, we introduced the MHD approximation and its equations and, in section 3.1, we will consider the dimensionless form of these equations used by `Diffin3d`. The quantities to be solved for are setup on a staggered mesh and this will be discussed in section 3.2. A sixth order error method is used to derive partial derivatives, whilst a fifth order accurate interpolation method shifts variables between the staggered grids. An explicit third order predictor-corrector method advances the solution in time. In section 3.3, we will examine each of these finite difference methods.

`Diffin3d` employs artificial diffusion in the forms of magnetic resistivity and viscosity. The exact form of each artificial diffusion component and the reason for using artificial diffusion will be discussed in section 3.4.

This code has been used for many different types of experiments and, although the initial setup of each problem can vary significantly, the basis of the code is common to all. In this way, the code can be considered as a "black box" – once the setup has been initialised the results can be analysed without specific knowledge of the inside workings of the code. In section 3.5, we will identify areas where individual choices can be made as to the setup of the each model. The exact initialisations used for the experiments comprising the research in this thesis will be discussed separately in the corresponding chapters.

Numerical simulations are computationally time consuming. To reduce the time taken for each

simulation, `Diffin3d` uses a parallelisation technique whereby it splits the computations over several processors. In section 3.6, we will consider how the parallelisation is actioned at runtime.

This code has been utilised for many plasma simulations. `Diffin3d` has been tested by checking the results produced from certain starting setups against the results from other codes when using those same setups. The testing runs for the flux emergence simulations will be discussed in section 3.7.

3.1 Equations

For each simulation, `Diffin3d` solves the 3D, time-dependent, resistive MHD equations numerically. In conservative form, these equations are:

$$\frac{\partial \rho}{\partial t} = -\nabla \cdot (\rho \mathbf{v}), \tag{3.1}$$

$$\frac{\partial (\rho \mathbf{v})}{\partial t} = -\nabla \cdot (\rho \mathbf{v}\mathbf{v} + \hat{\tau}) - \nabla p + \rho \mathbf{g} + \mathbf{J} \times \mathbf{B}, \tag{3.2}$$

$$\frac{\partial e}{\partial t} = -\nabla \cdot (e \mathbf{v}) - p \nabla \cdot \mathbf{v} + Q_{\text{Joule}} + Q_{\text{visc}}, \tag{3.3}$$

$$\frac{\partial \mathbf{B}}{\partial t} = -\nabla \times \mathbf{E}, \tag{3.4}$$

where

$$\mathbf{E} = -\mathbf{v} \times \mathbf{B} + \eta \mathbf{J}, \tag{3.5}$$

$$\mathbf{J} = \nabla \times \mathbf{B}, \tag{3.6}$$

$$p = \rho T, \tag{3.7}$$

with density ρ, velocity $\mathbf{v}$, viscous stress tensor $\hat{\tau}$, gas pressure p, acceleration of gravity $\mathbf{g}$, electric current density $\mathbf{J}$, magnetic field $\mathbf{B}$, thermal energy per unit volume $e = p/(\gamma - 1)$, Joule dissipation Q_{Joule}, viscous dissipation Q_{visc}, electric field $\mathbf{E}$, magnetic diffusivity η, temperature T.

There are three main points of difference between the MHD equations given in section 1.2 and those given here. Firstly, the energy equation is now written in terms of thermal energy per unit volume rather than pressure and, therefore, γ no longer proceeds the second term on the right-hand side of (3.3). Secondly, additional terms have been added to the energy equation that relate to the artificial diffusion, which will be discussed further in section 3.4. Thirdly, the equations have been non-dimensionalised. Dimensional quantities can be obtained by choosing three characteristic

values and then using the following relations to determine the remaining values:

$$v_0 = l_0/t_0, \tag{3.8}$$
$$e_0 = \rho_0 {v_0}^2, \tag{3.9}$$
$$B_0 = v_0\sqrt{\mu_0\rho_0}, \tag{3.10}$$
$$T_0 = \tilde{\mu}{v_0}^2/\tilde{R}, \tag{3.11}$$
$$E_0 = v_0 B_0, \tag{3.12}$$
$$J_0 = B_0/(\mu_0 l_0), \tag{3.13}$$

where l_0, t_0, v_0, ρ_0, e_0, B_0, E_0 and J_0 are the units of length, time, velocity, density, energy, magnetic field, electric field and current density, respectively. The independent constants take physical values as follows: $\mu_0 = 4\pi \times 10^{-7}$ H m^{-1} and $\tilde{R} = 8.3 \times 10^3$ m^2 sec^{-2} K^{-1}. The concept of dimensionality will be discussed further in chapter 4.

In order to solve these equations for a particular model, `Diffin3d` must perform multiple iterations over time. During each iteration, `Diffin3d` first evaluates the right-hand sides of (3.1) − (3.4), using interpolation and differentiation methods as necessary, before using a third order predictor-corrector method to perform numerical integration with respect to time.

The integration advances the solution by only a small period in time, giving updated values for the quantities ρ, e, **B** and **P**, which will be used during the next iteration. **P** represents momentum and is given by ρ**v**. Only the values of ρ, e, **B** and **P** are stored at the end of each iteration since all of the values required to evaluate the right-hand sides of (3.1) − (3.4) can be derived from these four. Successive iterations enable the solution to advanced in time.

3.2 Staggered Grid

`Diffin3d` works in a cartesian coordinate system (x, y, z). As illustrated in figure 3.1, the system is right-handed, with x as the vertical direction and y and z as horizontal directions. However, when most problems are posed, z is naturally considered as the vertical coordinate of a right-handed system, which we will call the "real" coordinate system. Since both the real and numerical coordinate systems are right-handed, it is very easy to transfer between the two. To move from the real to numerical coordinate system, the substitutions $x = -z$ and $z = x$ should be applied everywhere x and z appear in the real system.

For the remainder of this thesis, we will make all references to coordinates in terms of the real coordinate system. The information provided here is for completeness only.

We now consider the placement of variable values within the simulation domain. `Diffin3d`

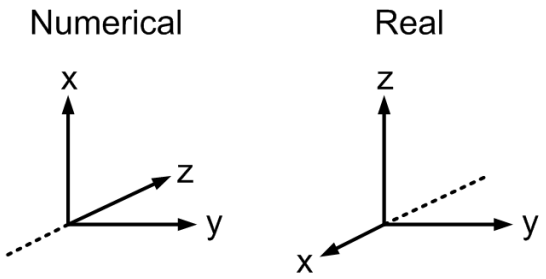

Figure 3.1: Right-handed numerical and real cartesian coordinate systems.

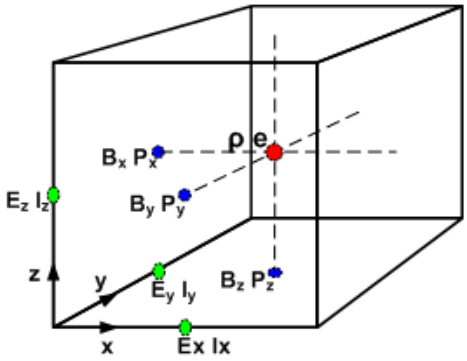

Figure 3.2: The staggered mesh system used by `Diffin3d` locates stored variables at different places on the unit cube.

uses a staggered grid system for all of the stored variables. Figure 3.2 demonstrates the location of the variable values on a unit cube. Density, ρ, and energy, e are volume centred but the stored values of the components of the magnetic field, **B**, and momentum, **P**, correspond to locations on the faces of the volume. As we will see in section 3.3, the finite difference methods return results which are shifted by half a grid cell in relation to their input values. Thus, the components of current density, **J**, and similarly the electric field, **E**, are edge centred.

Each quantity or component of a vector is stored in a 3D array, where all arrays are the same size and independent of the quantity's staggered location. The staggered arrangement of quantities on the grid results in arrays of individual quantities being offset from each other, as shown in figure 3.3. During calculations, all quantities must be evaluated at the same point in space and, thus, arrays must be reconfigured such that gridpoints with the same index in different arrays represent values at the same spatial locations.

As we will see in section 3.3, quantities can be automatically moved due the differentiation operator or moved with the interpolation operator. Although interpolation is often required in calculations, a staggered grid does have advantages. For simple second order centred difference methods, a staggered grid prevents chequerboard instability, whereby odd indexed cells become decoupled

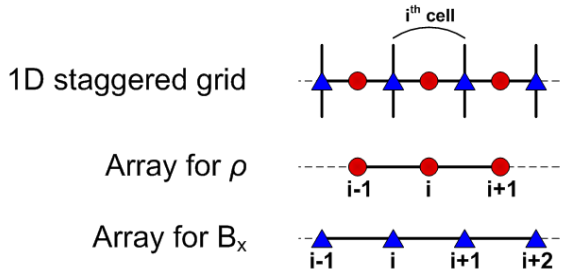

Figure 3.3: A segment of a row of staggered cells with cell centred ρ (red circles) and face centred B_x (blue triangles). Underneath the top row are the associated arrays used to stored the actual values of ρ and B_x. The location of the i^{th} gridpoint in the array for ρ corresponds to the centre of the i^{th} staggered cell but not the location of the i^{th} gridpoint in the array for B_x.

from even indexed cells.

The computational grid is comprised of a collection of unit cubes and, thus, it is easy to guess where the boundaries of the domain lie. However, when using arrays belonging to different quantities during calculations, consideration must be given as to where the boundaries lie in terms of array indices. This will be dependent upon the type of boundary in use and will be discussed further in section 3.5.1.

3.3 Finite Difference Methods

As mentioned in sections 3.1 and 3.2, evaluating the righthand side of (3.1) − (3.4) requires differentiation of quantities in the spatial coordinate system (x, y, z). In one dimensional situations, the derivative of a function $f(x)$ at the point x is defined by the limit

$$\lim_{h \to 0} \frac{f(x+h) - f(x)}{h}. \tag{3.14}$$

If h has a fixed, non-zero value, rather than approaching zero, the quotient $\frac{f(x+h)-f(x)}{h}$ is called a finite difference and gives an approximation to the derivative of f at x. Hence, we have

$$\frac{df}{dx} \approx \frac{f(x+h) - f(x)}{h}. \tag{3.15}$$

The derivative of f at the point x can also be derived by making use of the Taylor series. The Taylor series expansion for $f(x+h)$ about the point x is as follows

$$f(x+h) = f(x) + \frac{h}{1!}\frac{df(x)}{dx} + \frac{h^2}{2!}\frac{d^2 f(x)}{dx^2} + \frac{h^3}{3!}\frac{d^3 f(x)}{dx^3} + \ldots \tag{3.16}$$

By rearranging (3.16) we again arrive at (3.15), where the Taylor series expansion has been truncated from the $O\left(h^2 \frac{d^2 f(x)}{dx^2}\right)$ term onwards. This gives rise to a first order accurate finite difference method with a second order error. By increasing the number of terms in the finite difference method it is possible to increase the order of the error and, thereby, increase the accuracy of the derivative approximation.

We will now describe the finite difference methods used by `Diffin3d` for evaluating derivatives and carrying out interpolation. In section 3.3.2, we will present the predictor-corrector method used to advance the solution in time.

3.3.1 Differentiation and Interpolation Operators

`Diffin3d` uses a finite difference method with a sixth order error for differentiating the various quantities used in the calculations of the MHD equations. The method returns the derivative of a quantity at a half cell location, thus the returned data is shifted in comparison to the input data. For example, if the input data is centred on the grid cells then the returned results will be values for the cell boundaries. Similarly, for input data located at cell boundaries the returned results will be for the centre of the cell. Whether the data is shifted up or down by half of a grid cell will depend upon the particular difference method employed.

The prescribed method for the partial derivative of $f(x, y, z)$ with respect to x, whose result is returned shifted half a grid cell up in relation to the input data, is

$$\frac{\partial}{\partial x}\left(f_{i+\frac{1}{2}}\right) = \frac{a_1}{\triangle x}\left(f_{i+1} - f_i\right) + \frac{b_1}{\triangle x}\left(f_{i+2} - f_{i-1}\right) + \frac{c_1}{\triangle x}\left(f_{i+3} - f_{i-2}\right), \tag{3.17}$$

where $a_1 = 1 - 3b_1 - 5c_1$, $b_1 = -(1 + 120c_1)/24$ and $c_1 = 3/640$. For a 3D grid, i represents the array indices in the x direction, while j and k would represent indices in the y and z directions, respectively. By simply changing the indices in (3.17) from i to j or k and substituting y or z for x, we define operators for finding the partial derivatives with respect to y or z, respectively. By subtracting 1 from each of the indices of f, we can define an operator which returns the result shifted half a grid cell down from the input data.

As stated in section 3.2, each operation must act on quantities at the same spatial location during the evaluation of the right-hand sides of (3.1) − (3.4). Thus, due to the staggering of the grid and the shifted sixth order error derivative method, it is sometimes necessary to interpolate quantities before calculations can take place. For example, e is the conserved quantity in the energy equation, (3.3), and we know that e is cell centred. Hence, each of the right-hand side terms of (3.3) must also be cell centred before they are finally summed to give the total right-hand side value. If we

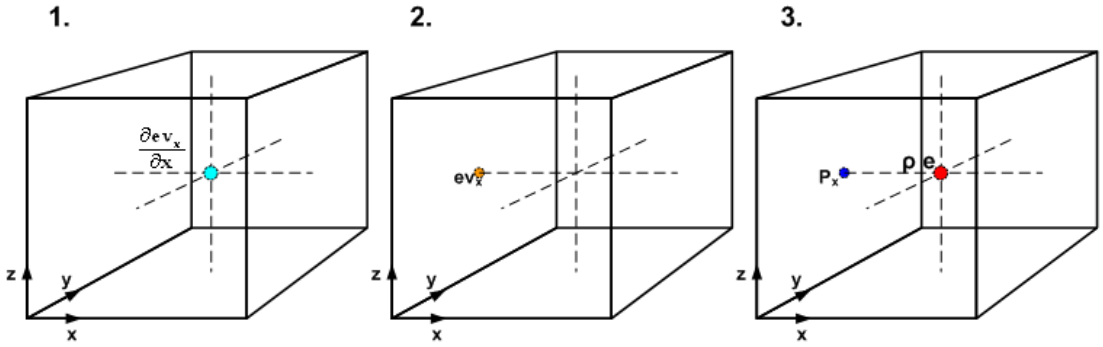

Figure 3.4: For the result of $\partial\left(ev_x\right)/\partial x$ to be cell centred (as in 1), the quantity ev_x must be face centred (as in 2). To derive this quantity from individual staggered quantities ρ, e and P_x (as in 3), interpolation must be carried out.

expand the first right-hand side term, $\nabla \cdot (e\mathbf{v})$, we have

$$\frac{\partial\left(ev_x\right)}{\partial x} + \frac{\partial\left(ev_y\right)}{\partial y} + \frac{\partial\left(ev_z\right)}{\partial z}. \tag{3.18}$$

We again consider only the first term, $\partial\left(ev_x\right)/\partial x$. The partial differentiation with respect to x will shift the result by half a grid cell and we require the result to be cell centred, as shown in figure 3.4. Thus, the input values of ev_x must be face centred. v_x is derived from the momentum component P_x, which is face centred, but ρ and e are both cell centred. Therefore, an interpolation method must be used to shift ρ and e prior to v_x being derived and ev_x being calculated. The positions of each of these intermediary quantities is demonstrated in figure 3.4. Alternatively, P_x could be interpolated to get a cell centred value and then, post-differentiation, a second interpolation would be required to find cell centred values for $\partial\left(ev_x\right)/\partial x$. Neither route appears to be more computationally efficient than the other and in both cases interpolation is required.

For interpolation, the following fifth order accurate method will return the value of f shifted half a grid cell up from the input data,

$$f_{i+\frac{1}{2}} = \frac{1}{2}\left[a_2\left(f_{i+1} + f_i\right) + b_2\left(f_{i+2} + f_{i-1}\right) + c_2\left(f_{i+3} + f_{i-2}\right)\right], \tag{3.19}$$

where $a_2 = 1 - b_2 - c_2$, $b_2 = -(1 + 24c_2)/8$ and $c_2 = 3/128$. This operator is independent of direction and, therefore, i, j and k can be easily interchanged for interpolation in each of the three directions. Again, equivalent operators exist for returning the result shifted down half a grid cell.

The derivations of the differentiation and interpolation methods can be found in appendix A.

We note that the up-shifting differentiation and interpolation methods use the same neighbouring six points to give the result. The only variations between the two methods are the values of

their coefficients $\{a_1, b_1, c_1\}$ and $\{a_2, b_2, c_2\}$. Similarly for the down-shifting methods. Both the differentiation and interpolation methods have the same order of accuracy and error. Additionally, choosing some of the coefficients to be zero changes the order of accuracy associated with the methods. For the differentiation method, if only c_1 is zero, the method reduces to third order accurate, while if both c_1 and b_1 are zero the method is only first order accurate. Similarly for the interpolation method.

As the edge of the domain is reached, the differentiation and interpolation methods can encounter difficulties. For both methods, three gridpoints are needed on either side of the point being calculated and, as the boundaries are approached, the methods will run out of gridpoints on one side. The resolution of this problem will depend upon the type of boundary in operation and will be considered further in section 3.5.1.

3.3.2 Advancing the Equations in Time

Once the right handside of (3.1) – (3.4) has been evaluated using the differential and interpolation operators described in section 3.3.1, the solution is numerically integrated over a small period of time using an Iterative Multistep (IMS) method. This consists of a predictor method of order o and a corrector step of order $o + 1$.

The particular IMS used by `Diffin3d` is the iterated leapfrog method by Hyman (1979). This combines a second order predictor step with a third order corrector step. The method will be applied to each of (3.1) – (3.4) to find values for ρ, e, **B** and **P** at the next time interval.

In the following, we will set r to be the ratio of the time periods between successive iterations, $r = (t_{n+1} - t_n)/(t_n - t_{n-1})$ where n is the iteration number. The predicted value of the quantity f is given by

$$f_{n+1}^{(*)} = p_1 f_{n-1} + (1 - p_1)\, f_n + q_1 \frac{\partial f_n}{\partial t}, \tag{3.20}$$

where $p_1 = r^2$, $q_1 = \Delta t(1 - r)$. Here $\Delta t = t_{n+1} - t_n$. The corrector step makes uses of the solution found by the predictor step as follows

$$f_{n+1} = p_2 f_{n-1} + (1 - p_2)\, f_n + q_2 \frac{\partial f_n}{\partial t} + w_2 \frac{\partial f_{n+1}^{(*)}}{\partial t}, \tag{3.21}$$

where $p_2 = 2(1 + r)/(2 + 3r)$, $q_2 = \Delta t(1 + r^2)/(2 + 3r)$ and $w_2 = \Delta t(1 + r)/(2 + 3r)$.

The solution, f_{n+1}, found by the corrector step will then be used by the differentiation and interpolation operators during the next iteration.

If used alone, the predictor step can cause problems affecting the solution. Hyman (1979) explains that the odd and even gridpoints are only weakly coupled when conservation laws are integrated, as here. Thus, waves with frequency twice the grid spacing distance can obscure the true solution with high frequency noise. The corrector step acts to couple the gridpoints over 3 consecutive iterations, thereby preventing this weak instability.

For accuracy of the solution, it is necessary that information does not propagate to a point outside of the numerical stencil during a single iteration. If Δx is the distance between consecutive grid cells and Δt is the time between consecutive time steps, then the maximum speed allowed is $M\Delta x/\Delta t$, where M is the number of gridpoints lying between the point being calculated and the edge of the stencil. For the differentiation and interpolation operators used by `Diffin3d` $M = 2.5$. This is the Courant-Friedrichs-Lewy (CFL) condition (Courant et al. 1928) and is formalised mathematically for a fluid as

$$\max\left(|v| + c_s\right) \leq M\Delta x/\Delta t, \tag{3.22}$$

where c_s is the local sound speed and $|v|$ is the local advection speed. This implies that if the fluid is moving as a whole under advection with a speed $|v|$ and it causes a disturbance that propagates at the local sound speed c_s, then the maximum speed it will move at is the sum of the two individual speeds. Hence, the chosen time step size must be less than the maximum sum of $|v|$ and c_s. For increased stability, `Diffin3d` chooses $M = 1$ and, thus, M will be dropped in the continued discussion of the CFL condition below.

For a plasma, the CFL condition must be modified to take into account the Alfvén speed, v_A. Rather than the local sound speed we use the fast speed, $c_f = \sqrt{{c_s}^2 + {v_A}^2}$, thus (3.22) becomes

$$\max\left(|v| + c_f\right) \leq \Delta x/\Delta t. \tag{3.23}$$

We cannot control the speed at which waves move and, therefore, we must ensure the CFL condition is satisfied by choosing a suitable time step. This is itself a problem, since it is impossible to know the exact speeds that will occur in an particular model prior to it being run. We cannot be certain that a time step chosen at the initialisation stage will be satisfactory over the whole time period of an experiment. Hence, `Diffin3d` makes use of variable time steps. Prior to the leapfrog method being applied, the CFL condition is evaluated and the time step chosen accordingly. Thus, the time period between consecutive time steps will vary throughout the simulation.

Rearranging (3.23), we have

$$\frac{\Delta t}{\Delta x}\max\left(|v| + c_f\right) \leq C, \tag{3.24}$$

where C is the Courant number. Following from (3.23) we have $C = 1$ for a 1D problem. For 3D simulations, $C = 1/\sqrt{3} \approx 0.58$. If the value of C is increased, then inaccuracy is introduced into the solution and, if C is reduced, diffusive effects become apparent. For the simulations described in this thesis, `Diffin3d` uses $C = 0.3$ to keep time truncation errors small and the time step well within the limits of the CFL condition. `Diffin3d` calculates

$$C\Delta x/\sqrt{\max\left(|v|^2 + {c_f}^2\right)}, \tag{3.25}$$

with the prescribed value for C to arrive at the time step, Δt, for the particular iteration.

`Diffin3d` uses the CFL condition in addition to similar conditions on the viscous and resistive diffusion. Thus, the choice of Δt arrived at by (3.25) must also satisfy

$$\frac{\Delta t}{(\Delta x)^2} f \max\left(\nu, \eta\right) \leq C, \tag{3.26}$$

where ν is viscous diffusivity and η is electrical resistivity. f is a factor associated with the artificial diffusion, which will be discussed in the section 3.4. For the particular diffusion quenching operator given by (3.30), f is chosen to be 20. If Δt does not satisfy (3.26), then it must be reduced further until it does.

Finally, in determining a suitable value for Δt, `Diffin3d` also takes into account gradients in energy and density with respect to time. If these gradients become to steep numerical error may give rise to negative values for these quantities, which is clearly not allowed. Thus, further reduction of Δt may be necessary to ensure accurate tracking of sharp changes in energy and density. Further measures, in the form of Newton cooling, can be initialised in `Diffin3d` to prevent negative energy arising and this will be discussed in section 3.5.4.

We note that the restrictions placed on the time step by the CFL and additional gradient conditions usually give Δt such that the solution is advanced by less than one whole time unit per iteration.

3.4 Artificial Diffusion

Although the numerical methods described in sections 3.3.1 and 3.3.2 have high orders of accuracy, small errors are still introduced and in the worst case are of $O\left(\Delta x\right)^6$. Under certain circumstances, these errors can grow in time and swamp the real solution with numerical noise. Therefore, `Diffin3d` uses artificial diffusion to counteract the numerical instabilities before they become a problem.

The artificial diffusion is employed in forms that would naturally arise in real astrophysical sit-

uations, namely viscosity and magnetic resistivity. In `Diffin3d`, viscosity enters the system through the divergence of the viscous stress tensor, $\hat{\tau}$, in the momentum equation, (3.2). Magnetic resistivity takes effect through the induction equation, (3.4), in the form of η. It should be noted that the artificial diffusion is not trying to correctly model real diffusion. It acts only to stabilise the code.

We begin by considering diffusion in the form of viscosity. This type of diffusion acts globally to correct amplitude errors for advection and phase errors for fast mode waves. These errors arise when wave numbers are large and, thus, the wave shape cannot be adequately mapped on the domain's grid. Additionally, the viscosity acts locally to prevent instabilities developing at shock wave fronts. For dimensional correctness in the momentum equation, the viscous stress tensor must have dimensions $\rho\mathbf{v}^2$. We define each individual element of the tensor as

$$\hat{\tau}_{ij} = \frac{\rho}{2}\left(\nu_{ij}\frac{\partial v_i}{\partial x_j} + \nu_{ji}\frac{\partial v_j}{\partial x_i}\right), \tag{3.27}$$

ν_{ij} is an element of the viscous coefficient matrix, ν, and is formed from a combination of the global and local viscosity functions. More precisely,

$$\nu_{ij} = \left(\nu_j^{(g)} q_{ji} + \nu_j^{(l)}\right). \tag{3.28}$$

Each of the terms comprising ν_{ij} will be described shortly. In this section, the subscripts i and j index elements in the arrays $\mathbf{v} = (v_x, v_y, v_z)$ and $\mathbf{x} = (x, y, z)$, in addition to $\hat{\tau}$ and ν.

For global diffusion, a fourth order diffusion operator of the form $-\nabla \cdot \left(\hat{\nu}\nabla^3\mathbf{v}\right)$ is used, where $\hat{\nu}$ is a function of viscosity. We consider how this operator works by examining a 1D problem with constant $\hat{\nu}$. We look for Fourier solutions of the form $v = \exp\left(ikx - i\omega t\right)$ to the equation

$$\frac{\partial v}{\partial t} = -\hat{\nu}\frac{\partial^4 v}{\partial x^4}. \tag{3.29}$$

Thus, $i\omega = \hat{\nu}k^4$ and the velocity is described by $v = \exp\left(ikx - \hat{\nu}k^4 t\right)$. For $\hat{\nu} > 0$, this corresponds to waves being damped since $\exp\left(-\hat{\nu}k^4 t\right)$ tends to zero as t tends to infinity, with damping acting as a function of wave length, k. By considering the e-folding time and distance we can explicitly determine how damping varies with wave length. The e-folding time is the time taken for a wave to reduce to $1/e \approx 37\%$ of its original size. For the fourth order diffusion operator, the e-folding time is $t_e = 1/\hat{\nu}k^4$. If a wave is travelling at speed c, the e-folding distance will be $l_e = c/\hat{\nu}k^4$. We can see that waves with larger wave number (and shorter wave length) will be damped more quickly and over a shorter distance. Thus, this diffusion operator will act weakly on long wave lengths and strongly on short, problematic wave lengths.

Nordlund and Galsgaard (1997) advise that the global viscosity should be of the form $\nu_j^{(g)} =$

$\Delta x_j \left(\nu_1 c_f + \nu_2 |v_j|\right)$, where ν_1 and ν_2 are scaling coefficients and c_f is the fast mode speed. Before the form of the global viscosity is complete, the order of $\nu_j^{(g)}$ must be increased such that its overall affect in the momentum equation will be as a fourth order operator. Thus, $\nu_j^{(g)}$ is multiplied by a quenching term of the form

$$q_{ji} = q_j(f_i) = \left| \frac{\partial^2 f_i}{\partial x_j^2} \right| / \left| \frac{\partial f_i}{\partial x_j} \right|, \tag{3.30}$$

in (3.28). For viscosity, $f_i = \partial v_i / \partial x_j$. As we will see shortly, the inclusion of diffusive operators requires corresponding additional terms in the energy equation, since when wave energy dissipates there must be associated heating. The given form of the quenching term ensures that the dissipation is positive and, thus, heating occurs in the correct manner in the energy equation.

To obtain stability at shock fronts, we must ensure that the jumps in momentum and pressure balance each other. This can be achieved by using local viscosity, providing the viscous stress tensor is of the order of the sum of the momentum flux and pressure. Using $c_s^2 = \gamma p / \rho$, gives the pressure as being of O $\left(\rho v^2\right)$. If we assume that the jump in the velocity, Δv_j, across the shock front is of the order of the velocity of the shock then

$$\rho v^2 \approx \rho \Delta v_j \Delta x_j \frac{\partial v_j}{\partial x_j}. \tag{3.31}$$

Comparing this form to the components of $\hat{\tau}$, we find that $\nu_j^{(l)} = \Delta x_j \Delta v_j$. We only require the viscosity to act where convergence is occurring, i.e. $-\nabla \cdot \mathbf{v}$. This can be incorporated by rewriting the shock viscosity function as

$$\nu_j^{(l)} = \nu_3 \Delta x_j^2 |\nabla \cdot \mathbf{v}|_-, \tag{3.32}$$

where ν_3 is a scaling coefficient and

$$|\nabla \cdot \mathbf{v}|_- = \begin{cases} 0, & \nabla \cdot \mathbf{v} \geq 0, \\ |\nabla \cdot \mathbf{v}|, & \nabla \cdot \mathbf{v} < 0. \end{cases} \tag{3.33}$$

Taking a similar approach we can define the form of the magnetic resistivity. As in the case of viscosity, the magnetic resistivity is comprised of global and local operators. In fact, the form of the global resistivity is the same as that of the global viscosity, $\nu_j^{(g)}$, with the scaling coefficients redefined. Thus, $\eta_j^{(g)} = \Delta x_j \left(\eta_1 c_f + \eta_2 |v_j|\right)$, where η_1 and η_2 are scaling coefficients. For the magnetic resistivity, the quenching function q_{ji} acts on components of the current $(f_i = J_i)$.

Like the global diffusion, the magnetic shock diffusion varies only very slightly from the term devised for the shock viscosity. Under magnetic diffusion, the velocity perpendicular to the magnetic

field transports the flux without regard to the constraints imposed in a "frozen-in" flux regime. Thus, at magnetic shocks only the perpendicular velocity field is responsible for changes in the magnetic field. Hence,

$$\eta_j^{(l)} = \eta_3 \Delta x_j^2 |\nabla_\perp \cdot \mathbf{v}|_-, \tag{3.34}$$

where η_3 is a scaling coefficient.

We define the combined global and local magnetic resistivity operator, η, to have elements

$$\eta_{ij} = \left(\eta_j^{(g)} q_{ji} + \eta_j^{(l)}\right). \tag{3.35}$$

η acts on $\mathbf{J}$ in the following manner

$$\eta\mathbf{J} = \frac{1}{2}\left(\{\eta_{xy} + \eta_{xz}\}J_x, \{\eta_{yx} + \eta_{yz}\}J_y, \{\eta_{zx} + \eta_{zy}\}J_z\right). \tag{3.36}$$

As discussed above, the inclusion of each diffusive form requires associated heating terms in the energy equation. In section 3.1, we simply referred to these terms as Q_{visc} and Q_{Joule} without any indication of how they were to be calculated. Now that we have discussed how $\hat{\tau}$ and η are determined, the two heating terms are simply calculated as follows

$$Q_{visc} = \hat{\tau} : \nabla\mathbf{v} = \rho \sum_i \sum_{j \neq i} \nu_{ij} \left(\frac{\partial v_i}{\partial x_j}\right)^2 + \rho \sum_i \nu_{ii} \left(\frac{\partial v_i}{\partial x_i}\right)^2, \tag{3.37}$$

$$Q_{Joule} = \eta\mathbf{J} \cdot \mathbf{J}. \tag{3.38}$$

3.5 Individual Model Choices

The elements of `Diffin3d` discussed so far provide the basic setup of the numerical code and are common to all simulations performed with this code. We now move on to consider the choices a user must make when setting up an individual experiment that will be run with `Diffin3d`.

One of the first choices a user must make is about the **physical coordinates** the system will represent. Given that `Diffin3d` works in cartesian coordinates, three values must be given corresponding to the total length of the domain in the x, y and z directions. The size of the domain will obviously depend upon the size of the event being modelled and any scaling in use.

The user will need to decide upon the **type of boundaries** employed in each of the three directions of the domain. `Diffin3d` provides options for closed and periodic boundaries and the implementation of these will be discussed in section 3.5.1. The type of boundaries used will depend

upon the nature of the event being modelled. For some events, periodic boundaries will be totally unsuitable. For example, when the bottom boundary of a domain represents a part of the solar interior and the upper boundary represents a layer of the corona we would not want information to pass out of the domain through one boundary and return through the other. In the case of closed boundaries, it is sometimes desirable to have a **damping zone** and the specifics of this will be presented in section 3.5.3.

Once the size of the domain has been determined, the user must decide the **number of gridpoints** that will be used to model the whole domain. Three integer values need to be provided that represent the number of gridpoints to be used in the x, y and z directions. Multiplying these three values together gives the total number of cells in the domain. In any of the three cartesian directions, the **decomposition of the gridpoints** in relation to the length of the domain can be treated in different ways. In section 3.5.2, we will consider uniform and stretched grid decomposition. The number of gridpoints and the grid decomposition will depend upon the scale at which the user wishes to discern smaller events in the overall event being modelled.

A start-up routine will need to be provided by the user if a suitable one does not already exist. This routine will specify the **environment throughout the domain** to be used at the beginning of the experiment. `Diffin3d` will then advance this initial domain in time. In chapters 4 and 5 we will consider the initialisation of our hydrostatic atmosphere and the magnetic flux tube used for the emerging flux simulations. Within the start-up routine, the user must specify the values of the four basic scalars and vectors (ρ, e, $\mathbf{B}$ and $\mathbf{P}$). It is possible to run `Diffin3d` under a hydrodynamic guise whereby all calculations involving the magnetic field are ignored and, thus, $\mathbf{B}$ is not specified in the start-up routine. The hydrodynamic feature may reduce the calculation time of each iteration but to model most astrophysical scenarios a magnetic field is required.

The modelling of a specific event may require more management than simply allowing the starting environment to evolve with time. In some cases, a **velocity driver** may be employed and this can either act for a certain period of time or over the whole length of the simulation. The velocity driver will impose a velocity over a certain region of the domain, the specifics of which will be dependent upon the individual model. `Diffin3d` will always assume that no driver is to be used unless the user specifies otherwise. Velocity drivers are not used in our emerging flux simulations and, thus, will not be discussed further.

As discussed in section 3.3.2, numerical overshoot can cause thermal energy to become negative. This is undesirable and can be prevented through artificial heating in the form of **Newton cooling**. This will be discussed in section 3.5.4. When modelling certain events **gravity** may be negligible whilst for others it is vitally important and, thus, `Diffin3d` provides an option to turn gravity off.

In appendix B, we give an example of an input file for use with `Diffin3d`. In this file, parameters

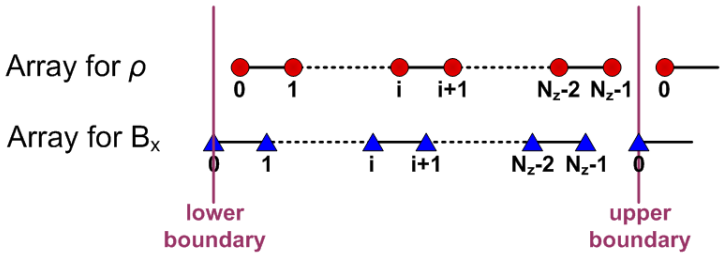

(a) Periodic

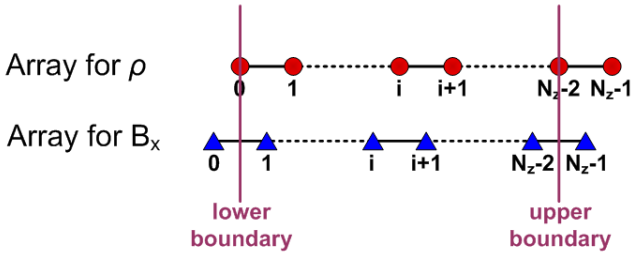

(b) Closed

Figure 3.5: The location of the boundaries of a 1D domain in relation to the array indices illustrated for a periodic and a closed grid, with cell centred ρ and face centred B_x.

for the choices described above are specified. It may be necessary for some parameters associated with the start-up routine to be given by the user at runtime and this can also be done through the input file.

3.5.1 Periodic or Closed Boundaries

`Diffin3d` offers options for both closed and periodic boundaries in the simulation domain. In the horizontal directions, x and y, the boundaries can be periodic or closed but in the vertical direction closed boundaries are enforced. As discussed in section 3.2, the staggered grid results in gridpoints of different arrays, but with the same index, holding values that correspond to different locations. This was illustrated in figure 3.3. Thus, we begin by considering the location of the boundaries in reference to the individual arrays containing quantity values.

We consider 1D arrays in the z direction that consist of N_z cells indexed from 0 to $N_z - 1$. For periodic boundaries, the first cells (in the periodic direction) of the face centred arrays hold boundary values for both ends of the domain. All of the gridpoints of all of the arrays lie within or on the domain boundaries, as shown in figure 3.5(a).

For closed boundaries, the limit of the domain (in the closed direction) falls in line with the cell centred quantities. Thus, the first and last cells (in the closed direction) of the face centred arrays hold values belonging to points half a cell's length outside of the domain. As discussed in

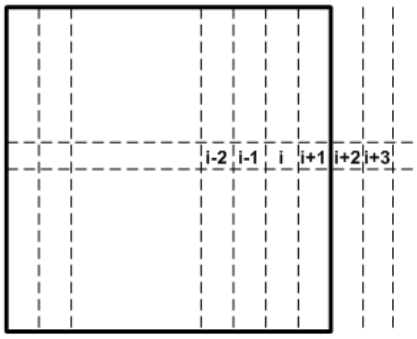

Figure 3.6: In a standard grid, the fifth order accurate methods will run out of gridpoints as the boundary is approached. Here, there are no values associated with the indices $i+2$ and $i+3$ since these locations lie outwith the domain.

section 3.2, all quantities are held in 3D arrays of the same size and, therefore the highest indexed cell in arrays of cell centred quantities belongs to a location outside of the boundary. This is demonstrated in figure 3.5(b) and will become important when we consider the arrangement of the physical domain dimensions to actual gridpoints. It is necessary for there to be face centred momentum components available that correspond to regions outwith the domain so that closed boundary conditions can be implemented. These conditions will be considered further shortly.

As discussed in section 3.3.1, without intervention, the differentiation and interpolation methods will run into trouble at the domain boundaries. Three gridpoints are required on either side of the point being evaluated and when the methods come to calculate values at the edge of the grid they will eventually fail to have enough points. This is illustrated in figure 3.6.

If a particular set of boundaries is chosen to be periodic, then the differentiation and interpolation methods will use a "wrap-around" effect. As shown in figure 3.7(a), when indexing runs over the edge of the grid during a calculation it is continued through the associated periodic boundary. The period boundary allows the same differentiation and interpolation methods to be used across the whole of the domain. Figure 3.7(b) shows how ghost cells can be introduced to aid calculations at periodic boundaries. These are "invisible" zones of extra cells that lie at the period boundaries. The values they contain are just copies of the values in the cells at the corresponding periodic boundary and do not affect the solution in any way. The grid stored at the end of each iteration is the standard domain without the ghost cells.

However, if the domain is closed there is no advantageous "wrap-around" effect when the edge of the grid is crossed and trouble arises. To avoid this problem, `Diffin3d` uses a combination of the different ordered methods to calculate the values of any one quantity across the whole of the domain. In the majority of the domain the highest order method will be used but, as the edge of the grid is reached, less points are available for each calculation so the order of the method is

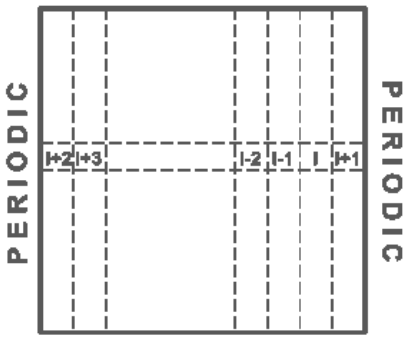

(a) The "wrap-around" effect for a periodic grid allows calculations to flow over the boundary of the domain.

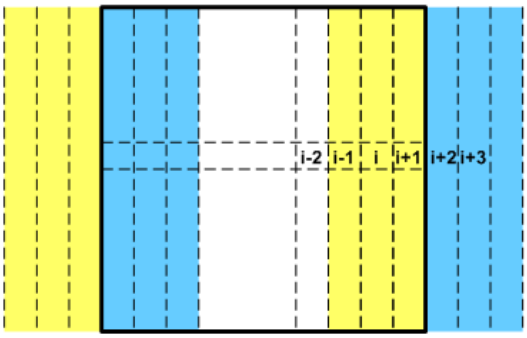

(b) Ghost zone layers at the edge of the periodic boundaries have copies of the values that lie just within the corresponding boundary. The values in the blue region in the domain are copied into the other blue region outside of the domain and similarly for the yellow zones.

Figure 3.7: Periodic boundaries allow the fifth order methods to continue to be used without problems when the domain boundary is crossed during a calculation.

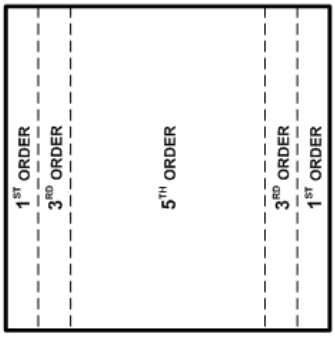

Figure 3.8: For a closed boundary domain, it is necessary to change the order of the method when the boundary is approached since higher order methods will run out of gridpoints.

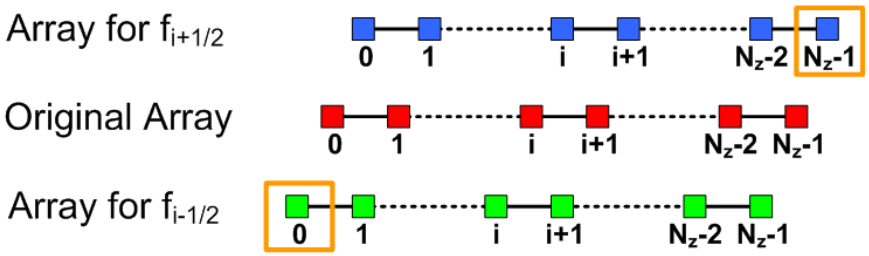

Figure 3.9: In the case of closed boundaries, even the first order methods have gridpoints that they fail to be able to calculate values for, as indicated by the orange squares. For the up-shifting methods, a finite difference on $N_z - 2$ and $N_z - 1$ gives $N_z - 2$ in the $f_{i+1/2}$ array but $N_z - 1$ remains empty. For the down-shifting methods, a finite difference on 0 and 1 gives 1 in the $f_{i-1/2}$ array but 0 remains empty.

dropped to take this into consideration, as shown in figure 3.8. The derivation of the 1^{st} and 3^{rd} order differentiation and interpolation methods was described in section 3.3.1.

Reducing the order of the methods does not solve all of the problems caused by using closed boundaries. Every time a differentiation or interpolation method is used, there will be a gridpoint that fails to be evaluated. This is demonstrated in figure 3.9 where the middle array is the array prior to any operation being performed. A first order method performed on gridpoints 0 and 1 of the original array will give the value for gridpoint 0 when solving for points $i + 1/2$ and gridpoint 1 when solving for points $i - 1/2$. This leaves gridpoint 0 empty when using a down-shifting method. Similarly at the other end of the array, a first order method performed on gridpoints $N_z - 2$ and $N_z - 1$ of the original array will give the value for gridpoint $N_z - 2$ when solving for points $i + 1/2$ and gridpoint $N_z - 1$ when solving for points $i - 1/2$. Again, this leaves a point unevaluated but this time it is the gridpoint $N_z - 1$ when using an up-shifting method.

These "empty" gridpoints can easily be solved for. We continue to consider a 1D array in z. Every time interpolation is carried out that shifts down or up in the closed boundary direction, the end gridpoints of the resulting array are set as follows:

$$f^s_0 = 2f_0 - f^s_1, \tag{3.39}$$

$$f^s_{N_z-1} = 2f_{N_z-1} - f^s_{N_z-2}, \tag{3.40}$$

where f^s is the shifted array and f is the original array. This is simply a rearrangement of the first order interpolation method. Similarly, every time differentiation is carried out that shifts down or up in the closed boundary direction, the end gridpoints of the resulting array are set as follows:

$$f^s_0 = f^s_1, \tag{3.41}$$

$$f^s_{N_z-1} = f^s_{N_z-2}. \tag{3.42}$$

This gives a constant gradient at the edge of the domain in the direction perpendicular to the closed boundaries.

These filling methods for the empty gridpoints are not the same as setting boundary conditions in the closed direction. This must be done separately for each of the four basic quantities. We wish to ensure no movement of material through the boundaries and, therefore, we must physically set the value of the momentum perpendicular to the closed boundary. For the 1D example in z, this would be

$$P_{z\,0} = -P_{z\,1}, \tag{3.43}$$

$$P_{z\,N_z-1} = P_{z\,N_z-2}. \tag{3.44}$$

This results in $P_z = 0$ at the lower and upper boundaries which fall between the last two gridpoints at each end of P_z.

For the magnetic field, we must make special effort to ensure $\nabla \cdot \mathbf{B} = 0$ at the closed boundaries. Evaluating this in turn determines the value for the component of the magnetic field perpendicular to the closed boundaries in the cells outside the domain. For the lower boundary we require

$$\left(\frac{\partial \mathrm{B}_x}{\partial x}\right)_{1/2} + \left(\frac{\partial \mathrm{B}_y}{\partial y}\right)_{1/2} + \left(\frac{\partial \mathrm{B}_z}{\partial z}\right)_{1/2} = 0, \tag{3.45}$$

where the partial derivatives are evaluated at the first half cell point in the direction of the closed boundary. The fifth order up-shifting differentiation methods operating in the periodic x and y directions will automatically give the first and second terms in the correct positions. Using a first order finite difference differentiation approach we have

$$\left(\frac{\partial \mathrm{B}_z}{\partial z}\right)_{1/2} = \left(\mathrm{B}_{z\,1} - \mathrm{B}_{z\,0}\right)/\Delta z. \tag{3.46}$$

Substituting (3.46) into (3.45) and rearranging we have

$$\mathrm{B}_{z\,0} = \mathrm{B}_{z\,1} + \Delta z \left(\left(\frac{\partial \mathrm{B}_x}{\partial x}\right)_{1/2} + \left(\frac{\partial \mathrm{B}_y}{\partial y}\right)_{1/2} \right). \tag{3.47}$$

Similarly at the upper boundary, satisfying $\nabla \cdot \mathbf{B} = 0$ yields

$$\mathrm{B}_{z\,N_z-1} = \mathrm{B}_{z\,N_z-2} - \Delta z \left(\left(\frac{\partial \mathrm{B}_x}{\partial x}\right)_{1/2} + \left(\frac{\partial \mathrm{B}_y}{\partial y}\right)_{1/2} \right). \tag{3.48}$$

ρ and e are cell centred values and, thus, lie exactly on the closed boundaries. No specific treatment is given to these quantities since the methods for evaluating the "empty" cells are adequate.

For all of the individual arrays, the gridpoint with the largest index lies outwith the upper boundary of the domain. Steps are taken every tenth iteration to prevent a runaway solution here. For the cell centred quantities, the values at the boundary are copied to the cells above the boundary. For the face centred quantities, except those perpendicular to the boundary, the values at the half cell location below the boundary are copied into the half cell location above the boundary.

3.5.2 Uniform or Stretched Grid

As discussed in section 3.5, the user must specify the domain size and the number of gridpoints to be used in each direction. For example, the dimensions may be $-60 \leq x \leq 60$, $-70 \leq y \leq 70$ and $0 \leq z \leq 90$ whilst the user wants 128 gridpoints in x, 140 in y and 300 in z.

For each coordinate, we assign a 3D grid to hold the dimensional value of each cell centred point of the staggered grid. The domain size in any particular direction refers to the coordinate distance between the boundaries of the domain. As we have seen in section 3.5.1, the location of the boundary in relation to the grid's staggered cells will depend upon the type of boundary being used. Thus, the type of boundary will also affect how the dimensional values are assigned to the coordinate arrays.

The simplest way to split the gridpoints over each dimensional length is to use uniform spacing. Thus, the total distance required in the x direction, say, would be divided equally amongst the number of gridpoints in x. If the x direction is periodic, then the distance between adjacent gridpoints would be $\Delta x = d_x/N_x$, where d_x is the total dimensional distance in x and N_x is the number of gridpoints in the x direction. To yield cell centred dimensional values we would use

$$x_i = x_{min} + \left(i + \frac{1}{2}\right)\Delta x, \tag{3.49}$$

where x_i is gridpoint i of the coordinate array for x and x_{min} is the dimensional value of x at the lower boundary. If the domain has closed boundaries in the x direction, then no shifting is required to make the dimensional values cell centred. However, the dimensional value will only be covered by the first $N_x - 1$ gridpoints since, as explained in section 3.5.1, the $N_x - 1^{\text{th}}$ centred cell location lies above the upper boundary of the domain. Thus, we have

$$x_i = x_{min} + i\Delta x^*, \tag{3.50}$$

where $\Delta x^* = d_x/(N_x - 1)$. Similarly, these methods are applied to the y and z directions when uniform spacing is required. The acceptable distance between gridpoints will be entirely dependent upon the situation being modelled. As a rule of thumb, the distances should be smaller than the smallest length-scale wishing to be modelled.

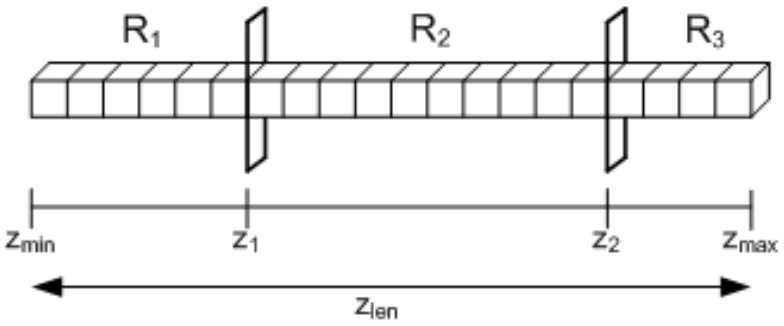

Figure 3.10: A 1D array of cells in the z-direction, which is divided into three sections: R_1, R_2 and R_3. In coordinate dimensions, the array covers a distance of z_{len}, ranging from z_{min} to z_{max}. The upper boundaries of R_1 and R_2 are given by z_1 and z_2.

Sometimes, finer details of events are required in a subset region of the domain. More information can easily be obtained by increasing the number of gridpoints. When using uniform grid spacing, we must increase the number of gridpoints over the whole of the domain in order to achieve smaller gridspacing for a select region. This can dramatically increase the computational time of the experiment, with time wasted producing finer detail results in regions where they are not required as well as where they are. Stretching the grid provides a solution to this problem by allowing variable grid spacing over the domain. `Diffin3d` is not an adaptive mesh code and, once this spacing is determined at the setup stage, it will remain the same for the rest of the experiment's run.

`Diffin3d` provides several different implementations for stretched grids. They include fitting the gridpoints to a `tanh` profile, such that gridpoints are clustered near the boundaries of the domain in the stretched direction, and fitting the gridpoints to several different polynomials within different regions of the domain. The later is the stretching routine that is used for all of the experiments detailed in this thesis and we shall, therefore, discuss it in more detail below.

For clarity, we will consider applying the polynomial fitting method to a 1D array of gridpoints in the z direction. Of course, this method can also be applied to gridpoints in the x and y directions too. We assume that the length of the domain in the z direction has already been determined by the user to be z_{len}, with z_{min} and z_{max} representing the upper and lower boundaries in the z direction, respectively. The domain is divided into three sections in the z direction (R_1, R_2 and R_3), as shown in figure 3.10. The upper boundaries of R_1 and R_2 are z_1 and z_2, respectively, and are specified by the user.

The user must also specify the proportion of the total number of gridcells in the z direction that will lie in regions R_1 and R_2. As in the uniform spacing case, the total number of gridpoints in the stretching direction will be N_z and $N_z - 1$ for periodic and closed z boundaries, respectively. If

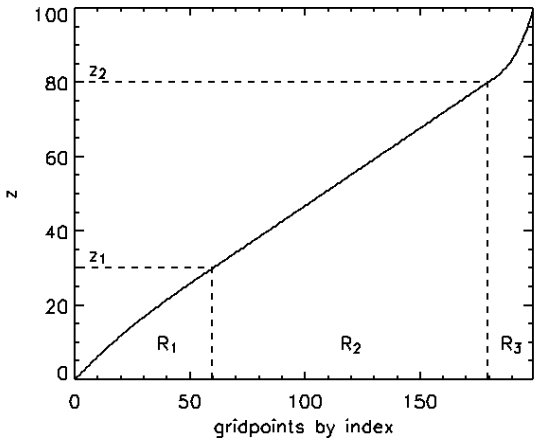

Figure 3.11: The results from using the polynomial fitting method to determine the relationship between the gridpoints and the stretched z dimension of the domain. Of the 200 gridpoints, 30% lie in R_1 and 60% reside in R_2. Region R_2 has uniform grid spacing while R_1 and R_3 have non-uniform spacing. Gridpoint indexing starts at 0.

the gridpoint proportions are p_1 and p_2 for R_1 and R_2 respectively, then the proportion of gridcells in the region R_3 is automatically given as $p_3 = 1 - p_1 - p_2$. Gridpoints in the middle section, R_2, are given uniform spacing. Using the polynomial fitting method described in appendix C, the grid spacing in the two end regions is determined. Under special circumstances, the grid spacing in either of these regions can also be uniform although, as will be demonstrated in appendix C, these end regions must then have the same spacing between cells as in the middle region.

The spacing of the cells in the end sections is determined such that there is no sudden jump in cell size at the boundaries z_1 and z_2. Additionally, the regions R_1 and R_3 must use the exact specified number of gridpoints between the boundaries of each region. In the case of closed boundaries, the dimensional value of the cell centred point lying outwith the domain (z_{N_z-1}) will be determined using the polynomial prescribing the grid spacing in section R_3. If using periodic boundaries, shifting will be required to retrieve values for cell centred positions. This may be done using the finite difference interpolation scheme described in section 3.3.1.

Figure 3.11 shows the results of applying the polynomial fitting method over a spatial distance of 100 units in the closed z direction. The distance is divided between 200 gridpoints, where 30% lie in the region $0 \leq z < 30$ and 60% lie in the region $30 \leq z < 80$. The 201^{th} gridpoint, which lies outside of the domain, is not shown.

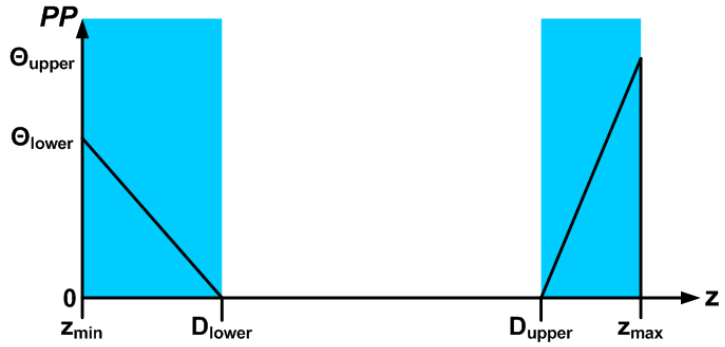

Figure 3.12: Over the regions $z_{min} \leq z \leq D_{lower}$ and $D_{upper} \leq z \leq z_{max}$ momentum is removed from the system in order to provide a damping regime near the boundaries, as indicated by the blue sections. The percentage of momentum removed per time unit, PP, at the lower and upper boundaries of the domain increases as the boundary is approached. PP reaches the values Θ_{lower} and Θ_{upper} at the lower boundary, z_{min}, and upper boundary, z_{max}, respectively.

3.5.3 Damping Zones for Closed Boundaries

In the event that closed boundaries are employed, a useful damping "zone" can be imposed. The damping zone is placed at the domain's closed boundaries and can be of any width. It aims to reduce the reflection of waves at the boundary by altering the momentum there. At the start of the damping zone the momentum remains unchanged and at the boundary a certain percentage, Θ, is removed per time unit. Moving from the start of the damping zone to the boundary there is a linear increase in the amount of momentum removed, up to the maximum amount Θ at the boundary.

We consider a grid whose boundaries in the z direction are at z_{min} and z_{max}, with $z_{min} \leq z_{max}$, as shown in figure 3.12. The damping zones at the lower and upper boundaries will start at D_{lower} and D_{upper} respectively, with $z_{min} < (D_{lower}, D_{upper}) < z_{max}$. At the lower and upper boundaries the percentage of the momentum removed will be Θ_{lower} and Θ_{upper} respectively.

The function prescribing the percentage of momentum, PP, to be removed per time unit is

$$PP(z) = \begin{cases} \Theta_{lower}\left(D_{lower} - z\right) / \left(D_{lower} - z_{min}\right), & z_{min} \leq z \leq D_{lower} \\ 0, & D_{lower} < z < D_{upper} \\ \Theta_{upper}\left(z_{max} - z\right) / \left(z_{max} - D_{upper}\right), & D_{upper} \leq z \leq z_{max} \end{cases} \tag{3.51}$$

The values of Θ_{lower} and Θ_{upper} are specified by the user and a value such as 1.0 would represent 100%.

As discussed in section 3.3.2, each iteration advances time by less that one time unit. However, we specified PP to be the percentage of momentum removed per time unit. Therefore, we must take into account the length of the time step between iterations when calculating the reduced

momentum in the damping zones. Thus, the final momentum, **P'**, with percentages removed in the damping zones will be

$$\mathbf{P'} = (1 - PP(z)\,\Delta t)\,\mathbf{P}, \tag{3.52}$$

where **P** is the momentum vector of that time step prior to reduction and Δt is the size of the time step between iterations.

`Diffin3d` currently only allows damping to be applied to the boundaries in two directions, namely z and y, giving a total of four possible boundaries at which a damping zone can be included. It is possible for `Diffin3d` to be run with damping occurring at any combination of the four boundaries, from none through to all four. It is also possible for damping to be imposed at only one of the boundaries in a particular direction. When damping is imposed at both boundaries in a given direction it is possible, and fully acceptable, for the damping zones to be of different widths to each other and to have $\Theta_{lower} \neq \Theta_{upper}$.

At any particular closed boundary, the width of the damping zone and the value chosen for Θ will depend upon a number of factors. The most important factor is the relative size of the velocities occurring at the closed boundary in relation to other velocities in the domain. In the setting up of a new model with closed boundaries, it would be ideal to run a test experiment with no damping zones to see the order and direction of any unwanted velocities arising. If any of the velocities are reflecting off the boundaries of the domain, then damping zones should be included only where appropriate.

3.5.4 Newton Cooling

The Newton cooling mechanism can be used to control temperatures within the domain. As discussed in section 3.3.2, numerical errors or overshoot can result in thermal energy becoming negative rather than just being very small. On the other hand, in some simulations it may be desirable to remove excess heat from a current sheet. Both of these situations are examples of when steep gradients in the thermal energy can dominate in the determination of the time step size and, in some cases, make the time step so small that a simulation stalls. Newton cooling can be used to stabilise temperatures and prevent thermal energy gradients from controlling the time step size.

`Diffin3d` allows for uniform cooling over the whole domain or cooling to different temperatures in different regions of the domain. Although described as cooling, the mechanism can heat or cool since it basically acts to return temperatures to some specified temperature.

The user specifies which of the modes of cooling to use and the time-scale over which cooling should occur. A very short time-scale will result in the temperature returning to the specified

value practically immediately. In the case of uniform cooling, the user must also specify one thermal energy value that the Newton cooling mechanism will try to return the whole domain to. For simulations where the required temperature varies with location, the user will need to have more input into deciding the cooling mechanism since this will depend upon the events being modelled and may need a special routine written for it.

`Diffin3d` also includes the option of no cooling, whereby the evolution of the domain continues under the equations given in section 3.1. All of the simulations described in this thesis have been carried out under this option and, thus, Newton cooling will not be discussed in any further detail.

3.6 Parallelisation

`Diffin3d` is written in the Fortran programming language, which is used widely for mathematical and scientific work. It is well suited for this type of work for a number of reasons. Fortran has a large library of standard mathematical functions such as $\cos(x)$, $\exp(x)$, etc. It has a range of data types (integers, decimals, complex numbers and boolean values) and can operate with a precision of at most 8 or 16 decimal places. Fortran has a well established standard, which makes the software extremely portable between different platforms.

`Diffin3d` exploits the Message Passing Interface (MPI) provided by Fortran. MPI is a library specification for message-passing, proposed as a standard by a broadly based committee of vendors, implementors, and users. MPI commands allow messages to be passed between processors and, therefore, enables the code to be run in parallel across any number of processors. The simulations described in detail in this thesis typically use 16 or 32 processors. Spreading the work load over several processors running in parallel can drastically reduce the run time of a simulation. It should be noted that the total number of computational hours for the simulation will not reduce since this is the sum of each processor's runtime.

The optimal number of processors for an individual simulation to be run over will be determined by several factors:

- the number of gridpoints in the computational domain,
- the time available for the code to run,
- any limit imposed on the size of individual files when data is output and stored individually for each processor.

Increasing the number of processors is not always advantageous since the inclusion of each new processor adds communication time, which is usually slower than the same calculation carried out

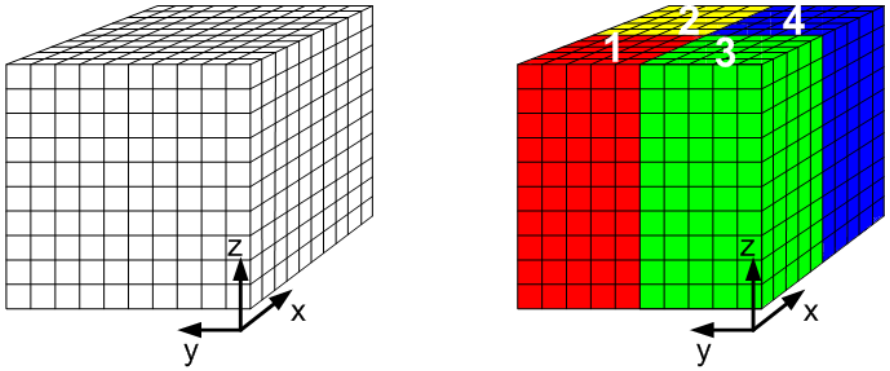

Figure 3.13: The computational grid is divided amongst the allocated processors, such that the cells in the same vertical strip are housed in the same processor. In this example, the grid has been split over 4 processors.

on a single processor.

When `Diffin3d` is run, the MPI commands divide the computational domain amongst the number of processors requested by the user. Division of the grid occurs only in the horizontal directions, thus data points in the same vertical column will be housed on the same processor, as shown in Figure 3.13.

During the finite difference operations in the horizontal directions, it is necessary for the processors to communicate with each other when the neighbouring points required lie across processor boundaries. Additionally, the use of periodic boundaries requires information to be transferred at grid boundaries. By using the virtual topologies provided with MPI, communication between the processors can be written in a simpler, minimal style within the code. A virtually topology is a mechanism for naming the processors being used such that each processor knows which other processors it is connected to.

`Diffin3d` uses the "cartesian virtual topology", which is suitable for grid-like topologies. As illustrated by Figure 3.14, each processor is connected to its neighbours on a virtual grid system and knows exactly which other processors lie immediately north, south, east and west of it. The use of the topology means data can be passed during the finite difference calculations without the code having to figure out exactly which processor corresponds to which gridpoints prior to each calculation.

3.6.1 Copson

The parallel computer network upon which the simulations in this thesis were run is called "Copson". It is housed in the Mathematics and Statistics Institute at St Andrews University and was

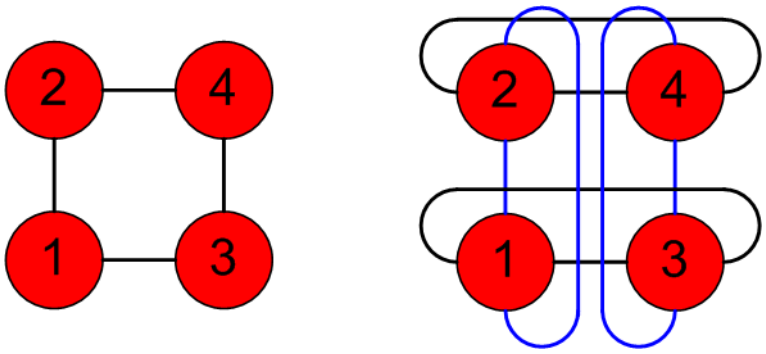

Figure 3.14: Cartesian topologies for grids with closed and periodic horizontal boundaries. The processors are indicated by the numbered red circles and the lines of communication by the black and blue lines between the processors. The example shown here consists of four processors and is rather a special example since all of the processors contain cells that correspond to the edge of the grid. For the closed boundaries grid, each processor on the edge of the grid only communicates information with two other processors. However, for a grid with periodic boundaries in both horizontal directions, each processor on the edge of the grid communicates with four other processors. In an example with a larger number of processors, there would be processors corresponding solely to the inner parts of the domain and, independent of the type of boundary, these would always communicate with four other processors.

installed in January 2003. The network contains 86 nodes with each node comprising of 2 processors. Each processor has 2 GB of RAM and, thus, the network as a whole has 172 GB.

The network is named after Professor Edward Copson (1908 – 1980). His links with the University of St Andrews began in 1930 when he was given lectureship in the Mathematics department. He left in 1934 but returned again in 1950 when he was appointed as professor to the Regius Chair of Mathematics. Copson's postings at St Andrews continued to increase in prestige, from Dean of the Faculty of Science between 1950 and 1953 to first Master of the United College in 1954. After his official retirement in 1969, Copson continued to teach, research and write books.

The network was bought on behalf of the Mathematics department and the University of St Andrews Solar Group. Funding came from the Scientific Research Investment Fund (SRIF) and the Particle Physics and Astronomy Research Council (PPARC).

Copson is available for use by those currently involved in research who are members either of the School of Mathematics and Statistics at the University of St Andrews or the UK MHD consortium.

3.7 Testing of `Diffin3d`

Previous flux emergence simulations have been carried out using `Diffin3d` and the results of these were discussed in chapter 2 (Archontis et al. 2004; Galsgaard et al. 2005; Archontis et al.

2005, 2006; Galsgaard et al. 2007). The first paper in this collection, Archontis et al. (2004), carried out an experiment whose setup was taken from Fan (2001) and recreated the results seen therein, thus giving confidence in the results produced by `Diffin3d` for this particular type of experiment. The setups we use in chapters 4, 5, 6 and 7 vary very little from the test experiment of Archontis et al. (2004) and, therefore, no specific additional testing of `Diffin3d` has been carried out during this thesis. Convergence testing of the results described in chapters 4, 5, 6 and 7 has been carried out and the specific details will be discussed in each chapter where appropriate.

`Diffin3d` has been used for a number of other studies including simulations of turbulence, stellar convection, dynamo action, coronal heating and buoyant magnetic flux tubes.

Chapter 4

Creating a Hydrostatic Atmosphere

For our flux emergence simulations, the 3D domain models several layers of the solar atmosphere, following the style of previous experiments. These layers are simplified representations of the convection zone, photosphere, transition region and corona. Into the solar interior we place a buoyant flux tube, which over time rises towards the photosphere. Unlike other simulations, the flux tube is the only magnetic element in our simulation domain. We require any motions in the domain at the start of the simulation to be from the magnetic flux tube only and, therefore, the ambient fluid in the domain should be static in the absence of the tube. In this chapter, we will present the hydrostatic environment used by the simulations described in chapters 5, 6 and 7.

As discussed in sections 1.4 and 3.7, flux emergence simulations have previously been carried out using `Diffin3d` and our domain's temperature, gas pressure and density profiles are taken from these. In section 4.1, we will introduce the analytical hydrostatic background model and consider how appropriate this model is in comparison to the actual solar profiles for these quantities.

The numerical code, `Diffin3d`, applied to the domain uses dimensionless equations. The analytical domain model must, therefore, be non-dimensionalised prior to being implemented. Additionally, previous simulations have considered domains with atmospheric magnetic fields (Archontis et al. 2004, 2005; Galsgaard et al. 2005; Archontis et al. 2006; Galsgaard et al. 2007) and, although we do not have such a field, we wish to create a general numerical model domain for use in situations where both magnetised and unmagnetised atmospheres are required. Hence, slight modifications must be made to the numerical solution that is originally derived from the analytical model with an unmagnetised atmosphere to enable this generality. The non-dimensionalising process and magnetised atmospheric modifications will be discussed in section 4.2.

The environment employed by the past and present simulations is in hydrostatic equilibrium when considered analytically. However, its numerical implementation does not result in a perfectly static

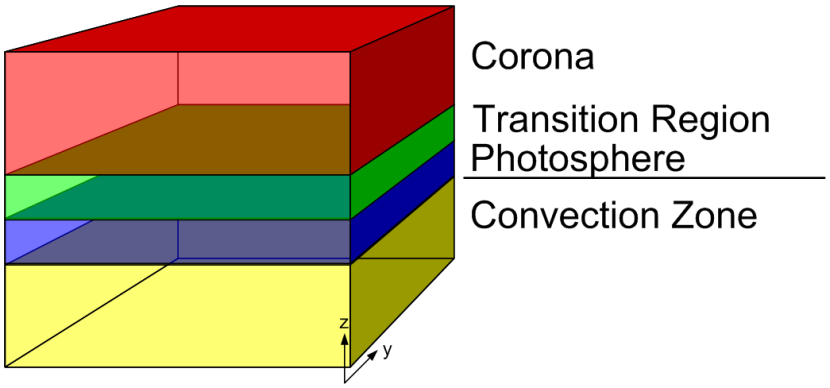

Figure 4.1: The simulation domain is divided into four horizontal regions representing the convection zone, photosphere, transition region and corona.

environment and, in section 4.3, we will present evidence of problems occurring when using this particular numerical atmospheric model.

In section 4.4, we will identify three specific problems with the numerical model that prevent hydrostatic equilibrium from being achieved within the domain. Then, using the initial numerical model as a basis, we will implement solutions to address each of the highlighted problems. Our aim will be to develop a new numerical model for the domain that achieves a better hydrostatic equilibrium.

Finally, in section 4.5, we will evaluate the effectiveness and computational efficiency of the new numerical model. Using this information, we will determine which of the solutions are feasible and should, therefore, be implemented in order to create the numerical environment of the domain.

4.1 The Analytical Atmosphere

We begin by introducing the analytical hydrostatic model. The model forms the basis for the numerical solar interior and atmospheric model employed in the simulations of chapters 5, 6 and 7. Inclusion of the magnetic flux tube within the solar interior will be left until these later chapters.

The simulation domain is comprised of four horizontal layers, as shown in figure 4.1. Each layer represents a simplified region of the Sun: the convection zone, photosphere, transition region and corona. The solar surface lies at the base of the photosphere, in the horizontal plane $z = 0$. Thus, the solar interior is defined by heights with $z < 0$ and the solar atmosphere by $z \geq 0$.

For each region, profiles must be found for the ambient environment's thermal energy and density. Here, we will consider finding profiles for the gas pressure and density, from which the thermal energy can be calculated. At the boundaries between each region, the functions prescribing these

quantities must be continuous but not necessarily continuously differentiable. Additionally, each quantity is uniform across the horizontal plane and varies only with height, z. Thus, these quantities will be given by functions of z only.

As discussed in section 1.1, the various solar atmospheric regions are distinguished by their temperature profiles. Hence, we define the temperature profile for the ambient fluid in each region and, in conjunction with the condition of hydrostatic equilibrium, vertical profiles for the gas pressure and density can then be calculated. Thus, in each region the gas pressure and density must be derived such that they adhere to the following

$$\frac{dp}{dz} = -\rho g, \tag{4.1}$$

$$p = \rho \tilde{R} T / \tilde{\mu}. \tag{4.2}$$

Firstly, we consider the convection zone. As stated in section 1.1, this solar region is characterised by convective motions. The Schwarzschild condition states that a convective instability will set in for an adiabatic fluid if the following criterion is satisfied (Priest 1982)

$$-\frac{dT}{dz} > \frac{\tilde{\mu} g}{\tilde{R}} \frac{\gamma - 1}{\gamma}, \tag{4.3}$$

where $\gamma = 5/3$ is the ratio of specific heats and $T(z)$ is the function prescribing the temperature. However, convection will add to the complexity of the simulation results and make it difficult to determine the physical processes that solely relate to the emergence event. Thus, we choose to make our subsurface region marginally stable to the instability and refer to it as the solar interior rather than the convection zone to avoid confusion. The inclusion of convection is left for future work. The temperature of the marginally stable solar interior region is given by

$$T_{si}(z) = T_{ss} - z\xi \frac{(\gamma - 1)}{\gamma}, \tag{4.4}$$

where the temperature at the solar surface is T_{ss} and $\xi = \tilde{\mu} g / \tilde{R}$.

We now use (4.1) and (4.2) to calculate $p_{si}(z)$ and $\rho_{si}(z)$. Rewriting (4.2) we have

$$\frac{p_{si} \tilde{\mu}}{\tilde{R} T_{si}} = \rho_{si}, \tag{4.5}$$

and substituting this into (4.1) yields

$$\frac{dp_{si}}{dz} = -\frac{p_{si} \xi}{T_{si}}. \tag{4.6}$$

Integrating this gives

$$p_{si} = \frac{p_{ss}}{T_{ss}^{\gamma/(\gamma-1)}} \left(T_{ss} - z\xi \frac{(\gamma-1)}{\gamma} \right)^{\gamma/(\gamma-1)}, \tag{4.7}$$

where p_{ss} is the gas pressure at the solar surface. Hence, from (4.5), the density is given by

$$\rho_{si} = \frac{\rho_{ss}}{T_{ss}^{1/(\gamma-1)}} \left(T_{ss} - z\xi \frac{(\gamma-1)}{\gamma} \right)^{1/(\gamma-1)}, \tag{4.8}$$

where $\rho_{ss} = p_{ss}\tilde{\mu}/\tilde{R}T_{ss}$ is the density at the solar surface. Thus, the gas pressure and density profiles are now known in the solar interior region.

Secondly, we consider the atmosphere. The VAL model, shown in figure 4.2, gives the average quiet Sun temperature profile from the solar surface, up through the chromosphere, to the start of the transition region (Vernazza et al. 1981). Over the height of the photosphere, the temperature falls as the distance from the solar surface increases. The top of the photosphere and the bottom of the chromosphere corresponds to the temperature minimum at ~ 500 km. The chromosphere can actually be divided into three sections: low, middle and high chromosphere. The low chromosphere, $500 - 1000$ km, is the region in which the temperature increases rapidly from the temperature minimum. In the middle chromosphere, $1000 - 2000$ km, the temperature increase occurs much more slowly with height and, thus, this region could be considered as having approximately constant temperature with height. The high chromosphere, $2000 - 2300$ km, is characterised by a jump in temperature from 7000 K to $24,000$ K, followed by a region of approximately constant temperature. The final jump in temperature at ~ 2300 km marks the start of the transition region, where the temperature increases extremely rapidly over a very short height, reaching 1 MK at the base of the low corona.

In terms of analytically modelling the solar atmosphere, the following simplifications are made:

- The temperature at the solar surface is again reached in the middle chromosphere. Thus, we choose to ignore the fluctuation in temperature in the photosphere and low chromosphere and model the first 1700 km of the atmosphere with a constant temperature profile. Hence, the solar photosphere, low and middle chromosphere are indistinguishable in the analytical model and are, therefore, referred to as solely the photosphere.

- From 1700 km up to the low corona, the temperature increases hugely through several individual jumps. We choose to model these jumps as one single rapid increase in temperature with height. Thus, the Sun's high chromosphere and transition region become combined in the analytical model and are referred to as the transition region.

- We choose to model only the low corona, extending to $\sim 12,000$ km above the solar surface.

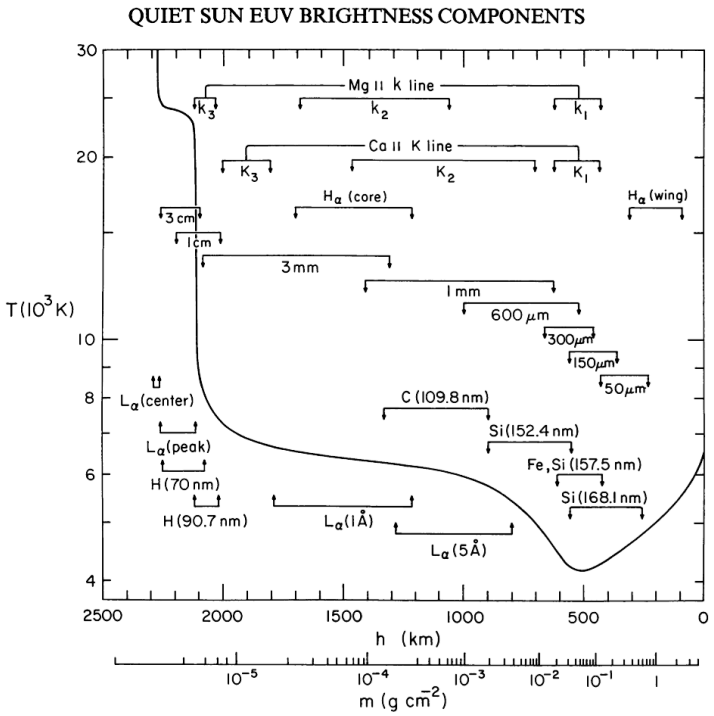

Figure 4.2: The average quiet Sun temperature profile with height from the solar surface, derived from the EUV continuum, the Lα line and other observations. This graph is Fig.1 from Vernazza et al. (1981).

With the exception of explosive events, the temperature of the solar corona is approximately constant over this range and, therefore, we model this region with a constant temperature profile with increasing height.

Figure 4.3 schematically illustrates this analytical temperature model for the solar interior and atmosphere.

From the discussion of the solar interior, we know that the temperature at the solar surface is T_{ss}. Hence, in our analytical model, the constant temperature function in the photosphere will be given by $T_{ph} = T_{ss}$. We will define the constant temperature profile of the corona as T_{cr}, the exact value of which will be given later. In a similar manner as for the solar interior, we use these temperature profiles together with (4.1) and (4.2) to find the gas pressure and density profiles for the photosphere and corona.

For the photosphere, (4.1) becomes

$$\frac{dp_{ph}}{dz} = -\frac{p_{ph}\tilde{\mu}}{H_{ss}}, \tag{4.9}$$

where $H_{ss} = \tilde{R}T_{ss}/g$ is the pressure scale height at the solar surface. Integrating this yields the

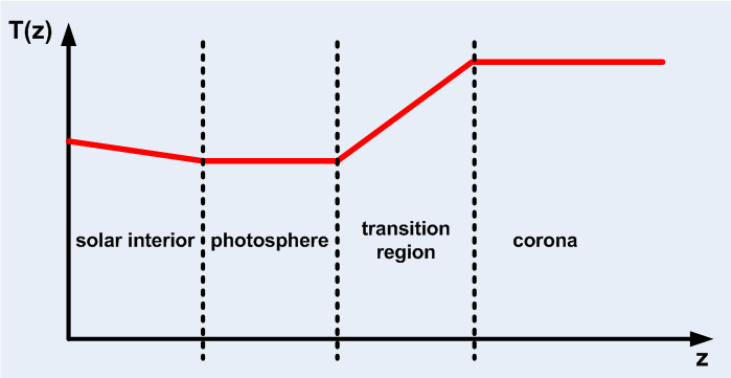

Figure 4.3: Schematic illustration of the simplified analytical atmospheric temperature model.

photospheric gas pressure function

$$p_{ph} = p_{ss} \exp(-\tilde{\mu} z / H_{ss}), \tag{4.10}$$

and, using (4.2), we have the photospheric density profile as

$$\rho_{ph} = \rho_{ss} \exp(-\tilde{\mu} z / H_{ss}). \tag{4.11}$$

Using a similar derivation method as for the isothermal photosphere, we have the coronal gas pressure profile as

$$p_{cr} = p_{tr}(z = z_{cr}) \exp(-\tilde{\mu} z / H_{cr}), \tag{4.12}$$

and the coronal density profile as

$$\rho_{cr} = \rho_{tr}(z = z_{cr}) \exp(-\tilde{\mu} z / H_{cr}), \tag{4.13}$$

where $H_{cr} = \tilde{R} T_{cr} / g$.

We use a power law profile to prescribe the steep temperature increase in the transition region. The exact form of this function is

$$T_{tr} = T_{ss} \left(\frac{T_{cr}}{T_{ss}} \right)^{\left(\frac{z - z_{tr}}{z_{cr} - z_{tr}} \right)}, \tag{4.14}$$

where z_{tr} and z_{cr} are heights denoting the start of the transition region and the corona, respectively. Again using (4.1) and (4.2), we have

$$\frac{dp_{tr}}{dz} = -\frac{p_{tr} \tilde{\mu} g}{\tilde{R} T_{tr}}, \tag{4.15}$$

which can be rewritten as

$$\frac{dp_{tr}}{dz} = -\frac{p_{tr}\tilde{\mu}}{H_{ss}}\left(\frac{T_{cr}}{T_{ss}}\right)^{\left(-\frac{z-z_{tr}}{z_{cr}-z_{tr}}\right)}. \tag{4.16}$$

Integrating this with respect to z gives the gas pressure profile in the transition region as

$$p_{tr} = p_{ph}(z=z_{tr})\exp\left(\frac{(z_{cr}-z_{tr})\,\tilde{\mu}}{H_{ss}\ln\left(\frac{T_{cr}}{T_{ss}}\right)}\left(\left(\frac{T_{cr}}{T_{ss}}\right)^{\left(-\frac{z-z_{tr}}{z_{cr}-z_{tr}}\right)}-1\right)\right), \tag{4.17}$$

which can be slightly simplified when rewritten in terms of T_{tr} to become

$$p_{tr} = p_{ph}(z=z_{tr})\exp\left(\frac{(z_{cr}-z_{tr})\,\tilde{\mu}}{H_{ss}\ln\left(\frac{T_{cr}}{T_{ss}}\right)}\left(\frac{T_{ss}}{T_{tr}}-1\right)\right). \tag{4.18}$$

Thus, the transition region density profile is

$$\rho_{tr} = \rho_{ph}(z=z_{tr})\tilde{\mu}\frac{T_{ss}}{T_{tr}}\exp\left(\frac{(z_{cr}-z_{tr})\,\tilde{\mu}}{H_{ss}\ln\left(\frac{T_{cr}}{T_{ss}}\right)}\left(\frac{T_{ss}}{T_{tr}}-1\right)\right). \tag{4.19}$$

We have now prescribed the temperature, gas pressure and density, through out the simulation domain, using the following continuous piecewise functions:

$$T\left(z\right),\ p\left(z\right),\ \rho\left(z\right) = \begin{cases} T_{si}(z),\ p_{si}(z),\ \rho_{si}(z) & z \le z_{ss}, \\ T_{ph}(z),\ p_{ph}(z),\ \rho_{ph}(z) & z_{ss} \le z \le z_{tr}, \\ T_{tr}(z),\ p_{tr}(z),\ \rho_{tr}(z) & z_{tr} \le z \le z_{c}, \\ T_{c}(z),\ p_{c}(z),\ \rho_{c}(z) & z \ge z_{c}. \end{cases} \tag{4.20}$$

The height of the solar surface has already been chosen to be $z_{ss} = 0$. The values of ρ_{ss}, T_{ss}, T_{cr}, z_{tr} and z_{cr} can be freely chosen but should be done so such that they reflect true solar values. From the discussion of the simplified analytical model above, we choose $z_{tr} = 1.7 \times 10^6$ m, $z_{cr} = 3.4 \times 10^6$ m, $T_{ss} = 5.6 \times 10^3$ K and $T_{cr} = 8.4 \times 10^5$ K. In line with actual solar values, the density at the solar surface is chosen to be $\rho_{ss} = 3 \times 10^{-4}$ kg m^{-3}. The remaining constants and their associated solar values are displayed in table 4.1.

Constant	Symbol	Physical Value	
surface gravity	g	2.7×10^2	$\mathrm{m\ s^{-2}}$
gas constant	$\tilde{R}$	8.3×10^3	$\mathrm{m^2\ s^{-2}\ K^{-1}}$
mean atomic weight	$\tilde{\mu}$	1	
magnetic permeability of free space	μ_0	$4\pi \times 10^{-7}$	$\mathrm{H\ m^{-1}}$

Table 4.1: The solar constants and their physical values.

4.2 The Numerical Atmosphere

As discussed in section 3.1, `Diffin3d` solves the dimensionless MHD equations. Thus, to implement the analytical solar interior and atmospheric model, determined in section 4.1, we must non-dimensionalise any constants and the functions $T(z)$, $p(z)$ and $\rho(z)$. This is achieved by defining dimensionless values for T, p and ρ at an arbitrary reference height and determining a conversion scheme for retrieving dimensional values from the new dimensionless functions. Similarly for the constants.

We choose the reference height to be the solar surface, $z = 0$. For ease, we begin by choosing the density and temperature to have dimensionless values of 1 at this height. We will denote dimensionless quantities by a superscript $'$ and, therefore, we have the following: $\rho'_{ss} = 1$ and $T'_{ss} = 1$. For conversion to dimensional units, we multiply these quantities by their values at the solar surface, chosen in section 4.1. For example, T_{ss} is given by $T'_{ss}T_0$, where $T_0 = 5.6 \times 10^3$ K, and ρ_{ss} is given by $\rho'_{ss}\rho_0$, where $\rho_0 = 3 \times 10^{-4}\ \mathrm{kg\ m^{-3}}$. The dimensional conversion quantities will be denoted by subscript 0. In a similar manner, the constants given in table 4.1 are also non-dimensionalised such that at the solar surface they all take a dimensionless value of 1.

Units of length are non-dimensionalised in terms of the pressure scale height at the solar surface. Rewriting $H_{ss} = \tilde{R}T_{ss}/g$, we have $H'_{ss}H_0 = \tilde{R}T'_{ss}T_0/g$. By choosing $H'_{ss} = 1$ and inserting values for the constants from table 4.1 and the paragraph above, we find that $H_0 = 1.7 \times 10^5$ m. Using the values calculated so far, together with the relations in section 3.1, it is possible to derive dimensional conversion values for all of the basic variables. These values are presented in table 4.2 and are used for all of the simulations within this thesis.

The analytical temperature, gas pressure and density profiles, derived in section 4.1, become drastically simplified when in their dimensionless format. For example, the temperature profile re-

Quantity	Symbol	Physical Units	
density	ρ_0	3×10^{-4}	$\mathrm{kg\ m^{-3}}$
temperature	T_0	5.6×10^{3}	K
length	H_0	1.7×10^{5}	m
velocity	v_0	6.8×10^{3}	$\mathrm{m\ s^{-1}}$
time	t_0	25	s
gas pressure	p_0	1.4×10^{4}	Pa
magnetic induction	B_0	1.3×10^{3}	T

Table 4.2: Dimensional conversion values for the basic quantities.

Constant	Dimensional Value		Dimensionless Value
z_{ss}	0	m	0
z_{tr}	1.7×10^{6}	m	10
z_{cr}	3.4×10^{6}	m	20
p_{ss}	1.4×10^{4}	Pa	1
ρ_{ss}	3×10^{-4}	$\mathrm{kg\ m^{-3}}$	1
T_{ss}	5.6×10^{3}	K	1
T_{cr}	8.4×10^{5}	K	150
H_{ss}	1.7×10^{5}	m	1
H_{cr}	2.6×10^{10}	m	150
$\xi = \tilde{\mu} g / \tilde{R}$	3.3×10^{-2}	$\mathrm{K\ m^{-1}}$	1

Table 4.3: Dimensional and dimensionless values of the constants used in the atmospheric model.

duces to

$$T(z)' = \begin{cases} 1 - z\frac{(\gamma-1)}{\gamma} & z \leq 0, \\ 1 & 0 \leq z \leq 10, \\ 150^{\left(\frac{z-10}{10}\right)} & 10 \leq z \leq 20, \\ 150 & z \geq 20 \end{cases}. \tag{4.21}$$

Table 4.3 gives the dimensional and dimensionless values associated with the constants introduced in section 4.1, some of which have been used in the simplification of the temperature profile. Similar simplifications are achieved for $p(z)'$ and $\rho(z)'$. Figure 4.4 illustrates the resulting temperature, gas pressure and density profiles over the height of the domain. By using dimensionless quantities the range of orders of magnitude is reduced and becomes more manageable computationally.

4.2.1 Constraints of an Atmospheric Magnetic Field

Although our experiments do not include an atmospheric magnetic field, the start-up routine we use does allow for this scenario. In the cases with an atmospheric magnetic field, the field is always

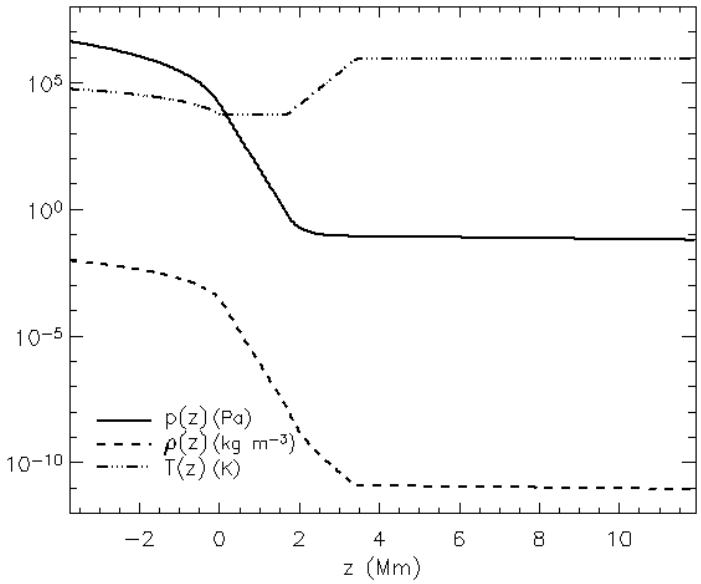

(a) Dimensional profiles.

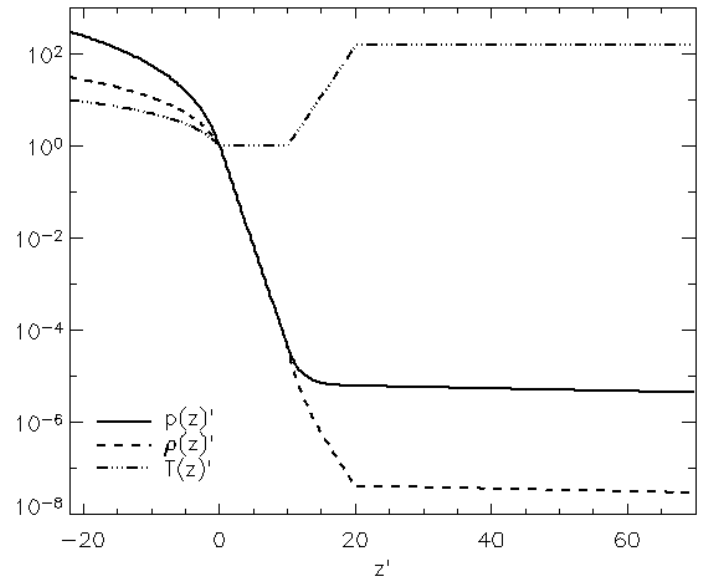

(b) Dimensionless profiles.

Figure 4.4: Graph of gas pressure, density and temperature over the height of the domain.

horizontal but can either be uniform in direction or sheared with height. The field is introduced in the photosphere, increasing from a strength of zero to some specified value by the start of the transition region. The increase is field strength with height follows a $\tanh$ profile and, within the photosphere, the field direction is uniform. The field then remains at the user specified strength through out the transition region and corona, although its direction can be uniform or sheared here.

Providing the atmospheric field remains at a constant strength, there will be no magnetic force acting on the hydrostatic environment, irrespective of whether the field is uniform or sheared in direction. Thus, the dimensionless analytical profiles prescribing pressure and density in the transition region and corona remain unchanged. However, within the photosphere, the varying strength of the field does produce a vertical magnetic force such that $(\mathbf{J} \times \mathbf{B})_z \neq 0$. Thus, (4.9) is modified to the dimensional equation

$$\frac{dp_{ph}}{dz} = -\frac{p_{ph}\tilde{\mu}}{H_{ss}} - \frac{1}{2}\frac{d}{dz}\left(B^2\right). \tag{4.22}$$

The $\tanh$ function associated with the magnetic field prevents this differential equation from being solved analytically. Therefore, the following first order finite difference method is employed to estimate the dimensionless gas pressure in the photosphere

$$p'_{k+1} = p'_k\left(1 - \Delta z\right) - \frac{(B'^2_{k+1} - B'^2_k)}{2}, \tag{4.23}$$

where k corresponds to grid indices in the domain's vertical direction and Δz is the spacing between consecutive gridpoints. Using this first order error gas pressure approximation, the photospheric dimensionless density profile is calculated.

The dimensionless analytical solutions for the gas pressure and density in the transition region and corona are programmed into the start-up routine used for the flux emergence simulations, together with the numerical photospheric gas pressure and density approximations. From the functions prescribing $p(z)'$, the basic quantity $e(z)'$ can be retrieved. Given that we have chosen to use the above numerical method to determine the photospheric gas pressure for all of the simulations in this thesis, the gas pressure in the photosphere will only be first order error irrespective of whether a coronal magnetic field is included.

The only differences between the numerical models used in the simulations described in chapters 5, 6 and 7, are the depth and height of the convection zone and corona, respectively.

NOTE: From this point forward, subscripts denoting dimensionless quantities and functions will be dropped. Unless otherwise stated, it should be assumed that all equations and values are in dimensionless form. Dimensional values will be identifiable by the inclusion of accompanying units of scale.

4.3 General Problems with the Numerical Model

The model atmosphere, which is described in sections 4.1 and 4.2, aims to create a hydrostatic background environment in the simulation domain. However, when simulations are run using the numerical model we find that hydrostatic equilibrium is not perfectly achieved. In the case of an unmagnetised domain, as shown in figure 4.5, spurious vertical velocities arise in the atmosphere. These velocities grow in magnitude over time and bounce up and down the atmospheric region of the domain. This causes fluctuations in the gas pressure, density and temperature profiles with time. Figure 4.6 gives an example of these fluctuations by considering the atmospheric temperature profile at two different times.

Figure 4.7 illustrates the vertical velocities that arise under three different experiment setups. The first two setups are very similar, both having unmagnetised atmospheres, except that the first includes a magnetic flux tube in the solar interior and the second does not. The rising flux tube can clearly be depicted since it is associated with the only vertical velocity in the solar interior. Other than this additional subsurface velocity, the atmospheric velocities arising in each of the models are the same. The velocity initially originates in the photosphere and an obvious assumption would be to attribute this to the errors arising from the use of a finite difference method to determine the gas pressure and density here. This will be verified in section 4.4.

The final model has a magnetised atmosphere but no flux tube. Comparison with the vertical velocity profile in the model with an unmagnetised atmosphere and no flux tube indicates that the addition of the atmospheric field enhances the vertical velocities arising in the upper region of the photosphere. In this region of the photosphere, the strength of the atmospheric magnetic field is being increased and the location of these velocities again points towards problems with the first order error method used to find the gas pressure and density profiles here.

In order to evaluate the significance of these velocities, they must be compared with the rise speed of the rising flux tube. Initially, the vertical velocity of the tube is greater than the spurious velocities generated in the atmosphere, as demonstrated by figure 4.7(a). However, as time passes, the tube speed ceases to be the most significant velocity, with the size of the spurious velocities approaching those of the tube.

Of greater importance than the magnitude of the spurious velocities, is the momentum associated with them. There is a decrease in density by eight orders of magnitude between the initial location of the tube in the convection zone and the corona. Thus, the momentum of the tube is far greater than that of the atmospheric flows and it could be argued that the atmospheric velocities are dynamically unimportant. However, in the sheared magnetic field case the atmospheric flows, which are separate from the emergence of the tube, could initiate instabilities and mask any effects caused by the emergence process.

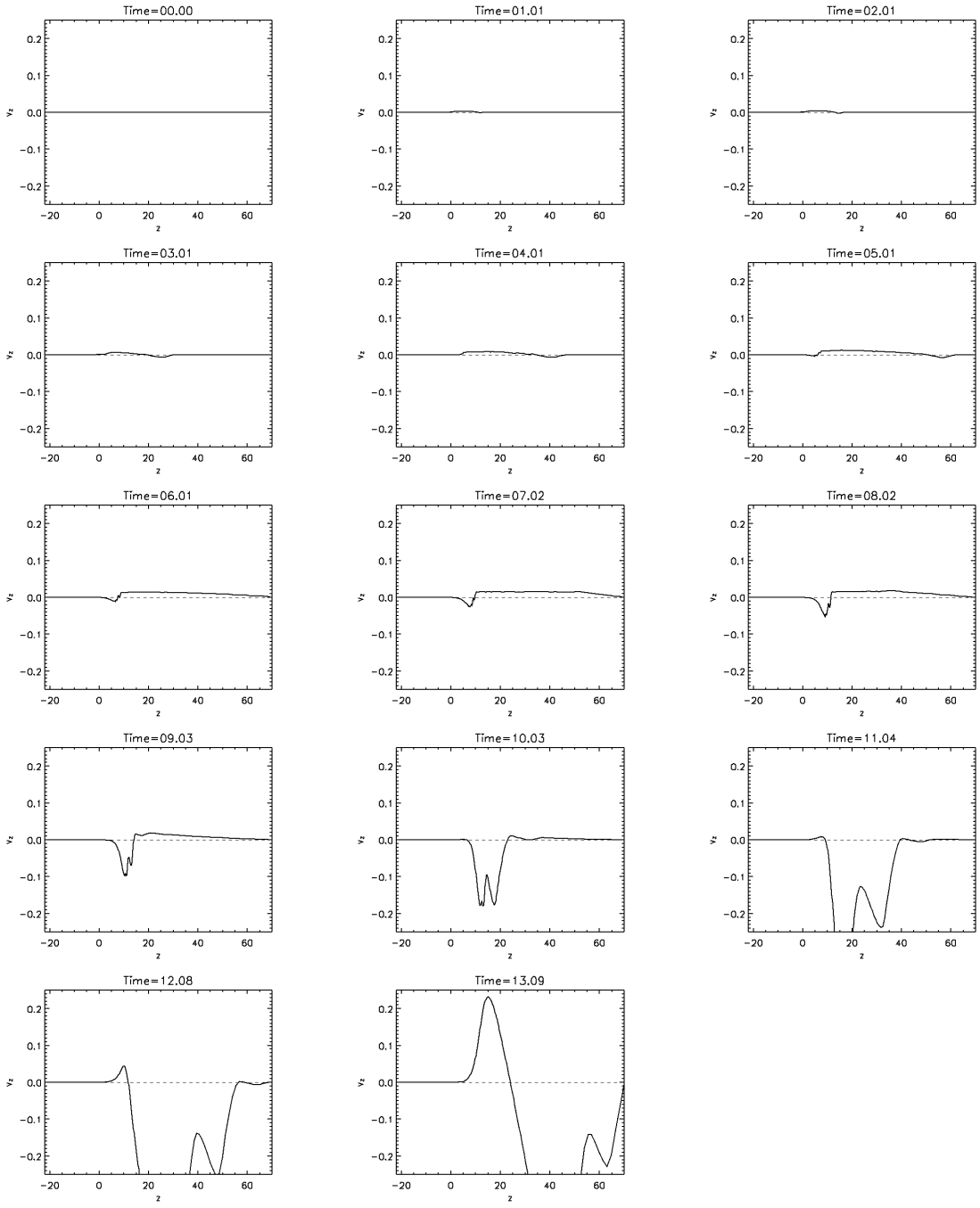

Figure 4.5: Vertical velocity against height at different times for an experiment with an unmagnetised atmosphere. The vertical velocity is measured along the central vertical line of the domain.

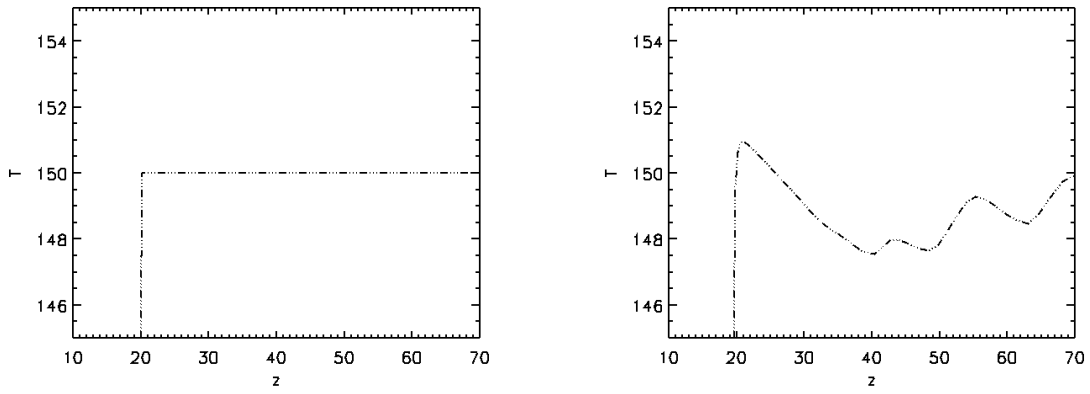

(a) $t = 0$. (b) $t = 13$.

Figure 4.6: Temperature profile in a domain with an unmagnetised atmosphere at two different times.

Regardless of the "dynamically unimportant" argument, we believe that the atmosphere should satisfy hydrostatic equilibrium as best as possible. In section 4.4, we will apply several modifications to the numerical model with the aim of creating an atmosphere which better achieves hydrostatic equilibrium.

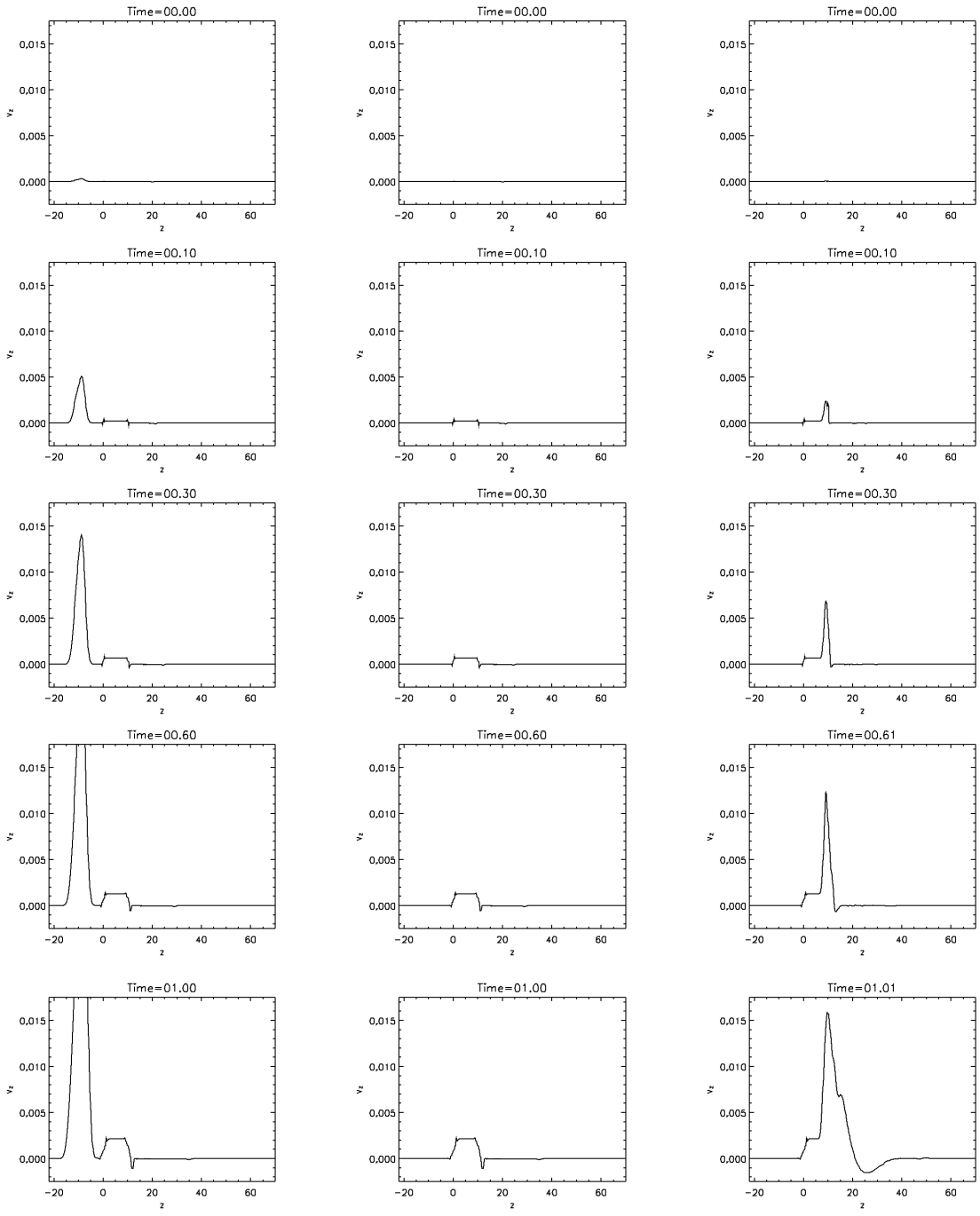

(a) Flux tube and an unmagnetised atmosphere.

(b) An unmagnetised atmosphere.

(c) A magnetised atmosphere.

Figure 4.7: Vertical velocity against height for three different experiment scenarios at different times.

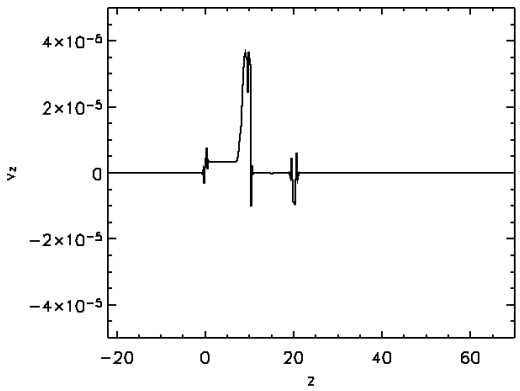

(a) Over the whole height of domain.

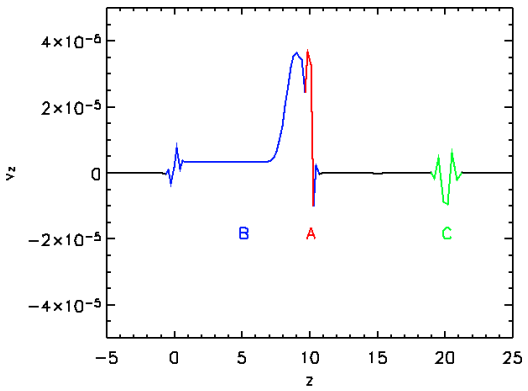

(b) Close-up of the region $-5 \leq z \leq 25$ in figure 4.8(a), with individual problem regions labelled A, B and C.

Figure 4.8: Vertical velocity at $t = 0.00156$, i.e. result after first iteration, for the experiment with a magnetised atmosphere.

4.4 Identifying Individual Problems & Solutions

In section 4.3, we considered experiments that can be subdivided into two categories: magnetised and unmagnetised atmospheres. The only variation in the vertical velocities occurring in these experiments is in the upper photosphere, where the magnetic field increases in strength, as illustrated in figure 4.7. Given this relation, we will first look to solve the problems in the case with an atmospheric field and, where appropriate show that the solutions also solve the problems experienced in the experiments with unmagnetised atmospheres.

Our discussion in the previous section, highlighted that the use of a first order error method to calculate the gas pressure and density in the photosphere could account for the origin of the vertical velocities there. Figure 4.8(a) shows the vertical velocity along the central vertical line of the domain after the first iteration of `Diffin3d`. From this it is possible to distinguish three locations where unexpected vertical velocities originate. These are labelled in figure 4.8(b) as A, B and C. A is at the interface of the photosphere and transition region, B covers the whole of the photosphere and C is at the interface of the transition region and corona.

We believe that by modifying the numerical model in three ways we can eradicate or significantly reduce the unwanted velocities that are currently arising. More specifically, this will be accomplished by reconsidering how the magnetic field is introduced into the atmosphere, the power law temperature profile in the transition region and the method used to calculate the initial the pressure and density in the photosphere.

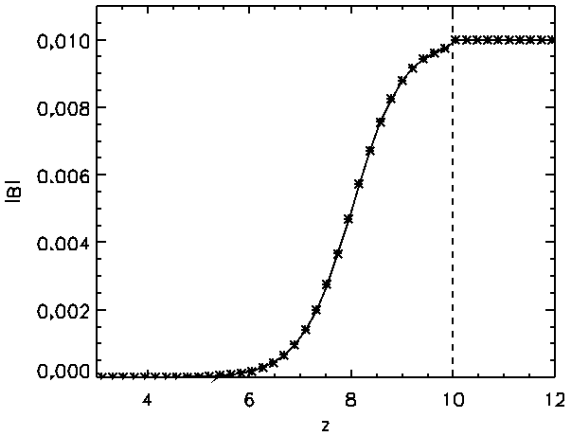

Figure 4.9: The field strength, $\mid \mathbf{B} \mid$, in the photosphere with the original $\tanh$ function. The dashed line indicates the interface between the photosphere and the transition region.

4.4.1 A: Interface of the Photosphere and Transition Region

Across the interface between the photosphere and transition region, the method by which the magnetic field is prescribed changes. Within the upper photosphere, the field strength increases with height using the following profile

$$\mid \mathbf{B} \mid = \frac{1}{2} B_A \left(\tanh \left(z_{gd} \left(z - z_{hs} \right) \right) + 1 \right) \tag{4.24}$$

where B_A is the constant strength of the atmospheric field in the transition region and corona, z_{hs} defines the height in the photosphere at which the field strength is $B_A/2$ and z_{gd} denotes the gradient of the $\tanh$ profile. For the magnetised atmosphere experiment presented in section 4.3 and the beginning of section 4.4, these parameters take dimensionless values as follows: $B_A = 0.01$, $z_{hs} = 8$, $z_{gd} = 1$. At the starting height of the transition region, the strength of the magnetic field is explicitly set to B_A.

Figure 4.9, illustrates the profile of magnetic field strength with height in the region where it increases from zero to B_A. Close inspection of this figure reveals that there is a sudden change in the gradient of $\mathbf{B}$ at the interface of the photosphere and transition region. The definition of the $\tanh$ profile states that, as z tends to infinity, the field strength will approach B_A. However, for the given values of z_{hs} and z_{gd} this does not happen quickly enough and, thus, a jump in $|\mathbf{B}|$ occurs. This results in the vertical velocity spike labelled A.

To remove this sudden vertical velocity, we must ensure that there is a smooth increase in the value of $\mid \mathbf{B} \mid$ between the top of the photosphere and the start of the transition region and not a jump as at present. By increasing z_{gd}, the $\tanh$ profile will steepen. This results in a smooth change

in | **B** | at the interface and, therefore, eradicates the vertical velocity A. However, increasing the steepness of the field strength profile causes the magnitude of the vertical velocities labelled B to increase. Alternatively, we could move the height at which the field strength is half the required value, z_{hs}, to a lower height in the photosphere. This also removes the A velocities but necessitates the magnetic field being introduced at a lower level in the photosphere. This is not ideal since we require the photosphere to be as unmagnetised as possible.

By changing the function used to increase the field strength to a sine function it is possible to:

1. impose a zero gradient in the field strength at the interface between the photosphere and the transition region;
2. prevent the magnetic field from being introduced at too low a height in the photosphere.

The profile we use is

$$| \mathbf{B} | = \begin{cases} 0 & z_{ss} \leq z \leq z_{A0}, \\ \frac{1}{2} B_A \left(\sin \left(\frac{\pi(2z - z_{A0} - z_{A1})}{2(z_{A1} - z_{A0})} \right) + 1 \right) & z_{A0} \leq z \leq z_{A1}, \\ B_A & z_{A1} \leq z \leq z_{tr} \end{cases} \tag{4.25}$$

where z_{A0} and z_{A1} are the heights at which we wish to ensure | **B** |$= 0$ and | **B** |$= B_A$, respectively. In addition, this function also ensures that at these heights we have a zero gradient in | **B** |. Figure 4.10(a) demonstrates the profile of the function given by (4.25) for $z_{A0} = 5$ and $z_{A1} = 10 = z_{tr}$. These parameter values provide a close match to the heights at which the original $\tanh$ function introduced the magnetic field and the field reached its full strength. The reduction in the gradient through the steepest section of the profile ensures that the vertical velocities B do not become larger than with the original $\tanh$ function.

Figure 4.10(b) illustrates the success of this modification to the numerical model. The vertical velocity A has been completely removed. For the remainder of this chapter, we will refer to this modification as solution A.

4.4.2 B: The Photosphere

The model we will now work with is the original numerical model with solution A implemented. Figure 4.11 shows the vertical velocity at $t = 0.1$ in cases with and without a magnetised atmosphere. We can see that, in the lower photosphere where there is no magnetic field, the vertical velocities are of the same size and the size of the velocity is independent of height here. In the upper photosphere, the introduction of the magnetic field causes additional velocities. These velocities were labelled B in figure 4.8(b).

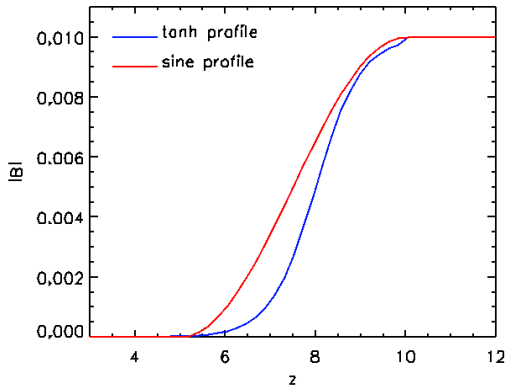

(a) Field strength, $|\ \mathbf{B}\ |$, in the photosphere with the original $\tanh$ function and the new sine function, (4.25).

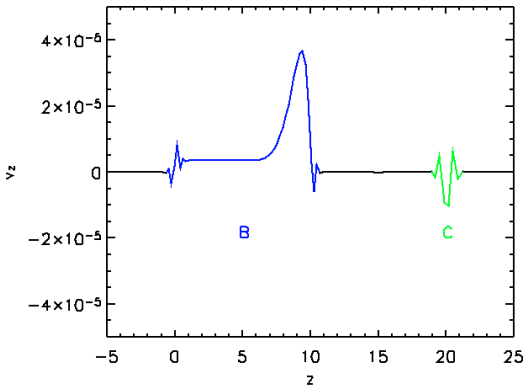

(b) Vertical velocity after the first iteration with the sine function implemented, $t = 0.00164$. Velocity A has been eradicated.

Figure 4.10: Effects of implementing a sine function to prescribe the field strength in the photosphere for a case with a magnetised atmosphere.

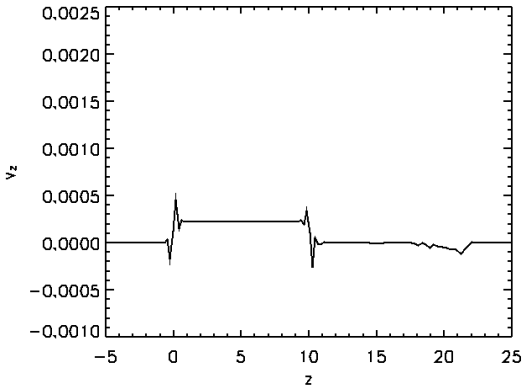

(a) An unmagnetised atmosphere.

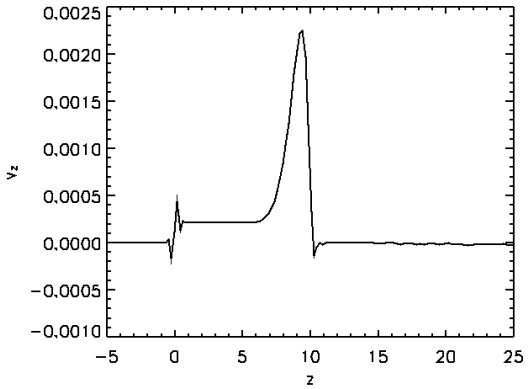

(b) A magnetised atmosphere.

Figure 4.11: Vertical velocity against height for the two different experiment scenarios at $t = 0.1$, using solution A.

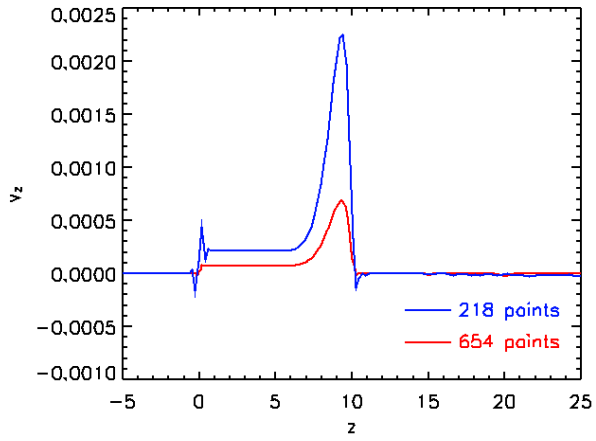

Figure 4.12: Vertical velocity at $t = 0.1$ for domains with different numbers of gridpoints in the vertical direction. When the number of gridpoints is increased by a factor of three, the magnitude of the vertical velocity decreases by the same factor.

The vertical velocities in the lower photosphere arise regardless of the inclusion of a magnetic field. This suggests that the underlying problem is in the initial gas pressure and density profiles for the photosphere. As discussed in section 4.2, the gas pressure is evaluated using a first order error method, (4.23). Hence, we would expect any errors to be proportional to the vertical grid spacing, Δz if this were the cause of the velocities. We find that increasing the number of gridpoints in the photospheric region by a factor of three reduces the size of the vertical velocities to a third of their original size, as shown in figure 4.12. This identifies that the velocities are arising due to the error associated with the finite difference method.

Furthermore, the first order error method (4.23) makes two estimations: the gradient of p and the gradient of $\mathbf{B}$. Thus, the inclusion of the magnetic field in the upper photosphere adds further to the errors in the calculations of gas pressure and density. Hence, when the atmosphere is magnetised, the vertical velocities in the upper photosphere are found to be larger.

One way to reduce all of these errors would be to increase the order of accuracy of the method used to calculate the photospheric gas pressure. However, now that the model uses a sine profile to prescribe the increasing strength of the magnetic field, it is possible to integrate (4.22) exactly. The resulting function for p_{ph} will ensure that the profile for the pressure satisfies hydrostatic equilibrium exactly.

As stated in section 4.2, the atmospheric magnetic field is horizontal and uniform in direction in the photosphere. This simplifies the evaluation of the new gas pressure and density profiles since the direction of the field can be ignored. We will solely use (4.25) for the description of the field

and, for simplicity in the upcoming calculations, this is rewritten as

$$| \mathbf{B} |= \begin{cases} 0 & z_{ss} \leq z \leq z_{A0}, \\ \frac{1}{2} B_A \left(\sin \left(Ez + F \right) + 1 \right) & z_{A0} \leq z \leq z_{A1}, \\ B_A & z_{A1} \leq z \leq z_{tr} \end{cases} \tag{4.26}$$

where

$$E = \frac{\pi}{z_{A1} - z_{A0}}, \tag{4.27}$$

$$F = \frac{\pi \left(z_{A0} + z_{A1} \right)}{2 \left(z_{A0} - z_{A1} \right)}. \tag{4.28}$$

Given that the function defining the field strength in the photosphere is piecewise, we will create a piecewise function for the gas pressure and density here too. We will refer to the region with no magnetic field as the lower photosphere, ph_l, the region where the field strength is increasing as the upper photosphere, ph_u, and the region where the field strength has constant value B_A the top of the photosphere, ph_t.

In the lower photosphere the magnetic field strength is zero and, thus, the gas pressure and density continue to be given by the dimensionless forms of (4.10) and (4.11). Respectively, these are

$$p_{ph_l} = p_{ss} e^{-z/H_{ss}}, \tag{4.29}$$

$$\rho_{ph_l} = \rho_{ss} e^{-z/H_{ss}}. \tag{4.30}$$

Similarly, at the top of the photosphere, the constant field strength results in the gas pressure and density being given by

$$p_{ph_t} = p_{ph_u} \left(z = z_{A1} \right) e^{-z/H_{ss}}, \tag{4.31}$$

$$\rho_{ph_t} = \rho_{ph_u} \left(z = z_{A1} \right) e^{-z/H_{ss}}. \tag{4.32}$$

In the upper photosphere, we must solve the following equation to determine the gas pressure:

$$\frac{dp_{ph_u}}{dz} = -\frac{p_{ph_u}}{H_{ss}} - \frac{1}{2} \frac{d}{dz} \left(B_u^2 \right), \tag{4.33}$$

where B_u is given by $|\mathbf{B}|$ in the region $z_{A0} \leq z \leq z_{A1}$. Substituting for B_u from (4.26), performing the corresponding differentiation and rearranging gives

$$\frac{dp_{ph_u}}{dz} + \frac{p_{ph_u}}{H_{ss}} = -\frac{1}{4} B_A^2 E \left(\sin \left(Ez + F \right) + 1 \right) \cos \left(Ez + F \right). \tag{4.34}$$

This first-order linear differential equation can be solved with the use of the integrating factor $e^{z/H_{ss}}$. Thus, (4.34) becomes

$$\frac{d}{dz}\left(p_{ph_u}e^{z/H_{ss}}\right) = -\frac{1}{4}B_A^2 E\left(\sin\left(Ez+F\right)+1\right)\cos\left(Ez+F\right)e^{z/H_{ss}}. \tag{4.35}$$

Integrating this yields

$$\begin{aligned} p_{ph_u} = \; & Ce^{-z/H_{ss}} \\ & -\tfrac{1}{8}B_A^2 E \left\{\frac{1}{4E^2+1/H_{ss}^2}\left(-2E\cos\left(2Ez+2F\right)+\frac{1}{2EH_{ss}}\sin\left(2Ez+2F\right)\right)\right. \\ & \left.+\frac{1}{E^2+1/H_{ss}^2}\left(\sin\left(Ez+F\right)+\frac{2}{H_{ss}}\cos\left(Ez+F\right)\right)\right\}, \end{aligned} \tag{4.36}$$

where C is the resulting constant of integration. At $z = z_{A0}$, we have $p_{ph_u} = p_{ph_l} = p_{A0}$ and, thus, the value of C is given by

$$\begin{aligned} C = \; & p_{A0}e^{z_{A0}/H_{ss}} \\ & +\tfrac{1}{8}B_A^2 E \left\{\frac{1}{4E^2+1/H_{ss}^2}\left(-2E\cos\left(2Ez_{A0}+2F\right)+\frac{1}{2EH_{ss}}\sin\left(2Ez_{A0}+2F\right)\right)\right. \\ & \left.+\frac{1}{E^2+1/H_{ss}^2}\left(\sin\left(Ez_{A0}+F\right)+\frac{2}{H_{ss}}\cos\left(Ez_{A0}+F\right)\right)\right\}e^{z_{A0}/H_{ss}}. \end{aligned} \tag{4.37}$$

Using (4.36) and (4.37), the function prescribing the density in the upper photosphere, ρ_{ph_u} can be calculated from the dimensionless ideal gas law, $p_{ph_u} = \rho_{ph_u}$.

Thus, the gas pressure and density profiles in the photosphere are given by

$$p_{ph}\left(z\right),\ \rho_{ph}\left(z\right) = \begin{cases} p_{ph_l}(z),\ \rho_{ph_l}(z) & z_{ss} \le z \le z_{A0}, \\ p_{ph_u}(z),\ \rho_{ph_u}(z) & z_{A0} \le z \le z_{A1}, \\ p_{ph_t}(z),\ \rho_{ph_t}(z) & z_{A1} \le z \le z_{tr}. \end{cases} \tag{4.38}$$

Figure 4.13 shows that the implementation of (4.38) eradicates the spurious velocities labelled B in the photosphere for cases with and without an atmospheric magnetic field. In comparison to the vertical velocity profile under solution A, shown in figure 4.11, this additional modification gives a vast improvement. For the remainder of this chapter, we will refer to this modification of solution A as solution B.

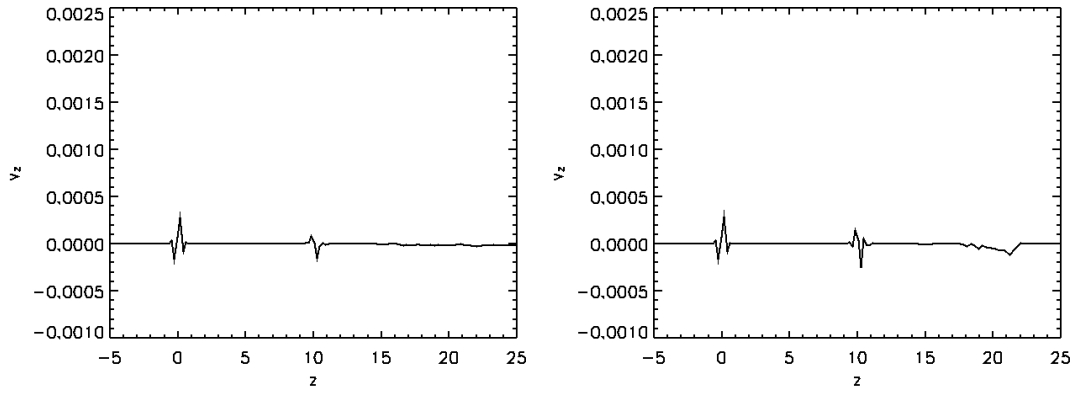

(a) Unmagnetised atmosphere at $t = 0.1$. (b) Magnetised atmosphere at $t = 0.1$.

Figure 4.13: The use of an analytical expression for the pressure in the photosphere causes a reduction in the vertical velocities here.

4.4.3 C: Interface of the Transition Region and Corona

The model we will now work with is the original numerical model with solution B implemented. In figure 4.8(b) we labelled the vertical velocity at the interface of the transition region and the corona as C. In the original numerical model, this velocity was small in comparison to the velocities in the photosphere and over a short period of time becomes increasingly insignificant relative to the other problems. However, solution B has been so successful that the velocities at the top of the transition region are now the fastest growing.

From figure 4.13 we can actually see that vertical velocities are originating at both ends of the transition region. We believe these to be associated with the function determining the temperature throughout the atmosphere. This function is piecewise and, at the interfaces between the photosphere and transition region and between the transition region and corona, is not continuously differentiable. Thus, small errors are introduced into the model when the initial gas pressure and density are calculated.

In section 4.1, we introduced the power law temperature profile currently used for the transition region. This is given by

$$T_{tr} = T_{ss}\left(\frac{T_{cr}}{T_{ss}}\right)^{\left(\frac{z-z_{tr}}{z_{cr}-z_{tr}}\right)}, \tag{4.39}$$

and is illustrated in figure 4.14. From this, we can see that there is a sudden change in the temperature gradient at the bottom, $z = 10$, and top, $z = 20$, of the transition region.

By using a temperature profile that has a smoother gradient change at the bottom and top of the

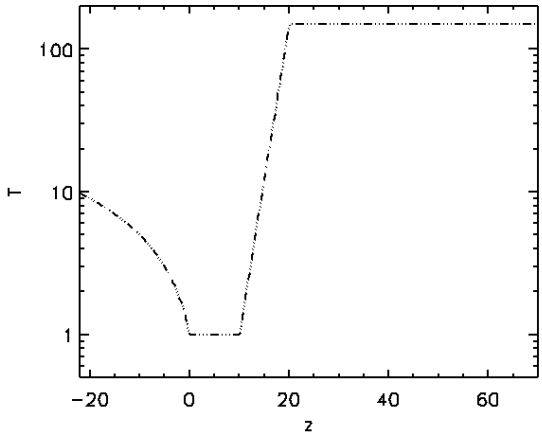

Figure 4.14: Temperature profile for the atmosphere, with a power law function used in the transition region.

transition region, it may be possible to reduce the vertical velocities at these locations. Following the approach used for solution B, we choose to use a sine function to describe the inverse temperature profile. This will enable us to ensure zero gradients at both ends of the transition region, which will match those of the adjoining constant temperature photosphere and corona. The exact function is as follows

$$\frac{1}{T(z)} = \frac{1}{2}\left(\frac{1}{T_{ph}} - \frac{1}{T_{cr}}\right)(\sin(Jz + K) + 1) + \frac{1}{T_{cr}} \tag{4.40}$$

where

$$J = \frac{\pi}{z_{tr} - z_{cr}}, \tag{4.41}$$

$$K = \frac{\pi(z_{cr} + z_{tr})}{2(z_{cr} - z_{tr})}. \tag{4.42}$$

The profile of the temperature given by this new function is shown in figure 4.15(a).

In section 4.1, we derived the gas pressure and density profiles for the transition region from the power law temperature function. Implementing (4.40) will require new analytical expressions for pressure and density to be derived. To satisfy the condition of hydrostatic equilibrium we must solve

$$\frac{dp_{tr}}{dz} = -\frac{p_{tr}}{T_{tr}}, \tag{4.43}$$

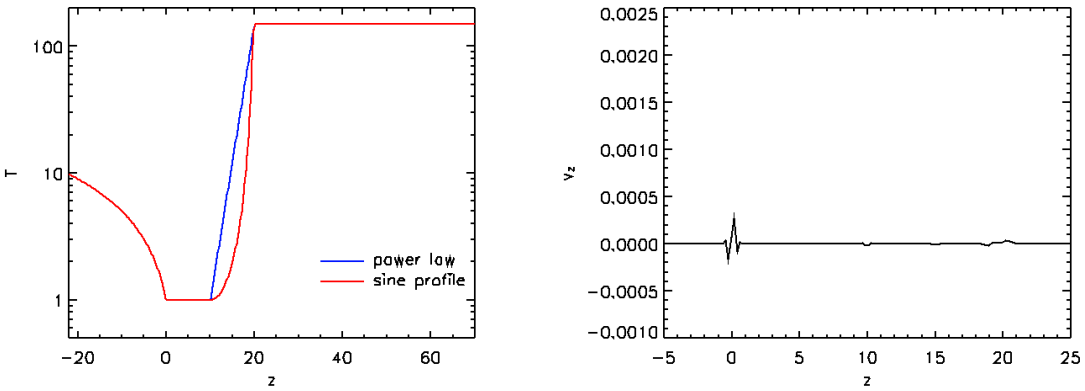

(a) Temperature in the transition region with the original power law and the new sine profile (4.40).

(b) Vertical velocity at $t = 0.1$ with the sine function implemented. The magnitude of velocity C has been reduced but not completely removed.

Figure 4.15: Effects of implementing a sine function for the temperature profile in the transition region for the case with a magnetised atmosphere.

which yields

$$p_{tr} = p_{pht}\left(z = z_{A1}\right) \exp\left(\frac{H_{ss}}{2JT_{cr}}\left(\left(T_{cr} - T_{ph}\right)\cos\left(Jz + K\right) + J\left(T_{ph} + T_{cr}\right)\left(z_{tr} - z\right)\right)\right). \tag{4.44}$$

Using the dimensionless ideal gas law, $p_{tr} = \rho_{tr} T_{tr}$, the function for the density in the transition region can be determined.

The effect of the new temperature, gas pressure and density profiles are shown in figure 4.15(b). This modification has practically eliminated the vertical velocities at the interface between the photosphere and the transition region. However, a slight fluctuation in velocity can still be seen at the interface between the transition region and the corona. For the remainder of this chapter, we will refer to this modification of solution B as solution C.

4.5 Conclusions

The majority of the atmospheric velocities that arise are due to the error associated with the first order error method used to calculate the gas pressure and density in the photosphere. The remaining velocities occur because of sharp gradient changes in the magnetic field profile and the temperature profile. The velocities are comparable in magnitude to the velocity of the buoyant flux tube and, therefore, should be removed to ensure the results from the emerging flux experiments

are dependent upon the rising tube and not the non-hydrostatic atmosphere.

We have shown that by modifying the profile for the increasing field strength in the photosphere from a tanh function to a sine profile, we can ensure there is a smooth transition in the field strength between the top of the photosphere and the transition region. This modification, solution A, eradicated the peak in velocity at $z = 10$. Using the sine profile for the magnetic field strength in the photosphere also enables an analytical expression to be derived for the gas pressure and density here. The use of the analytical expression over the finite difference method dramatically decreases the errors in calculating hydrostatic equilibrium and, therefore, the unwanted vertical velocities in the photosphere are greatly reduced. The reduction in vertical velocity due to the implementation of solution B is evident through the comparison of figures 4.7 and 4.16. These confirm that the solution is valid for domains with either a magnetised or unmagnetised atmosphere.

Solution B has also had a positive effect on the size of time step between consecutive iterations of `Diffin3d`. As discussed in section 3.3.2, the size of the time step is varied to ensure that information does not propagate out of the numerical stencil during a single iteration. By removing the sharp peaks and troughs in the vertical velocity, the size of the time step can be increased. For example, in the experiment with no tube and an atmospheric field the original numerical model uses a step size of 0.00156 time units. With the modifications of solution B, the time step size increases to 0.00169 time units. We note that the new numerical model for solution B may contain more calculations and will, therefore, require slightly more computational time. However, since this step is only carried out once per experiment the gain in fewer iterations from a larger time step size will easily out weigh any additional computational time required for the setup calculations.

Finally, modifying the temperature profile in the transition region from the power law to a sine function enables zero gradients to be imposed at the interfaces with the bounding regions. This modification removed the vertical velocity discontinuity at the interface between the photosphere and the transition region but was less successful at the interface between the transition region and the corona. This may be because the gradient in the temperature profile is greater at the top of the transition region and, thus, the turn over to a zero gradient must occur over a very small height, as shown in figure 4.17. If there are not enough gridpoints to accurately model the turn over, then errors can be introduced into the model. In addition, solution C actually leads to a decrease in the size of the time step to 0.00038 time units. This is smaller than that of the original numerical model and the model produced by solution B and, thus, a greater number of iterations would be required to reach the same point in time as the other models. In light of both of these facts, it does not seem advantageous to employ the new temperature profile and associated pressure and density profiles.

In conclusion, we find that solution B provides a clear improvement on the original numerical

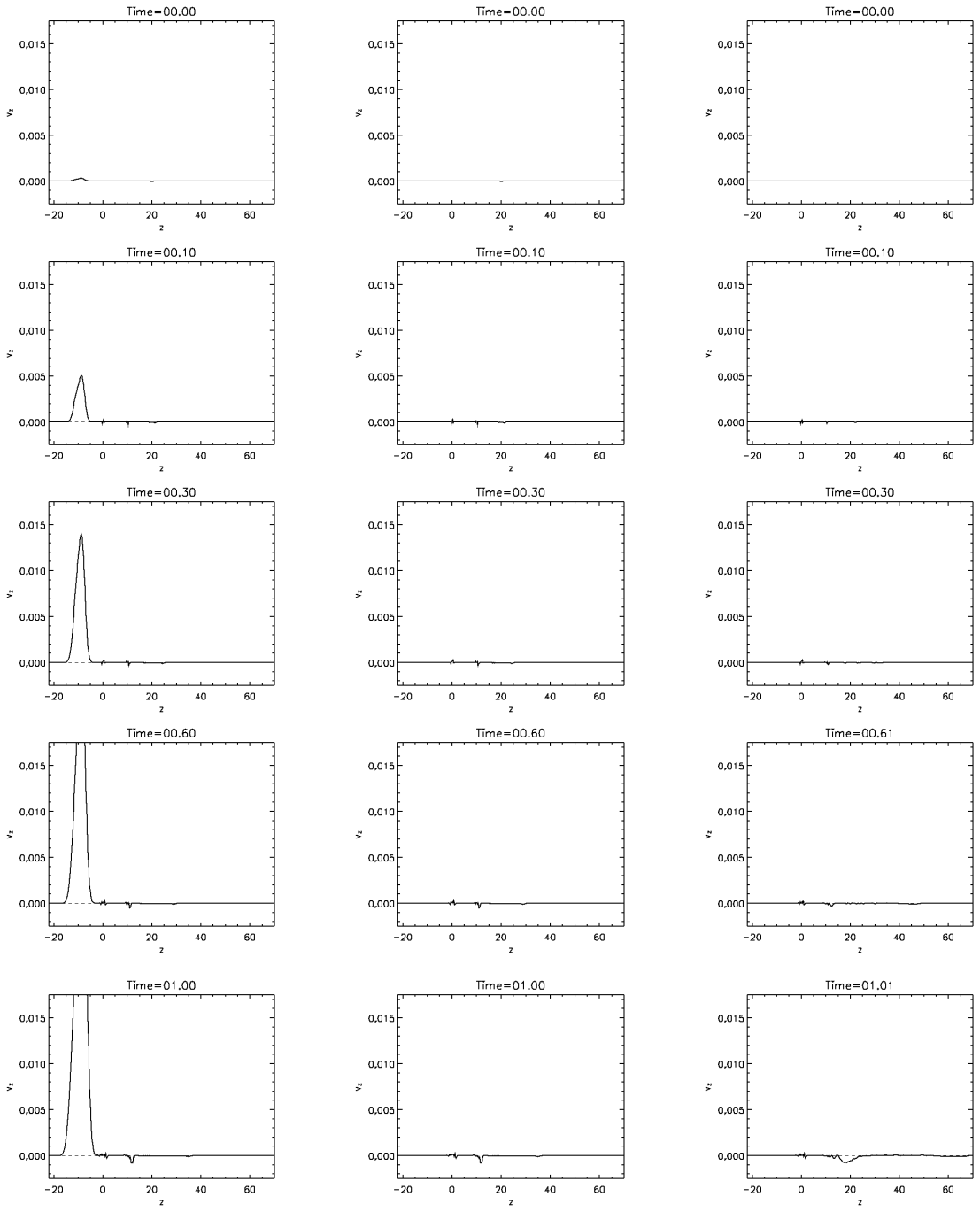

(a) Flux tube and an unmagnetised atmosphere.

(b) An unmagnetised atmosphere.

(c) A magnetised atmosphere.

Figure 4.16: Vertical velocity against height for three different experiment scenarios at different times, using the numerical model of solution B.

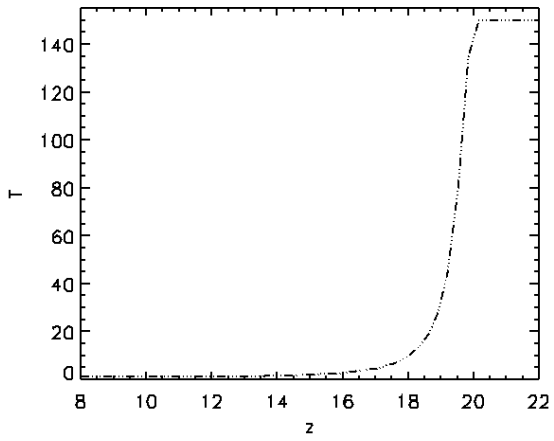

Figure 4.17: Temperature profile in the transition region using solution C, (4.40).

model and should, ideally, be used in any future flux emergence simulations using this model domain. However, it should be noted that the original numerical model will be used in the simulations in chapters 5, 6 and 7. By using the original model, clear comparisons will be able to be made between the results from previous simulations that have used the same model.

Chapter 5

Effects of Twist & Strength

Note: The material in this chapter has been published in Astronomy & Astrophysics. The reference is:
Murray, M. J., Hood, A. W., Moreno-Insertis, F., Galsgaard, K., and Archontis,V. (2006). 3D simulations identifying the effects of varying the twist and field strength of an emerging flux tube. *Astronomy & Astrophysics*, 460:909-923.

Previous emerging flux simulations have considered only a small region of the parameter space for the initial flux tube, as discussed in chapter 2. In this chapter, we will concentrate on two of the parameters associated with the constant twist flux tube, namely twist and axial field strength. By independently varying the values of these parameters, we aim to determine the individual effects of each parameter and their roles in the emergence process.

We have chosen to use a flux tube that has been used in multiple previous flux emergence simulations. In section 5.1, we will define the magnetic field of the flux tube and identify the parameter space to be tested for the two variables under consideration.

In chapter 4, we presented the hydrostatic simulation domain, which models the layers of the Sun from the solar interior up to the low corona. We place the flux tube in the domain's solar interior and choose it to be in radial force balance with the background plasma. In section 5.2, we will consider how the gas pressure, temperature and density profiles of the tube are chosen such that the tube is buoyant in comparison to the surrounding medium. Here, we will also detail the effects of changing the twist and field strength on the initial structure of the flux tube.

The first results we consider, in section 5.3, are those for the case with parameter values for the twist and field strength that most closely reflect the experiments of existing literature. These illustrate the general evolution of the tube during its rise through the solar interior and emergence

into the atmosphere. Following this, we consider the effects on the rise and emergence processes when the values of these parameters are varied. In section 5.4, we will present the results of solely varying the field strength and, in section 5.5, we will present the results of varying only the twist associated with the tube.

Finally, in section 5.6, we will summarise the modifications in the emergence of flux caused by varying the flux tube's field strength and twist and, using our findings, we will draw conclusions as to the robustness of the results from previous emergence simulations.

5.1 Defining the Magnetic Flux Tube

Most simulations of buoyant, twisted, flux tubes use a constant twist magnetic field for the flux tube. The concept of constant twist flux tubes was introduced in section 1.3.3. A large collection of papers actually use the same equations to define the constant twist magnetic field of the tube. In the cylindrical coordinate system, (r, θ, y), the popular magnetic field is given by $\mathbf{B} = (B_r, B_\theta, B_y)$, where

$$B_r = 0, \tag{5.1}$$

$$B_\theta = \alpha r B_y, \tag{5.2}$$

$$B_y = B_0 e^{-r^2/R^2}. \tag{5.3}$$

These equations ensure the field strength of the tube falls to zero at large radial distances from the axis. Hence, the tube can be considered as a distinct magnetic body in relation to the surrounding unmagentised environment. On the axis, the magnetic field has solely a B_y component, with direction given by the sign of B_0 and strength by $|B_0|$. At a distance R from the axis, the component of the field in the axial direction is 37% its original value. The value of R is held fixed at 2.5 over the series of experiments and B_0 and α are varied. The magnetic fieldlines of the tube twist around its axis and, using the definition in section 1.3.3, the twist is given by α.

The experiments are split into two groups, group 1 for those with fixed α and varying B_0 and group 2 for fixed B_0 with varying α. A summary of the values of B_0 and α under consideration is given in table 5.1. α is constant with radius in each of the experiments so that the tubes are uniformly twisted. Additionally, the group 1 cases, with α fixed at 0.4, are marginally unstable to the kink instability since $\alpha > 1/R$ (Fan et al. 1998b), however, we do not see the instability develop during the tube's rise through the solar interior in any of our experiments.

An immediate effect of varying these two parameters is seen in figure 5.1. Reducing α increases the rate at which the field strength of the tube fall off with radius. Increasing B_0 increases the

Group 1	Group 2
$B_0 = \{1.0, 2.0, 3.0, 5.0, 9.0\}$	$B_0 = 2.9$
$\alpha = 0.4$	$\alpha = \{0.1, 0.2, 0.3\}$

Table 5.1: Summary of the parameter space under investigation.

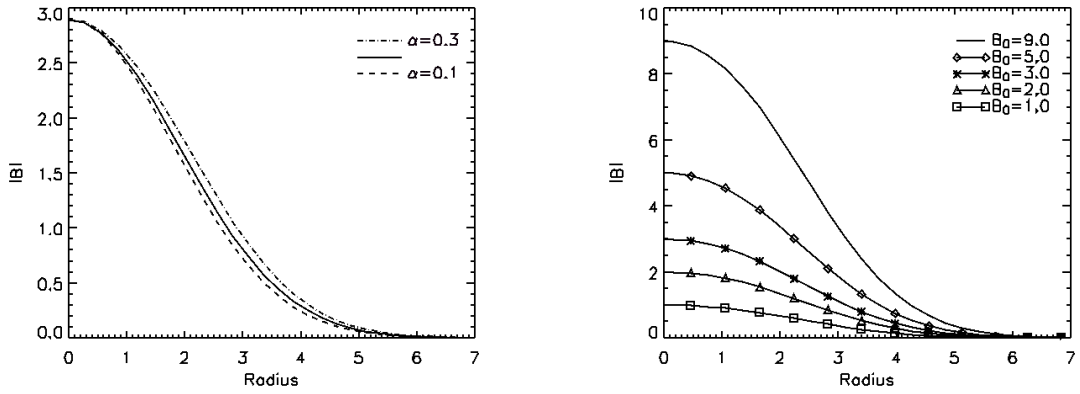

(a) α cases. (b) B_0 cases.

Figure 5.1: Radial distribution of the initial magnetic field strength, $|\mathbf{B}|$.

magnetic strength of the tube at all radii. As we will see in section 5.2, variations in the values of these parameters cause further modifications in the buoyancy of the tube.

We have identified seventeen papers that use exactly this field definition and a further four papers that modify the transverse field distribution (5.2) and so have a non-constant twist profile with radius. Each paper considers different combinations of values within the parameter space for B_0, α and R. To demonstrate how our study fits with and differs from those already carried out, we briefly outline the contents of these specific papers, many of which have been discussed in full in chapter 2.

Fan et al. (1998b) consider the rise of a highly twisted and, therefore, kink-unstable flux tube within the convection zone while Dorch et al. (2001) compares the rise of tubes in convective and non-convective flows. Moreno-Insertis and Emonet (1996), Emonet and Moreno-Insertis (1998), Abbett et al. (2000), Cheung et al. (2006) and Dorch (2003) vary the degree of twist of a tube rising though the convection zone. The first four papers aim to understand the fragmentation of the flux tube during its rise whilst the fifth considers the various instabilities arising from the different amounts of twist. The effects of variations in the magnetic field strength and twist of a tube rising though a convective flow are identified by Fan et al. (2003), while Cheung et al. (2007) considers these parameters' effects as the flux tube approaches and passes through the solar surface. Dorch et al. (1999) and Dorch (2007) carry out comparisons between the rise of horizontal and undular twisted flux ropes in both 2D and 3D during their rise through an unmagnetised and magnetised

convection zone, respectively.

The remaining papers consider the full emergence of the flux tube from the solar interior into the overlying atmosphere. Abbett and Fisher (2003), using two different computational codes to simulate the full emergence process, find that decreasing the twist of the flux tube increases the degree to which the initial emergence is force-free. Fan (2001) considers a tube which is stable to the kink-instability and reports on the dynamic evolution of the tube during the emergence process into an unmagnetised atmosphere. A whole series of further studies have sprung from the results of this single experiment. A variety of values for the field strength, twist and radius are used but each subsequent study considered just one value for each parameter.

Archontis et al. (2004) have further investigated the results of Fan (2001), reporting them in more detail and advancing the experiment by adding a magnetised atmosphere above the emerging flux tube. A number of papers (Galsgaard et al. 2005, 2007; Archontis et al. 2005, 2006) have varied the structure of the magnetised atmosphere and these use the same parameter values as Archontis et al. (2004). With the aim of generating a more self-consistent model, Archontis et al. (2007) set two buoyant tubes in the subphotospheric region such that the first tube emerges and creates a magnetised atmosphere into which the second emerges.

Manchester et al. (2004) use the same parameter values as the original experiment by Fan (2001) but they reduce the region over which the tube is buoyant and find a CME type event occurs once the tube has emerged into the atmosphere. Finally, Leake and Arber (2006) include a partially ionised region in the atmosphere of the domain to simulate the choromsphere. During the tube's emergence through this new region, ion-neutral collisions cause all cross-field currents to be dissipated and, as a result, a force-free field emerges into the corona.

The extensive use of the field structure given by (5.1), (5.2), (5.3), in emergence experiments warrants a comprehensive study of the parameter space. Figure 5.2 illustrates the limited exploration of the parameter space to date. We will vary the twist and strength of a magnetic flux tube and, for the first time in an emergence study, evaluate the effects of the variations. Our aim is to understand the role of twist and field strength in shaping the emergence process.

It should be noted that a parameter space investigation has been carried out by Magara (2001), in which the radius, twist and strength of an emerging flux tube were varied. Our study is different on several fronts.

- We use the field structure defined by (5.1), (5.2), (5.3), and this is not used by Magara (2001).

- The flux tube we define is fully buoyant and, therefore, prescribed with a buoyancy perturbation (described in section 5.2) to encourage the formation of an Ω-shaped loop. Following

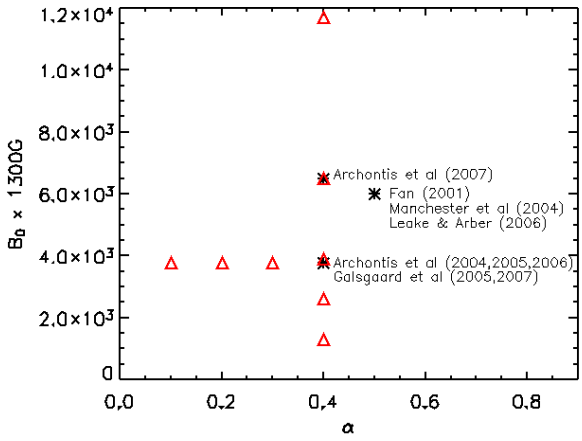

Figure 5.2: The B_0-α parameter space for the magnetic flux tube defined by (5.1), (5.2), (5.3). The red triangles indicate the cases under investigation in this chapter and the black stars demonstrate the B_0-α pairings used in previous flux emergence simulations.

this initialised perturbation we allow the system to evolve by itself. On the other hand, Magara (2001) choose to drive the central portion of the tube upwards by imposing a vertical fluid velocity.

- The values of the parameters were altered simultaneously by Magara (2001) and, therefore, it is difficult to quantify the independent impact of each on the emergence process. We aim to provide a clear explanation of how varying the twist and field strength of the flux tube, independently of each other, will alter the dynamics of the rise of the flux tube in the upper layers of the convection zone and its subsequent expansion into the atmosphere.

5.2 Placement of the Tube within the Hydrostatic Solar Interior

Each of the simulations described within this chapter is carried out in the dimensionless domain $(-60, 60) \times (-70, 70) \times (-22, 70)$ in the (x, y, z) coordinate system. This corresponds to a horizontal domain of size $20.4\ \mathrm{Mm} \times 23.8\ \mathrm{Mm}$ on the Sun, which extends to a depth of $3.7\ \mathrm{Mm}$ below the solar surface and an atmospheric height of $11.9\ \mathrm{Mm}$. The grid contains $148 \times 160 \times 218$ points, with uniform spacing in the horizontal plane and stretched spacing in the vertical direction. The numerical resolution is highest over the region from just below the initial location of the flux tube to just above the transition region. The gridspacing represents a physical distance of $4.77 \times 10^4\ \mathrm{m}$ at its smallest and $2.49 \times 10^5\ \mathrm{m}$ at its largest. The boundaries of the box are periodic in the horizontal directions and closed on the top and bottom. A damping region is included at both the top and bottom of the box to limit the reflection of waves.

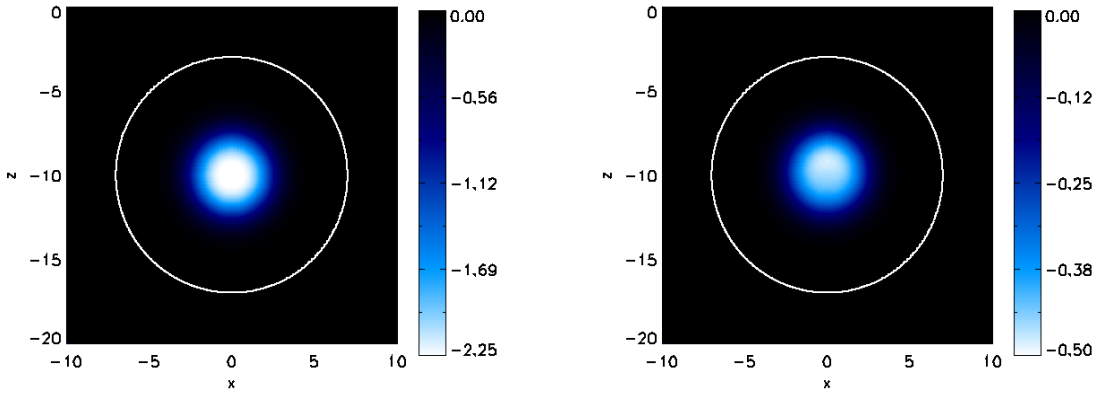

(a) Contours of pressure excess, p_{exc}.

(b) Contours of density excess, ρ_{exc}.

Figure 5.3: Variation in the excess quantities through the (x, z) plane at $y = 0$ in the case $B_0 = 3.0$ and $\alpha = 0.4$. The white circle has a radius of 7 units and indicates an approximate boundary for the tube.

We set up the domain of our simulation using the numerical solar interior and atmosphere described in section 4.2, where the solar surface is located at $z = 0$. The magnetic flux tube is then placed horizontally within the solar interior, with its axis initially located at $z = -10$. This corresponds to a depth of $1.7\mathrm{Mm}$ below the solar surface. At the commencement of the simulation, we require the tube to be in radial force balance with the external plasma. This prevents a sudden radial expansion or compression of the tube when the simulation begins.

The internal gas pressure of the tube, p_i, is defined as $p_e + p_{exc}$ where p_e is the external gas pressure and p_{exc} is the pressure excess. The pressure excess can be found by solving

$$\frac{dp_{exc}}{dr} = (\mathbf{J} \times \mathbf{B})_r \,, \tag{5.4}$$

where $\mathbf{B}$ is prescribed by (5.1), (5.2), (5.3). Integrating this with respect to r yields

$$p_{exc} = \frac{1}{2\mu} \left(\alpha^2 \left(R^2/2 - r^2\right) - 1\right) {B_y}^2 + C, \tag{5.5}$$

where C is a constant of integration. At large radial distances, the field strength diminishes to zero and, thus, we consider the tube boundary to have been reached. Hence, we also have $p_{exc} = 0$ at these large r and, thus, $C = 0$. Therefore,

$$p_{exc} = \frac{1}{2\mu} \left(\alpha^2 \left(R^2/2 - r^2\right) - 1\right) {B_y}^2. \tag{5.6}$$

Figure 5.3(a) illustrates the pressure excess, which increases radially from the axis of the tube.

As with the gas pressure, we define the density of the material in the tube, ρ_i, to be $\rho_e + \rho_{exc}$

where ρ_e is the external density and ρ_{exc} is the density excess. If we were to choose the whole of the tube to be in thermal equilibrium with its surroundings then the density excess would be given by

$$\rho_{exc} = \frac{\tilde{\mu} p_{exc}}{\tilde{R} T(z)} = \frac{\tilde{\mu}}{2\mu \tilde{R} T(z)} \left(\alpha^2 \left(R^2/2 - r^2\right) - 1\right) {B_y}^2. \tag{5.7}$$

The whole tube would then be buoyant when a density deficit exists, $\rho_{exc} < 0$.

We now consider what values the parameters are required to take in order to make the tube buoyant for all radii. If we want to have $\rho_{exc} < 0$ at all radii, then we must satisfy $\left(\alpha^2 \left(R^2/2 - r^2\right) - 1\right) < 0$ at all radii. We note that the criterion for buoyancy is independent of B_0. This criterion can be simplified to

$$\frac{R^2}{2} - \frac{1}{\alpha^2} < r^2. \tag{5.8}$$

Given that R and α are constants, the tube will be buoyant at all radii providing the axis is buoyant. Thus, the criterion reduces to

$$\alpha^2 < \frac{2}{R^2}. \tag{5.9}$$

and, for $R = 2.5$, the tube will be buoyant at all radii providing $|\alpha| < 0.57$. The values of α chosen for the tubes within groups 1 and 2 satisfy this criterion and, therefore, will be buoyant at all radii. The cross-sectional density excess of a tube is indicated in figure 5.3(b). The most buoyant region in the tube's cross-section sits slightly above the axis of the tube as a result of the specific ambient temperature profile chosen for the tube.

This profile of density excess given by (5.7) is independent of position in the axial direction and, therefore, the whole length of the tube will exhibit the density excess illustrated in figure 5.3(b). However, we wish to encourage the formation of an Ω-loop shape along the tube's length to promote emergence in just a section of the tube. Thus, we choose only the cross-section of the tube at $y = 0$ to have this complete buoyancy at all radii. The density deficit is reduced away from $y = 0$ following the Gaussian profile

$$\rho_m = \rho_{exc} e^{-y^2/\lambda^2}, \tag{5.10}$$

where $\lambda = 20$, such that the density in the tube is now given by $\rho_i = \rho_e + \rho_m$. The smaller density deficit for $|y| > 0$ implies that there is a corresponding increase in the temperature contrast between the tube and surroundings.

From (5.7) we can see that both the twist and the magnetic field strength play a role in determining how buoyant the flux tube will be. For group 2, the variation in α leaves the strength of the field at

the tube's axis unchanged and has little effect on the intensity of the magnetic field at outer radii, as shown in figure 5.1(a). However, increasing the amount of twist will increase the inwardly acting tension force more than the outwardly acting magnetic pressure force and, therefore, will alter the buoyancy of the tube. Thus, the tubes in group 2 are buoyant to varying degrees despite the small variation in their overall magnetic field intensity.

From figure 5.1(b) it can be seen that for the cases in group 1, there is a large variation in B_0, and, consequently, there will be a large variation in the initial buoyancy of the tube, both at the axis and at all radii until the edge of the tube is reached. Since, from (5.7), the density deficit is proportional to ${B_0}^2$, the tube with $B_0 = 9.0$ is 9 times more buoyant than that with $B_0 = 3.0$, which in turn is 9 times more buoyant than the tube with $B_0 = 1.0$.

5.3 Overview of the Tube's Evolution in the Common Case

For the tube with $B_0 = 3.0$ and $\alpha = 0.4$, from group 1, we see the same results as those described in Archontis et al. (2004). As the buoyant portion of the tube rises it compresses the plasma preceding it, which is rising more slowly. This compression causes the transverse magnetic field to be enhanced at the leading edge of the tube, thus the fieldlines turn further from the axial direction.

As the tube rises, it moves to heights where the external gas pressure is continually decreasing. The tube tries to maintain horizontal force balance and so expands. As a consequence of the expansion, there is a fall in the internal density but the tube becomes increasingly less buoyant in comparison with its surroundings. Eventually, parts of the tube become over dense whilst the tube is still in the solar interior. However, the tube continues to rise as a whole. By mass conservation and magnetic flux conservation, the magnetic field strength in the central part of the tube decreases due to the expansion of the tube during the rise.

The temperature in the photosphere is isothermal, hence the stratification is strongly subadiabatic and, following the classical Schwarzschild criterion, is stable against convection. Thus, the tube is no longer buoyant compared with its surroundings when it reaches the photosphere. Through the development of a magnetic buoyancy instability, the tube can rise into the atmosphere where it undergoes a marked expansion due to the sharp fall in background gas pressure with height. The rise of the tube through the solar interior and its expansion into the atmosphere is illustrated in figure 5.4. The axis of the tube reaches equilibrium at the photosphere and does not rise into the atmosphere within the limited time of the experiment.

We now consider how varying B_0 and α modifies the rise of the tube through the solar interior and its emergence into the atmosphere.

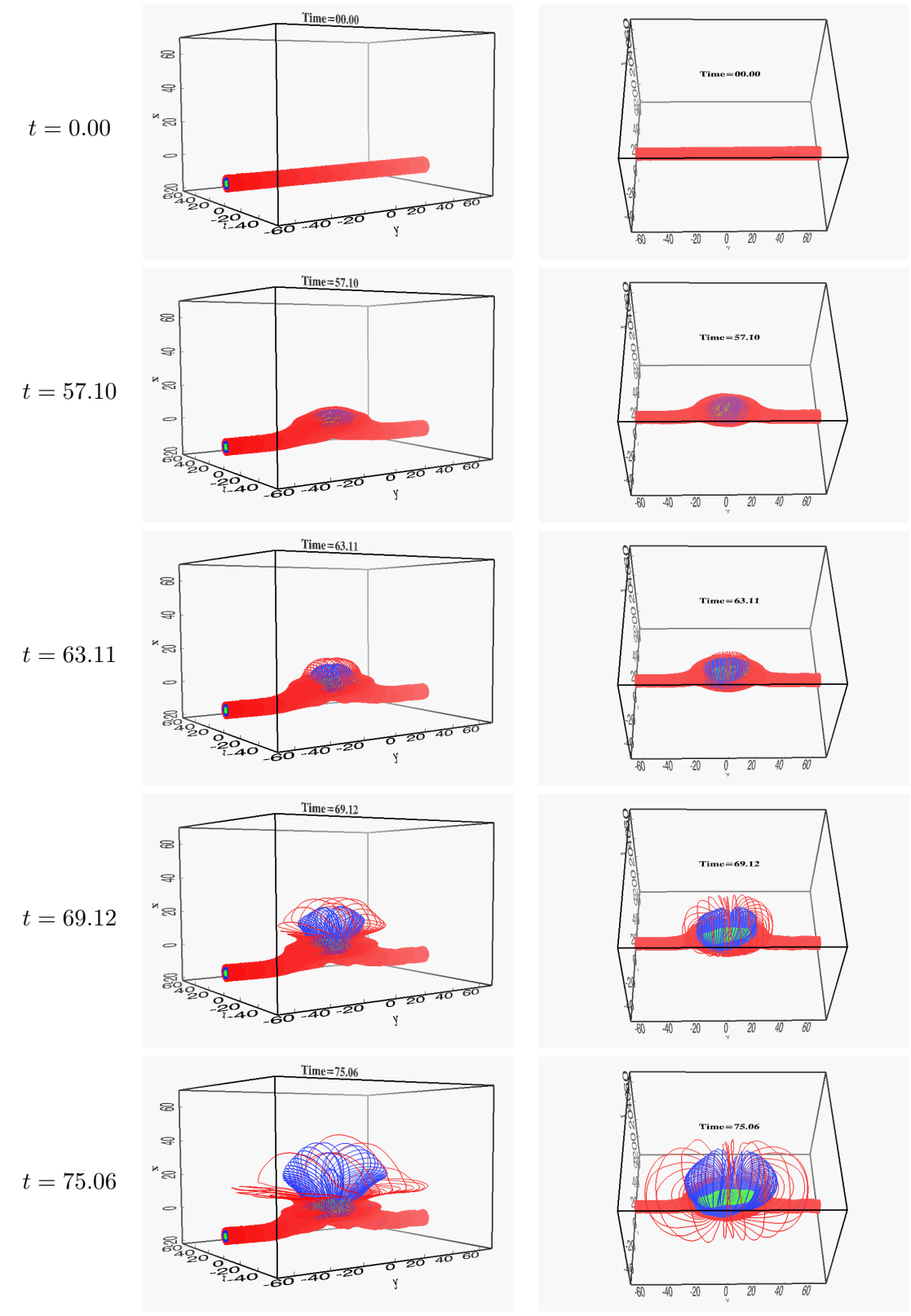

Figure 5.4: Fieldlines traced from the one end of the tube at several different times and from two different viewpoints. The tube shown here has parameters $B_0 = 3.0$ and $\alpha = 0.4$. The outer fieldlines (red) experience expansion first, followed by the inner fieldlines (blue). The fieldlines closest to the axis (green) remain trapped near the photosphere.

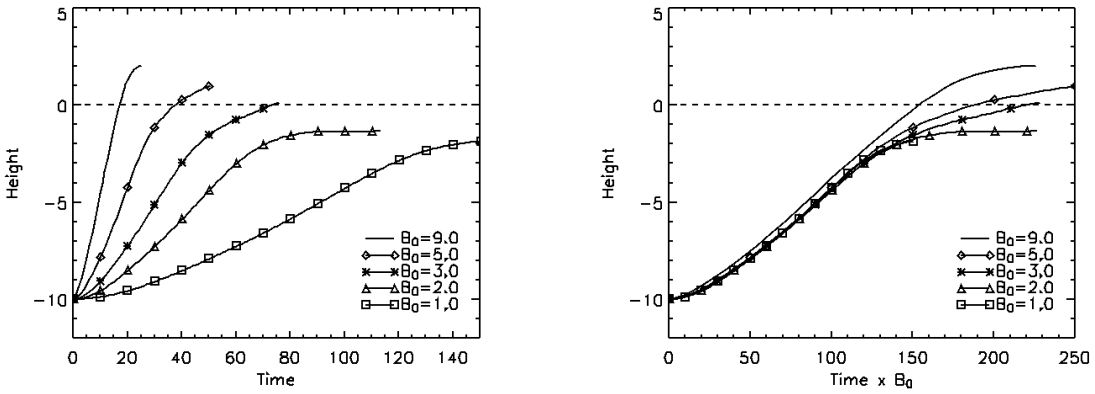

(a) Measured over time.

(b) Measured over rescaled time, $\bar{t} = tB_0$.

Figure 5.5: Height of the axis of the tube for the various B_0 cases.

5.4 Group1: Varying B_0 with Fixed α

5.4.1 Rise in the Solar Interior

All of the tubes are buoyant and initially at rest, thus the motion of the tubes at the start of the experiments is characterised by a vertical velocity. From (5.7), we know that the buoyancy force in the central portion of the tube is proportional to ${B_0}^2$ and therefore expect tubes with larger values of B_0 to have higher velocities and reach greater heights more quickly. This is confirmed by figure 5.5(a), which shows that the time taken for the axis of the tube to reach $z = -2$, a height just below the photosphere, in each of the cases is inversely proportional to B_0.

By redefining time as $\bar{t} = tB_0$ and rescaling the horizontal axis in figure 5.5(a) we find that the heights reached by the axes are similar to each other up until a time of approximately $\bar{t} = 150$. This is illustrated in figure 5.5(b). Rescaling time in this way is equivalent to measuring time on an Alfvén time-scale rather than a sound time-scale. A similar reliance on the initial field strength is found for the rise of the crests of the tubes through the solar interior. Thus, the heights of the axis and crest of each of the tubes are not only functions of time but also initial field strength, i.e. $H(\bar{t}) = H(tB_0)$ where H is the function giving the height of the axis or crest of the tube. This inverse scaling of the rise times of the tubes with B_0 in unconvective flows confirms the 2D results previously found by Fan et al. (2003).

Figure 5.6(a) illustrates the vertical velocity of the axis of the tube for the various cases. The initial acceleration of the tube is proportional to the buoyancy force acting on the tube and, therefore, the vertical acceleration will be proportional to B_0^2 for the group 1 cases. To make comparisons between the tubes when they are at the same heights we redefine time to be $\bar{t}$ using the scaling

described above. Thus, the vertical velocity as a function of height will be proportional to B_0, as verified by figure 5.6(b). Interestingly, the 2D study by Emonet and Moreno-Insertis (1998) found that variations in the initial plasma-β of the tube resulted in similar velocity profiles once the velocity scale was enlarged by a factor $\beta_0^{1/2}$ and the time scale was contracted by the same factor. Application of the $\beta_0^{1/2}$ scalings to our data reveals that the scalings we use provide greater similarity between the velocity profiles of our tubes during the acceleration phase.

Previous studies (Moreno-Insertis and Emonet 1996; Emonet and Moreno-Insertis 1998) distinguish different phases in the acceleration of a buoyant flux tube rising in a stratified medium. At the very beginning there is a free-fall period in which the acceleration of the tube is purely caused by its own buoyancy. Emonet and Moreno-Insertis (1998) give this free-fall acceleration at the tube's axis as

$$a_z = \frac{g}{i}\left|\frac{\triangle\rho}{\rho}\right|_{r=0}, \tag{5.11}$$

where $i = 2$ is the enhanced inertia factor due to the co-moving surrounding medium, $\triangle\rho$ is the density excess, ρ_{exc}, and ρ is the internal density. Both $\triangle\rho$ and ρ are measured at the axis at time $t = 0$. Integrating (5.11) with respect to t gives the vertical velocity, which is plotted as the dashed line in figure 5.6(b) and agrees relatively well with the vertical velocity of the tube's axis for the group 1 cases.

In the second phase, which starts when the axis is only a short distance from its initial height, Moreno-Insertis and Emonet (1996) and Emonet and Moreno-Insertis (1998) state that the acceleration diminishes due to the increasingly important aerodynamic drag exerted by the flows surrounding the tube. In fact, between the heights of $z \sim -9$ and $z \sim -6$ we find that there is a period of roughly constant, slower acceleration. As expected from the overlying of the curves in figure 5.6(b), during this period the vertical acceleration of axes of the tubes remains proportional to B_0^2, as illustrated by figure 5.6(c). Once this period of constant acceleration ceases, the acceleration continues to diminish as the tube rises higher.

The final, asymptotic phase, described in the papers mentioned above, represents the period when the buoyancy force and the aerodynamic drag balance each other, giving rise to a continued period of average zero acceleration. In our calculation, this asymptotic phase cannot be reached, since by then the tube is close to the photosphere and the acceleration of the tube is determined by additional factors, described in the following section, not present in the previous studies. In fact, in our case, when the axes of the tubes are at $z \sim -5$, the acceleration is momentarily zero before becoming negative. At the zero acceleration stage, the vertical magnetic forces only contribute $\sim 5\%$ towards the total unsigned force ($\mathbf{F}_z = |-\nabla p|_z + |\rho\mathbf{g}| + |\mathbf{J}\times\mathbf{B}|_z$) acting on the axis. Hence, the zero vertical acceleration at the axis occurs when the vertical gas pressure gradient approximately balances the buoyancy force. The decrease in the vertical velocity of the axis

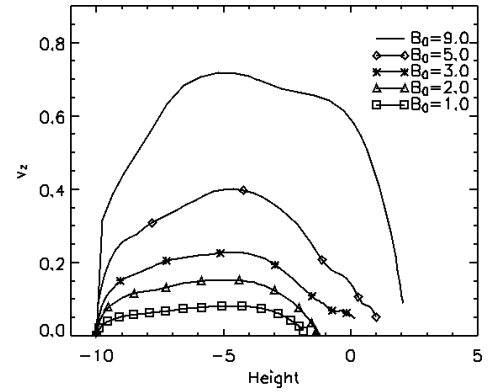

(a) Vertical velocity of the axis measured against the height of the axis.

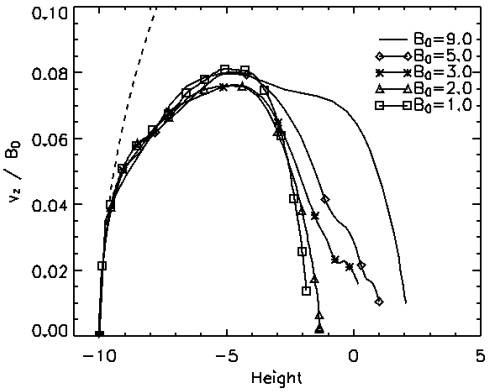

(b) Vertical velocity as a fraction of the initial field strength of the axis measured against the height of the axis. The dashed line is the vertical acceleration expected from free-fall alone and is given by integrating (5.11).

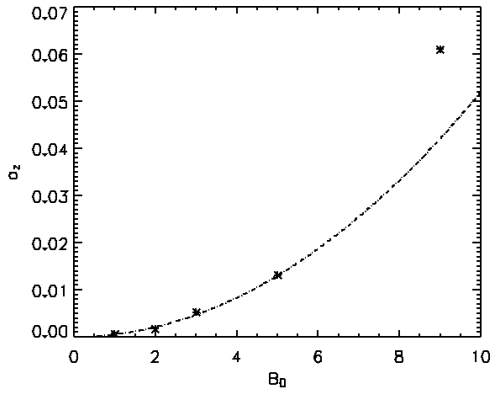

(c) Constant vertical acceleration (a_z) during the second period. The dot-dashed line is given by $a_z = 0.0005{B_0}^2$ and identifies the acceleration of the tube as proportional to ${B_0}^2$.

Figure 5.6: Measures of the rate of rise of the axis of the tube for the various B_0 cases.

occurs when the plasma there is still buoyant but the gradient in the gas pressure is the largest force.

Previous papers dealing with the 2D case (Moreno-Insertis and Emonet 1996; Emonet and Moreno-Insertis 1998; Cheung et al. 2006) have reported oscillations in the vertical velocity of the axis and crest of the tube. These oscillations are part of the internal torsional oscillations taking place in the interior of the rising tube (Emonet and Moreno-Insertis 1998). They decrease in amplitude as the tube rises, with the loss in energy occurring due to its transmission to the surroundings of the tube via pressure forces and internal diffusion. We do not see marked oscillations in our experiments. This may be due to a combination of factors. Firstly, our tubes are substantially thicker (compared to the local stratification scale height) than those of the previous calculations. The ratio of the oscillation period to the rise time across one scale height is therefore longer in our case. Secondly, our 3D case has lower numerical resolution and, hence, probably also higher numerical diffusion. Thirdly, in the 2D case, the whole length of the tube along its axis was oscillating with the same amplitude and in phase. This is no longer the case in the 3D experiment; the oscillation of the rising section of the tube is transmitted to the lower, non-rising stretches, and, therefore, the amplitude becomes smaller.

Also of interest are changes to the gas pressure and density profiles within the tube. The initial density deficit ($\rho_{exc} < 0$) and gas pressure deficit ($p_{exc} < 0$) in each tube are small in comparison to the external density and gas pressure. Thus, the internal density and gas pressure are dominated by their external values. As the tube rises, we find that this dominance is maintained and we see the density and gas pressure of the rising axis behaving as the external quantities at the associated height. Hence, the density and the gas pressure at the axis of the tube are given by

$$\rho_i\left(z_a\right) \propto \left(1 - 2z_a/5\right)^{3/2}, \tag{5.12}$$

$$p_i\left(z_a\right) \propto \left(1 - 2z_a/5\right)^{5/2}, \tag{5.13}$$

where z_a is the height of the axis and $z_a < 0$.

Figure 5.7 shows the density excess at the axis, given as a fraction of the initial unsigned density excess there, plotted against the height of the axis. It can be seen that the axes of the tubes becomes over dense ($\rho_{exc} > 0$) prior to them reaching the base of the photosphere. This indicates that, for each tube in group 1, all of the material above the axis of the tube also loses its buoyancy before reaching the photosphere. The density excess as a proportion of the actual internal density is small and, therefore, its growth is marginal in comparison to the overall fall in the internal density.

Figure 5.8 considers the change in the field strength at the axis of each tube, as a fraction of its initial field strength, and shows a similar pattern of decrease as each tube rises. The thin flux tube approximation states that $|\mathbf{B}|/\rho$ should be conserved but this approximation is only valid when the radius of the tube is negligible compared with the scale height of the surrounding unmagnetised

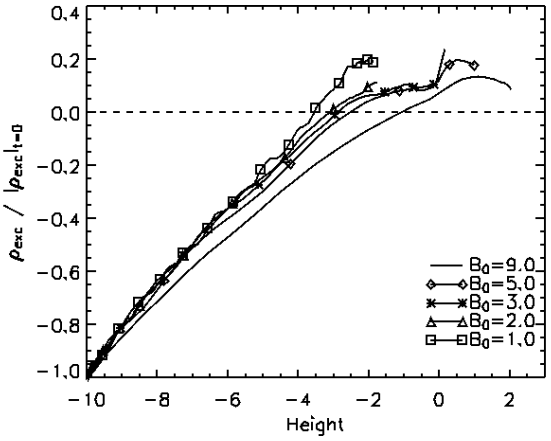

Figure 5.7: The increase in the density excess at the axis, as a fraction of the initial unsigned density excess there, plotted against the height of the axis for the various B_0 cases.

fluid and any scales of variation along the tube (see the review by Fan (2004) and references therein for a complete discussion). The flux tubes we consider have a radius that is 2.5 times the photospheric pressure scale height and are twisted so this approximation is not valid for the whole of the tube. However, since the fieldline pitch of the axis of the tube is zero and the most buoyant section at $(x = 0, y = 0)$ remains horizontal for all time, we find that

$$|B_y\,(z_a)\,| = \frac{|B_0|}{\rho_0}(1 - 2z_a/5)^{3/2}, \tag{5.14}$$

where ρ_0 is the density measured at the axis at $t = 0$, is in fact a good approximation.

The decrease shown in figure 5.8 is well prescribed by (5.14) (dashed line in figure 5.8) until the axes reach $z \sim -7$, a sizeable proportion of the total distance travelled by each axis. There is an 8% and a 21% deviation of the approximation from the simulation values when the axes reach heights of $z_a = -5$ and $z_a = -2$, respectively. This deviation occurs because the twisted nature of the fieldlines exerts an inwardly acting tension force that is absent in the TFTM. The tension force limits the radial expansion of the tube and, therefore, reduces the decrease in density and axial field strength expected from (5.14).

The discussion within this section has seen the rescaling of several quantities with respect to the only varied parameter of the model, B_0. By rescaling, we have been able to remove the dependence of B_0 from the model, revealing a *self-similar* evolution of the tubes during their rise through the solar interior. As we will see, this self-similarity is also visible when the tubes enter the photosphere and in those that emerge into the atmosphere.

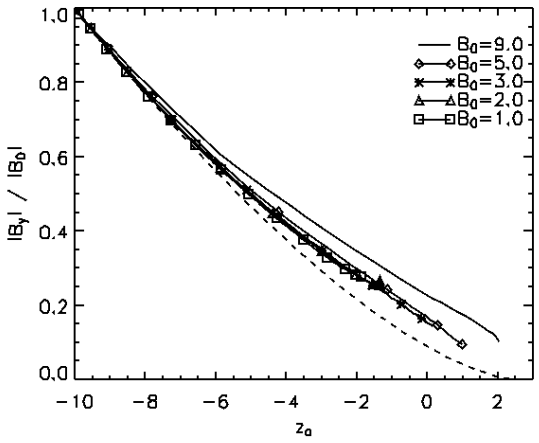

Figure 5.8: The decrease in the B_y component of the field at the axis, as a fraction of the initial field strength there, measured at $(x = 0, y = 0)$ and plotted against the height of the axis, z_a. The dashed line corresponds to the decrease in the axial magnetic field component, B_y, at the axis in accordance with the thin flux tube approximation given by (5.14).

5.4.2 Emergence into the Photosphere

As discussed in section 5.4.1, when the top of the tube rises through the last few remaining pressure scale heights of the solar interior it is over dense in comparison with the surrounding medium but continues to rise due to the external adiabatic stratification. However, the photosphere is strongly subadiabatic and, therefore, there is a rapid slowing of the rise of the crest of the tube when it enters the lower atmosphere.

The plasma in the upper part of the tube cannot continue to rise vertically due to the slowing of the crest and, it is forced to spread out horizontally at the photosphere to make way for the rising material below (Magara 2001; Archontis et al. 2004). The area of the interface between the solar interior and the photosphere that contains flux from the tube steadily increases with time, as shown in figure 5.9(a). Tubes with a stronger initial field strength spread out and cover a larger photospheric area more quickly than those with a lower initial strength. Figure 5.9(b) shows that the time taken for each of the tubes to cover the same sized area is proportional to B_0. This indicates that the faster spread of the higher strength tubes is purely due to their faster rise to the photosphere, which occurs due to their greater initial buoyancy force. Additionally, since only some of the tubes go on to fully emerge into the atmosphere (as will be discussed shortly) we know that this occupation of the photospheric plane is controlled purely by the tube plasma rising below the photosphere and is independent of the transportation of tube flux into the upper atmosphere.

Many studies have shown that over-dense flux can be transported into the atmosphere via the magnetic buoyancy instability. Perturbations that bend the fieldlines cause the instability to be

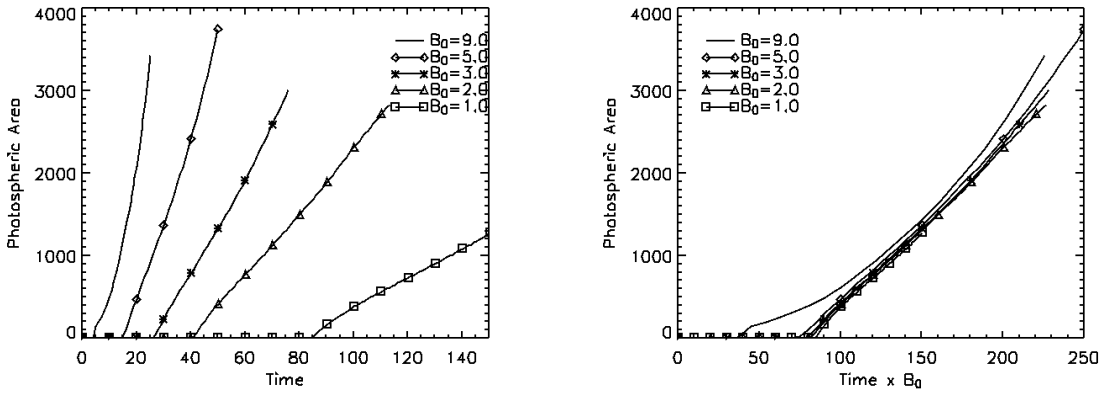

(a) Measured over time.

(b) Measured over rescaled time, $\bar{t} = tB_0$.

Figure 5.9: Measurements of the dimensionless area of the photospheric plane ($z = 0$) containing flux from the emerging tube for the various B_0 cases. The dimensionless length unit at the photosphere, L_{ph}, is equivalent to 170 Km.

launched more quickly. As discussed in section 2.2.2, emergence into the upper atmosphere occurs when

$$-H_p \frac{\partial}{\partial z} (\log B) > -\frac{\gamma}{2}\beta\delta + \tilde{k_\parallel}^2 \left(1 + \frac{\tilde{k_\perp}^2}{\tilde{k_z}^2}\right) \tag{5.15}$$

is satisfied (Newcomb 1961; Yu 1965; Thomas and Nye 1975; Acheson 1979; Archontis et al. 2004; Leake and Arber 2006). As a reminder, in this criterion we have the pressure scale-height, H_p, the ratio of specific heats, γ, the plasma-β and perturbations with wavevector $\mathbf{k}$ (where $\tilde{k_\parallel}$ and $\tilde{k_\perp}$ are the horizontal components parallel and perpendicular to the magnetic field and $\tilde{k_z}$ is the vertical component). The superadiabatic excess, δ is given by $\delta = \nabla - \nabla_{ad}$, where ∇ is the actual logarithmic temperature gradient in the equilibrium stratification and ∇_{ad} is its adiabatic value. The review by Moreno-Insertis (2005) considers the development of the terms in (5.15) prior and post instability development. Here, we investigate only the differences in the size of the terms of (5.15) between the various B_0 cases to understand why some tubes emerge whilst others do not.

Two of the tubes under consideration in group 1 do not emerge into the atmosphere and these are the ones with the lowest values of B_0, namely 1.0 and 2.0. Consideration of each of the terms in (5.15) clarifies why these tubes do not emerge. To make a comparison between the different cases we consider the left-hand and right-hand quantities of the criterion at the time when the criterion is first satisfied for each tube. This time is different for each of the three tubes that emerge and the times considered are $t = 15$, 27 and 49 for $B_0 = 9.0$, 5.0 and 3.0, respectively. Since two of the tubes do not emerge, (5.15) is never satisfied in these cases so we choose times such that the tops of these tubes have advanced into the photosphere. For $B_0 = 2.0$ and 1.0 we choose $t = 70$

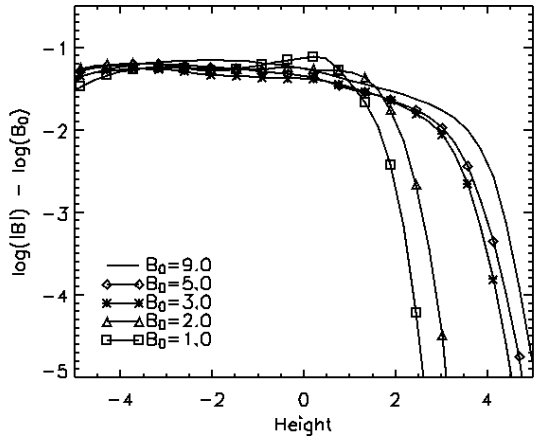

Figure 5.10: The natural logarithm of the magnitude of the magnetic field, where the magnitude of the field has been made independent of the initial field strength by subtracting the natural logarithm of B_0. The time at which the quantity is considered at varies with each tube and the times are $t = 15$, 27, 49, 70 and 152 for $B_0 = 9.0$, 5.0, 3.0, 2.0 and 1.0, respectively. The quantities are measured along $(x = 0, y = 0)$ and are plotted against height.

and 152. The term on the left-hand side of (5.15) corresponds to the compression of the magnetic field. Consider the decomposition of the magnetic field stength into the form $|\mathbf{B}| = f(B_0)B^*$, where f and B^* are functions describing the field strength's dependence and independence of B_0 respectively. The natural logarithm of the field stength is, therefore, $log(f) + log(B^*)$ and, once differentiated, solely the portion independent of the constant B_0 will remain. Hence, the left-hand term of (5.15) is independent of B_0. Figure 5.10 shows the natural logarithm of the magnitude of the magnetic field, where the magnitude of the field has been made independent of B_0, for the various group 1 cases at the times stated above. We consider this quantity at the height at which the instability terms, as calculated for figure 5.11, are non-zero for each tube, namely $z = 1$ and $z = 2$ for the $B_0 = 1.0$ and 2.0 cases respectively, and $z = 3$ for the remaining tubes. We can see that the tubes with the smaller values of B_0 have the steepest gradient at the given height.

The reason for this is related to the momentum of the rising tube. When the crest of the tube enters the photosphere it is forced to slow due to the change in the background stratification. The tubes with higher values of B_0 have a higher velocity when rising through the solar interior and, therefore, they have a higher momentum when their front reaches the photosphere so the velocity of the tube front does not decrease significantly. Equivalently, the tubes with smaller values of B_0 have a smaller velocity and, therefore, a smaller momentum so their tube fronts slow greatly in the photosphere. The axes of all the tubes are still rising and in the cases of $B_0 = 1.0$ and $B_0 = 2.0$ the distance between the crest and the axis begins to decrease again since the tube fronts are no longer rising as quickly. The material at the front of these tubes is therefore compressed to a greater extent and this results in the gradient of the magnetic field strength steepening.

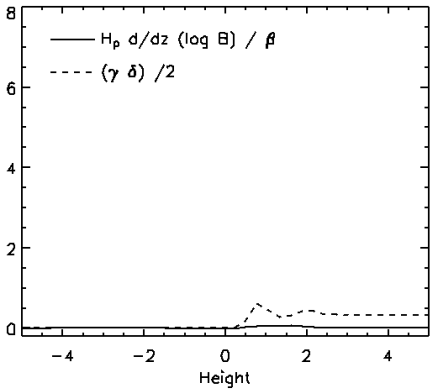

(a) For $B_0 = 1.0$ at $t = 152$.

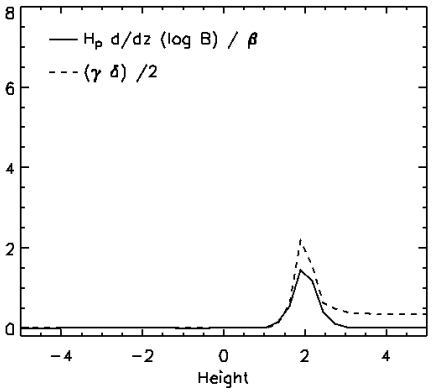

(b) For $B_0 = 2.0$ at $t = 70$.

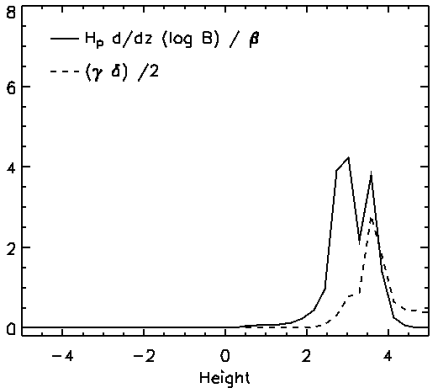

(c) For $B_0 = 3.0$ at $t = 49$.

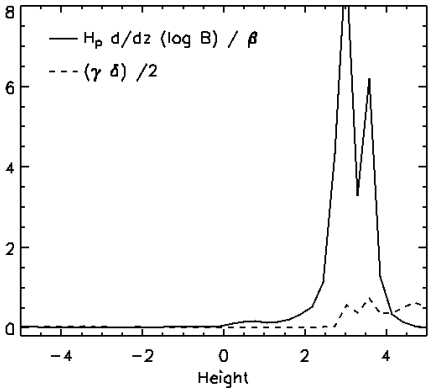

(d) For $B_0 = 5.0$ at $t = 27$.

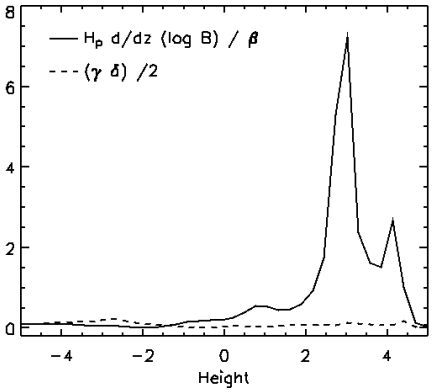

(e) For $B_0 = 9.0$ at $t = 15$.

Figure 5.11: The left-hand side and first right-hand side terms of (5.15), divided by the plasma-β, for the various B_0 cases. The quantities are measured along $(x = 0, y = 0)$ and are plotted against height.

The first term on the right-hand side of (5.15) contains the plasma-β. The initial plasma-β is significantly higher for those tubes with a smaller value of B_0. This is because these tubes have a larger internal gas pressure and a smaller magnetic pressure. Irrespective of B_0, as the tube rises the value of the plasma-β for the material in the front portion of the tube decreases but we note that the tubes with smaller values of B_0 still have the largest plasma-β since the magnitude of their magnetic field is smaller.

In figure 5.11, we show the left-hand and right-hand terms of (5.15), divided by the plasma-β, at the times previously specified for each tube.

From the discussion above, we know that the gradient in the magnetic field profile is smaller for higher valued B_0 tubes, with the left-hand term for the $B_0 = 9$ tube being $\sim 60\%$ of that of the $B_0 = 1$ tube. The plasma-β is also smaller for higher valued B_0 tubes, but the plasma-β for the $B_0 = 9$ tube is $\sim 5\%$ of the $B_0 = 1$ tube. This variation in the rate of decrease of the two terms with B_0 results in the left-hand term of (5.15), divided by the plasma-β, increasing as B_0 increases.

The convective term, given by the dashed line in figure 5.11, appears to increase as the value of B_0 increases up to the $B_0 = 3$ case and then decreases as B_0 increases further. For the tubes with smaller values of B_0 this term dominates and, therefore, the tubes do not undergo the buoyancy instability. However, for the tubes with larger values of B_0 the magnetic term, given by the solid line in figure 5.11, dominates and the tubes do suffer from the buoyancy instability and go on to emerge into the atmosphere.

The rightmost term of (5.15) is ~ 0.025 for all of the tubes and division by the plasma-β at the top of the tube gives the range of values $1.25 - 0.0025$ for the tubes, with the larger valued B_0 tubes taking the larger values in the range. These values are given for completeness only since we find that this term does not alter the outcome of the criterion in anyway.

Finally, we find that the axes of tubes with larger values of B_0 reach greater heights within the photosphere. This is because the higher B_0 tubes have larger velocities and, thus, larger momentums when the plasma becomes over-dense, carrying the tube (including the axis) higher into the photosphere. The heights observed for the axes are not necessarily the heights at which they will come to rest since they are over-dense and not at equilibrium with the environment. However, within the limited time of the experiments it is not possible to determine the height at which they will finally settle.

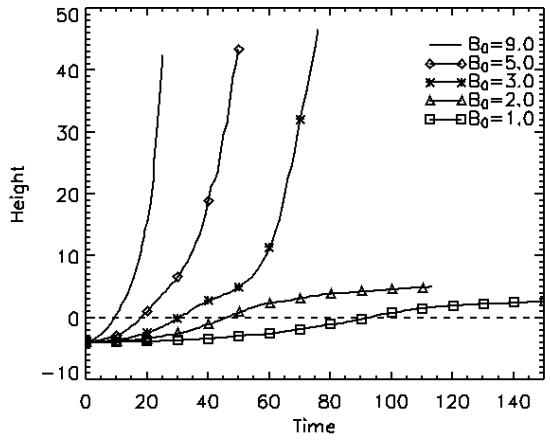

Figure 5.12: The height-time relation of the top of the flux tube for the various cases of B_0.

5.4.3 Expansion in the Atmosphere

As explained in section 5.4.2, only three of the five cases under consideration see the tubes advance beyond the photosphere, namely $B_0 = 3.0$, 5.0 and 9.0 (see figure 5.12). Within this section we will only be concerned with these tubes. Since the tubes experience different magnitudes of buoyancy forces, the crests of the tubes reach the photosphere, and start to advance into the upper atmosphere, at different times. By taking this time difference into consideration, we can make comparisons about the rate of rise of the tops of the tubes. We find that the tube with $B_0 = 9.0$ advances at the fastest rate and the tubes with $B_0 = 3.0$ and $B_0 = 5.0$ rise at the same rate as each other but at a slightly slower rate than $B_0 = 9.0$.

The rise speed of the tube in the atmosphere may be relatively independent of the strength of the tube but the amount of flux transported into the atmosphere is not. To quantify this, we take a horizontal plane at $z = 10$ and measure the amount of unsigned vertical flux intersecting this surface as a function of time. We find that the amount of flux in the atmosphere is directly proportional to B_0 and, by scaling time as $\bar{t} = tB_0$, we find a good agreement between the cases in the rate of the flux entering the upper atmosphere, figure 5.13.

5.5 Group2: Varying α with Fixed B_0

5.5.1 Rise in the Solar Interior

The twist of the magnetic field of a tube results in a tension force acting on the tube. Modifying α, the degree of twist, will alter the tension force and, therefore, change the buoyancy profile of

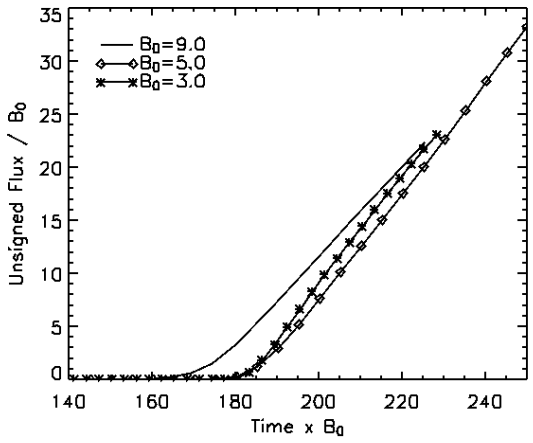

Figure 5.13: The total vertical unsigned flux from the tube, measured at the transition plane ($z = 10$), as a function of rescaled time, $\bar{t} = tB_0$.

the material in the tube. A comparison of the buoyancy profile for tubes with different values of α reveals that, as the value of α is reduced, the region around the axis becomes more buoyant, as shown in figure 5.14. However, the plasma is less buoyant at outer radii due to the smaller magnetic field strength there.

We find that the axis of the tube with the smallest value of α reaches the top of the solar interior in the shortest amount of time, figure 5.15(a). This is because the tube has a larger buoyancy force at the axis and a lower tension force throughout. Given that the axis of the $\alpha = 0.1$ tube is rising the quickest, it could be assumed that the front of this tube will also rise the quickest since the velocity of the material behind gives it momentum. However, figure 5.15(b) shows that there is little difference in the rate of rise of the fronts of the tubes during their rise though the solar interior for the various values of α. These tubes exhibit no clearly quantifiable self-similarity during their rise through the solar interior, unlike the group 1 cases, due to the complicated manner in which the tension force acts upon the tube.

As discussed in section 5.4.1 for the group 1 cases, as the buoyant section of the tube rises it compresses the slower moving material preceding it. This compression causes the field strength at the front of the tube to increase. However, the axial field is simultaneously being reduced due to horizontal expansion during the rise, which will be discussed in detail below. Therefore, the azimuthal field component increase in magnitude to a greater extent than the axial component and the magnetic fieldlines of the tube increase in pitch. Of the tubes under consideration in group 2, the faster rise of the axis of the $\alpha = 0.1$ tube causes this tube to have the shortest distance between its axis and front. Therefore, the field directly above the axis of the tube is compressed to a greater degree than in the two tubes with larger α values. To evaluate this compression we consider the azimuthal field with height at $(x = 0, y = 0)$, which is solely the B_x component of the field. To

5.5 Group2: Varying α with Fixed B_0

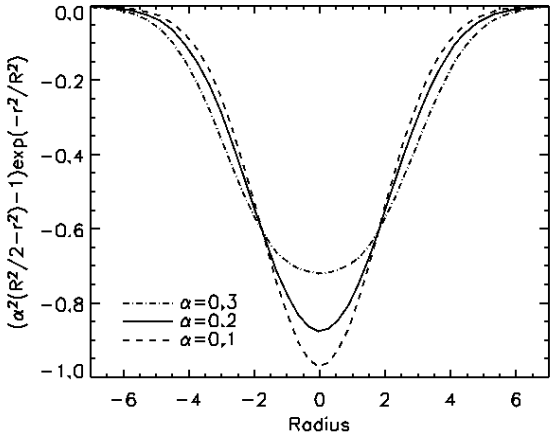

Figure 5.14: From (5.7), a measure of the buoyancy of the tube for the various α cases.

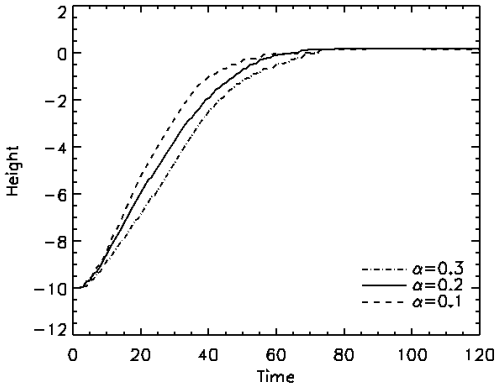

(a) Height of the tube's axis against time.

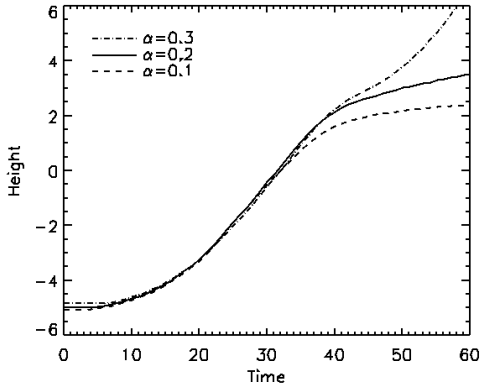

(b) Height of the tube's top against time.

Figure 5.15: Height-time relation of the tube for the various α cases.

make comparisons between the tubes we use a different time for each tube such that the top of the tube is just below the photosphere. Figure 5.16(a) illustrates an 83% increase in the maximum of the azimuthal field for the tube with $\alpha = 0.1$ compared with only 48% and 14% increases for the $\alpha = 0.2$ and 0.3 tubes respectively.

Whilst the azimuthal field is increasing in strength, the field in the axial direction is decreasing in magnitude due to the horizontal expansion experienced by the tube. The magnitude of the B_y component of the field is independent of α at the beginning of the experiments, since all of the tubes in group 2 are chosen to have $B_0 = 2.9$. We find that the decrease in B_y, as a function of the height of the tube, occurs at the fastest rate for the $\alpha = 0.1$ tube. As an illustration of this point, figure 5.17 shows the decrease in B_y, measured at the axis, compared with the height of the axis, z_a. The increased rate of decrease for the $\alpha = 0.1$ tube occurs because this tube has the smallest tension force and, therefore, horizontal expansion is less constrained.

Although the tube with the smallest value of twist has the greatest degree of compression above the axis, the actual magnitude of the azimuthal field, when compared with the other tubes, is significantly smaller. The combination of the smaller azimuthal field and the fastest decreasing axial field results in the magnitude of the magnetic field for the $\alpha = 0.1$ tube being the smallest and the gradient at the rising edge being the least steep, as shown by figure 5.16(c). For the higher α tubes, the increase in the azimuthal field due to the compression allows this field component to become larger than the axial component. Thus it dominates the magnetic profile as the tube approaches the surface, as shown in figures 5.16(a) and 5.16(b).

As already stated, the compression of the field causes the azimuthal component of the tube's field to increase and, therefore, the fieldlines turn further from the axial direction. For example, the smaller size of the azimuthal component of the field for the $\alpha = 0.1$ tube means that the pitch of the fieldlines to the axial direction is smaller. As the crests of the tubes enter the photosphere, the pitch angle of their fieldlines is maintained and, therefore, there are noticeable difference between the horizontal orientation of each tube's fieldlines.

Many studies have shown that the field of an emerging flux tube must be twisted about its axis if it is to rise through the solar interior without suffering distortion. For the values of α being considered here, we find varying degrees of distortion in the shape of the tube. The cases of $\alpha = 0.2$ and 0.3 maintain a radial decrease in the magnitude of the magnetic field for all θ. This is not true for the $\alpha = 0.1$ tube as shown by figure 5.18. The weaker tension force enables material to be dragged from the front of the tube towards the rear, as described by Moreno-Insertis and Emonet (1996). Two side lobes begin to form and further distortion is prevented by the tube's arrival at the photosphere.

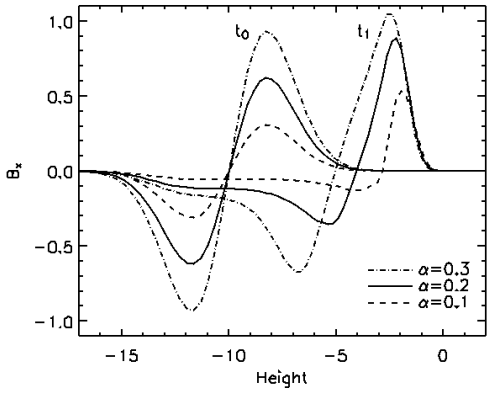

(a) Transverse component of the magnetic field, B_x.

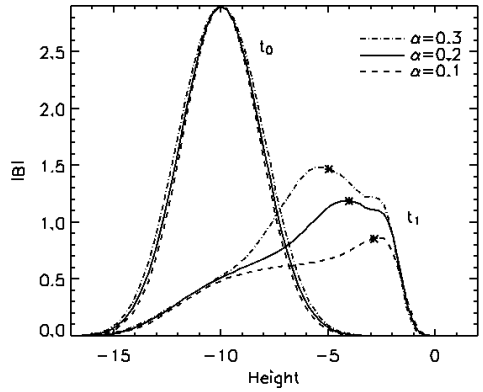

(b) Magnitude of the magnetic field, $|B|$.

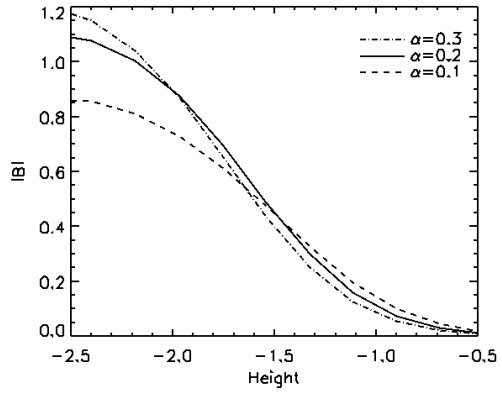

(c) Close-up of (b) for the region between the heights $z = -2.5$ and $z = 0$.

Figure 5.16: Measurements of the magnetic field with height at $(x = 0, y = 0)$ for the various α cases. The three lines labelled by t_0 in (a) and (b) are calculated at $t = 0$. Those labelled by t_1 are at $t = 29$ for $\alpha = 0.1$ and $t = 28$ for $\alpha = 0.2$ and 0.3. At these times the tops of the tubes are just approaching the photosphere. The stars on (b) indicate the height of the axes of the tubes at t_1.

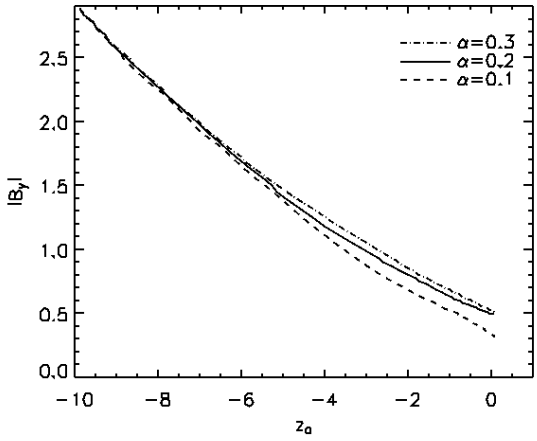

Figure 5.17: The decrease in the B_y component of the field at the axis plotted against the height of the axis, z_a, for the various α cases.

5.5.2 Emergence into the Photosphere

Once the top of the tube reaches the photosphere, it is forced to advance at a slower pace due to the change in stratification. As discussed in section 5.4.2, it is possible to lift over dense material into the atmosphere via the magnetic buoyancy instability. The values of α under consideration here give three different types of behaviour when the tops of the tubes reach the bottom of the photosphere. We find that the tube with $\alpha = 0.1$ fails to emerge into the upper photosphere, as shown in figure 5.19. However, the two tubes with larger values of α do emerge but with different configurations to each other.

For the $\alpha = 0.3$ tube, it is the central portion of the tube in the axial direction which emerges first, giving rise to a dome shaped emerging front, figure 5.20(a). The $\alpha = 0.2$ tube exhibits a different emergence pattern. Portions of the tube either side of the central section lead the emergence into the upper photosphere, figure 5.20(b). This result has undergone convergence testing in a domain twice the size in the horizontal directions but with the same grid spacing and in a domain the same size with 50% more gridpoints in the horizontal directions. The matching results of these tests confirm that the double emergence is not a boundary or numerical artifact. For $\alpha = 0.1$, we find that the tube does not emerge into the atmosphere and flattens out in a pancake shape at the solar interior photosphere interface, figure 5.20(c).

The evolution of each individual tube is determined by the magnetic buoyancy instability criterion, (5.15). Figure 5.16(c) shows that the field at the front of the $\alpha = 0.3$ tube has the steepest gradient when it reaches the photosphere. Additionally, the stronger field means the plasma-β is smaller for the $\alpha = 0.3$ tube both initially and when it arrives at the photosphere. Thus, (5.15) is easily satisfied at the crest of the tube and the emergence proceeds.

5.5 Group2: Varying α with Fixed B_0

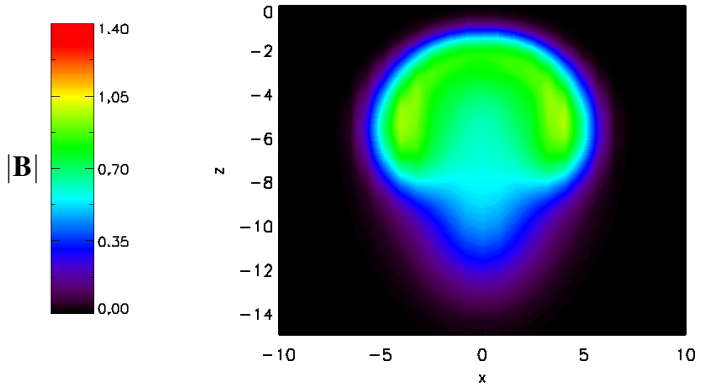

(a) $\alpha = 0.1$ case.

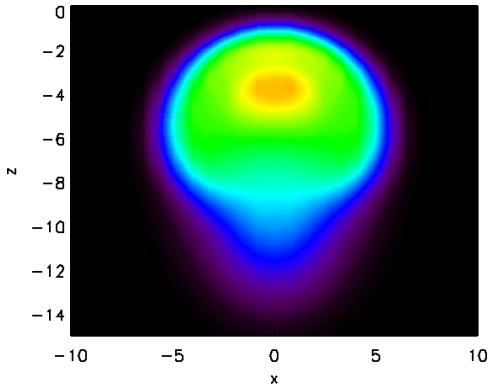

(b) $\alpha = 0.2$ case.

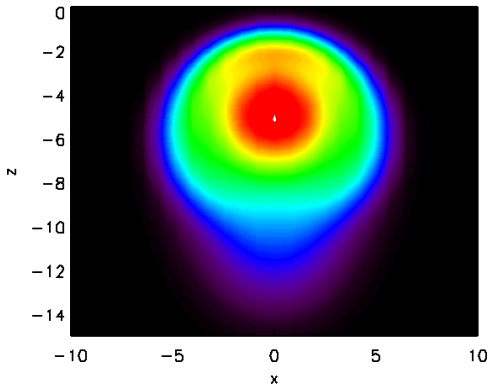

(c) $\alpha = 0.3$ case.

Figure 5.18: Contours of the magnitude of the field strength of the tube, $|\mathbf{B}|$, viewed in the transverse cross-sectional plane $(y = 0)$ at time $t = 30$ for the various α cases.

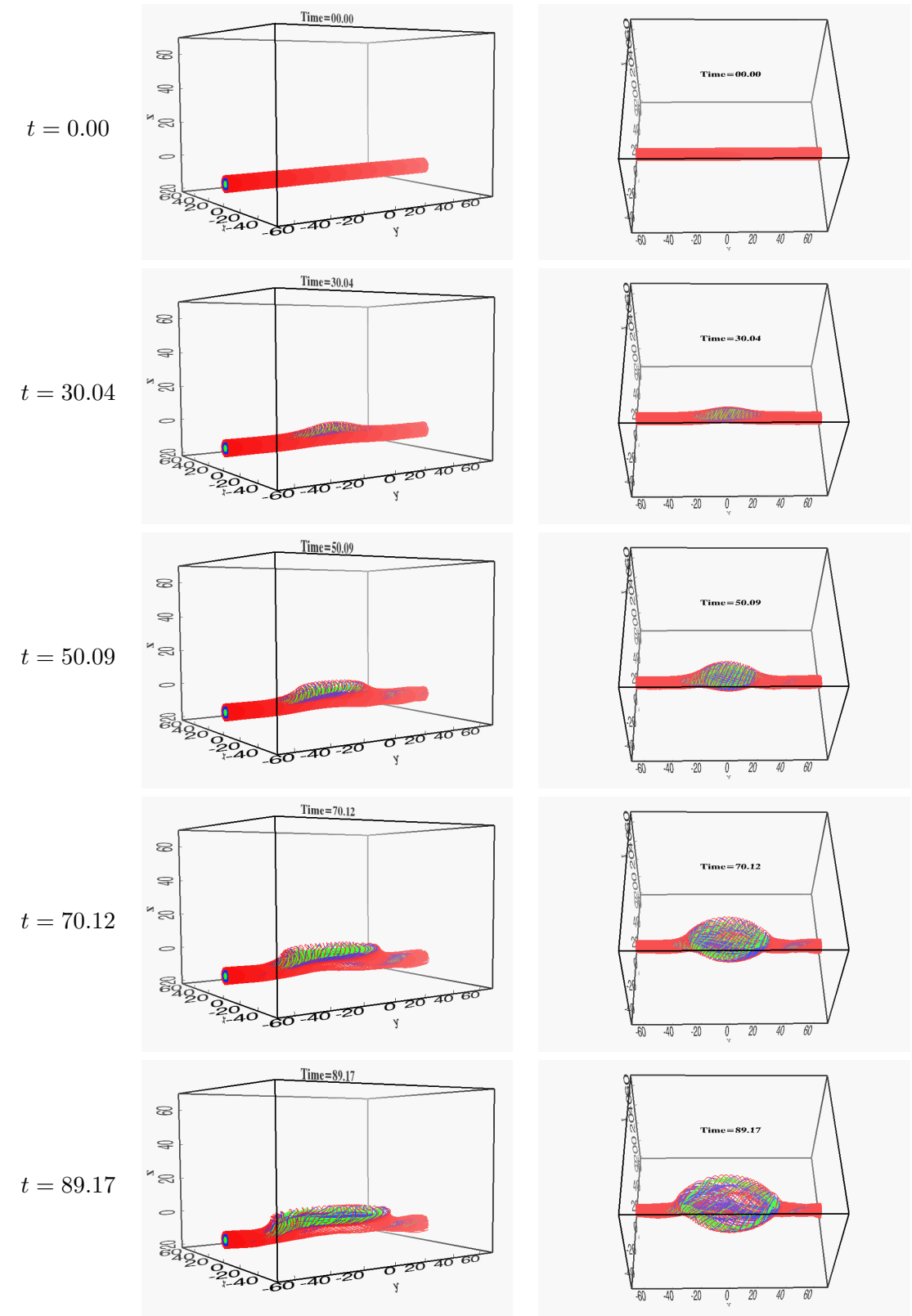

Figure 5.19: Fieldlines (red, blue, green) traced from the one end of the tube at several different times and from two different viewpoints. The tube shown here has parameters $B_0 = 2.9$ and $\alpha = 0.1$. The tube remains trapped in the photosphere and flattens out.

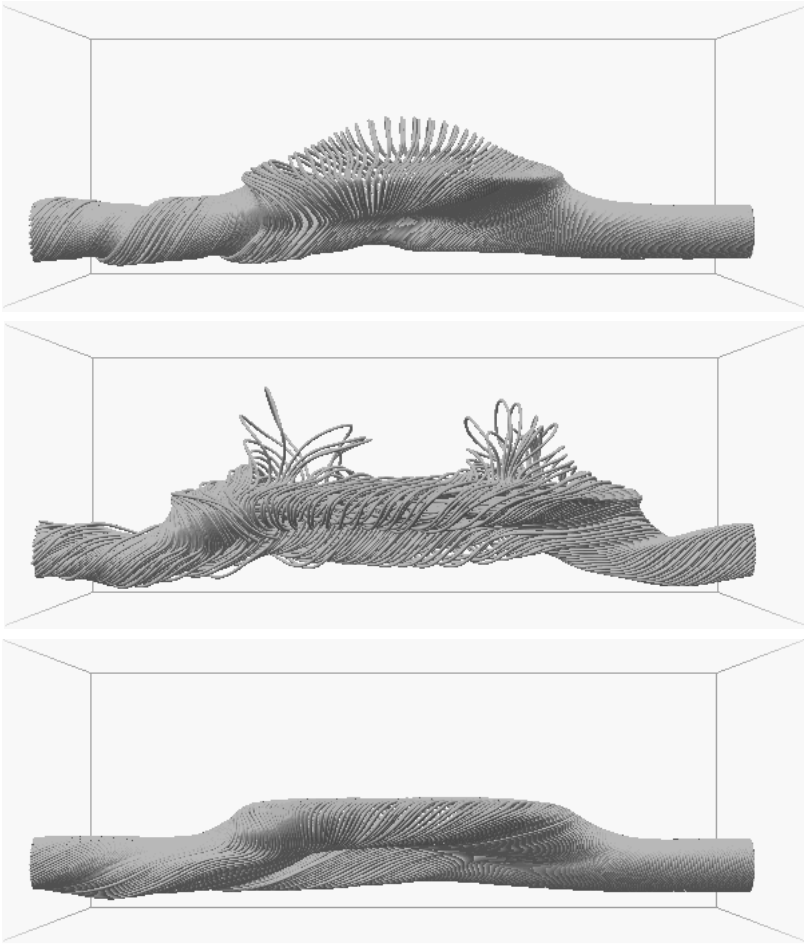

(a) $\alpha = 0.3$ at $t = 65$.

(b) $\alpha = 0.2$ at $t = 104$.

(c) $\alpha = 0.1$ at $t = 70$.

Figure 5.20: Axial view of the outer fieldlines of the flux tube for the various α cases.

The strength of the field is greatly reduced for the $\alpha = 0.1$ tube and it has the least steep field gradient at its front. The front of this tube also does not rise as high into the photosphere as the other two cases and, therefore, the external gas pressure remains slightly higher and the plasma-β cannot be reduced by this secondary route. The combination of these two effects results in this tube not being able to emerge into the atmosphere.

For $\alpha = 0.2$, the tube front reaches the same height as the $\alpha = 0.3$ case and, therefore, experiences the same external gas pressure. However, the plasma-β does not fall as low as for the $\alpha = 0.3$ tube because the field strength of the tube is smaller. Figure 5.21(a) shows that the field compression and convective terms of the buoyancy criterion, (5.15), are practically equal at the central location. However, with the inclusion of a value of 0.05 for the rightmost term of (5.15) divided by the plasma-beta at the top of the tube, the buoyancy criterion is not satisfied. To understand why emergence is possible at the two side locations for this tube, we measure the quantities comprising (5.15) at these locations, namely $(x = 0, y = -19)$ and $(x = 0, y = 20)$.

At the height where we find the instability occurs, namely $z = 2.7$, we find that the magnitude of the magnetic field takes the same value at all three locations, as shown by figure 5.22. The gas pressure at this height is also very similar for all three locations and, therefore, there is little variation in the value of the plasma-β at $z = 2.7$.

Additionally, we find no variation in the gradient of the magnitude of the field at $z = 2.7$ at the three locations although there is variation both at lower and higher heights. The gradient in the gas pressure is marginally steeper for these two side locations around the height where the instability takes hold, thus the pressure scale height, H_p, is smaller than in the central location. The smaller pressure scale height results in the left-hand term of (5.15) being smaller at $z = 2.7$ for the two side locations, as confirmed by figures 5.21(a), 5.21(b) and 5.21(c).

Figures 5.21(a), 5.21(b) and 5.21(c) identify that the convective term, right-hand term of (5.15), is smaller at the two side locations. This term is controlled by the gradient in the logarithmic temperature and, since temperature is defined by gas pressure and density via the ideal gas law, we can determine why the convective term varies by considering these alternative quantities. Above we have stated that the gas pressure takes the same values for the three locations at a height of $z = 2.7$ and that there is little variation in the gradient of the gas pressure, thus we turn our attention to the density.

For all of the tubes in groups 1 and 2, we find downflows along the outer most fieldlines when the tube top flattens out at the photosphere, as indicated by the black arrows in figure 5.23(a) for the $\alpha = 0.2$ case. For the tubes whose central portion emerges into the atmosphere, these downflows are maintained due to the draining of plasma as the tube expands into the atmosphere. However, for the tubes that do not undergo the buoyancy instability at $y = 0$, we find the draining at this central location ceases as the field here continues to flatten. As the rest of the tube continues to rise

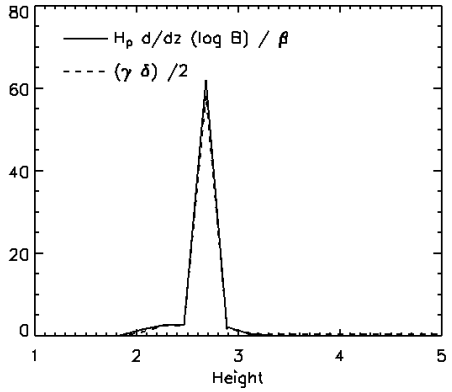

(a) Measurements in height at $(x = 0, y = 0)$ at $t = 60$.

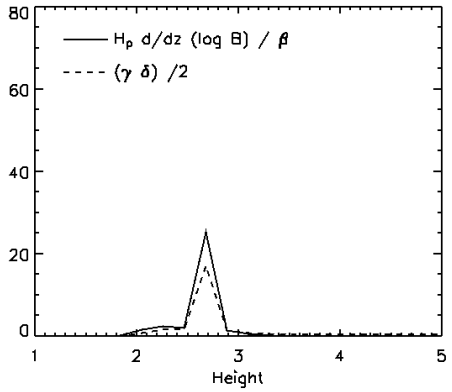

(b) Measurements in height at $(x = 0, y = -19)$ at $t = 71$.

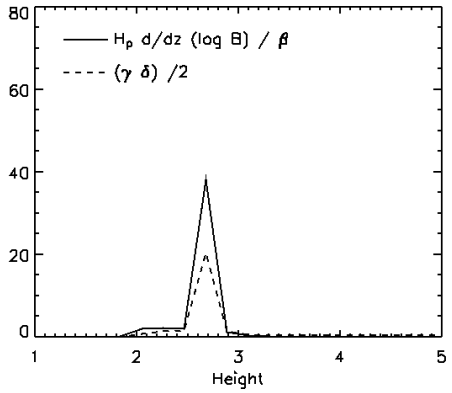

(c) Measurements in height at $(x = 0, y = 20)$ at $t = 72$.

Figure 5.21: The left-hand side and first right-hand side terms of (5.15), divided by the plasma-β, for the $\alpha = 0.2$ case measured at three separate locations.

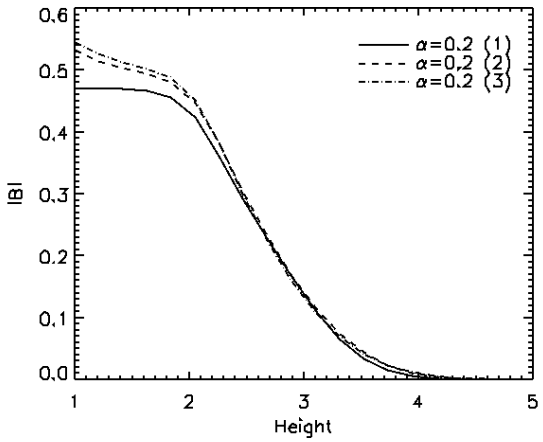

Figure 5.22: The magnitude of the magnetic field in height for the $\alpha = 0.2$ case measured at three separate locations. In the figure's key, the labels (1), (2) and (3) correspond to the locations $(x = 0, y = 0)$, $(x = 0, y = -19)$ and $(x = 0, y = 20)$ respectively. The measurements are taken at $t = 60$, 71 and 72 for locations (1), (2) and (3) respectively.

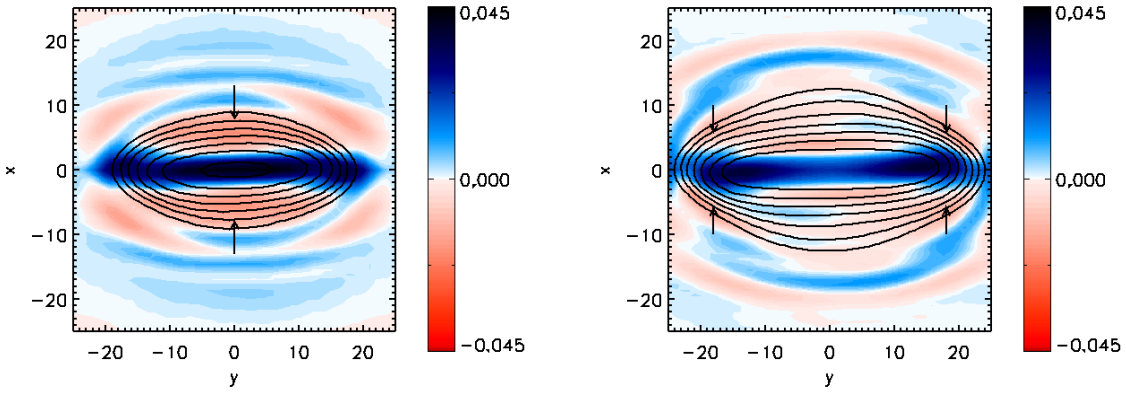

(a) $t = 50$. (b) $t = 58$.

Figure 5.23: Red-blue scale map of vertical velocity measured in the horizontal plane at a height of $z = 1.8$ for the $\alpha = 0.2$ tube at two different times. The colouring in both (a) and (b) is scaled such that dark blue indicates a maximum upflow of $v_z = 0.045\ H_{\rm ph}\ t_{\rm ph}^{-1}$ and bold red indicates a maximum downflow of $v_z = -0.045\ H_{\rm ph}\ t_{\rm ph}^{-1}$. The black elliptical contours are of $|\mathbf{B}|$ and give the location of the tube, which dissects the plane. The black arrows indicate specific regions of downflow within the tube itself.

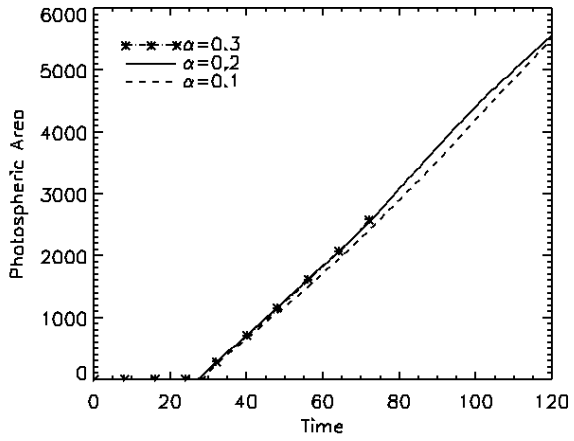

Figure 5.24: Measurements of the area of the photospheric plane $(z = 0)$ containing flux from the emerging tube for the various α cases as a function of time.

up to the photosphere, the location of the draining moves outwards in the positive and negative y directions and reduces in intensity. The black arrows in figure 5.23(b) identify the shift in draining locations over a period of 8 time units for the $\alpha = 0.2$ case. The twisted nature of the tube's field means the plasma drained around $y = 0$ accumulates in the troughs of the fieldlines in the centrally risen portion of the tube. However, the plasma draining around $y = \pm 20$ sinks down to the foot-points of the Ω-loop in the solar interior where we find an accumulation of dense plasma.

At the times considered in figures 5.21(a), 5.21(b) and 5.21(c) for the $\alpha = 0.2$ tube, we find that there is a greater difference between the density at the top of the tube and the environment in the central location than at the two side regions. The enhanced reduction in density in the central portion occurs since the draining is occurring at a faster rate here. At a height of $z = 2.7$, the gradient in the density at the two side locations is larger thus the convective term is smaller here. Hence, emergence ensues at the two side locations as a result of the marginal variations in the gas pressure gradient and the larger variations in the density gradient.

Independent of whether or not the tubes of the group 2 cases emerge, we find the evolution of the tubes has several common properties. Firstly, the slow down in the rise speed of the crest of the tube, as it approaches the photosphere, forces the vertically rising plasma in the remainder of the tube to spread out horizontally at the photosphere. Figure 5.24 shows that the growth of the photospheric area containing flux from the tube occurs at a rate that is mostly independent of α. This comparable rate of coverage occurs because the tops of the tubes rise through the solar interior with the same speed and all of the tubes experience a similar braking effect upon reaching the photosphere, as discussed in section 5.5.1. Secondly, regardless of the amount of twist in the tube, the axes of the tubes tend to the same height, namely $z = 0$.

5.5.3 Expansion in the Atmosphere

As stated in section 5.5.2, only two of the three tubes in the group 2 cases emerge above the photosphere and these have values of $\alpha = 0.2$ and $\alpha = 0.3$. In this section we will be considering just these two cases.

We find that although the tops of the tubes reach the photosphere at the same time, the tube with $\alpha = 0.2$ spends longer in the photosphere while waiting for the buoyancy instability to occur, as shown in figure 5.25. Results from a simulation by Archontis et al. (2005) fit well with the height-time relation shown here. Their study considered an emerging tube with $\alpha = 0.4$ but all other tube parameters remain the same as those used in this series of simulations. Independent of the value of α the tube reaches the base of the photosphere at a time $t \sim 30$ and, as expected, the $\alpha = 0.4$ tube reaches the transition region at an earlier time, $t \sim 60$. The top of this tube spends less time in the photosphere since it experiences a greater degree of compression of the magnetic field at the tube front and, therefore, the buoyancy instability occurs at an earlier time.

We now return to the $\alpha = 0.2$ and $\alpha = 0.3$ tubes. Taking into account the different lengths of time the tops of the two tubes spend waiting for the buoyancy instability to develop, we find that once the highest emerging point of the tubes reaches the transition region the further rise of this point to the lower corona occurs at the same rate. To quantify the emergence of flux into the atmosphere we consider a horizontal plane at the start of the transition region, $z = 10$. A comparison of the area of this plane containing flux from the tube, figure 5.26(a), identifies that when the tops of the tubes are at the same height within the transition region the same sized area of the plane is occupied. However, as the tubes enter the mid-corona, a height of $z \sim 27$, we see a difference in both the rise rate of the top of the tube and the size of the transition region plane occupied by flux.

For the $\alpha = 0.2$ tube there comes a time when the boundaries of the two emerging domes will come into contact with each other and this occurs when the domes have reached a height of $z \sim 27$ at 104 time units. At this time we see a plateau in the rise of the tube, which occurs while the domes expand horizontally to fill any gaps left between themselves at the touching boundaries. After this, the rise continues at a similar rate to that of the tube rising through the transition region and the rise of the $\alpha = 0.3$ tube. However, the area of the transition region plane containing tube flux is now significantly higher for the $\alpha = 0.2$ tube and, although the areas occupied by flux increase with height at the same rate for both the tubes as they continue to rise through the mid-corona, once the tubes reach a height of $z \sim 35$ the area occupied by the $\alpha = 0.3$ tube is just 62% that of the $\alpha = 0.2$ tube. Although the highest point of the tubes are rising at the same rate, the difference in the occupied area of the plane occurs because the emergence of the $\alpha = 0.2$ tube is being driven from two locations in comparison to just one for the higher α tube. We note that the difference in the area is almost half and, therefore, conclude that the rates of expansion of the two emerging

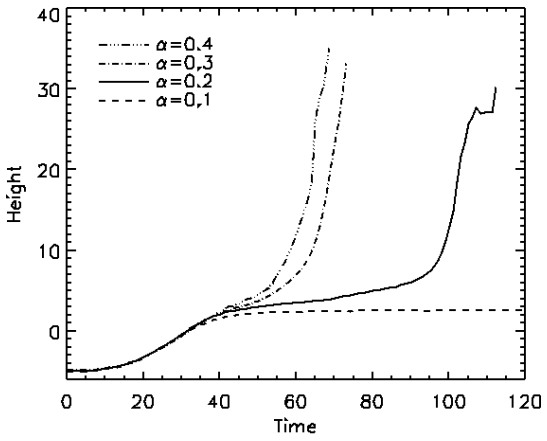

Figure 5.25: Height-time function of the top of the tube for the various α cases. The triple-dot dashed line giving information for the $\alpha = 0.4$ case is a result obtained in a simulation by Archontis et al. (2005) where a tube emerges into an unmagnetised corona.

fronts of the $\alpha = 0.2$ tube are practically the same as that of the single front of the $\alpha = 0.3$ tube.

Figure 5.26(b) shows that the total unsigned flux emerging into the atmosphere, measured at the transition region plane, occurs at a faster rate for the tube with $\alpha = 0.3$ even though the tops of the emerging domes, one in the case of $\alpha = 0.3$ and two for $\alpha = 0.2$, are rising into the atmosphere at the same rate. When the field was at the photosphere, the magnetic strength was smaller for the $\alpha = 0.2$ tube, thus the field being transported into the atmosphere is also weaker and this manifests itself as a slower rate of increase in the total unsigned flux.

5.6 Conclusions

In this chapter, we have presented results from 3D MHD simulations of buoyant flux tubes rising through the solar interior and emerging into the atmosphere. We have varied the values of two of the parameters defining the magnetic structure of the flux tube, namely the magnetic field strength, B_0, and the twist of the tube's field, α. Our aim was to understand the individual effect of each on the emergence process and draw conclusions as to the robustness of the results of previous flux emergence simulations.

When varying the magnetic field strength of the tube, we have found self-similarity in the tube's evolution. When the difference in the strengths of the tubes is taken into consideration, we find that the rise time through the solar interior, the increase in the area of the photospheric plane containing flux from the tube, and the increase in unsigned flux into the atmosphere each occur at the same rate for all the tubes. The velocity and magnetic strength of the axes of the tubes also show self-

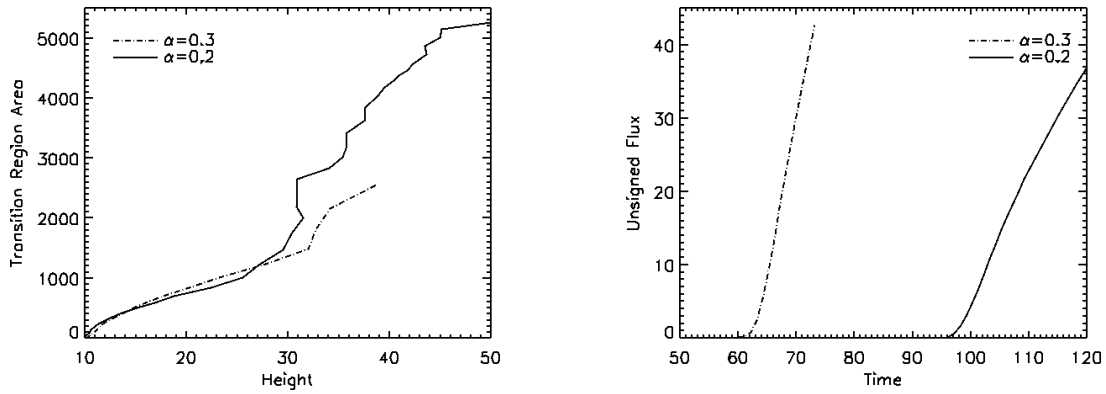

(a) Area of the plane containing flux from the tube.

(b) Total unsigned vertical flux from the tube passing through the plane.

Figure 5.26: Measurements of flux taken at the transition region plane ($z = 10$) as functions of time.

similar behaviour with dependence upon B_0 being easily removed with appropriate scaling. Over the initial rise period the decrease in the strength of the axes of the tubes is described reasonably well by the thin flux tube approximation.

We find that if the magnetic field strength of the tube is initially too small, the magnetic buoyancy instability does not occur when the tube reaches the top of the solar interior and, therefore, it is not possible for the tube to expand into the atmosphere. The magnetic buoyancy instability criterion (5.15) is valid when considering a static equilibrium situation and is not strictly applicable when the tube is rising, as in our cases. However, in this study the stronger tubes have only small vertical velocities associated with them ($\mathbf{v} \ll$ Alfvén speed) and so the criterion holds approximately. We have shown that it correctly predicts which tubes will emerge and which will not by checking the relative sizes of the magnetic and convective terms, thereby justifying its use.

We find that the case with $B_0 = 9.0$ exhibits different behaviour to the other tubes and fits less well with the self-similar advancement of the tubes. When this tube is initialised in the upper layers of the solar interior the plasma-β of the material in the tube is considerable lower than the other cases due to the large magnitude of the tube's magnetic field. There is over two orders of magnitude difference between the plasma-β of the $B_0 = 9.0$ and $B_0 = 1.0$ tubes. We believe that the lower plasma-β in the $B_0 = 9.0$ case, a value of only 0.9 at the axis, causes this tube's evolution to be dominated by the magnetic forces whilst the gas pressure and density play a more active role in determining the progression of the other tubes.

The variation in the twist of the flux tube does not result in such clearly quantifiable self-similar behaviour during the rise through the solar interior. The lower value of twist for the $\alpha = 0.1$ tube allows for distortion in the shape of the tube during its rise and, thus, when it approaches the

photosphere the field is too weak to enable the buoyancy instability to occur. This tube can only flatten out in the lower photosphere and does not advance into the upper atmosphere. The usual pattern of emergence, led from the crest of the tube, is seen for the higher twist tube. For the first time, we see emergence of a buoyant flux tube occurring away from the crest of the tube for a value of twist that is neither too weak nor too strong. The emergence of flux from the $\alpha = 0.2$ tube at two side locations occurs as a result of draining of plasma from the upper part of the tube. This may suggest that flux tubes with weaker magnetic magnitude, but which are more highly twisted, may be able to emerge through a similar process of draining.

Although we see multiple differences when the twist of the flux tube is varied, we also see several similarities between the experiments. The rate of expansion of the tube at the photosphere and the rate of expansion of any emerging tube sections each occur at similar rates.

Our results reveal that in the cases where emergence does occur, the general results from previous emergence simulations are robust. Emergence occurs due to a magnetic buoyancy instability and the flux expands both horizontally and vertically into the atmosphere. With the exception of the $\alpha = 0.2$ case, whose results appear to be non-generic and highly dependent on the twist and radius parameters, emergence develops from a single central region. Comparison of speed and flux values from simulations with atmospheric observations should be made carefully since we have shown that these are highly dependent on the initial magnetic field strength and twist parameters chosen for the seed flux tube.

Our results also raise several further questions relating to the previous emergence studies. In the experiments of this chapter the atmosphere is unmagnetised but this is certainly not the case with the Sun's corona. How would the faster rise of the stronger flux tubes affect the reconnection between two correctly aligned flux systems? Would reconnection between a magnetised atmosphere and a tube be complicated by flux emerging at two locations from the tube? Flows in the photospheric domain have been shown to propagate through to the corona (Ryutova and Shine 2006) so would the variation in rise speed of the emerging subphotospheric flux cause variations in the corona?

Investigation of these issues is beyond the scope of this chapter but they illustrate that further modelling of flux emergence from the solar interior into the atmosphere will be key to obtaining a better understanding of the dynamic, complicated, and visible processes occurring in the Sun's atmosphere.

Chapter 6

Effects of Non-Constant Twist

Of the emerging flux tube simulations presented in chapter 2, fifteen out of nineteen chose the seed flux to be either a Gold-Hoyle or constant twist flux tube. The classification of these previous simulations according to the type of twist of their flux tube is given in table 6.1. The simulations that use non-constant twist flux tubes transport the flux into the atmosphere kinematically and are concerned only with the subsequent development of the coronal magnetic field. Thus, to date, there have been no self-consistent models of flux emergence where the flux tube has not been initially prescribed with constant twist. There is no reason to assume that flux tubes formed in the solar interior should have constant twist and, therefore, in this chapter we will investigate whether changing the twist of the tube to be non-constant modifies the emergence process.

In section 6.1, we will consider the existing literature relating to this topic. We will consider the observational evidence that indicates flux tubes exist in a twisted state prior to emergence and a parameter study of non-constant twist flux tubes rising through the solar interior.

We will introduce the non-constant twist profiles in section 6.2 and the details of our domain model in section 6.3. We will be testing two different flux tube profiles that give decreasing and increasing twist with radius. For each of these profiles, we will also perform a parameter study in order to understand the importance of the rate of change of the twist with radius.

In sections 6.4, 6.5 and 6.6, we will present the results from simulations that use flux tubes with the two different twist profiles as the seed magnetic field. In particular, we will highlight the similarities and differences of the rise in the solar interior and the emergence process that are consequences of the twist profiles and their associated parameter spaces.

Finally, in section 6.7 we will outline our conclusions and consider these in the context of the robustness of simulation results to date.

Gold-Hoyle	Constant Twist	Non-Constant Twist
Magara (2001)	Archontis et al. (2004)	Fan (2005)
Magara (2004)	Archontis et al. (2005)	Fan and Gibson (2003)
Magara (2006)	Archontis et al. (2006)	Fan and Gibson (2004)
Magara and Longcope (2001)	Archontis et al. (2007)	Gibson and Fan (2006)
Magara and Longcope (2003)	Fan (2001)	
	Galsgaard et al. (2005)	
	Galsgaard et al. (2007)	
	Leake and Arber (2006)	
	Manchester et al. (2004)	

Table 6.1: Classification of the previous emerging flux tube simulations according to the flux tube's type of twist.

6.1 Existing Literature

It is widely believed that, prior to emerging, the subsurface flux is concentrated into some type of twisted and intertwined rope structure. The observational evidence in support of the theory that flux ropes existing in a sheared state pre-emergence has developed substantially since it was first proposed (Babcock 1961; Piddington 1975). The evidence is as follows:

1. The orientation of newly emerging field changes with respect to the polarity inversion line of the active region (Frazier 1972; Lites et al. 1995; Schmieder et al. 1996). The first loops to emerge are perpendicular to this line, while the orientation of successively emerging loops appears to rotate such that the final loops are practically parallel to the inversion line. The polarity inversion line itself does not rotate but the changing loop orientation follows from the separation of the strongest magnetic field concentrations over time in directions parallel to the inversion line. The rate at which the loops rotate is far greater than typical photospheric motions of ~ 0.5 km s^{-1} (Lites et al. 1995) and flows around sunspots are radially outwards over the moat rather than rotational (Piddington 1981).

2. There is no significant delay between the emergence of the new field and the detection of currents in the photosphere (Leka et al. 1996). Thus, the current must be associated with the field before it emerges since motions in the photosphere would take too long to tangle the field and generate the current.

3. Comparisons of Hα and X-ray structures with potential (Leka et al. 1996) and linear force-free (Schmieder et al. 1996) field extrapolations do not agree, indicating that the emerging field is in a non-potential state.

All of these points strongly support a model in which the field of the rope is twisted prior to its arrival in the photosphere.

To date, there have been no observational studies carried out that give any indication as to the expected nature of the twist in the flux tube prior to its emergence. We know that the orientation of the fieldlines must move away from the axial direction of the tube with increasing radius to comply with observations, but the rate of the change of this orientation with respect to radius has not yet been determined. Thus, simulations of emerging flux have considered constant twist flux tubes for simplicity and to aid comparison between experiments. The general results of these constant twist emergence simulations were discussed in chapters 2 and 5. From the new results in chapter 5, we know that as a flux tube with low twist rises through the solar interior it will suffer from distortion and, thus, will not be susceptible to the buoyancy instability upon entering the photosphere.

There is no reason to assume that a flux tube formed in the solar interior will have constant twist and, therefore, in this chapter we will be investigating the emergence process of non-constant twist flux tubes. By modifying the twist of the tube to be non-constant with respect to radius, we will also be affecting the size of the tension force in the tube. This will be discussed in more detail in section 6.2. Hughes et al. (1998) have carried out a study of constant twist flux tubes rising through the solar interior in comparison with non-constant twist tubes. They found that, in the latter case, the maximum strength of the tube's transverse field needed to prevent distortion was smaller. For the levels of twist we will be considering, we do not expect to find the distortion described by Hughes et al. (1998), which results in the tube developing side lobe structures. The results from this study will be discussed further in section 6.4 when we present the results from our non-constant twist simulations.

6.2 Defining the Non-Constant Twist Profiles

We choose to define the magnetic field of the flux tube using the field given in chapter 5. In the cylindrical coordinate system, (r, θ, y), this was given by $\mathbf{B} = (B_r, B_\theta, B_y)$, where

$$B_r = 0, \tag{6.1}$$

$$B_\theta = \alpha r B_y, \tag{6.2}$$

$$B_y = B_0 e^{-r^2/R^2}. \tag{6.3}$$

In chapter 5, B_0, R and α were constants and the parameter spaces of B_0 and α were independently investigated. Here, we choose $B_0 = 3.0$ and $R = 2.5$ for all of the experiments within this chapter. Hence, the axial component of the tube's magnetic field, B_y, will be the same in all of the simulations at $t = 0$.

α_1		α_2	
$k_1 = \{1.75$	(blue solid),	$k_2 = \{1.0$	(red solid),
2.5	(blue dashed),	1.75	(red dashed),
5.0	(blue dot-dashed),	2.5	(red dot-dashed),
10.0	(blue triple dot-dashed),	5.0	(red triple dot-dashed)$\}$
10000.0	(black solid)$\}$		

Table 6.2: Summary of the k_1 and k_2 parameter spaces under investigation and information regarding the line used to represent each in the figures of this chapter.

As discussed in section 1.3.3, the twist of the flux tube is given by

$$\Phi = \frac{B_\theta}{r\, B_y}, \tag{6.4}$$

and, using (6.2) and (6.3), we have $\Phi = \alpha$. In order to create a non-constant twist profile with radius, α must be a function of r. We will be investigating two different profiles given by the functions α_1 and α_2, where

$$\alpha_1(r) = c\exp(-r^2/k_1^2), \tag{6.5}$$

$$\alpha_2(r) = c(1-\exp(-r^2/k_2^2)). \tag{6.6}$$

α_1 and α_2 give twist profiles that decrease and increase with radius, respectively. We choose $c = 0.5$ and will be investigating the parameter spaces of k_1 and k_2.

The values of k_1 and k_2 determine the rate of change of the twist with radius. As $k_1 \to \infty$ and $k_2 \to \infty$, we retrieve the constant twist profiles with $\alpha_1 = 0.5$ and $\alpha_2 = 0.0$ respectively. On the other hand, as $k_1 \to 0$ and $k_2 \to 0$, δ functions develop at the axis that give $\alpha_1 = 0.5$ and $\alpha_2 = 0.0$ there and $\alpha_1 = 0.0$ and $\alpha_2 = 0.5$ everywhere else. If the grid spacing was such that the axis fell in between two gridpoints, then it may be possible to obtain numerically what appear to be constant twist profiles for $\alpha_1 = 0.0$ and $\alpha_2 = 0.5$.

Table 6.2 summaries the values of k_1 and k_2 under consideration in this chapter and figure 6.1 illustrates the twist profiles of α_1 and α_2 for these values of k_1 and k_2.

In the case of α_1, the values of $k_1 = 1.75$ and 2.5 result in the fieldlines at the periphery of the tube being untwisted, while all values of k_2 for α_2 result in the fieldlines around the axis being untwisted. Untwisted fieldlines allow for the distortion of the tube as it rises through the solar interior and the severity of the distortion in these cases will be discussed in section 6.4. It can be seen that a value of 10000.0 for k_1 is sufficiently large to yield a constant twist profile for α_1. We will use this case as the common case against which to make comparisons between the two twist profiles.

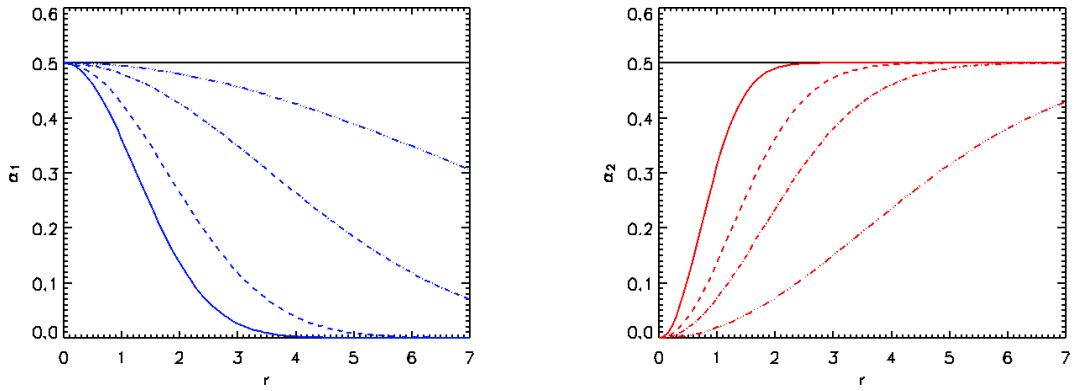

(a) α_1 cases.

(b) α_2 cases.

Figure 6.1: Non-constant twist profiles, α_1 and α_2, as functions of radius for parameter spaces k_1 and k_2 respectively.

Although the twist profiles look sufficiently different to each other, the B_θ component of the magnetic field is relatively similar, as shown in figure 6.2. Considering (6.2), we can see that this similarity is due to the scaling with r, which gives $B_\theta = 0$ at the axis, and the Gaussian B_y component, which gives a smooth decrease to $B_\theta = 0$ at the edge of the tube.

The tension force of a magnetic field is given by $(\mathbf{B} \cdot \nabla)\,\mathbf{B}/\mu$. Using (6.1), (6.2) and (6.3), we find that the tension force of the tube acts radially inwards with magnitude ${B_\theta}^2/\mu r$. This is dependent on the form of α and, thus, in both the k_1 and k_2 parameter spaces we can divide the cases into two categories, namely low and high tension. We note that for increasing values of k_1 and decreasing values of k_2, the flux tubes have increasingly strong tension forces. For example, the lower tension cases are given by $k_1 = 1.75, 2.5$ and $k_2 = 2.5, 5.0$. If the tension is sufficiently low in these cases then we would expect to see some distortion to the shape of the tube during its rise through the solar interior and, upon reach the photosphere, the flux may fail to initiate a magnetic buoyancy instability.

When discussing the results from the simulations, in addition to considering the two profiles individually, we will divide the simulations generally into cases with an initially low or high tension force, as specified above. In this way, we hope to be able to identify the individual properties of the tube's field that are important for emergence rather than specific to the individual twist profiles. When referring to the high and low tension cases, the word "initially" will be omitted but it is implied unless otherwise stated.

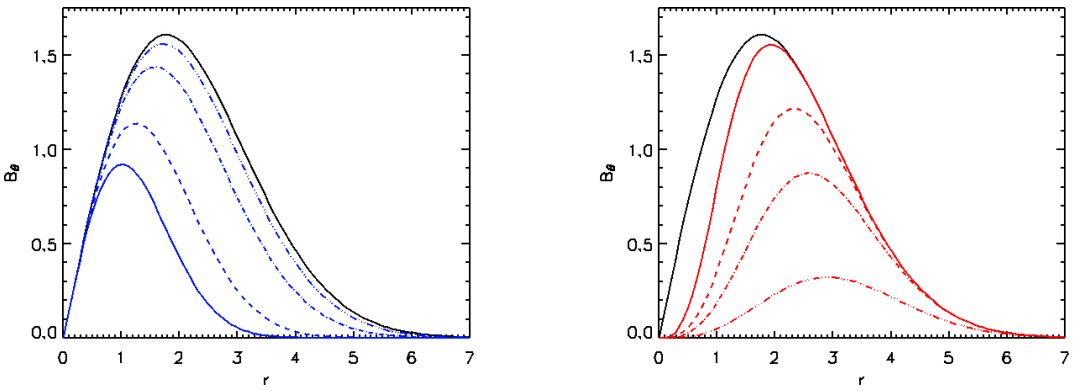

(a) α_1 cases.

(b) α_1 cases.

Figure 6.2: Azimuthal component of the magnetic field, B_θ, as a function of radius.

6.3 Placement of the Tube within the Hydrostatic Solar Interior

For all of the simulations in this chapter, we choose to copy the setup of the domain and the location of the tube from chapter 5. Please refer to section 5.2 for the description.

The axis of the flux tube is initially set at a height of $z = -10$, positioning it within the solar interior. By changing the twist to be a function of radius, we have modified the magnetic forces within the tube from those given in chapter 5. We must, therefore, re-evaluate the gas pressure inside the tube if we are to achieve radial force balance at $t = 0$ and prevent a sudden radial expansion or compression of the tube once the simulation begin.

As before, we define the gas pressure inside the tube to be $p_i = p_e + p_{exc}$, where p_e is the external gas pressure and p_{exc} is the pressure excess given by solving

$$\frac{dp_{exc}}{dr} = (\mathbf{J} \times \mathbf{B})_r \,. \tag{6.7}$$

Integrating this with respect to r and setting the constant of integration to zero yields

$$p_{exc\,1} = \frac{1}{2\mu} \left\{ {\alpha_1}^2 \left(\frac{{d_1}^2}{2} - r^2 \right) - 1 \right\} {B_y}^2, \tag{6.8}$$

$$p_{exc\,2} = \frac{1}{2\mu} \left\{ {\alpha_2}^2 \left(\frac{{d_2}^2}{2} - r^2 \right) - 1 + c^2 \left(\frac{R^2}{2} - \frac{{d_2}^2}{2} - 2 \left(\frac{R^2 {d_2}^2}{R^2 + {d_2}^2} - \frac{{d_2}^2}{2} \right) \exp\left(-r^2/{k_2}^2\right) \right) \right\} {B_y}^2, \tag{6.9}$$

where $p_{exc\,1}$ and $p_{exc\,2}$ correspond to the integration of (6.7) with α_1 and α_2 substituted into B_θ

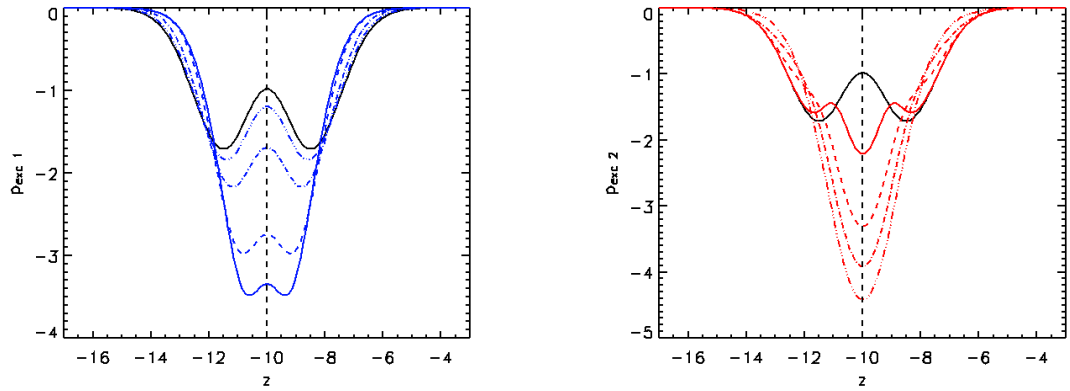

(a) α_1 cases.

(b) α_2 cases.

Figure 6.3: Pressure excess, p_{exc}, at $t = 0$, measured at $(x = 0, y = 0)$. The vertical dashed line at $z = -10$ indicates the location of the axis in all cases.

respectively. The new constants are defined as

$$d_1{}^2 = \frac{R^2 k_1{}^2}{R^2 + k_1{}^2}, \tag{6.10}$$

$$d_2{}^2 = \frac{R^2 k_2{}^2}{R^2 + k_2{}^2}. \tag{6.11}$$

Figure 6.3 shows the variation in the pressure excess for α_1 and α_2 for the various values of k_1 and k_2. The tubes with a lower tension force have a lower pressure excess at their centre in order for the inward acting gas pressure excess gradient to accommodate the increase in the outward acting Lorentz force.

We define the density in the tube to be $\rho_i = \rho_e + \rho_{exc}$, where ρ_e is the external density and ρ_{exc} is the density excess given by evaluating

$$\rho_{exc} = \frac{\tilde{\mu} p_{exc}}{\tilde{R} T(z)}. \tag{6.12}$$

As in chapter 5, if the whole tube where in thermal equilibrium with the surroundings then we would have

$$\rho_{exc\,1} = \frac{\tilde{\mu} B_y{}^2}{2\mu \tilde{R} T(z)} \left\{ \alpha_1{}^2 \left(\frac{d_1{}^2}{2} - r^2 \right) - 1 \right\}, \tag{6.13}$$

$$\rho_{exc\,2} = \frac{\tilde{\mu} B_y{}^2}{2\mu \tilde{R} T(z)} \left\{ \alpha_2{}^2 \left(\frac{d_2{}^2}{2} - r^2 \right) - 1 + c^2 \left(\frac{R^2}{2} - \frac{d_2{}^2}{2} - 2 \left(\frac{R^2 d_2{}^2}{R^2 + d_2{}^2} - \frac{d_2{}^2}{2} \right) \exp\left(-r^2 / k_2{}^2 \right) \right) \right\}, \tag{6.14}$$

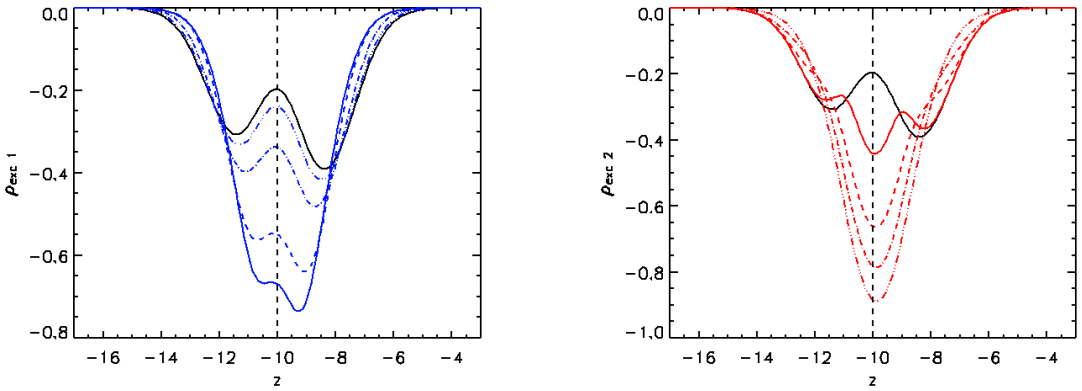

(a) α_1 cases.

(b) α_2 cases.

Figure 6.4: Density excess, ρ_{exc}, at $t = 0$, measured at $(x = 0, y = 0)$. The vertical dashed line at $z = -10$ indicates the location of the axis in all cases.

where $\rho_{exc\ 1}$ and $\rho_{exc\ 2}$ correspond to twist profiles α_1 and α_2 respectively.

The whole tube would then be buoyant when a density deficit exists, $\rho_{exc} < 0$. However, to encourage the formation of an Ω-shaped loop along the tube's length we reduce the deficit away from $y = 0$ following the Gaussian profile

$$\rho_m = \rho_{exc} e^{-y^2/\lambda^2} \tag{6.15}$$

where $\lambda = 20$, such that the density in the tube is now given by $\rho_i = \rho_e + \rho_m$. The smaller density deficit for $|y| > 0$ implies that there is a corresponding increase in the temperature contrast between the tube and surroundings. Figure 6.4 shows the variation in the density excess for α_1 and α_2 for the various values of k_1 and k_2. The tubes with a lower tension force have a lower density excess at their centre in order to accommodate the lower gas pressure excess and ensure the ideal gas law is satisfied. Thus, these tubes are more buoyant at the start of the simulations.

6.4 Rise towards the Solar Surface

At the start of the experiments, the only force acting on the tubes is a buoyancy force in the positive vertical direction. Given that the explicit expression for the initial buoyancy force is known, it should be possible to scale the vertical velocity of the tube by this force and retrieve a profile that can then be used to predict the vertical velocity for any value of k_1 or k_2 for α_1 or α_2 respectively.

Rather than considering the whole tube, we will consider the axis of the tube since this is a well

defined point. At the axis, $r = 0$, the buoyancy force is proportional to

$$\begin{aligned} Q_1 &= \frac{c^2 {d_1}^2}{2} - 1, \\ &= \frac{c^2 R^2 {k_1}^2}{2\left(R^2 + {k_1}^2\right)} - 1, \end{aligned} \tag{6.16}$$

$$\begin{aligned} Q_2 &= c^2 \left(\frac{R^2}{2} + \frac{{d_2}^2}{2} - \frac{2R^2 {d_2}^2}{\left(R^2 + {d_2}^2\right)} \right) - 1, \\ &= c^2 \left(\frac{R^2}{2} + \frac{R^2 {k_2}^2}{2\left(R^2 + {k_2}^2\right)} - \frac{2R^2 {k_2}^2}{\left(R^2 + 2{k_2}^2\right)} \right) - 1, \end{aligned} \tag{6.17}$$

for twist profiles α_1 and α_2 respectively.

Thus, the initial acceleration should also be proportional to Q_1 and Q_2 for cases with α_1 and α_2 respectively. Firstly, for the α_1 cases we have

$$\frac{\partial v_z}{\partial t} \propto Q_1, \tag{6.18}$$

or, alternatively,

$$\frac{\partial}{\partial h}\left(\frac{{v_z}^2}{2}\right) \propto Q_1, \tag{6.19}$$

where h has units of length and measures the distance the axis has travelled from its initial position. Integrating (6.19) with respect to h yields

$${v_z}^2 \propto Q_1 h + C, \tag{6.20}$$

where C is the constant of integration. Initially $h = 0$ and, at this time, $v_z = 0$. Hence, $C = 0$. Rearranging (6.20) gives

$$v_z / \sqrt{Q_1} \propto \sqrt{h}. \tag{6.21}$$

Using the same analysis for the α_2 cases, we find

$$v_z / \sqrt{Q_2} \propto \sqrt{h}. \tag{6.22}$$

Using (6.21) and (6.21), we can now scale the vertical velocity of the axis with respect to the square root of the distance travelled by the axis. Figure 6.5 demonstrates this scaling of the axial vertical velocity for the α_1 and α_2 cases. The axis of the tube has been identified as the point measured at $(x = 0, y = 0)$ where B_θ reverses sign. The above scaling is correct for the initial rise of the tube but, after rising only a short height, the scaling begins to fail. This failure occurs

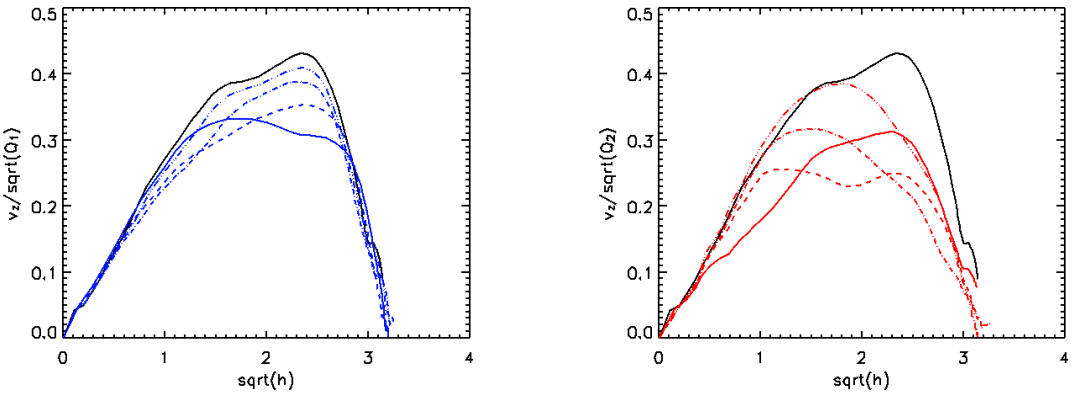

(a) α_1 cases.

(b) α_2 cases.

Figure 6.5: Scaled axial vertical velocity plotted against the square root of the distance travelled, h, measured at $(x = 0, y = 0)$.

when the initially balanced radial Lorentz force and the gradient of the pressure deficit in the tube fall out of balance with each other. Thus, the buoyancy force is no longer the only force determining the rise of the tube. Both of the initially balanced forces reduce in size as the tube rises but, at the rear of the tube the pressure gradient decreases quicker than the Lorentz force, while at the front of the tube it decreases slower than the Lorentz force.

The differential buoyancy of the tube's plasma, in the $x - z$ plane, causes parts of the magnetic field to rise faster than others. In cases where the tension force is weak, we see an evacuation and accumulation of the magnetic field which distorts the tube from its initial cylindrical structure. This redistribution of field can be seen in the asymmetric field strength profiles of figure 6.6. In all cases the axis has moved away from the rear of the tube, which was less buoyant, and in the cases with a weak tension force the axis has moved towards the front of the tube, which also lacks buoyancy. In the cases with a strong tension force, the distance between the axis and the front of the tube has been approximately maintained.

In cases where the movement of the magnetic field is limited by the strong tension force, the imbalance in the radial forces remains smaller for all time. At the rear of the tube, the lack of evacuation of field maintains the gradient of the gas pressure deficit and, thus, the gradient decreases more slowly than for the cases with low tension forces. At the front of the tube, the lack of accumulation maintains the magnetic pressure gradient here and, thus, the imbalance is smaller than in the cases with low tension forces.

As the tube rises, it moves into regions where the external gas pressure and density are smaller. The reduction in the gas pressure gradient between the internal and external medium causes the tube to expand horizontally. Hence, there is a corresponding decrease in the axial component

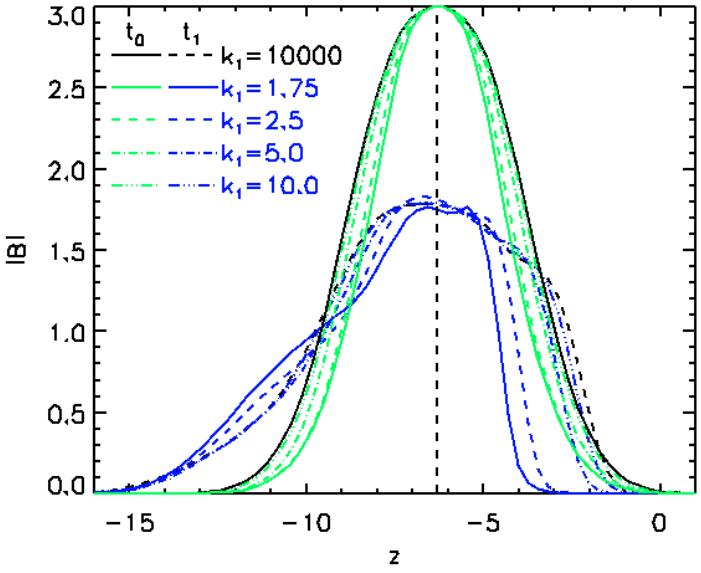

(a) α_1 cases.

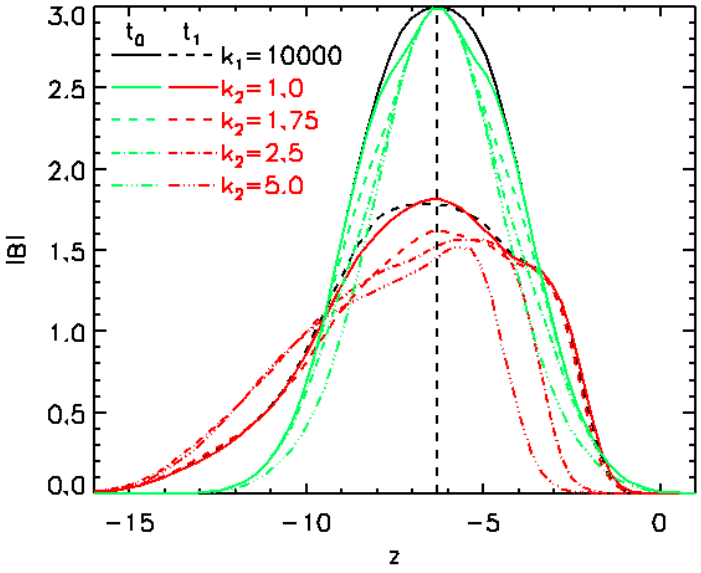

(b) α_2 cases.

Figure 6.6: Field strength, $|\mathbf{B}|$, as a function of height, z, measured at $(x = 0, y = 0)$, at two distinct times in each case. The t_0 lines are the original profiles of the field strength at $t = 0$, shifted in height such that the axes are at $z = -6.3$ (indicated by the dashed vertical line). The t_1 lines represent field strength profiles at one individually selected later time for each experiment when the axes of the tubes are at a height of $z = -6.3$. For the α_1 cases, the t_1 lines represent $k_1 = 1.75, 2.5, 5.0, 10.0, 10000.0$ at $t = 18, 20, 24, 26, 27$, respectively. For the α_2 cases, the t_1 lines represent $k_2 = 1.0, 1.75, 2.5, 5.0$ at $t = 27, 26, 21, 18$, respectively, and $k_1 = 10000.0$ at $t = 27$.

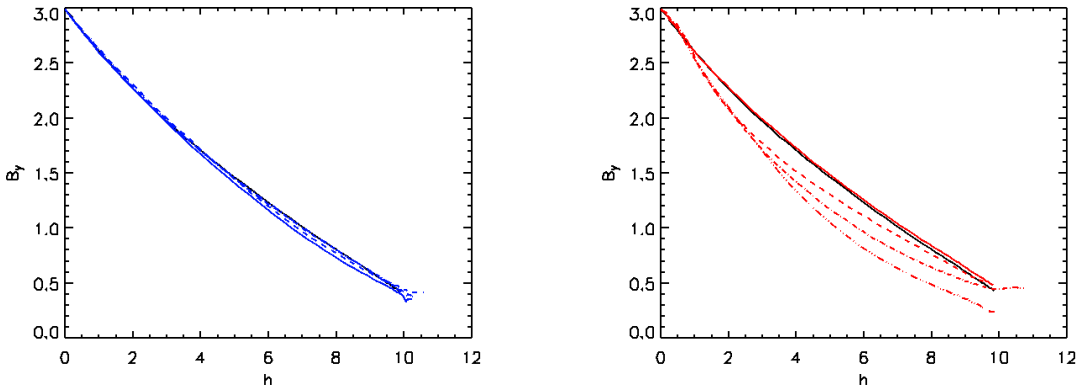

(a) α_1 cases.

(b) α_2 cases.

Figure 6.7: Field strength at the axis, B_y, as a function of distance travelled, h, measured at $(x = 0, y = 0)$.

of the tube's magnetic field, B_y, so as to maintain conservation of flux. In order to evaluate the degree of expansion suffered by the different tubes, we consider the axes of the tubes as an example location. For the α_1 cases, the decrease in B_y with respect to distance travelled by the axis is independent of k_1, as shown in figure 6.7. However, for the α_2 cases, we find that there is a greater decrease in B_y with distance travelled as k_2 increases. Thus, the α_1 cases experience the same degree of expansion as they rise irrespective of k_1 but the α_2 cases experience a greater degree of expansion as k_2 increases.

The expansion of a tube ceases once the horizontal gas pressure gradient at the new height balances the Lorentz force. For tubes with a larger inwardly directed tension force, the degree of expansion will be smaller and, therefore, the rate of decrease in B_y with distance travelled will also be smaller. Figure 6.8 shows the differing tension forces acting on the tubes at $t = 0$. For the α_1 cases, there is the same non-zero gradient in the tension force surrounding the axis and, thus, these tubes undergo the same degree of expansion. However, for the α_2 cases there is a zero gradient in the tension force at the axis and, away from the axis, this force increases at varying rates dependent on k_2. As k_2 increases, the tension force increases more slowly with radius and, thus, there is a greater degree of expansion for the tube.

The expansion of the tube and the compression of the field at the front of the tube result in a decrease in the axial field component and an increase in the azimuthal component, respectively. This modification in the ratio of the field components causes the pitch of the tube's fieldlines to change. The pitch of a fieldline is defined as the angle, ϕ_p, it makes with the axis and is given by

$$\tan(\phi_p) = \frac{B_\theta}{B_y}. \tag{6.23}$$

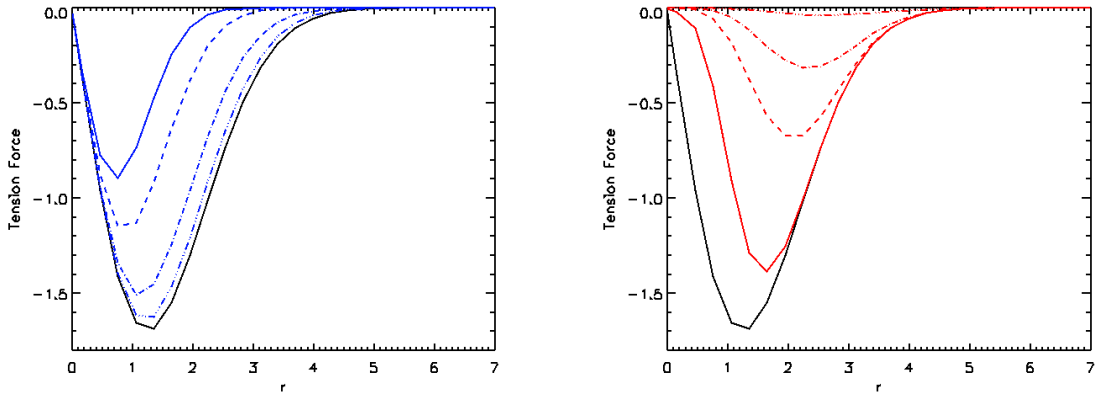

(a) α_1 cases. (b) α_2 cases.

Figure 6.8: Tension force as a function of radius at $t = 0$.

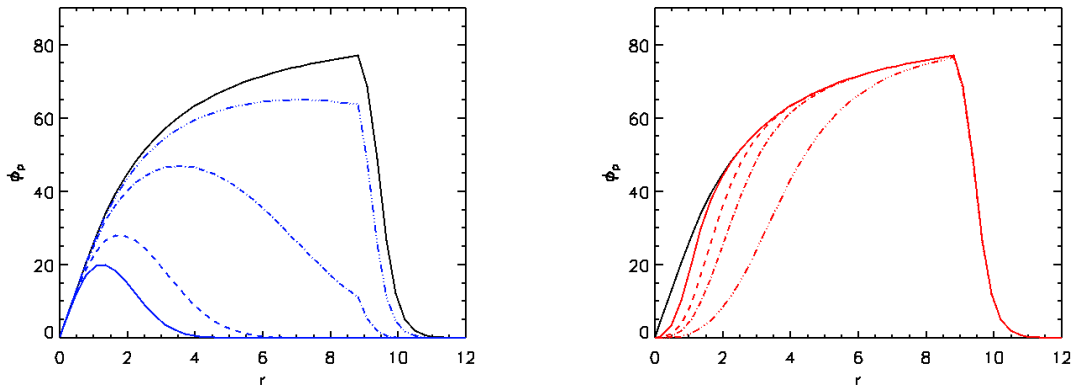

(a) α_1 cases. (b) α_2 cases.

Figure 6.9: Pitch of the fieldlines, ϕ_p, as a function of radius at $t = 0$.

Figure 6.9 shows the initial fieldline pitch generated by the chosen twist profiles. All of the tubes have a maximum pitch angle above that prescribed by Emonet and Moreno-Insertis (1996), which is required to avoid a tube splitting into two parts during its rise in the solar interior.

For the α_1 profile, we find that in each case the pitch in the region around the axis remains unchanged as the tubes rise through the solar interior. However, for the α_2 cases, the pitch increases in magnitude for all of the cases. These variations between the two twist profiles are as a result of the differing manner in which the axial component of the field decreases, which was discussed above. However, away from the axis, there is an increase in the pitch of the fieldlines in all of the cases due to the expansion and compression of the tube described earlier. Irrespective of the twist profile, the low tension cases, which initially have the smallest overall pitch, see the largest increase in pitch. The different increases in pitch experienced by the tubes are due to the variation

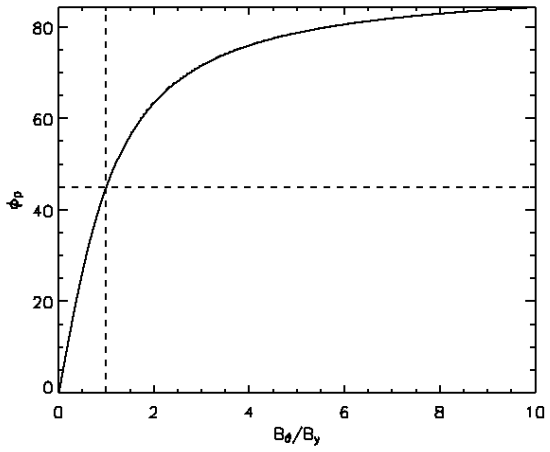

Figure 6.10: Pitch angle, ϕ_p, given by the function $\arctan(B_\theta/B_y)$. The intersection of the dashed lines indicates $\arctan(1) = 45^o$. Below this pitch, the function has a practically linear profile but is highly asymptotic above 45^o.

in the $\tan$ profile at small and large B_θ/B_y ratios, as illustrated in figure 6.10. Changes in B_θ or B_y cause a much greater change in the pitch if the pitch is initially small but will have only a marginal effect when the pitch is already large.

Upon reaching the photosphere, there is little difference in the pitch profiles between the α_1 and α_2 cases, as shown in figure 6.11. The three α_1 cases characterised by a decreasing pitch profile at outer radii have undergone two significant modifications in order to have pitch profiles that look like the other cases' profiles. Firstly, there has been an increase in pitch throughout the tubes, such that there is no longer a gentle decrease to zero pitch at the tubes' fronts but a steep gradient. This result has previously been noted by Emonet and Moreno-Insertis (1998), who consider flux tubes rising through the solar interior, which are defined by non-constant twist profiles. Secondly, the location of the maximum pitch has migrated towards the front edge of the tube. This is inline with the work of Hughes et al. (1998), who found that after only a short rise through the solar interior, tubes with initially decreasing twist profiles actually had pitch profiles much the same as tubes prescribed with constant twist. Furthermore, they suggest that it is the maximum value of the transverse field component, B_θ, that is important for maintaining a cohesive tube structure, free from the development of side lobes. We do not see this level of distortion here and, thus, cannot comment on whether the maximum value of the transverse field is a key parameter for cohesion.

In summary, we find that the initial vertical velocities of the tubes are well defined by the different buoyancy forces of the α_1 and α_2 twist profiles. However, an imbalance quickly develops between the radial pressure excess gradient and the Lorentz force of the tubes, causing the scaling of the vertical velocity with respect to the buoyancy to fail. The imbalance is largest for the cases with a low tension force due to the greater degree of evacuation and accumulation of magnetic field

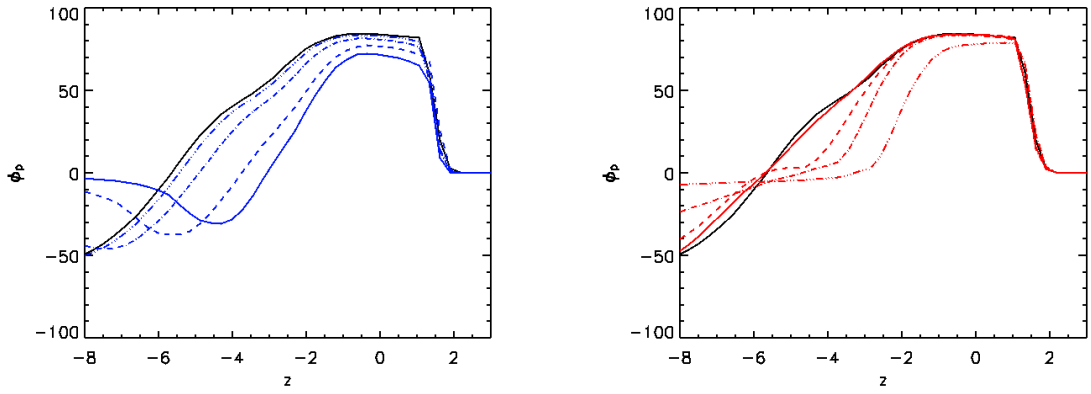

(a) α_1 cases.

(b) α_2 cases.

Figure 6.11: Pitch of the fieldlines, ϕ_p, as a function of height, z, at $t = 30$, measured at $(x = 0, y = 0)$.

they experience. We see differing rates of change in the field strength of the axis for the two twist profiles. For the α_1 cases, the tension force surrounding the axis is the same and, thus, the tubes experience the same amount of expansion and decrease in B_y with distance travelled. For the α_2 cases, the tension force increases more slowly with increasing k_2 and, therefore, the tubes experience different rates of expansion and decreases in the axial field component. Once the tubes reach the photosphere, their pitch profiles are relatively similar. There is no longer a smooth decrease in the pitch at outer radii for the three α_1 cases with the lowest tension forces. The rate of change of the pitch with radius will be an important characteristic of the magnetic field once it expands into the atmosphere and, thus, we shall consider this in detail in section 6.6.

6.5 Emergence through the Photosphere

As the top of the tube passes through the solar surface, it is forced to reduce its vertical velocity due to the change in stratification of the background medium. The solar interior is marginally stable to the convective instability and, therefore, when the tube became over dense compared with the surrounding it still continued rising. However, the photosphere is strongly subadiabatic and the overdense tube cannot proceed without the occurrence of a magnetic buoyancy instability, as discussed in chapter 5.

We find that in the cases with a low tension force, the magnetic buoyancy instability fails to occur and flux remains trapped in the photosphere, as shown in figure 6.12. The criterion governing the instability was given in sections 2.2.2 and 5.4.2. Here, we find that as soon as the plasma-β is less than 1, the instability criterion becomes satisfied and flux can freely rise into the atmosphere.

This is also found by Magara (2001). For all of the α_1 emerging cases, we find that the instability occurs at ~ 44 time units but, for the α_2 emerging cases, the instabilities occur over the range of $44 - 48$ time units.

For the low tension cases, $k_1 = 1.75$ and $k_2 = 5.0$, the plasma-β fails to fall below 1 for two reasons. Firstly, the distance between the front edges and axes of the tubes decreases quickest for these tubes due to their low tension forces and subsequent accumulation of magnetic field. Thus, at the time of these tubes' fronts entering the photosphere, their axes are at a higher location in the solar interior. Therefore, the tubes have experienced greater expansion that results in their field strengths being smaller. Secondly, these tubes fail to penetrate as high into the photosphere as the others and, therefore, are surrounded by fluid with a higher gas pressure. These points are illustrated in figure 6.13, where we have compared the magnetic pressure and gas pressure for these cases and the $k_1 = 10000.0$ emerging case.

Of the cases where the instability does occur, we find there is variation in the growth time of the instability. This is illustrated in figure 6.12 where we can see that the time between the instability criterion being satisfied and the fastest rise phase increases as k_1 decreases and k_2 increases. For long perturbation wavelengths, as is the case here, Parker (1979a) states that the growth time of the instability is inversely proportional to the Alfvén speed, $V_A = B_0/\sqrt{\rho}$. As shown in figure 6.14, we find that as k_1 decreases and k_2 increases, the Alfvén speed reduces as required to correspond to increasing growth times. The smaller Alfvén speed for the cases with a lower tension force is as a result of these tubes having a lower field strength at the time of the instability. As discussed above, the field strength is lower because the axes of these tubes are higher at this time and, therefore, the tubes have experienced a greater degree of expansion.

When the tubes first pass through the solar surface, they cause gravity or buoyancy waves to be generated there. The Brunt-Väisälä frequency for gravity waves, ω_g, is given by

$$\omega_g{}^2 = \frac{g}{H_0^*} - \frac{g^2}{{c_s}^2}, \tag{6.24}$$

where g is gravity, H_0^* is the local density scale height and c_s is the local sound speed (Roberts 1991). We must convert this frequency into a dimensionless quantity, in order to correctly determine the frequency and period of the oscillations associated with any gravity waves in our dimensionless domain.

We first rearrange (6.24) such that it is simplified into a form that excludes the local density scale height. Given that the photosphere is isothermal, the density scale height is the same as the pressure scale height. Thus, in dimensional units we have

$$H_0^* = H_0 = \frac{\tilde{R}T_{ss}}{\tilde{\mu}g}, \tag{6.25}$$

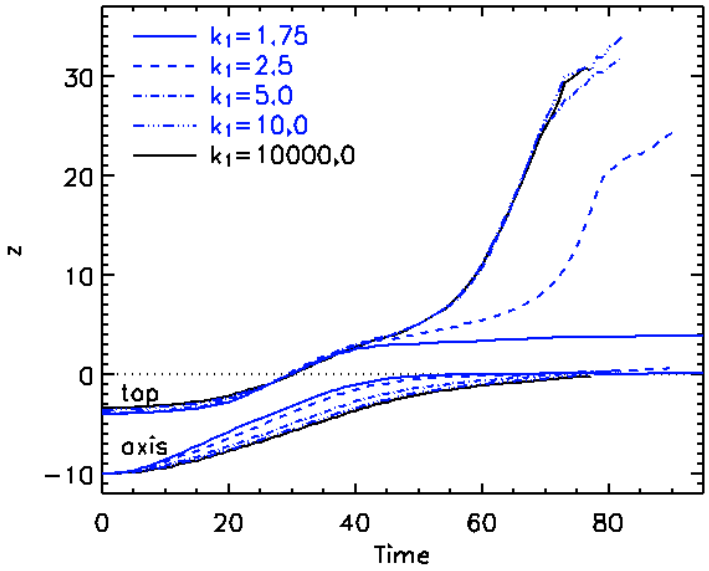

(a) α_1 cases.

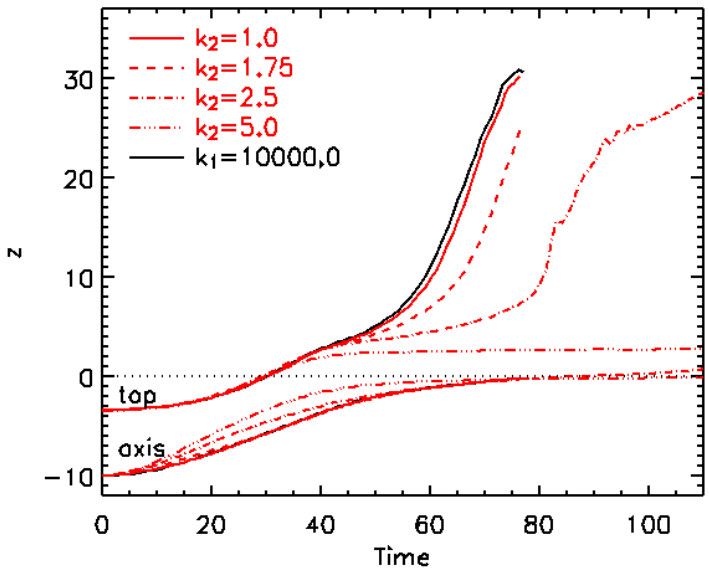

(b) α_2 cases.

Figure 6.12: Height of the top and axis of each tube over time, measured at $(x = 0, y = 0)$. The dotted horizontal line at $z = 0$ indicates the height of the solar surface.

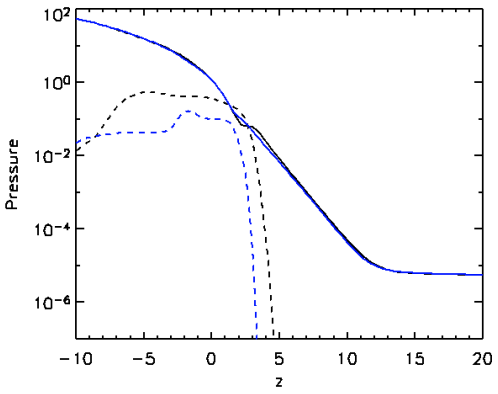

(a) $k_1 = 10000.0$ (black) and $k_1 = 1.75$ (blue) cases.

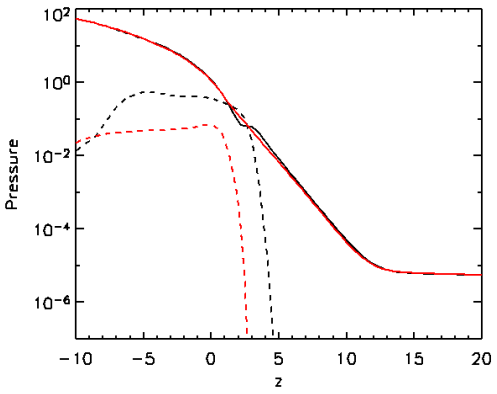

(b) $k_1 = 10000.0$ (black) and $k_2 = 5.0$ (red) cases.

Figure 6.13: Gas pressure (solid lines) and magnetic pressure (dashed lines) at $t = 46$, measured at $(x = 0, y = 0)$.

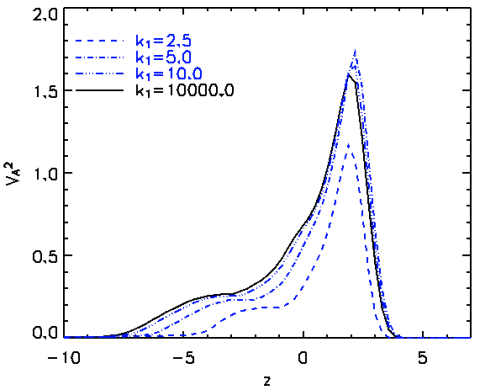

(a) α_1 cases.

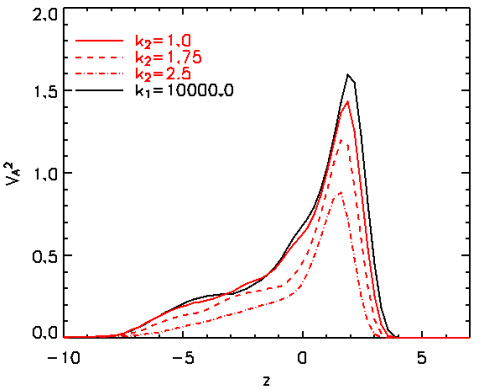

(b) α_2 cases.

Figure 6.14: Square of the Alfvén velocity in height, z, at $t = 46$ for the emerging cases, measured at $(x = 0, y = 0)$.

and, using the ideal gas law, this can be rewritten as

$$H_0^* = \frac{p_{ss}}{\rho_{ss} g}. \tag{6.26}$$

At the solar surface, the sound speed is defined as $c_s = (\gamma p_{ss}/\rho_{ss})^{1/2}$. Rearranging this and substituting the result into (6.26) yields

$$H_0^* = \frac{{c_s}^2}{\gamma g}. \tag{6.27}$$

Thus, the dimensional Brunt-Väisälä frequency can be rewritten as

$${\omega_g}^2 = \frac{g^2}{{c_s}^2}(\gamma - 1). \tag{6.28}$$

To transform (6.28) into a dimensionless formula we must consider the units we have used to define the dimensionless units of our experiments. The Brunt-Väisälä frequency can be written as

$$\omega_g = \omega_g' \omega_{g0}, \tag{6.29}$$

where ω_g is the dimensional quantity, ω_g' is the dimensionless quantity and ω_{g0} is a dimensional conversion value. This notation follows that used in section 4.2 where the hydrostatic atmosphere of the simulation domain was setup. We already know ω_g from (6.28) and, by finding ω_{g0}, we can evaluate ω_g'.

In order to find ω_{g0}, we firstly consider the units of time. As with the frequency, time can be written as

$$t = t' t_0, \tag{6.30}$$

where t is the dimensional unit, t' is the dimensionless unit and t_0 is a dimensional conversion value. From section 3.1, $t_0 = l_0/v_0$ and, in section 4.2, we chose the dimensional length-scale, l_0, to be the pressure scale height, H_0, and the dimensional speed, v_0, to be the scaled sound speed, $c_s/\sqrt{\gamma}$. Thus, the dimensional conversion value for time is

$$t_0 = H_0\sqrt{\gamma}/c_s. \tag{6.31}$$

Frequency has dimensional units $1/t_0$, therefore, the dimensional conversion value for the frequency is

$$\omega_{g0} = c_s/H_0\sqrt{\gamma}. \tag{6.32}$$

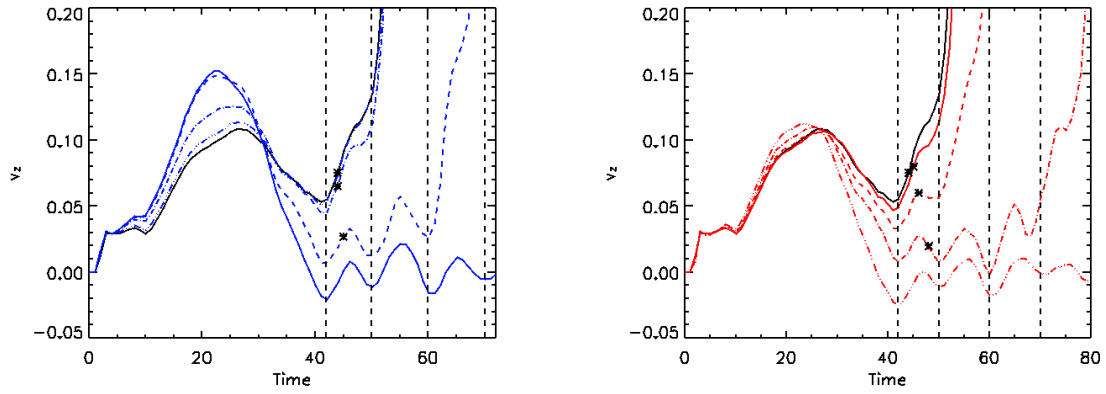

(a) α_1 cases.

(b) α_2 cases.

Figure 6.15: Vertical velocity at the front of the tube over time, measured at $(x = 0, y = 0)$. The star on each line indicates the time at which a magnetic buoyancy instability is satisfied for each case. The instability is never satisfied for the $k_1 = 1.75$ and $k_2 = 5.0$ cases. The dashed vertical lines indicate the troughs in the oscillating vertical velocity, which has a period of $\sim$ 10 time units. This is inline with the dimensionless period expected from the Brunt-Väisälä frequency for gravity waves.

Again, using $H_0^* = H_0$ and (6.27), the dimensional conversion value for the frequency becomes

$$\omega_{g0} = \sqrt{\gamma} g / c_s. \tag{6.33}$$

Substituting (6.28) and (6.33) into (6.29), yields the dimensionless Brunt-Väisälä frequency

$$\omega_g'^2 = \frac{\gamma - 1}{\gamma}. \tag{6.34}$$

In these experiments, the ratio of specific heats has been chosen as $\gamma = 5/3$. Hence, $\omega_g' = \sqrt{2/5}$ and, therefore, the dimensionless period of the oscillations will be 9.9 time units. By examining the vertical velocity of the flux at the front of the tubes, shown in figure 6.15, we can see that there is a clear oscillation with this period prior to the sudden increase in the vertical velocity associated with the growth of the magnetic buoyancy instability, which eclipses the gravity waves.

In summary, during the occurrence of the buoyancy instability at the base of the photosphere, the variations in the two twist profiles seem to be of little consequence. Of more importance, is the initial tension force associated with the tubes, since the degree of distortion determines whether the buoyancy instability will occur at all and the growth rate of the instability when it does occur. For both profiles, the cases with a low tension force fail to undergo the magnetic buoyancy instability and those just above the tension threshold initially rise more slowly into the atmosphere.

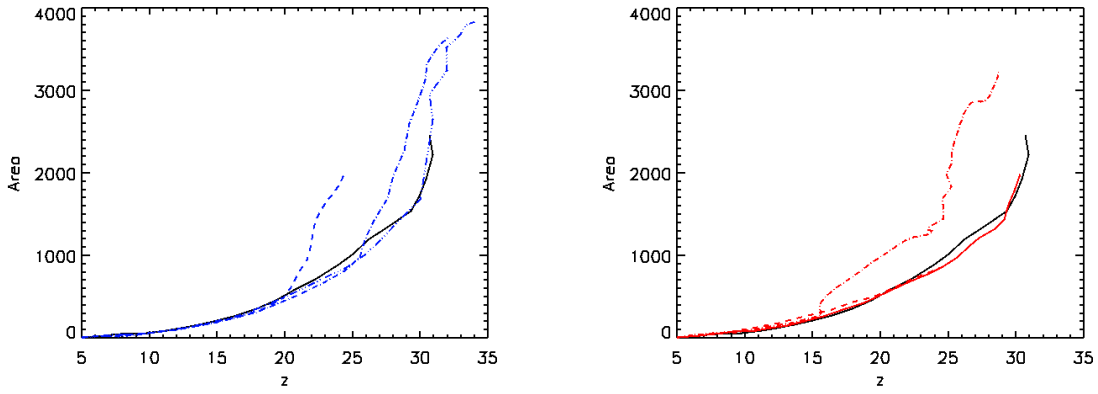

(a) α_1 cases.

(b) α_2 cases.

Figure 6.16: Area of the $x-z$ plane at $y=0$ (for $z>5$) with flux passing through it as a function of the height of the top of the tube.

6.6 Atmospheric Expansion

In this section, we will only be concerned with the cases for which we find emergence. Thus, we will not be discussing the results from the $k_1 = 1.75$ and $k_2 = 5.0$ cases any further.

As the magnetic field of the tube advances into the atmosphere, the field undergoes rapid horizontal and vertical expansion due to the lower atmospheric gas pressure. As a measure of this expansion, we evaluate the area of the $x-z$ plane above $z=5$ at $y=0$ with field passing through it. The results for the various cases are shown in figure 6.16, where the area of the plane containing flux has been plotted against the height of the top of the tube. We can see that when the tubes' tops are at the same height, the cases with lower tension forces occupy a greater area of the plane and have, therefore, experienced a greater degree of horizontal expansion. This is not surprising since a tube with a low tension force lacks the ability to constrict its expansion.

Figure 6.17 shows the amount of flux measured in the same $x-z$ plane above $z=5$ as a function of time. We can see that the time at which the first flux is seen in the plane increases as we move from the high to low tension cases. This is as a result of the slower growth rate of the buoyancy instability for the lower tension cases, which occurred when the fronts of the tubes were at a height of $z<5$ and, thus, the different rates at which the tubes' fronts advance into the atmosphere.

If all of the emerging plasma had a vertical velocity matching that of the tube front, then we could expect to see a similar increase in the gradient of the time-flux profile as we see in the vertical velocity of the tubes' fronts. However, as shown in figure 6.17, we see an approximately linear increase in all cases, indicating that the new flux entering the plane is the same at each time step but different for each case since the constant gradients are not prescribed by the same value. We

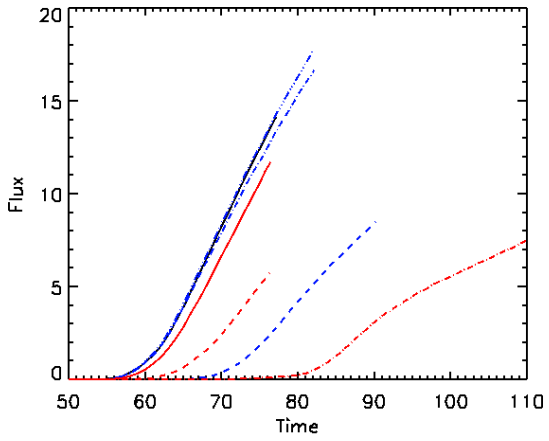

Figure 6.17: Sum of the flux passing through the $x - z$ plane at $y = 0$ (for $z > 5$) plotted against time.

find that the flux accumulates more slowly in the atmosphere for the cases with a low tension force and, therefore, flux is being transported into the atmosphere more slowly in these cases.

The different constant gradients illustrate that as each new flux layer of an individual tube satisfies the instability, it experiences the same instability growth time. Thus, at any given height, here $z = 5$, a constant amount of flux will pass over the threshold with time, as found in these simulations. As a consequence of the differing growth rates between the tubes, when the tubes' fronts are at the same height, different amounts of flux have been transported into the atmosphere, as shown in figure 6.18.

As discussed in section 6.4, the pitch of the tubes' fieldlines change as the tubes rise through the solar interior, with the biggest increases seen in the α_1 cases with a low tension force. However, at the time of entering the photosphere, there are still clear differences between the pitch of the fieldlines for the cases with high and low tension forces, as shown in figure 6.11. At the fronts of the tubes, there is a noticeable difference in the pitch of the emerging α_1 cases but no difference in the emerging α_2 cases. As we move from the high to low tension cases, there is a steeper fall in the pitch as the axis is approached from the tube front. This is as a consequence of the shorter distance between the axis and the front of the tube but, when the gradient of the pitch is measured as a function of the fractional radius, we find that the α_1 cases have the same gradient and the α_2 cases do not.

As the tubes rise into the atmosphere, it is the field at the front of the tubes that experiences expansion. The expansion is both vertical and horizontal, which causes decreases in all of the components of the field and changes in the fieldline pitch. Figure 6.19 shows the fieldline pitch once the tubes' fronts have reached a certain height in the atmosphere. We find that there is little

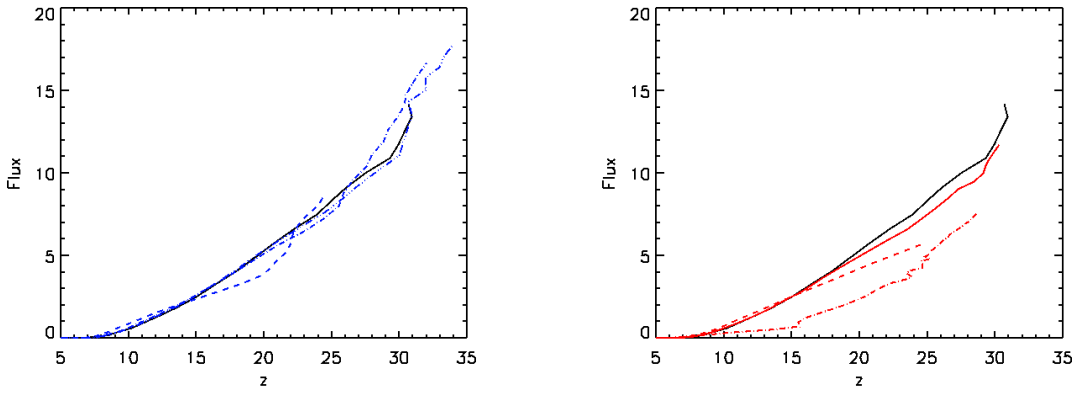

(a) α_1 cases. (b) α_2 cases.

Figure 6.18: Sum of the flux passing through the $x-z$ plane at $y=0$ (for $z>5$) plotted against the height of the top of the tube.

difference in the pitch of the α_2 cases but a more significant difference can be seen in the pitch of the α_1 cases. This would suggest that the actual pitch angle and not the gradient in the pitch of the pre-emergence field are key in determining the resulting pitch of the atmospheric field.

In summary, for the cases with low tension forces, we find that the field experiences a greater degree of expansion. Although flux is transported into the atmosphere at a constant rate in all of the experiments, the rate of transport is slower for the tubes with low tension forces due to their associated longer instability growth time. The pitch of the fieldlines are very similar in all of the α_2 cases but for the α_1 cases there is a clear difference in the pitch angle as a function of height between the high and low tension tubes.

6.7 Conclusions

In this chapter we have carried out simulations of flux tubes with two different non-constant twist profiles as the seed field. The α_1 and α_2 twist profiles are characterised by decreasing and increasing twist with radius, respectively. For each profile we considered a parameter space which varied the rate at which the twist profile increased or decreased with radius. When the twist profile increases quickly towards a constant twist value of 0.5 and decreases slowly away from this value, the flux tubes have an associated high tension force. When the twist profile increases slowly from 0.0 and decreases quickly towards this value, the flux tubes have a low tension force.

Although the twist profiles are sufficiently different from each other, our results have shown that there are both similarities and differences in the rise, emergence and expansion stages of the emergence of non-constant twist seed flux tubes.

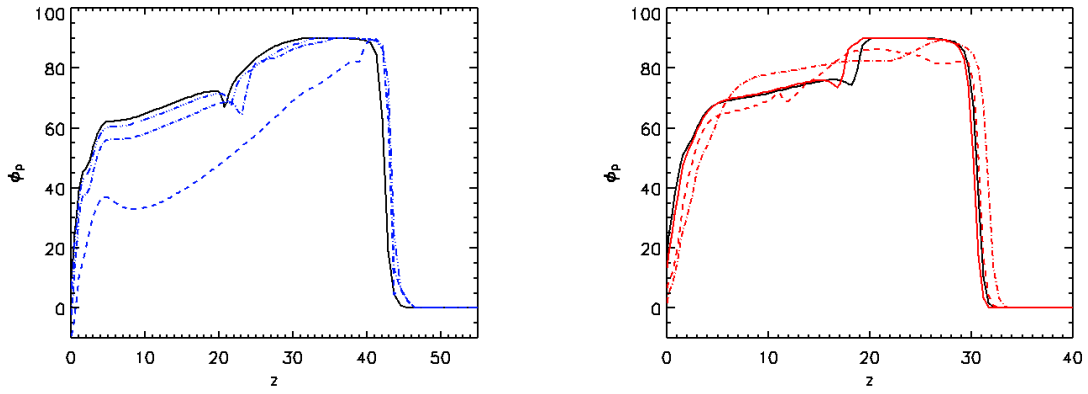

(a) α_1 cases.

(b) α_2 cases.

Figure 6.19: Pitch of the fieldlines as a function of height, z, measured at $(x = 0, y = 0)$. The times at which the lines are plotted is different for each case and have been chosen such that the top of the tubes are at the same height of $z = 30$ and $z = 25$ for α_1 and α_2 cases respectively.

The similarities encompass events where, regardless of the twist profile, the low tension cases act similarly and the high tension cases act similarly. During the tubes' rise through the solar interior, we find that the magnetic field evacuates the lower region of the initial cylindrical structure and accumulates in the front portion to a greater degree for the low tension cases. This is due to the inability of a low tension force to maintain the structure of the tube. Although the vertical velocity of the tube is initially well prescribed by the buoyancy force, an imbalance in the radial forces grows and is most exaggerated for the low tension cases due to the reorganisation of the field. Once the tubes surface in the photosphere, a magnetic buoyancy instability will occur if the plasma-β falls below 1. However, the instability does not occur for the low tension cases since they have experienced greater horizontal expansion during their rise to the surface and, therefore, have a weaker magnetic field and higher plasma-β. Post-instability, the growth rate increases as we move towards higher tension cases and, thus, these tubes rise into the atmosphere quicker. The tubes with the faster growth rate transport more flux into the atmosphere as a function of time and height of the top of the tube, while the tubes with the lower tension force, and longer growth time, experience greater horizontal expansion in the atmosphere.

The differences in the twist profiles arise when the nature of the tension force becomes important as opposed to solely its magnitude. For the α_1 cases, the non-zero tension force is the same size in the immediate vicinity of the axis and, thus, the tubes experience the same horizontal expansion and decrease in the axial field strength as they rise. However, the tension force increases at varying rates with radius in the α_2 cases and, therefore, these tubes experience different degrees of expansion and rates of decrease in the axial field strength depending upon their individual tension profiles. All of the cases see an increase in the pitch of the fieldlines but the α_1 cases, with initially decreasing pitch at outer radii, see the largest increase. At the time of emergence, all of

the tubes have non-zero pitch at their front edges. However, the magnitude of the non-zero pitch angle at the front varies in the α_1 cases and, thus, we see differences in the pitch profiles of the atmospheric field with height, while the α_2 cases have no significant differences.

From our results, it appears that the twist profile of the tube bears little significance in determining whether the field will emerge and that the strength of the magnetic field is actually of key importance. The field strength is determined by the degree of horizontal expansion of the tube while it rises through the solar interior and this, in turn, is governed by the height of the axis and the tension profile in the vicinity of the axis. In terms of these quantities, neither profile appears to be significantly better than the other for instigating emergence. Considering the overall profile of the transverse component of the field, B_θ, we find that the $k_1 = 1.75$ and $k_2 = 2.5$ cases have approximately the same maximum value for B_θ from figure 6.2. However, the former case does not emerge while the latter does and this indicates that the location of the maximum B_θ is more important than the actual maximum value. Perhaps, therefore, the amount of flux in the tube is the key factor governing emergence.

In terms of observations, there is very little discernable difference between the pitch angle of the fieldlines once the tension force is reasonably high but the degree of horizontal expansion may give some indication as to the twist of the tube. We believe that a wide scale observational study is required in order to determine whether the strength of the field at the time of emergence influences the rate of rise of the flux into the atmosphere, as our results from this chapter and chapter 5 imply. Given that the initial details of the twist profile appear to be lost by the time of emergence in the simulations, it will probably be exceedingly difficult to find features in solar observations that give any greater insight into the nature of the twist pre-emergence.

Regardless of the individual characteristics of the twist profiles, we find that when emergence does occur the general results from previous simulations are reproduced by both twist profiles and, therefore, are robust. For the overdense flux to rise into the atmosphere a magnetic buoyancy instability must occur and, once into the atmosphere, the field expands rapidly both vertically and horizontally. Additionally, since the characteristics of the twist profiles are lost by the time the instability occurs, providing the flux tube has sufficient pitch at its front edge the emergence results should be reasonably similar.

6.7 Conclusions

Chapter 7

Effects of a Complex Seed Field

Note: The material in this chapter has been published in Astronomy & Astrophysics. The reference is:
Murray, M. J. and Hood, A. W. (2007). Simple Emergence Structures From Complex Magnetic Fields. *Astronomy & Astrophysics*, 470:709-719.

Single flux tubes have become the standard objects used in the 3D modelling of large-scale emerging flux regions. As discussed in chapter 2, these simulations have provided results that compare favourably with observations. The flux seed is placed a short distance under the surface and rises either under buoyancy or via an imposed initial velocity. However, subsurface convective flows have been shown to distort twisted and untwisted magnetic flux tubes (Fan et al. 2003; Abbett et al. 2004; Cheung et al. 2007). Hence, these emergence models have come under criticism for using an initial field structure which is too organised and, therefore, would not be expected to occur naturally in the Sun. The simulations in this chapter aim to create a more complex subsurface field through the interaction of two flux tubes within the solar interior. From studying the subsequent emergence of our flux system, we aim to provide an insight into how the structure of the field below the surface can manifest itself in atmospheric observations.

We will consider the existing literature relating to this topic in section 7.1. In particular, we will be concerned with information provided by observations that indicates the nature of the subsurface field at sites of large-scale emergence sites and simulations in which two flux tubes interact.

In section 7.2, we will explain the setup of our domain model. Here, we will present the atmospheric stratification and give details of the magnetic structure and placement of the two tubes.

In sections 7.4, 7.5, 7.6 and 7.7, we will present the results of our simulations looking at both the pre- and post-emergence evolution of the flux systems, discussing our results in the context of

existing literature.

Finally, in section 7.8, we will summarise the modifications in the emergence of flux caused by using a complex subsurface field, paying particular attention to the features that can be observed and measured by astronomers. Using our findings, we will draw conclusions as to the robustness of results from previous flux emergence simulations that use a single flux tube.

7.1 Existing Literature

The form of the field prior to emergence is, to a large extent, unknown. Using observational measurements, theoretical models for general and individual flux emergence events have been created, which make predictions about the subsurface magnetic field. Glackin (1975) developed a model in which the upper fieldlines of the emerging tube are more twisted than the lower fieldlines in order to explain the 90^o rotation in alignment of the rising arches in an AFS during the creation of a new active region. Parker (1979b) models a sunspot such that above the surface the field appears to belong to one cohesive tube structure but below the surface the sunspot is actually comprised of several distinct medium sized flux tubes, each consisting of many smaller sized flux tubes. The collection of tubes below the surface is assumed to occur due to the interchange instability here, which lowers the magnetic energy of the system by fragmenting the large tube with strong magnetic curvature into many smaller ones (Solanki 2003). The emergence of a closed toroidal magnetic system is used by Lites et al. (1995) to explain the the formation and subsequent evolution of a particular δ sunspot event. In order to explain the formation of alignments of faculae during sunspot pore development, Strous and Zwaan (1999) propose a model in which the arch filament system is comprised of several parallel vertical sheets. In each sheet, undulatory flux tubes rise up to the surface under buoyancy and emerge into the atmosphere.

Models formed as a result of observations have provided input for many of the simulations studying both the evolution of rising tubes within the convection zone and the process of flux emergence. From these simulations we know that the field of a flux bundle must be intertwined or twisted if it is to rise through the convection zone without suffering from significant distortion and shredding (Moreno-Insertis and Emonet 1996; Dorch and Nordlund 1998). We also know that when the field reaches the surface, there must be a negative gradient in its strength with increasing height if a magnetic buoyancy instability is to occur and emergence ensue.

In order to create a more complex magnetic field below the surface we will initialise two flux tubes such that reconnection will eventually take place, changing the topological structure of the seed flux. Dahlburg et al. (1997) observe a filamentary structure in the flux tubes of their simulation after they reconnect in a low-β environment. The authors conclude that should reconnection occur between flux tubes in the convection zone, the emerging tubes are likely to have a fine scale

internal structure too. The occurrence and observational signatures of this fine scale structure will be discussed further in section 7.8.

There have been multiple simulations that find reconnection occurring between two flux tubes. Fan et al. (1998a) considers the 2D rising motion of two parallel buoyant flux tubes in the convection zone, which are separated by both a horizontal and vertical distance. They find the lower tube can be drawn into the wake of the upper tube as they both rise and, eventually, the tubes will merge with dissipation of oppositely directed field components occurring at the interface between the tubes. The other simulations place more focus on studying the reconnection process between two interacting flux tubes but they have all been carried out in a low plasma-β environment, with the aim of understanding whether the event provides the trigger for flares in the Sun's atmosphere. The most comprehensive study of reconnecting flux tubes is carried out by Linton et al. (2001), who classified the interactions of the tubes into four distinct classes dependent upon the orientation of the tubes to each other. Unlike Fan et al. (1998a), the flux tubes are placed one above the other in these simulations and this is the model we choose to follow for our tubes in the convection zone.

There are significant differences between the simulations of this chapter and the other "reconnecting tubes" studies (see Linton et al. (2001), Linton (2006) and references therein). Unlike the work of Linton, we will use the buoyancy of one of the tubes to initialise the interaction between the tubes rather than imposing a stagnation point flow to drive the two tubes together. The reconnection in our models will occur within the solar interior and will, therefore, be within a high plasma-β environment. These differences will enable us to confirm the general nature of some of the results of previous colliding flux tube simulations. Finally, we will examine the effects of reconnection on the structure of emerging flux, an event that has not previously been studied.

7.2 Structure & Placement of the Magnetic Flux Tubes

An integration box of $148\times160\times218$ points is used to model the dimensionless domain $(-60,60)\times(-70,70)\times(-52,40)$ in the (x,y,z) co-ordinate system. On the Sun this corresponds to a domain of $20.4\ \mathrm{Mm}\times23.8\ \mathrm{Mm}\times15.6\ \mathrm{Mm}$. Uniform grid spacing is employed in the horizontal plane but the grid is stretched in the vertical direction. The numerical resolution is highest over the region $-33<z<-9$, which includes the initial locations of the tubes' axes and the region where we expect the reconnection to be initialised. At its smallest and largest, the grid spacing represents a physical distance of 4.77×10^4 m and 2.55×10^5 m respectively. We operate periodic boundaries in the horizontal directions and closed boundaries at the top and bottom of the domain. Additionally, we include damping regions on the closed boundaries to limit the reflection of waves off them.

The background stratification is setup using the numerical solar interior and atmosphere discussed

in section 4.2. The solar interior region is chosen to extend to a depth of -8.84 Mm below the solar surface, while only the first 3.4 Mm of the corona are modelled.

We define two horizontal flux tubes in the solar interior and these have the same profile as described in section 5.1. Here, we use have changed the cylindrical coordinate system to (r, θ, y'), with the magnetic field of each tube given by

$$B_r = 0 \tag{7.1}$$

$$B_\theta = \alpha r B_{y'} \tag{7.2}$$

$$B_{y'} = B_0 \exp\left(-r^2/R^2\right). \tag{7.3}$$

As previously discussed, these equations ensure the magnitude of the field falls with distance from the axis following a Gaussian profile. B_0 is the magnitude of the field at the axis and R specifies the radius at which the axial field measures 37% of B_0. This magnetic field profile results in the field strength being exactly zero at $r = \infty$ but the strength actually becomes computationally negligible at some finite radius. We call this finite radius the outer radius of the tube. The twist of the fieldlines about the axis is again given by α.

The axis of the upper tube is situated at a depth of $z = -10$ and the axial direction, y', is set to be the cartesian coordinate y. The azimuthal and radial coordinates of the tube are, therefore, comprised of the cartesian x and z directions, with $x = r\cos\theta$ and $z = -10 + r\sin\theta$. We set $B_0 = 3$ and choose the tube to be in radial force balance and density equilibrium with its environment, thus it is slightly cooler than the surroundings. The axis of the lower tube is situated at $z = -30$, with $B_0 = 15$, as illustrated in figure 7.1. As in chapter 5, this tube is chosen to be in thermal equilibrium with the environment so that it will be buoyant and, therefore, rise and interact with the upper tube. Following the experiments of Fan (2001) and Archontis et al. (2004) and those in chapter 5, we wish to encourage the formation of an Ω-shaped loop, thus we decrease the temperature away from the central portion of the lower tube, following a Gaussian profile.

We choose $\alpha = -0.4$ and $R = 2.5$ for both of the tubes. The negative value for α results in both of the tubes having left-hand twist about the axis. We leave the study of differently twisted tubes for a later date. The larger value of B_0 for the lower tube gives the axial field a strength of 5.52 at a radius R, in comparison with 1.1 at the same radius for the upper tube. This means that the radius at which the field becomes negligible for the lower tube is greater than that of the upper tube. Hence, the pitch of the fieldlines at this larger outer radius of the lower tube is also greater. The plasma-β at the axes of the upper and lower tubes measures 11.13 and 4.86, respectively, at $t = 0$.

One aspect of our experiments is to demonstrate that, when the initially separate flux domains of the two tubes come into contact with each other, reconnection will occur if the fields of the tubes

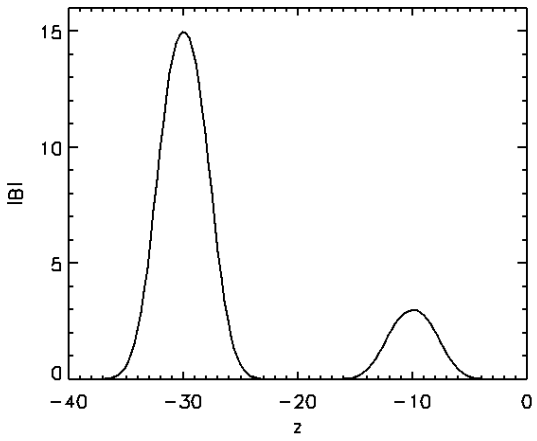

Figure 7.1: The magnetic field strength of the tubes, $|\mathbf{B}|$, measured along the vertical line through $(x = 0, y = 0)$.

are suitably aligned. Therefore, the orientation of the lower tube, in reference to the axial direction of the upper tube, will be varied to identify how the changing orientation of the flux systems alters any reconnection and resulting complexity of the magnetic field.

As discussed above, we fix the axial direction of the upper tube to be in the y direction. In model 1, we choose the axis of the lower tube to be parallel to the axis of the upper tube and, thus, the azimuthal and radial coordinates are the same as for the upper tube. In model 2, we choose the axes of the two tubes to be orthogonal, with the axis of the lower tube (y') in the $-x$ cartesian direction and, thus, its azimuthal and radial components will be prescribed by $y = r\cos\theta$ and $z = -30 + r\sin\theta$ components of the cartesian geometry.

In addition to these two cases, we perform a reference experiment to check the evolution and emergence pattern of the lower tube in the absence of the upper tube and this will be referred to as model 0. The positioning of this single flux tube is the same as that of the lower tube in model 1.

For clarity and brevity, we will refer to the upper flux tube as ft1 and the lower flux tube as ft2 in the remainder of the chapter. When describing the components of the field we will use the terms axial and transverse to allow for comparison between the models since the axes of the tubes and the horizontal component of the azimuthal field actually have different cartesian directions. Table 7.1 summaries the cartesian components prescribing the axial and transverse field components for ft1 and ft2 in all three models.

	ft1		ft2	
	axial	transverse	axial	transverse
Model 0	–	–	y	$\pm x$
Model 1	y	$\pm x$	y	$\pm x$
Model 2	y	$\pm x$	$-x$	$\pm y$

Table 7.1: The relationship between axial and transverse components and the cartesian coordinate system for tubes ft1 and ft2 in the three models. The transverse component is proceeded by $\pm$ since the transverse directions of the field at the top and bottom of each tube will be exactly opposite to each other.

7.3 Evolution in Model 0

We begin by giving an overview of the results from model 0, which includes only ft2. Independent of the orientation of the lower tube, all of the models would show this evolution in the absence of ft1.

Under buoyancy, the central portion of the tube begins to rise and compressional effects at the front of the tube cause the orientation of the fieldlines to turn more towards the transverse direction. Due to continual small-scale horizontal expansion, the tube experiences a decrease in both the strength of its axial field component and its internal density. The tube eventually becomes overdense whilst still in the solar interior but keeps rising due to the marginally stable nature of the surrounding environment to convective motions.

Once the tube front reaches the photosphere it experiences a rapid deceleration due to the strongly subadiabatic nature of the photosphere. However, through the nonlinear development of a magnetic buoyancy instability, the tube advances into the atmosphere and undergoes both horizontal and vertical expansion. This evolution is illustrated in figure 7.2. The axis of the tube remains confined to the solar interior during the limited time of the experiment.

This general evolution of a rising flux tube and its emergence into an unmagnetised atmosphere has previously been discussed in chapters 2 and 5. The specific measurements obtained from model 0 will be used to understand how the introduction of ft1 modifies the evolution of ft2 in the solar interior and the atmosphere.

7.4 Rise of the Tubes Prior to Contact

In all three models, the only variation in ft2 is the orientation of the axial (and therefore transverse) component of the tube's field with respect to the cartesian coordinate system. Hence, one would expect the initial evolution of ft2 to be similar in all models, with only significant changes

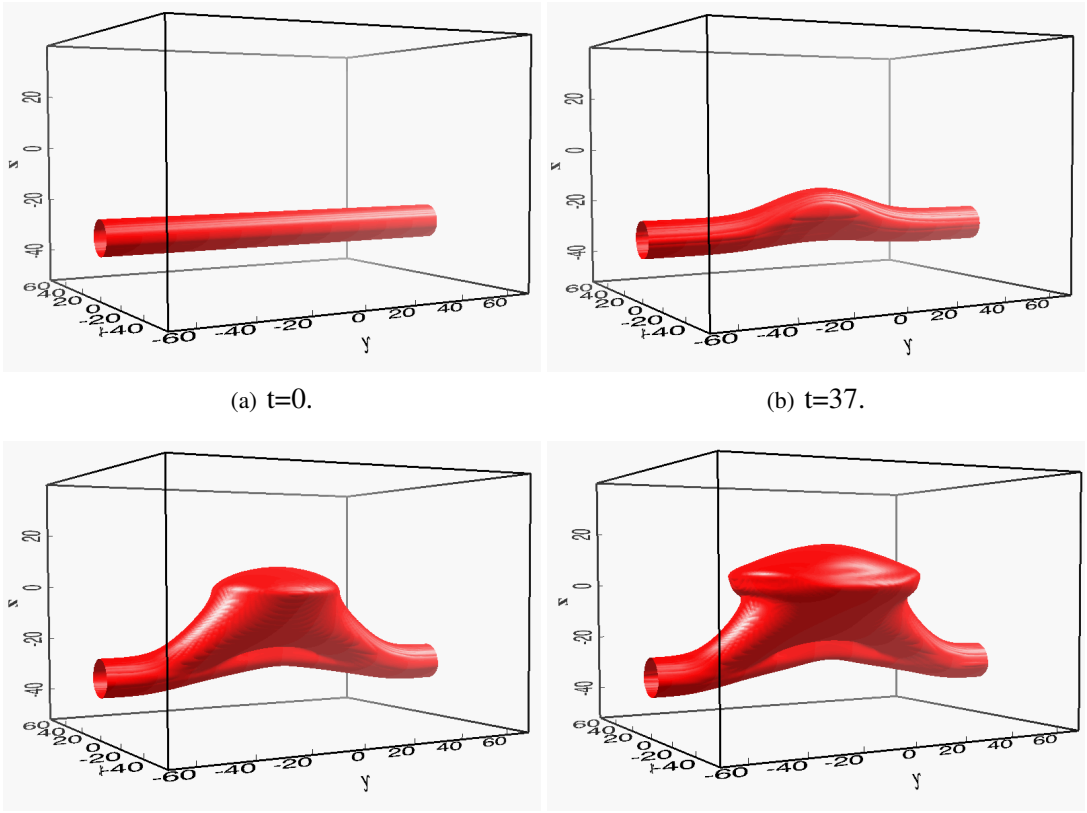

(a) t=0.

(b) t=37.

(c) t=77.

(d) t=87.

Figure 7.2: Isosurface of the magnetic field strength, $|\mathbf{B}| = 0.05$, of ft2 in model 0 at different times.

occurring once ft2 is in close proximity to ft1. In figure 7.3, we track the evolution of the top, axis and bottom of ft1 and the top and axis of ft2 along the central vertical line of the domain at $(x = 0, y = 0)$. Thus, we see that ft2 does indeed undergo the same evolution in all three models until $t = 28$. As can be seen from label A in figure 7.3, at this time the top of ft2 comes into contact with the bottom of ft1 in models 1 and 2.

For all three models we find the same behaviour for many of the physical quantities over the first 28 time units. Thus, the qualitative description of ft2 given in section 7.3 is quantitatively the same in all three models. However, we do find variations in the changing orientation of the fieldlines of ft2 in models 1 and 2 compared to model 0. The field at the front of ft2 increases away from the axial field direction by ~ 10 degrees during this early rise phase in models 1 and 2, such that it is practically in the transverse direction. In model 0, we find only a ~ 5 degree increase during this time period. Hence, we conclude that the compression of the field at the front of ft2 is caused not only by the enhanced buoyancy in the centre of the tube but also by the presence of ft1. The mass and rigid magnetic structure of ft1 act to slow the advance of the front of ft2 while the axis of ft2 continues to evolve as though ft1 were not present, thus resulting in the additional compression.

In models 1 and 2, ft1 first starts to move upwards at $t = 3$. The initial movement is caused by the launch of an upward moving compression wave at the beginning of the simulation due to the sudden motion of ft2 and the reaction of the surrounding plasma. This wave has previously been discussed by Archontis et al. (2004), who found that whilst the wave has small amplitude in the solar interior it steepens significantly in the atmosphere to become a shock wave. We find that this wave has no effect on ft1 other than to provide it with a small amount of positive vertical momentum. The further acceleration of ft1 occurs when the plasma above ft2 is displaced upwards by the buoyancy of this lower tube.

When the two tubes come into magnetic contact with each other at $t = 28$, the location of the bottom of ft1 and the top of ft2 becomes identical. The two touching surfaces act as one and, due to the differing field orientations of the two flux systems across the interface, a current sheet forms here. Reconnection between the two tubes ensues and the exact properties of this process are discussed in sections 7.5 and 7.6.

7.5 Current Sheets & Reconnection

Ft2 was chosen to be most buoyant in its central portion $(x = 0, y = 0)$ and, therefore, it is in this region that the flux systems of ft1 and ft2 first come into contact with each other at $t = 28$. The differences in the initial setup between models 1 and 2 now begin to play a role.

For model 1, the axes of the two tubes are in the same direction but, due to the tubes having the

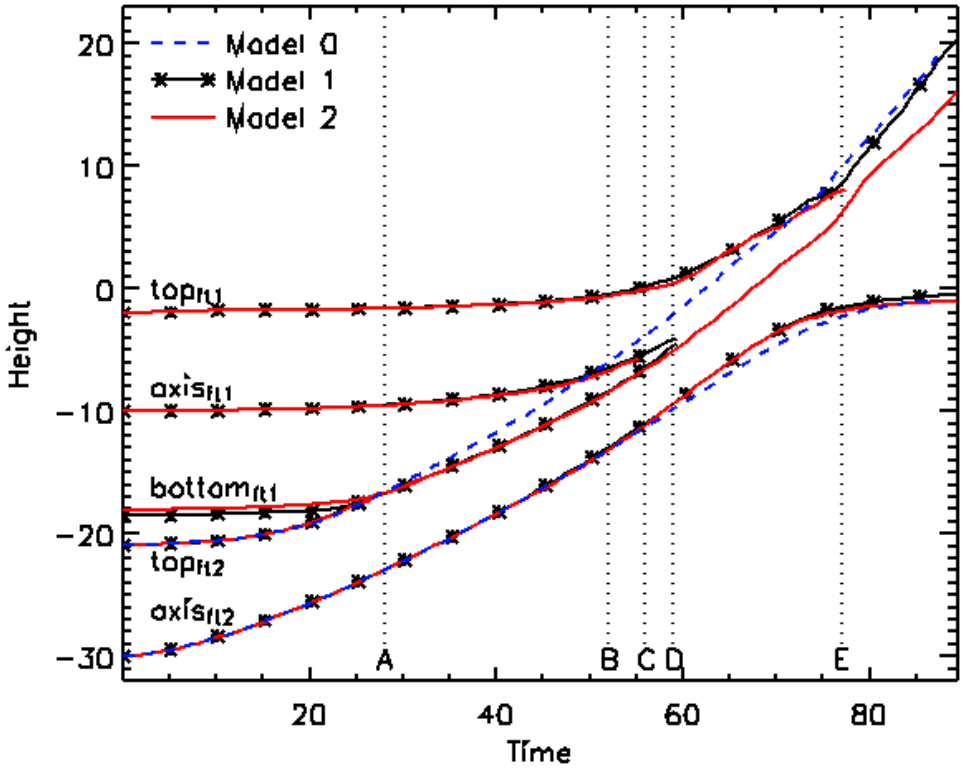

Figure 7.3: Height of various points of the flux tubes over time for model 0 (blue), model 1 (stars) and model 2 (red). The top, axis and (unreconnected) bottom of ft1 are tracked and the top and axis of ft2 are tracked. The vertical lines and labels describe the following: A ($t = 28$) – first contact of the two tubes; B ($t = 52$) – axis of ft2 begins to rise faster in models 1 and 2 than model 0; C ($t = 56$) – axis of ft1 reconnects in model 2; D ($t = 59$) – axis of ft1 reconnects in model 1; E ($t = 76$) – magnetic field of ft2 becomes uppermost flux in model 2.

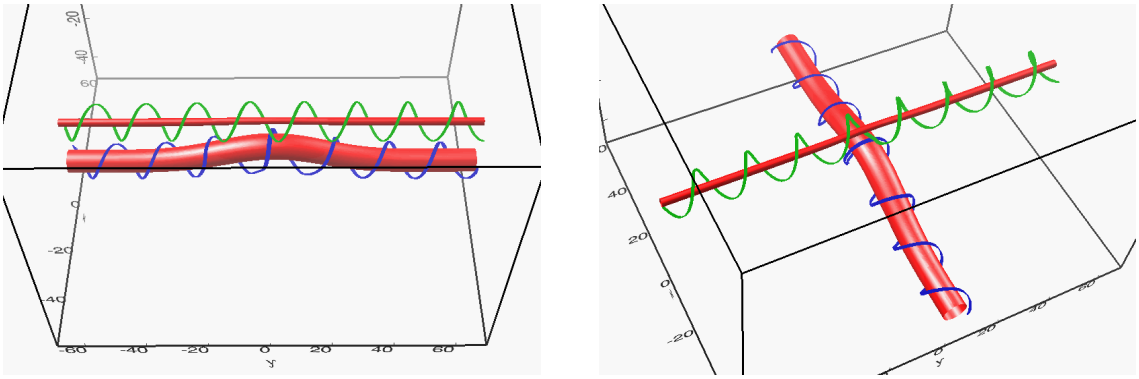

(a) Model 1 at $t = 30$.

(b) Model 2 at $t = 34$.

Figure 7.4: Outer fieldlines of ft1 (green) and ft2 (blue) for the various two tube models. The red isosurfaces show the magnetic field strength, $|\mathbf{B}|$, at a level of 2.5 for both models.

same sense of twist, the magnetic fields at the bottom of ft1 and top of ft2 have oppositely directly transverse field components, as shown in figure 7.4(a). For model 2, on the other hand, both the axial and transverse magnetic field components of the two tubes are differently directed at the contact interface. This results in the field at the bottom of ft1 being virtually antiparallel to the field at the top of ft2 in model 2, as shown in figure 7.4(b).

The non-parallel magnetic fields at the bottom of ft1 and the top of ft2, for both models 1 and 2, cause a current sheet to build up between the two tubes. The current sheet is centred about the point of first contact $(x = 0, y = 0)$. The simulations of Galsgaard et al. (2005) found that, when two differently directed flux systems come into contact with each other, the current sheet that forms between them is orientated at an angle between the differently directed field components, with the exact angle being determined by the magnitude of the non-reconnecting field component on either side of the sheet. The current sheets we see agree with this finding. When the tubes are parallel, as in model 1, the current sheet takes the form of a thin ribbon that is parallel to the axial direction of the flux tubes, figure 7.5(a). When the tubes lie orthogonal to each other, as in model 2, the current sheet is much shorter and lies orthogonal to the practically antiparallel fields of the two touching systems, figure 7.5(b).

Reconnection between the magnetic fields of ft1 and ft2 begins at $t = 30$ for model 1 and $t = 35$ for model 2, following the same general pattern in both models. The field in the current sheet, at the interface of the two tubes, reconnects such that the fieldlines of ft1 become wrapped around ft2 and vice versa. Reconnected fieldlines are ejected from the current sheet by flows, thus ensuring the reconnection region does not become clogged and reconnection can continue. If this reconnection was occurring in a low plasma-β environment, we would expect to find jets with velocities below the order of the local Alfvén speed directed along fieldlines (Archontis et al. 2005). However, the jets are obscured by both the high plasma-β surroundings, where the Alfvén

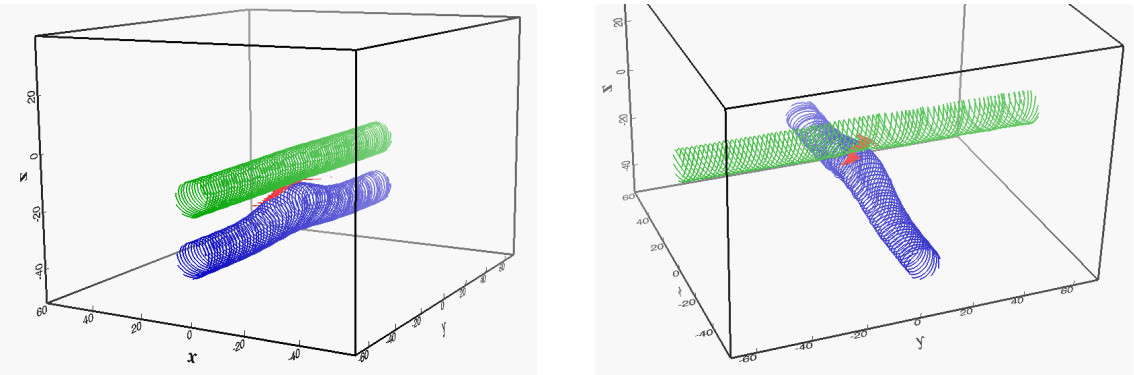

(a) Model 1 at $t = 30$.

(b) Model 2 at $t = 34$.

Figure 7.5: Outer fieldlines of ft1 (green) and ft2 (blue) for the various two tube models. The red isosurfaces show the current sheet, calculated as $|\mathbf{J}|/|\mathbf{B}|$, between the two flux systems. at a level of 5.6 and 4.9 for models 1 and 2, respectively.

speed is small compared to the sound speed, and the general motion of the tubes and surrounding plasma. The continued rise of ft2 under its own buoyancy ensures that the current sheet does not diffuse away between the two systems but is pushed upwards over time. As time progresses, the height of the strongest point in the current sheet matches the heights of the top of ft2 and bottom of ft1, shown in figure 7.3.

The reconnection of fieldlines proceeds from the outside of each tube moving towards their axes. The rate at which the reconnection advances towards the axis of an individual tube is dependent upon the amount of flux lying between the outer edge of the tube and its centre, measured along a radial line. Although the strength of ft2's magnetic field decreases overall as the tube rises, when the tubes make contact, the field strength on the axis of ft2 is still 3.3 times larger than that of ft1 in both models 1 and 2. Hence, the amount of flux in the vertical column lying between the axis of ft2 and its approximate front edge is much greater than that lying between the bottom edge of ft1 and its axis. Thus, the axis of ft1 is drawn into the reconnection region when the axis of ft2 is still surrounded by some of its original fieldlines. Therefore, the axis of ft1 reconnects with twisted fieldlines of ft2 and becomes wrapped around the axis of ft2, as shown in figure 7.6. Taking measurements along the central vertical line of the domain ($x = 0, y = 0$), it is no longer possible to detect the axis of ft1 once its reconnection occurs at $t = 59$ and $t = 56$ for models 1 and 2 respectively. This is shown by the disappearance of the lines representing ft1's axis for both models 1 and 2, labelled D and C in figure 7.3. The greater flux of ft2 results in the reconnection region never reaching its axis and, thus, the axis persists for the length of the simulation.

The rise of a flux tube in a domain with an overlying flux of significant strength has been considered by Dorch (2007) and Galsgaard et al. (2005) for the convection zone and corona respectively. They found that the inclusion of the flux sheet slows the rise of the tube, regardless of whether

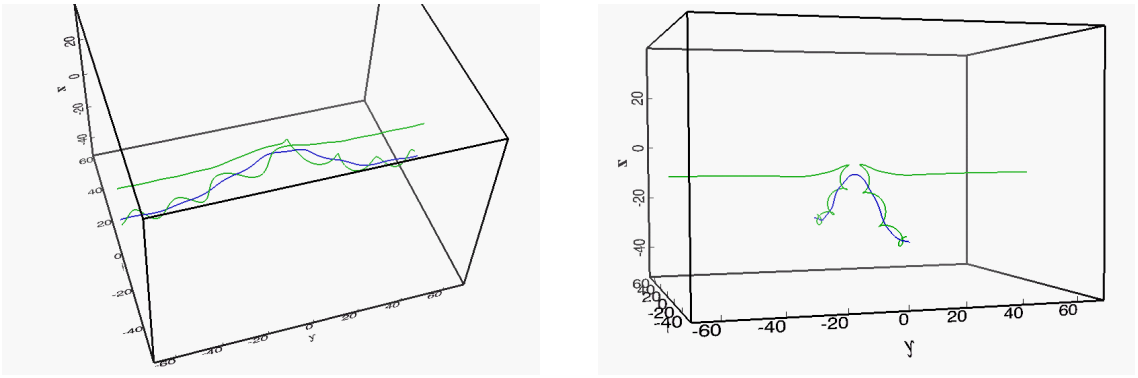

(a) Model 1 at $t = 59$.

(b) Model 2 at $t = 56$.

Figure 7.6: The axes of both ft1 (green) and ft2 (blue) for the various models. In both models the axis of ft1 has reconnected with twisted fieldlines lying above the axis of ft2 and, thus, the axis of ft1 has become wrapped around the axis of ft2.

reconnection occurs between the two magnetic systems. This slow down is due to the presence of an increased downward acting tension force associated with the "dented" flux sheet. There is a similar increase in the tension force when the horizontal sheet is replaced by a flux tube and we find a corresponding slower rise of the top of ft2 when ft1 is included in models 1 and 2.

The deceleration of the top of ft2 causes the field between the front and axis of ft2 to become compressed. There is a consequential increase in the upward directed magnetic pressure force above the axis. Thus, the axis experiences a slight acceleration in models 1 and 2 at ~ 52 time units, labelled B in figure 7.3. However, in model 0 there is less compression of the field situated above the axis and, therefore, the axis rises more slowly. Regardless of this acceleration, we find that in all of the models the axis of ft2 remains within the solar interior within the time of the experiments. Measurements of field strength, density and gas pressure identify that the presence of ft1 has little effect on the evolution of the axis of ft2.

During the reconnection process, ft2 is still rising through the solar interior. For the field of ft2 that does not undergo reconnection, the magnetic field strength, density and gas pressure have the same evolution with respect to time as they would if ft1 were not there, as shown by the evolution of the axis of ft2. When the first magnetic flux appears at the photosphere, there is still reconnection occurring in models 1 and 2. The effects of this and the emergence process of all three models will be discussed in section 7.7.

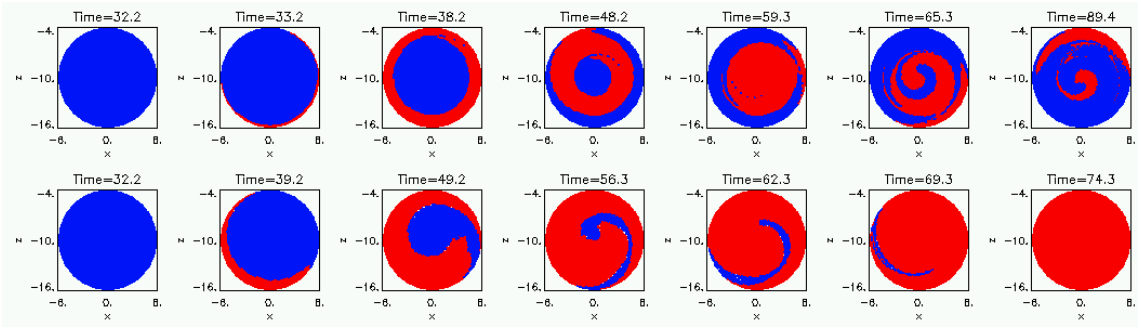

Figure 7.7: Fieldlines traced from one end of ft1 and coloured according to where each fieldline ends. Blue fieldlines start at one end of ft1 and end at the other end of ft1 and red fieldlines start at one end of ft1 and end in either end of ft2. The top and bottom rows of images are for models 1 and 2 respectively.

7.6 Connectivity & Reconnected Flux

To determine how the reconnection proceeds and differs in each of the models, we consider how the connectivity of fieldlines changes over time. We trace a large number of fieldlines (4881) from starting points that reside in one end of ft1 and calculate whether the endpoints lie in ft1 or ft2, a technique previously used by Parnell and Galsgaard (2004). The start points are divided between 39 concentric circles whose locus is $(-10, 0)$ in the (z, x) plane at $y = -70$, where the 39^{th} circle corresponds to a radius of $r_1 = 5.85$ units.

Before using this technique, we have analysed the velocities in the footpoints of ft1. For both models we find no signs of rotation in the start or end points of the fieldlines of ft1. Measurements of velocities in this region show the vertical velocity to be $\ll 1\%$ of the local sound speed throughout the tubes and 2% of the local Alfvén speed at the axis. Similarly, the transverse velocity is 0.2% of the local sound speed and has a peak of $< 0.7\%$ of the local Alfvén speed. Hence, we can be confident that there is no large scale movement of the footpoints. We cannot state emphatically that we trace the same fieldline over time when using the same starting point but, as we will see below, the general evolution of the footpoints gives a definite guide for where reconnection occurs and how the field connectivity changes.

The results of the connectivity technique are shown in figure 7.7 for model 1 *(top row)* and model 2 *(bottom row)*. Fieldlines whose end points lie within a radius $1.5r_1$ of the initial locus on the $y = 70$ plane are deemed to be fieldlines of ft1 and their start points are coloured blue. If a fieldline's end point lies within a suitable radius of the axis of ft2 on either the $\pm y$ planes for model 1 or the $\pm x$ planes for model 2, then the fieldline is considered to have reconnected and its start point is coloured red. Fieldlines whose end points meet none of these criteria are indicated by white start points but, as illustrated by figure 7.7, these occurrences are rare.

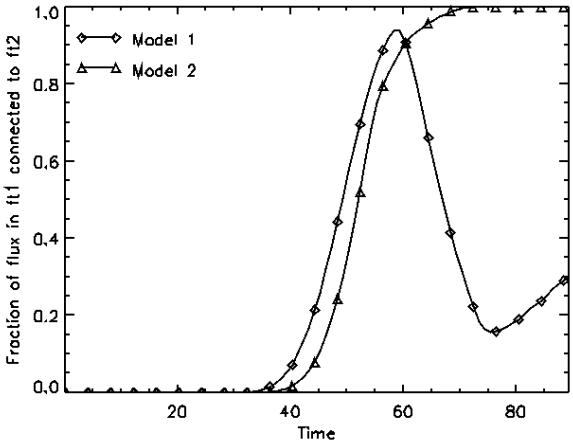

Figure 7.8: Fraction of the magnetic flux associated with the start points of ft1 that have endpoints in ft2 as a function of time for models 1 (diamonds) and 2 (triangles).

Figure 7.7 shows very different connectivity patterns for models 1 and 2, indicating that the reconnection proceeds in a different manner in each model. Additionally, figure 7.8 demonstrates that whilst the percentage of reconnected ft1 flux increases continually in model 2, there is an oscillating variation of reconnected flux with time for model 1.

7.6.1 Model 1 – Parallel Tubes

As previously stated, the current sheet formed between the two flux tubes in model 1 is long and thin, lying in the same direction as the axes of the two tubes. It is the outermost fieldlines of ft1 that will experience reconnection first as these are the first ones to come into contact with the field of ft2. For the fieldlines on this outer radius of ft1, reconnection occurs first for the fieldlines passing through the central point of the current sheet ($x = 0, y = 0$) above the most buoyant portion of ft2, as shown by figure 7.9(b). Over time, the location of the reconnection for the outer set of fieldlines moves away from the central point of the current sheet and migrates towards its flanks, illustrated in figure 7.9(c). Once the reconnection of fieldlines on a particular radius moves towards the flanks of the current sheet, reconnection will begin for the next inner radius of fieldlines, again starting in the centre of the current sheet, as shown in figure 7.10. And so the reconnection continues, for each radius starting in the middle of the current sheet and migrating to the flanks.

The fieldlines are highly twisted on the edge of ft1, thus all fieldlines on a certain radius will reconnect in the current sheet over a short period of time and a short length of the current sheet. At $t = 38.2$, figure 7.7 shows all of the fieldlines on the outer radii have reconnected with fieldlines from ft2 and, thus, their endpoints are now in ft2. However, ft2 is buoyant along a large portion of

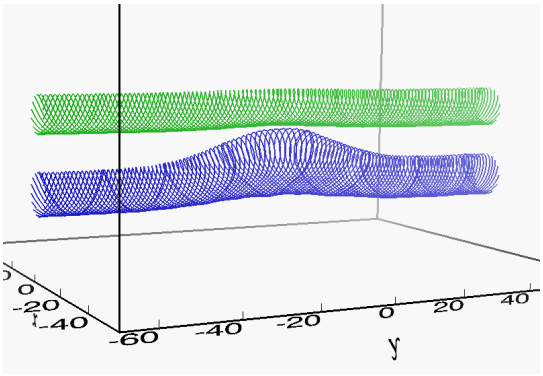

(a) $t = 35$.

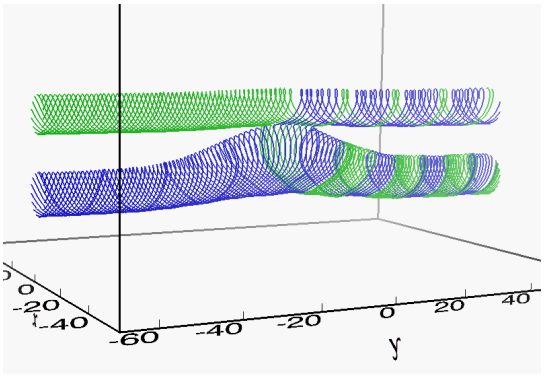

(b) $t = 37$.

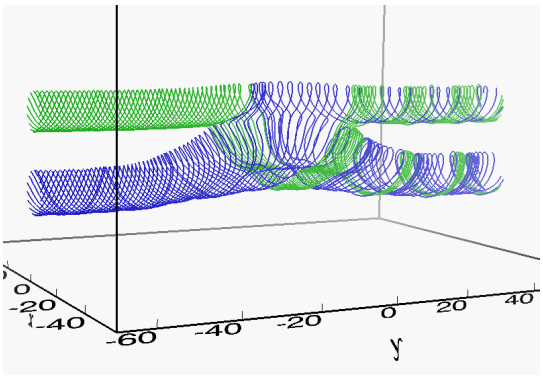

(c) $t = 48$.

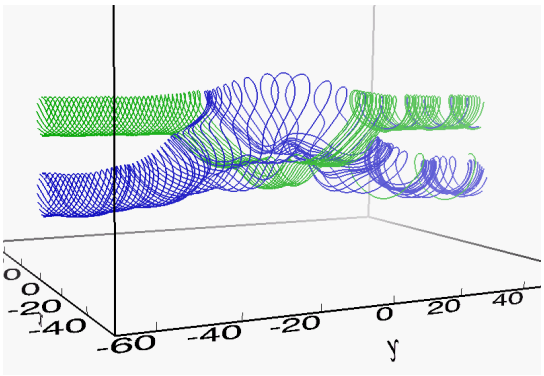

(d) $t = 65$.

Figure 7.9: For model 1, twisted outer fieldlines of ft1 (green) and ft2 (blue) at different times. Reconnection for these radii begins in the centre of the current sheet and over time moves out towards the flanks of the sheet. The fieldlines are traced from the $y = -70$ boundary.

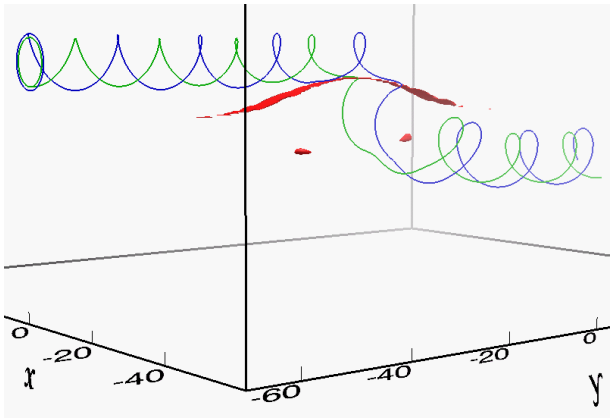

Figure 7.10: For model 1 at $t = 40$, the red isosurface indicates the current sheet at $|\mathbf{J}|/|\mathbf{B}| = 5.0$. The outer blue fieldline, traced from the blue circle with a radius of 4.5, is reconnecting in the flank of the current sheet while the inner green fieldline, traced from the green circle with a radius of 3.9, is reconnecting at the centre of the current sheet. The fieldlines are traced from the $y = -70$ boundary.

its length, with lessening degree away from $(x = 0, y = 0)$. Thus, the current sheet continues to extend in the axial direction as more of the outer fieldlines of each tube are brought into contact with each other. Fieldlines that have already experienced reconnection find themselves passing through the more recently created flanks of the current sheet. Hence, they undergo multiple and continual changes of connectivity during our experiment, figure 7.9(d). This is also visible in figure 7.7 from the changing spiraling patterns of colour at $t = 65.3$ and $t = 89.4$.

As the reconnection proceeds, the radius of the fieldlines, which are experiencing their first reconnection, migrates in towards the axis of ft1. The number of rotations of the fieldlines about the axis reduces as their distance from the axis reduces, according the constant twist definition. Thus, the fieldlines of inner radii will pass through the current sheet less times, with the inner most passing through only once. Figure 7.7 shows that once the central fieldlines have reconnected once they do not change their connectivity again within the time of the experiment. At $t = 59$, the time at which the axis of ft1 undergoes reconnection, we find that 94% of the flux belonging to ft1 has reconnected into ft2. Once the axis of ft1 has been reconnected, the central part of the current sheet diffuses away since the field above the axis of ft1 is orientated in the same direction as the field of ft2 it is coming into contact with.

The continuous reconnection of fieldlines gives rise to the oscillatory changes in the percentage of reconnected flux in figure 7.8. The fieldlines with start points nearer the locus of the circle have a greater amount of flux associated with them since the field strength increases with decreasing distance to the axis and, therefore, they influence the percentage of reconnected flux the most. These inner fieldlines are also the least twisted and have the greatest period of time between changes of connectivity. The initial period of increasing reconnected flux corresponds to reconnection of the inner circles for the first time, with the peak in the reconnecting flux occurring when the axis of ft1 changes connectivity. The decrease and subsequent increase in reconnected flux takes place as these inner fieldlines reconnect for a second and third time respectively. We believe the oscillatory pattern of figure 7.8 would continue if the experiment ran for longer, with the oscillation period increasing due to the decreasing buoyancy of ft2's legs with distance from the initial, central reconnection location.

By the end of the simulation, $t = 89$, the flux system in the centre of the domain is tube-like with fieldlines winding around the non-reconnecting core of ft2. The windings per unit length of the tube have reduced by a factor of 2. These findings are inline with those of Linton et al. (2001) and Linton (2006) and indicate a merging action in progress. If the experiment was run for longer, we believe the central single flux tube region would be extended as reconnection continues, although it is unclear whether a complete merger along the entire lengths of the tubes would occur.

7.6.2 Model 2 – Orthogonal Tubes

For model 2, the current sheet is much shorter since the orientation of the tubes brings a smaller area of them into contact with each other. At the start of the reconnection period, the current sheet is almost entirely horizontal and the particular twist constant chosen for the tubes results in even the greatly twisted outer fieldlines only passing through the current sheet once and, therefore, experiencing only one potential reconnection site.

For each circle of start points, reconnection begins with the fieldlines in the central location of the current sheet and then moves to the fieldlines in contact with the flanks of the current sheet. Hence, reconnection spreads both clockwise and anticlockwise on each circle between $t = 39.2$ and $t = 49.2$ in figure 7.7. The reconnected fieldlines are moved out of the reconnection region in a direction parallel to the reconnecting components. However, the twisted nature of the field prevents the fieldlines from escaping far from the interaction site of the two tubes.

At the time when the axis of ft1 reconnects, $t = 56$, 75% of the flux of ft1 has reconnected into ft2, figure 7.8. This is smaller than the level of reconnected flux experienced in model 1 by the time of its axis reconnection because the region of contact in model 2, and thus the current sheet, is much smaller. This allows fewer fieldlines to reconnect prior to the axis being reached. However, once the axis of ft1 has reconnected, the field above ft1's axis still has a differing orientation to the field of ft2 it is in contact with. Hence, the reconnection continues and the percentage of reconnected flux increases further. As can be seen from the isosurfaces of field magnitude in figure 7.11, the rise of ft2 causes ft1 to take on an Ω shape along its length and, thus, the current sheet between the two systems becomes more curved over time, though still ribbon like and with the same orientation.

The fieldlines of ft1 that reconnect in the centre of the current sheet belong to a special group of fieldlines. During their first reconnection, the majority of the axial and transverse components of these ft1 fieldlines were annihilated with the corresponding components of the ft2 fieldlines, leaving the vertical component as the most significant in size. The reconnection effectively "cut" these ft1 fieldlines and they lie on either side of ft1. Figure 7.11(a) illustrates the post-reconnection fieldlines on one side of ft1, which are traced from the footpoint of ft1 and are coloured by their B_z component. As the mass of ft2 continues to rise, these fieldlines become less curved with time and their B_z component diminishes. However, the reduction in B_z increases the significance of the small axial component, B_y, of the fieldlines and their orientation moves towards the axial direction, as shown in figure 7.11(b). The fieldlines become increasingly curved over the shoulder of ft2 and the return of a field component oppositely directed to the surrounding field results in a second reconnection located in one flank of the current sheet. This returns the end points of the set of fieldlines with start points in ft1 to ft1.

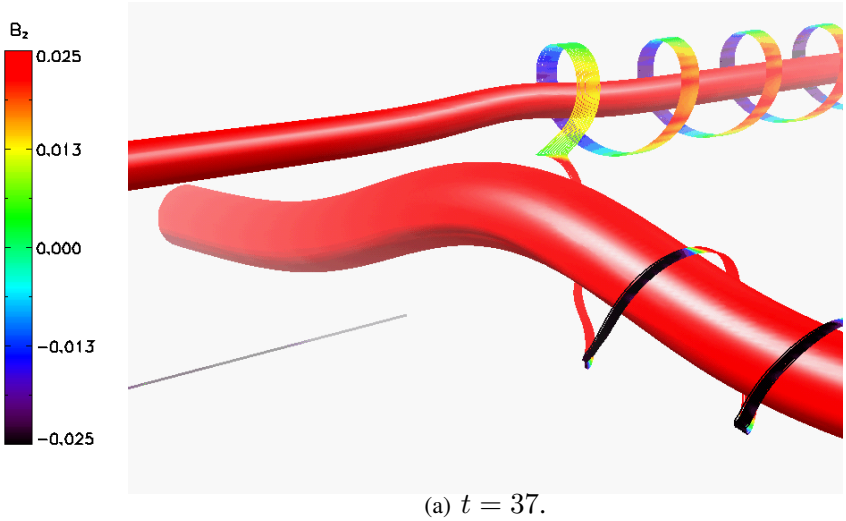

(a) $t = 37$.

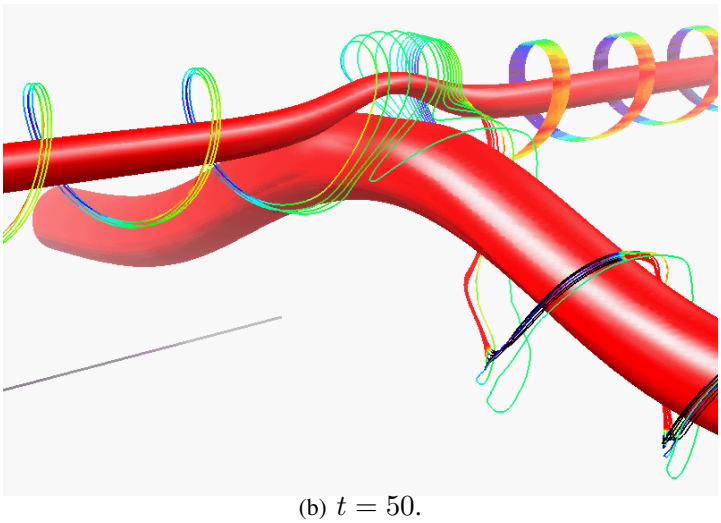

(b) $t = 50$.

Figure 7.11: For model 2, a selection of outer fieldlines traced from one end of ft1 at different times. The fieldlines are coloured along their length according to B_z and the right-hand colour bar indicates the scaling in use. The red isosurfaces give $|\mathbf{B}| = 2.0$.

This process of changing orientation and reconnection is replicated for the fieldlines on the other side of ft1. However, rather than the footpoints of the special group of fieldlines returning to ft1 through this secondary reconnection we find that the fieldlines that reconnect on one side of ft1 are the same fieldlines that will reconnect on the other side of ft1 and, thus they experience a total of three reconnections with their footpoints ultimately terminating in ft2. This is due to the specific twist of ft1 and radius of ft2. If the twist of ft1 had been less or the radius of ft2 has been greater we believe that, once the reconnection process finished, some fieldlines of ft1 would have had footpoints in ft2 whilst others would have had their footpoints returned to ft1.

If all of the fieldlines of ft1 reconnected only once we could expect to see symmetrical growth and slowdown in the rate of change of reconnected flux at the start and end of the reconnection phase respectively displayed in figure 7.8. This is because ft2 reconnects first with the weaker outer, then stronger inner and finally weaker outer field of ft1 as it "carves" its way to the surface. However, the reconnection slowdown occurs over a much longer period of time than the growth phase and this is as a result of the multiple reconnections of the select group of fieldlines.

All of the fieldlines associated with the 4881 chosen start points belong to one of two categories, either reconnecting once or three times and, therefore, when reconnection ends at $t = 74.3$ all of the fieldlines have their end points in ft2, figure 7.7.

From the results of Linton (2006), we would expect this orientation of equal strength tubes to result in them performing a slingshot action due to their low level of twist. We certainly see the start of this interaction, with the fieldlines of ft1 wrapping around the two legs of ft2 after the reconnection. However, once the reconnection ends we do not see a complete slingshot, which would have resulted in two differently connected and distinct tubes. This is because the tubes differ in strength by a factor of ~ 3.3 when they first come into contact with each other and the reconnection starts. For a complete slingshot it is necessary for the axis of ft1 to reconnect with the axis of ft2 but in our simulation this does not happen. Thus, we end up with the weaker tube hanging off the core of the stronger tube. This end state is also found by Linton (2006), whose tubes differed in strength by a factor of two.

7.7 Emergence

We must first establish the topology of the uppermost magnetic field prior to its arrival at the photosphere in models 1 and 2, before understanding how the emergence occurs. As discussed in section 7.6, reconnection changes the footpoints of the fieldlines originally belonging to both ft1 and ft2. Prior to emergence this process occurs at the interface between ft1 and ft2, which is situated away from the top edge of ft1. When considering the 3D structure of the flux, it becomes increasingly difficult to distinguish between the two tubes in the centre of the domain

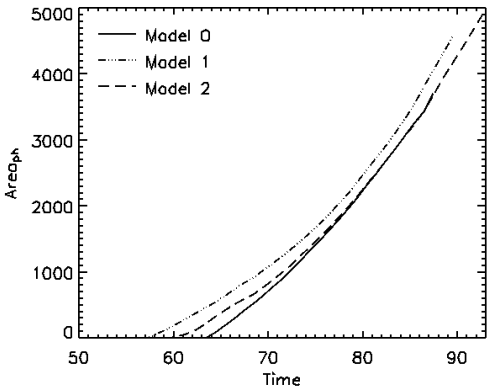

(a) Increase in the area of the photospheric plane $z = 0$ containing flux over time.

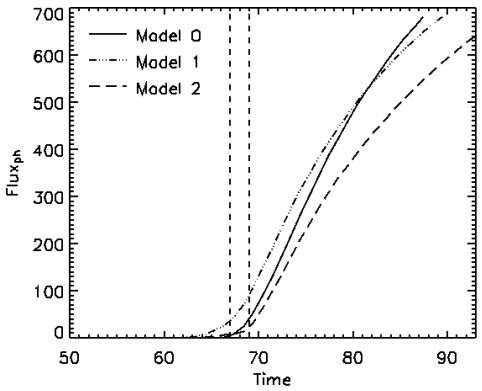

(b) Change in the vertical unsigned flux passing through the photospheric plane $z = 0$ over time. The time at which the buoyancy instability is satisfied for models 0 and 1 $(t = 67)$ and model 2 $(t = 69)$ is indicated by the first and second lines, respectively.

Figure 7.12: Measures of flux at the photospheric plane $z = 0$ for models 0 (solid), 1 (dot-dashed) and 2 (dashed).

as the reconnection advances. Although the field initially closest to the photosphere was that of ft1, reconnection means that these fieldlines could now belong to ft1, ft2, or have an endpoint situated in each. However, since reconnection occurs at the interface of ft1 and ft2 we know that the field segments at the top of the magnetic flux system, which originally belonged to ft1, remain unchanged and have approximately their original ft1 field strength. These segments are directly above the fastest rising portion of ft2, and, thus, it is this flux that will enter the photosphere first for models 1 and 2.

The flux at the photospheric plane $(z = 0)$ appears at different times for each of the models, namely $t = 63$, $t = 58$ and $t = 60$ for models 0, 1, and 2 respectively. This can be seen in figure 7.12(a) where the area of photospheric surface containing flux is charted over time. For model 0, the first flux will only be seen in the photosphere when the top of ft2 reaches the top of the convection zone. However, in models 1 and 2 ft1 lies between the top of ft2 and the photosphere. With ft2 pushing upwards at ft1's lower edge, the original top of ft1 can enter the photosphere whilst the top of ft2 is still several scale heights below the solar interior photosphere interface. Thus, accounting for the arrival for flux at the photosphere at an earlier time in models 1 and 2 than in model 0. The increase in the area of the photosphere containing flux occurs at a similar rate for all three of the models since this is related to the rise velocity of flux through the solar interior, initialised by the same buoyancy force for ft2 in each model.

As discussed in chapters 2 and 5, the transfer of the non-buoyant, magnetic flux into the atmo-

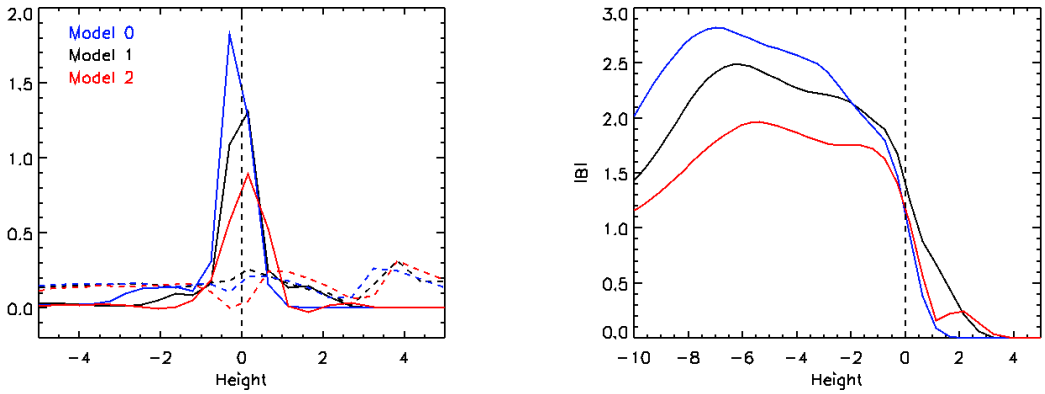

(a) The magnetic (solid lines) and convective (dashed lines) terms comprising the buoyancy instability (7.4).

(b) The magnitude of the field, $|\mathbf{B}|$.

Figure 7.13: Measurements associated with the magnetic buoyancy instability criterion, (7.4). The blue, black and red lines represent quantities in models 0, 1 and 2 respectively.

sphere occurs through a magnetic buoyancy instability. The instability is launched most easily by perturbations that bend fieldlines and specifically occurs when the following criterion is satisfied

$$-H_p \frac{\partial}{\partial z} (\log B) > -\frac{\gamma}{2}\beta\delta + \tilde{k_\parallel}^2 \left(1 + \frac{\tilde{k_\perp}^2}{\tilde{k_z}^2}\right). \tag{7.4}$$

We refer the reader to chapters 5 and 6 for details of the terms comprising this criterion. Dividing through the left-hand and right-hand terms of the inequality by β, we describe them simply as the magnetic and convective terms respectively.

This inequality was used effectively in chapter 5 and by Moreno-Insertis (2006) to demonstrate that tubes, whose magnetic field satisfies (7.4) when in the photosphere, will emerge. Figure 7.13(a) shows the magnetic and convective terms comprising the criterion at time $t = 67$ for model 0 and 1 and $t = 69$ for model 2. At these times the criterion is satisfied for the first time in the photosphere.

The instability is dependent upon the gradient in the field being sufficiently large that it exceeds the convective term. For model 0, the field at the front of the tube has a naturally steep profile due to the decrease in the field strength with increasing radius, as shown in figure 7.13(b). The gradient of the profile must still be steepened further but this happens relatively quickly resulting in a difference of only 4 time units between the first field entering the photosphere and the instability occurring. As stated above, when the magnetic field enters the photosphere in models 1 and 2, it is flux that originally belonged to ft1 and, therefore, it is much weaker than the first field that enters in model 0, which belongs to ft2. As in model 0, the buoyancy instability cannot occur

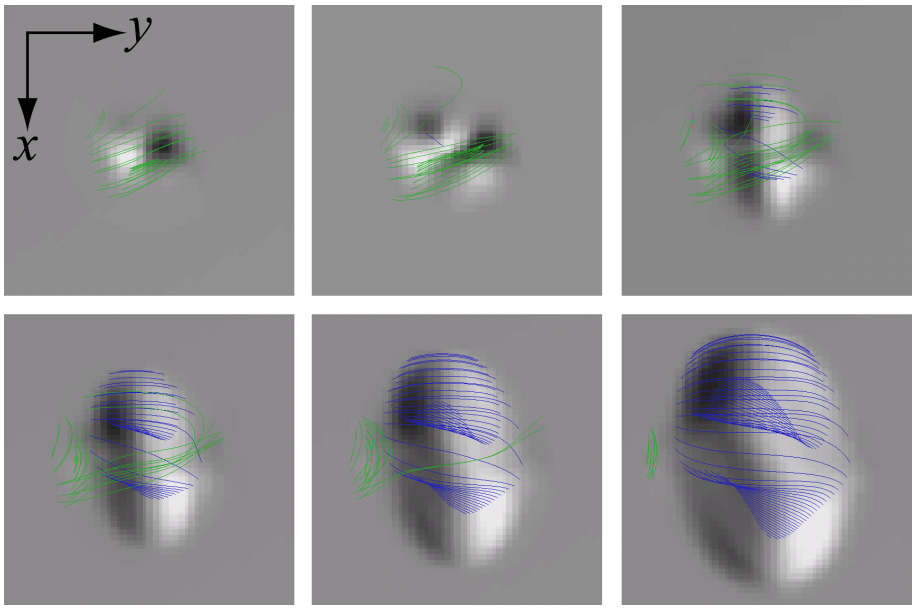

Figure 7.14: For model 2, synthesised magnetograms at the horizontal plane $z = 0$, with a selection of atmospheric fieldlines traced from the subsurface footpoints of ft1 (green) and ft2 (blue). Darker and lighter colourings represent $B_z < 0$ and $B_z > 0$ respectively, with the background grey giving the reference for $B_z = 0$. The images correspond to $t = 65,\ 67,\ 69$ *(top left, middle, right)* and $t = 71,\ 73,\ 76$ *(bottom left, middle, right)*.

immediately and, in both models 1 and 2, there is a delay of 9 time units until the stronger field of ft2 enters the photosphere and its profile steepens sufficiently.

Examining figure 7.12(b), we can see that once the buoyancy instability occurs there is a sharp change in the rate of increase of flux in the photospheric plane for each model. Once emergence starts, stronger tube flux starts to pass through the photosphere on its way to the upper atmosphere, which would have remained trapped below the photosphere had the instability not occurred. Flux can now advance into the transition region and on towards the corona.

For models 0 and 1, there is little noticeable difference during the first stages of flux emergence. In contrast, we find an initially complex evolution of the active region for model 2. Figure 7.14 shows synthesised magnetograms at the photospheric plane for model 2. Overlying the plane, are a selection of green and blue fieldlines traced from ft1 and ft2 respectively. When the first flux appears at the plane, it is orientated positive negative when crossing left to right. However, over the course of 11 time units the orientation switches to negative positive from left to right. The reconnection below the surface reduces constraints on the fieldlines and allows them to move. Hence, the segments of field of ft1, which were originally the uppermost, sink below the photosphere revealing the flux of ft2 as the uppermost flux, labelled E in figure 7.3. From $t = 76$ onwards, the evolution of model 2 continues as for the other models.

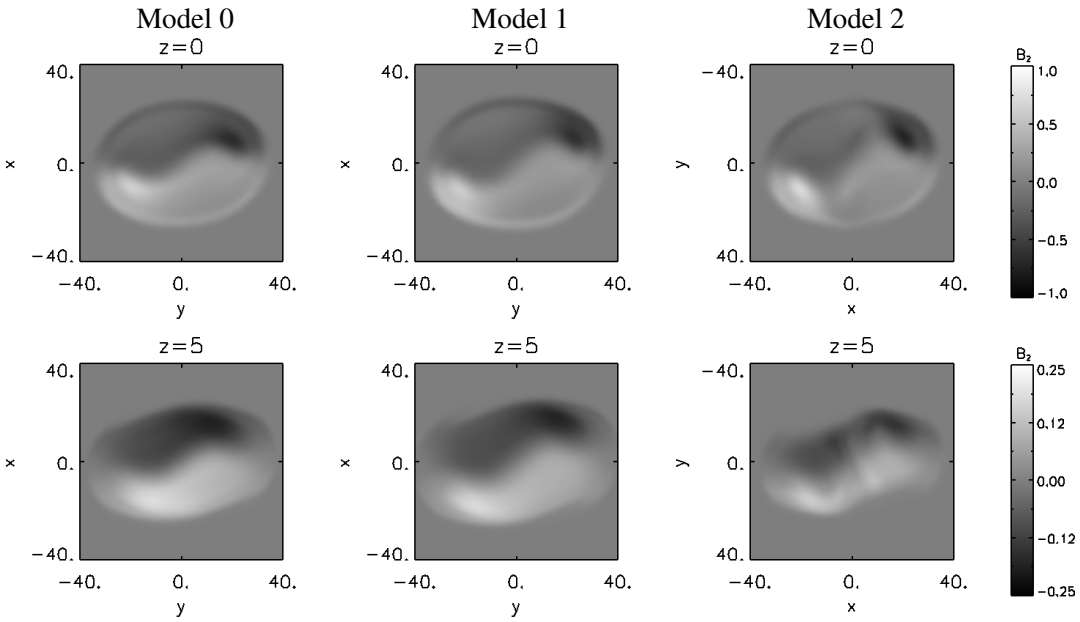

Figure 7.15: Synthesised magnetograms for the various models, constructed at horizontal planes corresponding to $z = 0$ *(top row)* and $z = 5$ *(bottom row)*. These measure the line of sight magnetic field component, B_z.

At $t = 80$, the flux pattern at the photospheric plane is the same for all of the models, as shown in figure 7.15. Concentrations of positive and negative flux form at opposite edges of the emergence region, where the minimum and maximum line of sight component of the field (B_z) is -0.7 and 0.7 respectively for all three models. As time advances, we find that the peak positive and negative strength in the bipoles increases and, at $t = 86$, the differences of these values between the three models are only ~ 100 Gauss. Study of the vertical field at a plane halfway through the photosphere, $z = 5$, shows slight differences arise in the case of initially orthogonal tubes. This difference occurs due to a variation in the line along which the buoyancy instability takes place.

At the photospheric plane, we find diverging horizontal velocity flows away from the centre of the flux region, with the strongest flows towards the concentrated bipolar sites. In the three models, the minimum and maximum values of these flows differ by only ~ 0.1, equivalent to $680\ \mathrm{m\ s^{-1}}$.

7.8 Conclusions

We have performed three simulations of solar flux emergence. Model 0 consists of a single twisted tube within the solar interior and the other models have two twisted flux tubes below the surface. In models 1 and 2, the tubes are orientated parallel and orthogonal to each other, respectively.

Through the interaction of the two tubes in models 1 and 2, a subsurface magnetic field of greater

complexity is created. The new flux system still has tube-like qualities such as a dominant orientation of the axial field and fieldlines twisting about a central structure. Our results are in line with those of previous "reconnecting tubes" studies (Linton et al. 2001; Linton and Antiochos 2005; Linton 2006). We can, therefore, conclude that the interaction of the tubes is independent of the force driving the tubes together and the plasma-β of the environment where the collision event occurs.

In all of our models, the subsurface field emerges into the atmosphere via a magnetic buoyancy instability. At this time reconnection is still occurring in the solar interior in both models 1 and 2. However, this is only evident in the atmospheric observations for the case when the two tubes are orthogonal, for which we see a reversal of the bipolar region during flux emergence. To our knowledge, this reversal has not been observed and there are two possible reasons for this. Firstly, the reversal does not occur either because flux tubes in the interior are not orthogonal and, therefore, do not reconnect in this way or because reconnection happens when the tubes are deeper within the solar interior and finishes by the time the emergence occurs. Secondly, the event we see occurs over a period of 4.5 mins but the cadence of MDI magnetograms is 5 mins so the event could pass completely unrecorded. With the launch of Hinode, we hope to be able to resolve the issue of whether bipolar reversal of emerging flux occurs since SOT will produce data with a cadence of ~ 45 s.

Our synthesised magnetograms, atmospheric fieldline traces and measurements of velocity reveal little difference. This is because emergence in the later stages is dominated by the field of the stronger tube, ft2. We, therefore, conclude that from these measurements alone it is not possible to determine whether the subsurface field is constructed from one or two flux tubes. A study by Linton and Priest (2003) investigated the interaction of two orthogonal, untwisted flux tubes when driven together. The tubes flattened into flux sheets and reconnected to form a single twisted flux tube. This suggests that interacting flux sheets would also show no difference during emergence.

At the experiment initialisation stage, we chose the lower tube to be much stronger than the upper tube since the results from chapters 5 and 6, together with previous studies, have shown that a flux tube's field strength will decrease as it rises (Archontis et al. 2004; Leake and Arber 2006). Although the field strength of the lower tube decreases during its rise, it is still much stronger than that of the upper tube upon contact, as discussed in section 7.5. Thus, the atmospheric results are dominated by the stronger lower tube. We believe that varying the ratio of the tubes' field strengths when they first come into contact will produce few visible atmospheric differences in the case of two parallel tubes but will have greater impact when simulating two orthogonal tubes.

If the orthogonal tubes are of equal strength when they first come into contact, we expect their axes to reconnect with each other, following the findings of Linton et al. (2001). Whether the two tubes would then be able to perform a complete slingshot action prior to emergence is hard to say.

This is a highly non-generic case but, if the tubes were to remain entwined during emergence, more complex photospheric patterns would surely be observed. If the lower tube is weaker than the upper tube upon contact, then the active region would presumably reflect the orientation of ft1 rather than ft2. The results would again be similar to those of models 0 and 1, without the need to rotate the simulation domain in order to achieve similar orientation of the active region. However, these effects are speculative and the necessary investigations have been left for a later date.

From our results we believe that, when studying and investigating generic flux emergence from an atmospheric viewpoint, it is acceptable to simplify simulations and use a single twisted flux tube as the subsurface source of the flux since the atmospheric field gives no indication of the structure of the subsurface field. Regardless of the seed flux, emergence into the atmosphere is characterised by rapid horizontal and vertical expansion and, thus, we conclude that the general results from previous flux emergence simulations are robust.

7.8 Conclusions

Chapter 8

Conclusions

To date, there have been a large number of simulations aiming to emulate solar flux emergence events. The results of these were presented in chapter 2. The simulations found that flux initially seeded in the solar interior cannot emerge into the atmosphere without the occurrence of a magnetic buoyancy instability. Post-instability, the magnetic field expands rapidly both vertically and horizontally into the atmosphere. The aim of this thesis was to determine the robustness of these general results upon the seed magnetic field. We identified four characteristics of the seed field which could affect the emergence of flux and that had previously not been studied in detail. These were the field strength and degree of twist of a constant twist flux tube, the use of non-constant twist flux tubes as a seed field and the complexity of the seed field.

In order to test the robustness of the general results, it was necessary to carry out further emergence simulations. `Diffin3d`, the numerical code for the simulations, was presented in chapter 3. `Diffin3d` is a finite difference code that advances a simulation domain in time by solving the MHD equations.

In chapter 4, we discussed the setup of the hydrostatic atmosphere within the simulation domain, which had been used extensively in previous emergence experiments (Archontis et al. 2004, 2005, 2006; Galsgaard et al. 2005, 2007) and would be used in all of the simulations comprising this thesis. The atmospheric temperature profile used in this setup lead to the introduction of unwanted vertical velocities when implemented numerically since hydrostatic balance was not perfectly created. We considered several adjustments to the temperature profile and the calculation of the gas pressure and density profiles in order to correct this. In the photosphere, we modified the function prescribing the increase in the strength of the atmospheric magnetic field and the improvements associated with this have been twofold. Firstly, the magnetic profile at the interface of the photosphere and transition region is now continuous providing that the grid spacing is not chosen to be too large. Secondly, hydrostatic balance in the photosphere can now be implemented via an

analytical expression rather than a numerical method, the latter being less accurate. These modifications have greatly reduced the size of the unwanted vertical velocities arising in the domain and increased the size of the time step between successive iterations, thus reducing the number of iterations required to complete a time unit. We recommend that this new atmospheric setup should be used in all future flux emergence simulations.

Constant twist flux tubes have been used in all of the previous emergence simulations that take a flux tube as the seed magnetic field. In chapter 5, we independently varied the parameters of the flux tube that prescribed the field strength and twist of the flux tube.

When the field strength was varied, we discovered that the tubes exhibit a self-similar evolution. This means that the differences in a quantity, such as the rise time of the tube in the solar interior, between two or more flux tubes can solely be attributed to their differing field strengths. Thus, by appropriate scaling, a distinct profile for the quantity as a function of time can be retrieved that is independent of the field strength. We found this also extended to the magnetic strength of the tube's axis, the area of the photospheric plane containing flux and the amount of flux transported into the atmosphere. Additionally, we found that the thin flux tube approximation, although not strictly applicable, correctly describes the decrease in the strength of the axis and, therefore, the expansion of the tube during its initial rise phase. For the particular flux tube we considered, a low field strength results in the tube remaining trapped in the low photosphere due to its failure to initiate the magnetic buoyancy instability. Conversely, flux tubes with a strong axial field component are able to emerge and expand into the atmosphere following the general results of previous simulations.

When the value prescribing the constant twist of the flux tube was varied, we did not see such easily quantifiable self-similar behaviour. Reducing the degree of twist causes a reduction in the tension force across the tube and, consequently, reduces the ability of the tube to remain a cohesive structure as it rises through the solar interior. In the low twist case that we simulated, the distortion prevented a magnetic buoyancy instability from being initiated once the tube arrived in the photosphere. For higher twist cases, we found that the tubes were able to emerge and expand into the atmosphere following the general results. Interestingly, we found that in the region of the parameter space between low twist and high twist, which do not and do emerge respectively, double emergence events are possible. In these cases, emergence fails to be initiated at the buoyant crest of the tube but, due to draining of plasma along fieldlines, magnetic buoyancy instabilities occur at two separate side locations and emergence ensues from these regions.

In chapter 6, we investigated the effects of using non-constant twist flux tubes as the seed flux. To date, there have been only a few studies that consider this type of tube rising through the solar interior and no self-consistent simulations of flux emergence using non-constant twist flux tubes. We chose two different twist profiles and explored their parameter spaces that govern the rate of

change of the twist as a function of radius. We found that the occurrence of a magnetic buoyancy instability is highly dependent on the strength of the field when it reaches the photosphere and is relatively independent of the original twist profile of the tube. In general, a high tension force is required to prevent the tube from expanding too greatly when it rises through the solar interior and, thus, the field strength reducing to the extent that the instability fails. Of the cases where emergence does occur, the high tension force cases accelerate into the atmosphere quicker, transporting more flux with them, while the lower tension cases experience greater horizontal expansion. Once the field has expanded into the atmosphere, the characteristics of the initial twist profile are by and large lost. Therefore, we expect observations of solar flux emergence events to fail to find distinctive features of the magnetic field that would provide specific details of the twisted nature of any flux tubes prior to their emergence.

In a move to increase the complexity of the seed field, we placed two flux tubes below the solar surface in the simulations of chapter 7. One of the tubes was chosen to be stronger and was set slightly deeper in the solar interior. Two simulations were performed with the tubes at parallel and orthogonal orientations to each other. In both cases we found that, when the two tubes come into contact with each other, a current sheet develops and reconnection ensues. In the case of two parallel tubes, the reconnection changes the topology of the magnetic field such that the two tubes begin to merge into one single tube. In the case of two orthogonal tubes, the reconnection results in the weaker upper tube hanging of the core of the lower tube. Upon emergence, there is only a small initial time period during which it is possible to distinguish the difference between the parallel and orthogonal cases. After this finite period, the emergence is observationally the same in the simulations with two tubes and the control simulation, which contains only the lower stronger tube, reproducing the standard emergence results. This indicates that the stronger tube is the dominant emergence feature and, in these simulations, the reconnection had limited success in increasing the complexity of the subsurface magnetic field.

In conclusion, we find that all of the aspects of the seed field that we have tested, contain a region of the parameter space that is capable of reproducing the general results of previous emergence simulations. Hence, we conclude that these general results are robust. However, we have also found that there is a section of the parameter space under which emergence fails. More specifically, emergence does not occur for constant twist flux tubes with low field strength or low twist or for non-constant twist flux tubes with low tension forces. Although in cases of emergence the fastest rate of rise of the tube into the atmosphere is largely independent of the field strength and twist, we find that the amount of flux transported into the atmosphere is highly dependent on the initial parameter values of the seed field and, therefore, comparisons with observations should be made carefully.

8.1 Suggestions for Future Work

In this thesis, we have investigated the effects of modifying the seed magnetic field in emerging flux simulations. The background atmospheric environment of the domain has remained the same in all of the experiments. In order to fully understand the emergence process, there are a number of further studies that should be carried out, which involve modifying the seed magnetic field and the atmospheric structure of the domain.

Our investigations of the field strength and degree of twist of the flux tube, in chapter 5, revealed that low parameter values resulted in no emergence. We believe that these results are in fact strongly dependent upon the amount of flux contained within the flux tube, such that if the tube contains too little flux it will not be able to emerge. Hence, a low twist but stronger flux tube or a high twist but weaker flux tube may actually be able to emerge due to its increased levels of flux. In order to determine whether the amount of flux is the dominant factor, a study of the effects of the radius of the tube on the emergence process should be carried out, since this parameter is key in determining the amount of flux in the tube initially.

As discussed in chapter 2, few emerging flux tube simulations set the seed flux in a convecting solar interior. By failing to reflect the true atmospheric conditions under which solar flux emerges, the results from emergence simulations will always be simplified in comparison with observations. The work of Tortosa (2007) is making headway in this area by forcing the tube to rise through a convecting region prior to arriving at the photosphere and emerging into the atmosphere. The author has found that convective motions hinder and distort the flux tube as it rises and, thus, we expect that the inclusion of convection will alter the values of the parameters of the tube which support emergence in a marginally stable convective regime. The amount of flux in the tube may well need to be considerably higher and this would increase the minimum field strength and twist parameters required for emergence in chapter 5. Therefore, a full parameter space study should be carried out in a fully convecting regime in order to determine the required level of flux for emergence to occur.

The simulations in chapter 7 aimed to create a more complex seed field but, prior to emergence, the new flux system still had many tube-like characteristics. For this reason, the differences in the emergence process between a single flux tube and the resulting complex field were very slight. We would like to simulate the emergence of a truly random and complex field in order to identify whether the emerging simulations using a flux tube as the seed field better represent large-scale solar emergence events. As for the form of this random seed field, we are unsure as to how it should be defined and initialised.

There have been many previous simulations that include an atmospheric field in the corona into which the seed flux emerges. However, there has been no investigation into how the relative

strength of the coronal field and the emerging flux modifies the atmospheric expansion and reconnection processes. Increasing the strength of the coronal field will cause increases in the atmospheric flux, tension force and Alfvén speed and decreases in the plasma-β. In the cases where no reconnection is possible between the two flux systems, the back-reaction of the coronal field will be much stronger when it becomes dented and, thus, we would expect to see the emerging flux decelerate quicker. In the cases where reconnection does occur, we would expect any reconnection jets to be slower since the magnetic pressure gradient along the reconnected fieldlines will be smaller. Alternatively, as found in chapter 5, increasing the strength of the emerging field will increase the amount of flux in the atmosphere available for reconnection. If reconnection was to occur at the same rate, tubes with more flux should be subject to reconnection for a longer period of time, thus allowing them to rise higher into the atmosphere.

These are just a few areas of flux emergence simulations that could be investigated further. The most immediately useful studies will be those that produce comparable results with solar observations. However, these simulations require the inclusion of complex and interacting physics and, therefore, it can be difficult to understand the individual effect of each different physical aspect. Simplified simulations are vital for providing this knowledge and, although they often produce exceedingly simplified results in comparison to solar observations, they remain an incredibly important tool.

Appendix A

Derivation of `Diffin3d`'s Finite Difference Methods

Following on from the discussion in section 3.3.1, we now present the derivation of the finite difference methods used by `Diffin3d` for performing differentiation and interpolation operations.

We begin by considering the sixth order error differentiation scheme. To find the derivative of the function f at the point $i+\frac{1}{2}$, we will use the neighbouring 3 points on either side in the direction of the derivative, namely the set $\{i-2, i-1, i, i+1, i+2, i+3\}$. On a uniform grid, the distance between these points is constant. To give this explanation more context, we will consider finding $\left(\frac{\partial f}{\partial x}\right)_{i+\frac{1}{2}}$, where the distance between each point is Δx, say.

From this point forward, we will use the notation $\frac{\partial f_{i+\frac{1}{2}}}{\partial x}$ to represent the partial derivative of f with respect to x, evaluated at the point $i+\frac{1}{2}$.

Only information at full gridpoints is know, thus we make a change of variable to enable us to evaluate the derivative at the half grid point without interpolation. We choose $j = i + \frac{1}{2}$ and set $2\Delta y = \Delta x$. Thus, the original six neighbouring points are modified such that the set becomes $\{j-5, j-3, j-1, j+1, j+3, j+5\}$ and the distance between neighbouring points is Δy, as illustrated in figure A.1.

Using a Taylor series expansion, we can calculate the value of a function, f, at any point using only the value of the function at the point j and the derivatives of the function evaluated at the same point. For example,

$$f_{j+1} = f_j + \frac{\Delta y}{1!}\frac{\partial f_j}{\partial x} + \frac{\Delta y^2}{2!}\frac{\partial^2 f_j}{\partial x^2} + \frac{\Delta y^3}{3!}\frac{\partial^3 f_j}{\partial x^3} + O\left(\Delta y^4 \frac{\partial^4 f_j}{\partial x^4}\right) + \ldots. \tag{A.1}$$

Appendix A

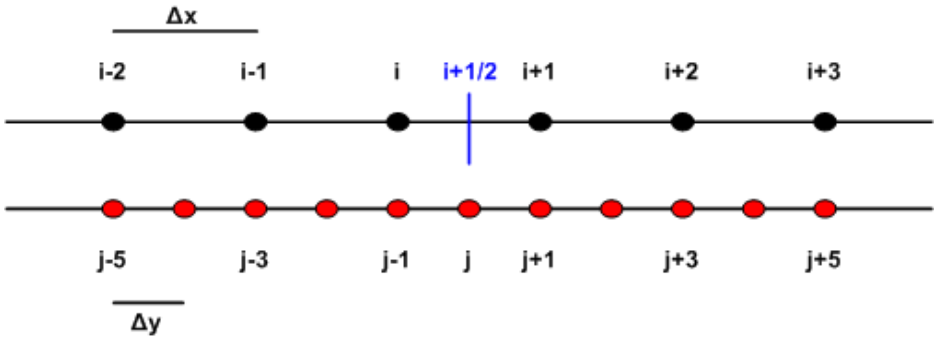

Figure A.1: The points of the array are originally labelled with i-indices and have a uniform spacing of Δx. In order to determine the derivative at the point $i + \frac{1}{2}$, the subscripts of the points are changed to have j-indices, with the spacing between consecutive points now Δy.

Δy gives the distance between the point at which the function is being calculated and the point upon which the calculation is based. We can calculate the function at any non-neighbouring point to j by multiplying Δy by a constant such that it represents the distance between the two points. For example, to find a value for f at $j + 3$ calculated about j we would use $3\Delta y$. Hence, the Taylor expansion would be

$$f_{j+3} = f_j + \frac{3\Delta y}{1!}\frac{\partial f_j}{\partial x} + \frac{3^2\Delta y^2}{2!}\frac{\partial^2 f_j}{\partial x^2} + \frac{3^3\Delta y^3}{3!}\frac{\partial^3 f_j}{\partial x^3} + O\left(\Delta y^4 \frac{\partial^4 f_j}{\partial x^4}\right) + \ldots . \tag{A.2}$$

We note that evaluation of points below f_j introduces negative signs in front of the the terms with partial derivatives raised to odd powers. We use this approach to derive expansions for all of the points in the set $\{j-5, j-3, j-1, j+1, j+3, j+5\}$.

We now subtract the points pairwise, such that a pair comprises of equidistant points from j. Equal weighting is given to the values comprising each pair, although different weightings are applied to each individual pair. Thus, we have

$$a_1\left(f_{j+1} - f_{j-1}\right) + b_1\left(f_{j+3} - f_{j-3}\right) + c_1\left(f_{j+5} - f_{j-5}\right). \tag{A.3}$$

By combining the values in this way and substituting the appropriate Taylor expansion for each j-point, all of the even ordered terms are removed from (A.3), including f_j. (The order of each term is given by the power Δx or Δx it is raised to.) We now have (A.3) being equivalent to the following

$$k\frac{\Delta y}{1!}\frac{\partial f_j}{\partial x} + l\frac{\Delta y^3}{3!}\frac{\partial^3 f_j}{\partial x^3} + m\frac{\Delta y^5}{5!}\frac{\partial^5 f_j}{\partial x^5} + O\left(\Delta y^7 \frac{\partial^7 f_j}{\partial x^4}\right) + \ldots, \tag{A.4}$$

where k, l and m are expressions in terms of a_1, b_1 and c_1.

With the removal of the f_j term and the terms with even partial derivatives, the remaining leading

term is a factor of $\frac{\partial f_j}{\partial x}$ and $O(\Delta x)$. Hence, by setting the coefficients of all but the new leading term to zero it becomes possible to evaluate the first partial derivative of f_j with respect to x. Thus we must solve the following

$$a_1 (f_{j+1} - f_{j-1}) + b_1 (f_{j+3} - f_{j-3}) + c_1 (f_{j+5} - f_{j-5}) = k \frac{\Delta y}{1!} \frac{\partial f_j}{\partial x}, \tag{A.5}$$

for a_1, b_1 and c, where we choose $k = 2$ for convenience.

Although we have set the coefficients of the higher order terms to zero, we must still use them to find the values of a_1, b_1 and c_1. Given that we have six neighbouring points, the largest polynomial that we can uniquely solve for will be fifth order and, thus, there will be an associated error term. The use of six points determines that we only use the remaining terms up to, and including, the $O\left(\Delta x^5\right)$ term. Comparison of likewise ordered terms, provides the following three equations:

$$2(a_1 + 3b_1 + 5c_1)\frac{\Delta y}{1!}\frac{\partial f_j}{\partial x} = 2\frac{\Delta y}{1!}\frac{\partial f_j}{\partial x}, \tag{A.6}$$

$$2(a_1 + 3^3 b_1 + 5^3 c_1)\frac{\Delta y^3}{3!}\frac{\partial^3 f_j}{\partial x^3} = 0, \tag{A.7}$$

$$2(a_1 + 3^5 b_1 + 5^5 c_1)\frac{\Delta y^5}{5!}\frac{\partial^5 f_j}{\partial x^5} = 0. \tag{A.8}$$

Removing common factors from each equation, we are left to solve the following matrix problem to find a_1, b_1 and c_1

$$\begin{pmatrix} 1 & 3 & 5 \\ 1 & 3^3 & 5^3 \\ 1 & 3^5 & 5^5 \end{pmatrix} \begin{pmatrix} a_1 \\ b_1 \\ c_1 \end{pmatrix} = \begin{pmatrix} 1 \\ 0 \\ 0 \end{pmatrix}. \tag{A.9}$$

Solving (A.9) yields $a_1 = 1 - 3b_1 - 5c_1$, $b_1 = -(1 + 120c_1)/24$ and $c_1 = 3/640$.

Reverting to subscript i and Δx in (A.5), we have

$$\frac{\partial f_{i+\frac{1}{2}}}{\partial x} = \frac{a_1}{\Delta x}(f_{i+1} - f_i) + \frac{b_1}{\Delta x}(f_{i+2} - f_{i-1}) + \frac{c_1}{\Delta x}(f_{i+3} - f_{i-2}), \tag{A.10}$$

with the values of a_1, b_1 and c_1 remaining unchanged.

The highest order term considered was of $O\left(\Delta x^5\right)$ and the $O\left(\Delta x^6\right)$ term disappeared during the subtraction phase in (A.3) leaving the error term as $O\left(\Delta x^7\right)$. However, since we have divided by Δx in (A.10) the error is reduced to $O\left(\Delta x^6\right)$. Thus, we have a fifth order accurate derivative method, which returns values at half grid points. It should be noted that a fifth order accurate method is equivalent to a method with a sixth order error.

Appendix A

To derive the fifth order accurate interpolation method, we use a very similar process as that for finding the differentiation method. We consider finding $f_{i+\frac{1}{2}}$ using the values of the neighbouring points in the x direction. We use the same six points $\{i-2, i-1, i, i+1, i+2, i+3\}$ to find the interpolated value at the point $i+\frac{1}{2}$ and, again, convert these into points with j subscripts. We use the same j-indexed pairings as before but, this time, we add the elements of each pair. Thus, we have

$$a_2\left(f_{j+1}+f_{j-1}\right)+b_2\left(f_{j+3}+f_{j-3}\right)+c_2\left(f_{j+5}+f_{j-5}\right). \tag{A.11}$$

Substituting in Taylor series expansions for each point gives (A.11) equivalent to

$$nf_j+p\frac{\Delta y^2}{2!}\frac{\partial^2 f_j}{\partial x^2}+q\frac{\Delta y^4}{4!}\frac{\partial^4 f_j}{\partial x^4}+O\left(\Delta y^6\frac{\partial^6 f_j}{\partial x^6}\right)+\ldots, \tag{A.12}$$

where n, p and q are expressions in terms of a_2, b_2 and c_2. We wish to obtain a value for f_j and, therefore, choose to set the coefficients p and q to zero. Hence, we must solve

$$a_2\left(f_{j+1}+f_{j-1}\right)+b_2\left(f_{j+3}+f_{j-3}\right)+c_2\left(f_{j+5}+f_{j-5}\right)=nf_j, \tag{A.13}$$

for a_2, b_2 and c_2, where we choose $n=2$ for convenience.

Again, we can only uniquely solve for a fifth order polynomial with the six input points. Thus, we consider only the remaining terms up to, and including, the $\mathrm{O}(\Delta x^4)$ since the $\mathrm{O}(\Delta x^5)$ term has already been eradicated. Hence, we must solve the following three equations:

$$2(a_2+b_2+c_2)f_j = 2f_j, \tag{A.14}$$

$$2(a_2+3^2b_2+5^2c_2)\frac{\Delta y^2}{2!}\frac{\partial^2 f_j}{\partial x^2} = 0, \tag{A.15}$$

$$2(a_2+3^4b_2+5^4c_2)\frac{\Delta y^4}{4!}\frac{\partial^4 f_j}{\partial x^4} = 0, \tag{A.16}$$

which reduces to the matrix problem

$$\begin{pmatrix}1 & 3 & 5\\ 1 & 3^2 & 5^2\\ 1 & 3^4 & 5^4\end{pmatrix}\begin{pmatrix}a_2\\ b_2\\ c_2\end{pmatrix}=\begin{pmatrix}1\\ 0\\ 0\end{pmatrix}. \tag{A.17}$$

Solving this gives $a_2=1-b_2-c_2$, $b_2=-(1+24c_2)/8$ and $c_2=3/128$.

Returning to subscripts i and Δx in (A.13) yields

$$f_{i+\frac{1}{2}}=\frac{1}{2}\left[a_2\left(f_{i+1}+f_i\right)+b_2\left(f_{i+2}+f_{i-1}\right)+c_2\left(f_{i+3}+f_{i-2}\right)\right], \tag{A.18}$$

with the values of a_2, b_2 and c_2 remaining unchanged.

For the interpolation method, the highest order term considered was of $O\left(\Delta x^4\right)$ and the $O\left(\Delta x^5\right)$ term disappeared during the addition phase in (A.11), leaving the error term as $O\left(\Delta x^6\right)$. Here, we have not been required to divided by Δx and, therefore, the error term does not decrease in order. Thus, we have a fifth order accurate and sixth order error interpolation method, which returns values at half grid points.

Hence, both the differentiation and interpolation methods used by `Diffin3d` are fifth order accurate, which is equivalent to having a sixth order error.

Appendix A

Appendix B

Input file for `Diffin3d`

Input files give `Diffin3d` the values of required parameters and allow the user to input parameter values specific to the particular setup of their model. Each simulation requires one input file. The contents of the file should be as follows:

`201,100,100,8,2`	: [1] N_z, N_y, N_z, HD/MHD, CPU_x
`loop_fan_smooth.start`	: [2] Name of start-up routine for model
`init.fe`	: [3] Name of existing data files, if any
`fan_along.fe`	: [4] Name to be given to data files
`fan_along.time`	: [5] Name to be given to time file
`1,1,`	: [6] $\mathrm{Snapshot}_{\mathrm{in}}$, $\mathrm{Snapshot}_{\mathrm{out}}$
`5000,100,1.,`	: [7] N_t, $\mathrm{Iteration}_{\mathrm{gap}}$, t_{gap}
`92,140,120,`	: [8] z_{len}, y_{len}, x_{len}
`0.0d-1, 3.0d-1, 2.0,`	: [9] ν_1, ν_2, ν_3
`0.0d-2, 3.0d-1, 5.0d-1,`	: [10] η_1, η_2, η_3
`1,`	: [11] Inclusion/exclusion of gravity
`,1e-5,,.3,`	: [12] t_0, Δt_{min}, Δt_{prev}, C
`0.0,0.,0.0,`	: [13] $e_{equilib}$, t_{cool}, t_{rise}
`1.66666666,0.0,0.,0, 0,`	: [14] γ, chi (t_rho), Driver, ρ_0, e_0
`22,42,92,.33,.33,`	: [15] z_1, z_2, z_{max}, p_1, p_2
`70,35,1,`	: [16] y_{max}, y_{half}, type_y
`60,30,1,`	: [17] x_{max}, x_{half}, type_x
`22.,32.,42.,1.,150.,1.,1.,1.,`	: [18] Atmospheric parameters
`2.5,2.9,.4,12.,20.,`	: [19] Magnetic parameters
`2,82,92,.3,.3,`	: [20] $D_{z\ lower}$, $D_{z\ upper}$, z_{max}, $\Theta_{z\ lower}$, $\Theta_{z\ upper}$
`-55,55,60,-.5,-.5,`	: [21] $D_{y\ lower}$, $D_{y\ upper}$, y_{max}, $\Theta_{y\ lower}$, $\Theta_{y\ upper}$

Appendix B

For each line of the file, any text after the ":" is treated as a comment and ignored. The lines have been numbered only to aid discussion of their implication. Similarly, the horizontal bold lines do not appear in a true input file but have been included to indicate the section of the input file (lines [15]–[19]) that is unique to the initialisation of a particular model. We will now consider each line of the file and its meaning in turn:

[1] The first three parameters give the number of gridpoints in the z, y and x dimensions. Following this, an integer is given to indicate whether to use the code under a hydrodynamic guise (`5`) or use the full MHD equations (`8`). This integer corresponds to the number of basic stored variables from the set $\rho, e, \mathbf{P}, \mathbf{B}$ that will be used. The final integer states the number of processors to be allocated in the x direction (the number of processors in the y direction will be given when the simulation is submitted for running).

[2] This is the name of the start-up routine for the particular model with `.start` concatenated to the subroutine's name.

[3] In the case of continuing an experiment, this line indicates the prefix name of the existing data files followed by `.fe`. For example, if the simulation's data files are named `fan_along.0.1.fe`, then the prefix would be `fan_along` and the line would read `fan_along.fe`. Otherwise, if starting an experiment from scratch, this line would read `init.fe`.

[4] This is the prefix name to be given to the data files produced during this particular run of the simulation. Each data file will also be numbered according to the processor it was produced by.

[5] This is the name given to the time file, which shows the progress of the simulation while it is running. The time file contains a single line stating the number of iterations that have been carried out so far during the run, the actual value of time, t, this corresponds to and the size of the current time step, Δt.

[6] While the simulation is running, data is output at intervals and is stored in data files where the next snapshot's quantities follow immediately on from the previous snapshot's. The number of a snapshot corresponds to the number of outputs so far and is used to index into the data files and retrieve data. These two integers indicate the snapshot to start the experiment at and the snapshot to output the first data to. In the case of starting an experiment from scratch, these will both be 1.

[7] The first integer states the total number of iterations of the code to be made. Once this number is reached the simulation will be stopped regardless of its current status. During the simulation, data is recorded at given intervals and stored in the data files in the form of a

snapshot. A snapshot will be output every $\mathrm{Interation}_{\mathrm{gap}}$ iterations or once enough iterations have occurred such that t_{gap} time units have passed since the last recorded snapshot.

[8] These three values give the total length of the domain in the z, y and x directions.

[9] These three values correspond to the viscosity coefficients, discussed in section 3.4.

[10] As for the previous line, these values correspond to the magnetic resistivity coefficients. The user can request uniform resistivity by setting the value of the first coefficient to be negative, although the actual value of the coefficient will be taken as positive inside `Diffin3d`. Under uniform resistivity, the values of ν_2 and ν_3 are not required but proxy values should still be included in their place.

[11] This parameter prescribes the value for the gravity constant g_0, where $\mathbf{g} = g_0\hat{\mathbf{z}}$. If this value is set to 0, then gravity is effectively turned off.

[12] These four values are associated with the simulation's time steps. t_0 gives the starting value for t, from which the simulation will iterate forwards in time. If left blank, then $t_0 = 0$ is automatically assumed. Δt_{min} is the minimum size that the time step can reduce to and, if the time step size drops below this value, the simulation will be prematurely halted. During the step in which the solution in iterated forward in time, the ratio between the current and previous time step size, r, is used, as discussed in section 3.3.2. Δt_{prev} represents the size of the previous time step. In the absence of this value, `Diffin3d` will automatically determine the ratio r at the start of a simulation and a value will be assigned to Δt_{prev} after the first iteration in time. C is the value of the Courant number to be used during the simulation.

[13] The three parameter values on this line are used for uniform Newton Cooling though out the domain. $e_{equilib}$ gives the value that the thermal energy should be maintained at within the system. t_{cool} gives the timescale over which the thermal energy should be returned to $e_{equilib}$ while t_{rise} is currently an unused parameter in `Diffin3d`.

[14] The first parameter gives the value of the ratio of specific heats, γ. Setting the value associated with Driver to 0 indicates that there is no velocity driver used with this simulation, while any other value indicates that a driver is to be invoked.

In this example input file, lines [15]–[19] are used by the setup routine `loop_fan_smooth`, which corresponds to a particular flux emergence model. The first three lines of this section indicate how the gridspacing in the domain is to be arranged. The z direction will have stretched spacing and the input parameters for the polynomial stretching routine are given on line [15]. The x and y directions will have uniform spacing, with periodic boundaries. In lines [16] and [17],

the parameters type_x and type_x indicate how the domain length will be related to actual coordinates in the x and y directions. Type 1 corresponds to the coordinates being centred about 0 and extending over the range $-x_{max} \leq x \leq x_{max}$ and $-y_{max} \leq y \leq y_{max}$ in the x and y directions, respectively. The parameters in lines [18] and [19] are used for setting up the background atmosphere and magnetic field in the flux emergence model. Other setup routines may have more or less lines of required parameter values.

[20] These five parameters prescribe the damping in the z direction, as described in section 3.5.3. A negative value for Θ_{zlower} or Θ_{zupper} indicates that no damping is to be applied at the lower or upper end of the domain, respectively, in the z direction.

[21] As for the line above, these parameters describe the damping in the y direction. Again, negative values for Θ_{ylower} or Θ_{yupper} indicates that there will be no damping at the lower or upper end of the domain, respectively, in the y direction.

Appendix C

Stretched Grid Decomposition for `Diffin3d`

The experiments described in chapters 4, 5, 6 and 7 all employ a stretched grid in the vertical direction of the simulation domain. The stretching routine used for determining the spacing between gridpoints was outlined in section 3.5.2 and uses a polynomial fitting method. In this appendix, we will present the mathematical formulation of the function prescribing the grid spacing.

As in section 3.5.2, we will consider stretching a 1D array of cells in the z direction. Following the notation used in section 3.5.2, z_{min} and z_{max} will represent the upper and lower boundaries in the z direction respectively. We begin by dividing the vertical length into three sections: $z_{min} \leq z \leq z_1$ named R_1, $z_1 \leq z \leq z_2$ named R_2, and $z_2 \leq z \leq z_{max}$ named R_3. The parameters z_1 and z_2 can be freely chosen providing $z_{min} < z_1 < z_2 < z_{max}$.

The next step is to decide what percentage of the vertical gridpoints we wish to lie in each section. We set N_z equal to the total number of gridpoints in the chosen dimension. p_1 and p_2 will represent the proportion of N_z in the regions R_1 and R_2 respectively. We require $0 \leq p_1 \leq 1$, $0 \leq p_2 \leq 1$ and $0 \leq p_1 + p_2 \leq 1$. Hence, the proportion of gridcells in R_3 is $p_3 = 1 - p_1 - p_2$.

We define a helper coordinate s, with range $[0, 1]$, that will be used to assign dimension values to the gridpoints. Each gridcell is initially assigned an s value according to its index. For example, the gridpoint with index i will be given the s value $i/(N_z - 1)$, where the gridpoints are indexed $0 - (N_z - 1)$. The difference in s values between consecutive gridpoints is constant. We then define a function f whose input will be s and whose output will be z. By applying the function $f(s)$ to the gridcells, their contents are transformed to the appropriate z coordinate values. This process is summarised in figure C.1.

Appendix C

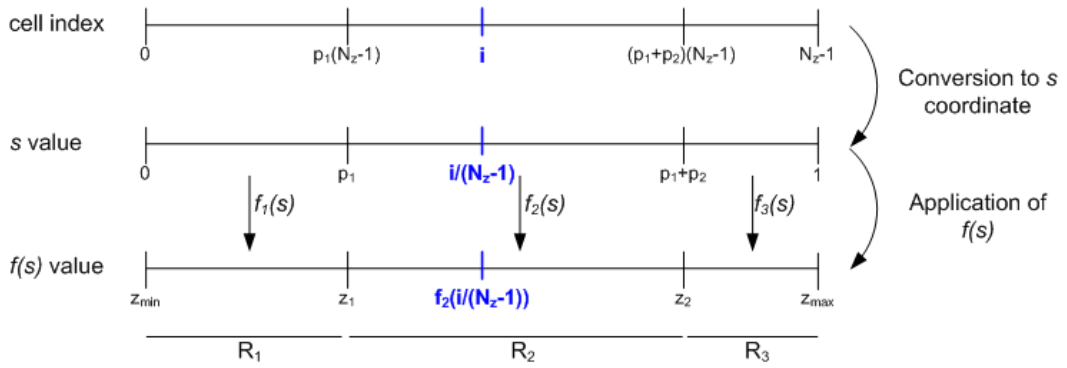

Figure C.1: Gridpoints in the 1D array are given values in the s coordinate according to their indices. The function $f(s)$ is applied to the values of s to give the appropriate z value for each gridpoint. The function $f(s)$ is actually piecewise and comprised of the functions $f_1(s)$, $f_2(s)$ and $f_3(s)$, which act on different segments of the array.

Several properties of the function $f(s)$ are already know:

$$f(0) = z_{min}, \tag{C.1}$$

$$f(p_1) = z_1, \tag{C.2}$$

$$f(p_1 + p_2) = z_2, \tag{C.3}$$

$$f(1) = z_{max}. \tag{C.4}$$

These conditions are illustrated in Figure C.2. We will use them to determine f for each region. Additionally, we require $df/ds > 0$ such that our dimensional values of z are always increasing with s. This will be addressed at the end of this appendix.

In region R_2 we impose uniform grid spacing. However, regions R_1 and R_3 may not have constant grid spacing and, therefore, our function $f(s)$ becomes piecewise such that

$$f(s) = \begin{cases} f_1(s) & 0 \leq s \leq p_1 \\ f_2(s) & p_1 \leq s \leq p_2 \\ f_3(s) & p_2 \leq s \leq 1 \end{cases} \tag{C.5}$$

$f_1(s)$ denotes the function in region R_1, and similarly $f_2(s)$ and $f_3(s)$ for regions R_2 and R_3, respectively.

In R_2, we find that uniform grid spacing and conditions (C.2) and (C.3) give

$$f_2(s) = z_1 + d_z(s - p_1), \tag{C.6}$$

for $z_1 \leq s \leq z_2$, where the gradient in this region is $d_z = (z_2 - z_1)/p_2$. In the two remaining

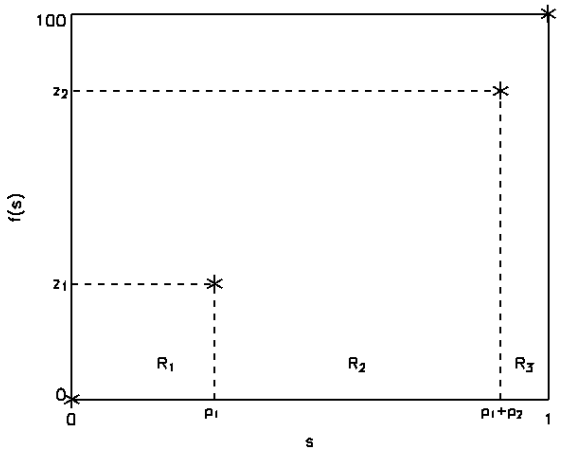

Figure C.2: The function $f(s)$ must comply with the conditions (C.1) – (C.4). These conditions are labelled on the graph and $f(s)$ must pass through the four intersection points indicated by stars. We have arbitrarily chosen $z_{min} = 0$ and $z_{max} = 100$.

regions, R_1 and R_2, we define third order polynomials. By matching the gradients of these polynomials to the gradient of $f_2(s)$ at $s = p_1$ and $s = p_2$, we can ensure a smooth transition of the grid spacing from one region to the next, as shown in figure C.3.

Firstly, we consider the lower region, R_1, where we must solve for a_1, b_1, c_1 and d_1 in the function

$$f_1(s) = a_1 s^3 + b_1 s^2 + c_1 s + d_1. \tag{C.7}$$

In defining $f_1(s)$, we must satisfy conditions (C.1) and (C.2), in addition to

$$\left(\frac{df}{ds}\right)_{p_1} = d_z, \tag{C.8}$$

$$\left(\frac{d^2 f}{ds^2}\right)_{p_1} = 0. \tag{C.9}$$

Condition (C.1) yields

$$d_1 = z_{min}, \tag{C.10}$$

whilst (C.9) gives

$$b_1 = -3a_1 p_1. \tag{C.11}$$

Substituting (C.10) and (C.11) into (C.7), we now have

$$f_1(s) = a_1 s^3 - 3a_1 p_1 s^2 + c_1 s + z_{min}. \tag{C.12}$$

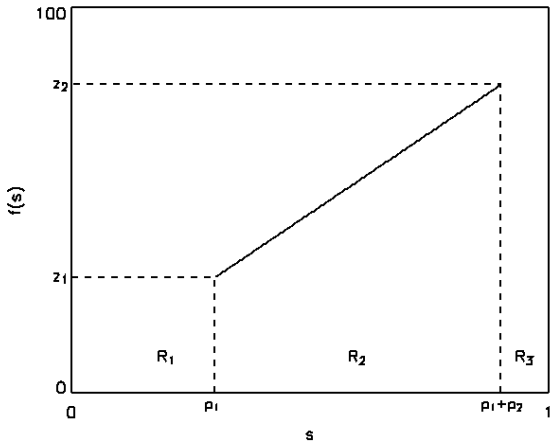

Figure C.3: $f_2(s)$ gives uniform grid spacing in the region R_2. At the boundaries between the three regions, the gradient in $f_1(s)$ and $f_3(s)$ must match the gradient of $f_2(s)$.

Differentiating (C.12) with respect to s and applying the condition (C.8) reveals that

$$c_1 = d_z + 3a_1{p_1}^2. \tag{C.13}$$

Finally, by substituting this information for c_1 into (C.12) and using condition (C.2), we find that

$$a_1 = (z_1 - z_{min} - d_z p_1)/{p_1}^3. \tag{C.14}$$

Now all of the coefficients of $f_1(s)$ have all been determined and, therefore, $f_1(s)$ is completely known.

For the region R_3 we must find a_3, b_3, c_3 and d_3 of the function

$$f_3(s) = a_3 s^3 + b_3 s^2 + c_3 s + d_3. \tag{C.15}$$

Here, conditions (C.3) and (C.4) must be adhered to, in addition to

$$\left(\frac{df}{ds}\right)_{(1-p_3)} = d_z, \tag{C.16}$$

$$\left(\frac{d^2 f}{ds^2}\right)_{(1-p_3)} = 0. \tag{C.17}$$

Following a similar derivation to that for $f_1(s)$ in R_1, we find that

$$a_3 = \frac{z_{max} - z_2 - d_z p_3}{p_3^3}, \tag{C.18}$$

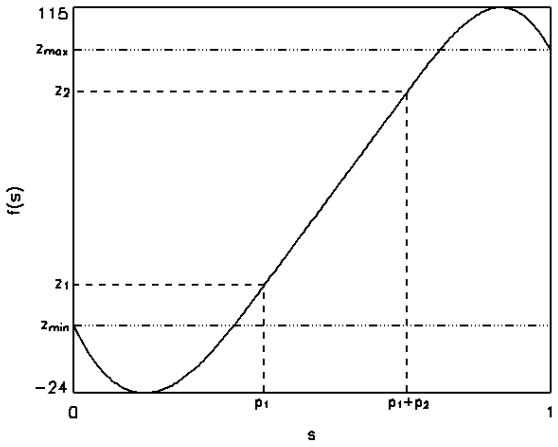

Figure C.4: Some combinations of parameter values for z_1, z_2, p_1 and p_2 result in $f(s)$ having turning points. Here, we have chosen $z_{min} = 0$, $z_1 = 15$, $z_2 = 85$, $z_{max} = 100$, $p_1 = 0.4$ and $p_2 = 0.3$.

$$b_3 = -3a_3(1-p_3), \tag{C.19}$$

$$c_3 = d_z + 3a_3(1-p_3)^2, \tag{C.20}$$

$$d_3 = z_{max} - d_z - a_3(1-3(1-p_3)+3(1-p_3)^2). \tag{C.21}$$

Using (C.6) and the complete solutions for (C.7) and (C.15), we know $f(s)$ throughout the vertical domain. However, when deriving the functions f_1 and f_3 we have matched the functions to the boundaries of f_2 but have made no attempt to ensure that f_1 and f_2 have positive gradients for all s. A negative gradient in a section of f_1 means the function must have a local minimum, while a negative gradient in a section of f_3 means the function must have a local maximum, as illustrated in figure C.4. The turning point results in non-unique values of z being assigned to the gridpoints and in most situations is highly undesirable.

If f_1 or f_3 have a turning point, then f_s will have a negative gradient at the boundary $s = 0$ or $s = 1$, respectively. If we consider the $s = 0$ boundary first, we require

$$\left(\frac{df_1}{ds}\right)_0 \geq 0, \tag{C.22}$$

to ensure there are no local minimum in the region $0 < s \leq p_1$. Differentiating (C.7) with respect to s and substituting for b_1 and c_1 using (C.11) and (C.13) gives

$$\frac{df_1}{ds} = 3a_1(s-p_1)^2 + d_z. \tag{C.23}$$

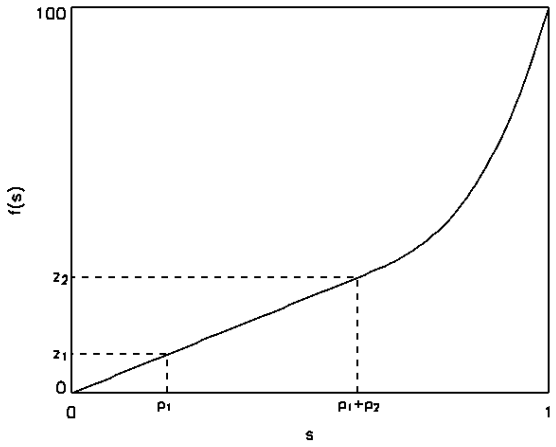

Figure C.5: Regions R_1 and R_2 have uniform grid spacing, while R_3 has non-uniform spacing. Of the 100 gridpoints, 20% lie in R_1 and 40% reside in R_2. Region R_1 occupies $0 \leq z \leq 10$ and region R_3 occupies $30 \leq z \leq 100$.

Using the condition (C.22) and substituting for a_1 and d_z, we find that (C.23) reduces to

$$\frac{3L_1}{2L_2} \geq \frac{p_1}{p_2}, \tag{C.24}$$

where $L_1 = z_1 - z_{min}$ and $L_2 = z_2 - z_1$. Similarly, satisfying

$$\left(\frac{df_3}{ds}\right)_1 \geq 0, \tag{C.25}$$

for no local maximum in the region $p_1 + p_2 \leq s < 1$, requires

$$\frac{3L_3}{2L_2} \geq \frac{p_3}{p_2}, \tag{C.26}$$

where $L_3 = z_{max} - z_2$. Thus, to ensure there are no maxima or minima in $f(s)$ the user must satisfy (C.24) and (C.26) when choosing the values of the parameters z_1, z_2, p_1 and p_2.

As discussed in section 3.5.2, it is possible for either of the regions R_1 or R_3 to also have uniform spacing. This is illustrated in figure C.5 where regions R_1 and R_2 have uniform grid spacing and R_3 has non-uniform spacing. Uniform grid spacing in either of R_1 or R_3 would require the third order polynomial, which describes the grid spacing of the region, to become first order. Thus, $a_1 = 0$ and $b_1 = 0$ for uniform spacing in R_1 and $a_3 = 0$ and $b_3 = 0$ for uniform spacing in R_3. Given these conditions, we see that it is necessary for the size of the grid spaces in regions R_1 and R_3 to match that of R_2 if they are to have uniform spacing. In terms of the proportion of

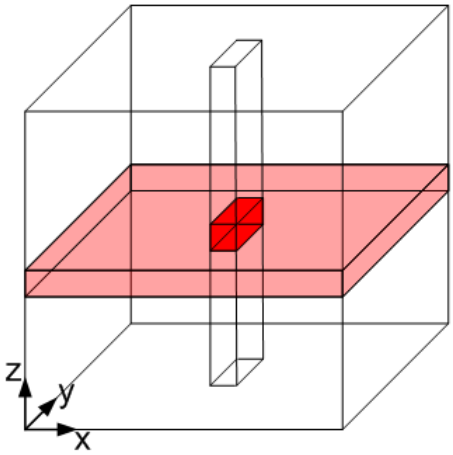

Figure C.6: The values of z in the vertical 1D strip of cells are copied across the entire horizontal layer of the 3D grid.

gridpoints in each region, we require

$$\frac{L_1}{p_1} = \frac{L_2}{p_2}, \tag{C.27}$$

for uniform spacing in R_1 and

$$\frac{L_3}{p_3} = \frac{L_2}{p_2}, \tag{C.28}$$

for uniform spacing in R_3.

In deriving this polynomial fitting method, we have considered a 1D array in z. This is easily generalised to a 3D grid. In `Diffin3d`, the stretching performed along each vertical strip of the grid is independent of the horizontal location of the strip within the grid. Thus, all of the cells in the same horizontal plane will have the same value of z, as shown in figure C.6. This is independent of whether stretching has also been performed in any of the other coordinates.

As stated in section 3.5.2, polynomial fitting is just one method that can be used to perform grid stretching.

When a stretched grid is used, the sixth order error differentiation method, given in appendix A, is no longer appropriate. This is because during its derivation we assumed that the grid spacing was uniform. If the grid spacing is not uniform, then the even order terms cannot be eliminated when the Taylor series of pairwise points are subtracted and, therefore, the order of the method is dramatically reduced. For stretched grids, the evaluation of the derivative of g with respect to z at

index $i + \frac{1}{2}$ can be written as

$$\left(\frac{\partial g}{\partial z}\right)_{i+\frac{1}{2}} = \left(\frac{\partial g}{\partial s}\right)_{i+\frac{1}{2}} \left(\frac{ds}{dz}\right)_{i+\frac{1}{2}} . \tag{C.29}$$

The spacing of s is uniform and, therefore, the first term on the right-handside of (C.29) can once again be evaluated using the sixth order finite difference method derived in appendix A. Thus, we have

$$\left(\frac{\partial g}{\partial s}\right)_{i+\frac{1}{2}} = \frac{a_1}{\Delta s}\left(g_{i+1} - g_i\right) + \frac{b_1}{\Delta s}\left(g_{i+2} - g_{i-1}\right) + \frac{c_1}{\Delta s}\left(g_{i+3} - g_{i-2}\right), \tag{C.30}$$

with $a_1 = 1 - 3b_1 - 5c_1$, $b_1 = -(1 + 120c_1)/24$ and $c_1 = 3/640$.

The second term on the right-handside can be written as

$$\left(\frac{1}{\left(\frac{dz}{ds}\right)}\right)_{i+\frac{1}{2}} , \tag{C.31}$$

and this is equivalent to

$$\left(\frac{1}{\left(\frac{df}{ds}\right)}\right)_{i+\frac{1}{2}} . \tag{C.32}$$

Depending upon which section of the s domain the $i+\frac{1}{2}$ index belongs to, (C.32) can be accurately evaluated from the derivative of the know analytical functions $f_1(s)$, $f_2(s)$ and $f_3(s)$, derived in this appendix.

Thus, when a stretched grid is used the accuracy of the finite difference differentiation method will not be decreased if the above modifications are made and it will continue to have a sixth order error.

Appendix D

Accompanying CD-ROM

This thesis is accompanied by a CD-ROM, which can be found on the inside of the back cover. The CD-ROM contains movies of certain aspects of the results in the thesis and are complementary to the figures in the chapters.

The contents of the CD-ROM are sorted into directories by chapter and labelled according to the figure they accompany. For example, the file `Fig1.7.avi` in the directory `Chapter1` is the observational movie from which the images of figure 1.7 of chapter 1 are taken.

To play the movies on a computer with a Linux operating system, use a terminal window to navigate to the CD-ROM and the required chapter directory. To play a movie in that directory, Fig1.7.avi say, type

```
mplayer Fig1.7.avi
```

or

```
mplayer -loop 0 Fig1.7.avi
```

to play the movie once or loop indefinitely, respectively. Using `MPlayer`, a movie can be paused using the spacebar key. `MPlayer` offers various options for controlling how a movie is played and these can be found by typing `man mplayer` into the terminal window.

Appendix D

The movies contained on the CD-ROM are as follows:

- Chapter1:
  - Fig1.7.avi;
- Chapter4:
  - Fig4.5.mpg, Fig4.7.mpg, Fig4.7a.mpg, Fig4.16.mpg;
- Chapter5:
  - Fig5.4a.mpg, Fig5.4b.mpg, Fig5.18.mpg, Fig5.19a.mpg, Fig5.19b.mpg, Fig5.20b.mpg;
- Chapter7:
  - Fig7.2.mpg, Fig7.7.mpg, Fig7.9.mpg, Fig7.11.mpg.

Bibliography

Abbett, W. P. and Fisher, G. H. (2003). A Coupled Model for the Emergence of Active Region Magnetic Flux into the Solar Corona. *ApJ*, 582:475–485.

Abbett, W. P., Fisher, G. H., and Fan, Y. (2000). The Three-dimensional Evolution of Rising, Twisted Magnetic Flux Tubes in a Gravitationally Stratified Model Convection Zone. *ApJ*, 540:548–562.

Abbett, W. P., Fisher, G. H., Fan, Y., and Bercik, D. J. (2004). The Dynamic Evolution of Twisted Magnetic Flux Tubes in a Three-dimensional Convecting Flow. II. Turbulent Pumping and the Cohesion of Ω-Loops. *ApJ*, 612:557–575.

Acheson, D. J. (1979). Instability by magnetic buoyancy. *Solar Physics*, 62:23–50.

Archontis, V., Galsgaard, K., Moreno-Insertis, F., and Hood, A. W. (2006). Three-dimensional Plasmoid Evolution in the Solar Atmosphere. *ApJ*, 645:L161–L164.

Archontis, V., Hood, A. W., and Brady, C. (2007). Emergence and interaction of twisted flux tubes in the Sun. *A&A*, 466:367–376.

Archontis, V., Moreno-Insertis, F., Galsgaard, K., Hood, A., and O'Shea, E. (2004). Emergence of magnetic flux from the convection zone into the corona. *A&A*, 426:1047–1063.

Archontis, V., Moreno-Insertis, F., Galsgaard, K., and Hood, A. W. (2005). The Three-dimensional Interaction between Emerging Magnetic Flux and a Large-Scale Coronal Field: Reconnection, Current Sheets, and Jets. *ApJ*, 635:1299–1318.

Babcock, H. W. (1961). The Topology of the Sun's Magnetic Field and the 22-YEAR Cycle. *ApJ*, 133:572–+.

Batchelor, G. (1967). *An Introduction to Fluid Dynamics*. Cambridge University Press, Cambridge, U.K.

Brants, J. J. (1985). High-resolution spectroscopy of active regions. III - Relations between the intensity, velocity, and magnetic structure in an emerging flux region. *Solar Physics*, 98:197–217.

Brekke, P., Kjeldseth-Moe, O., and Harrison, R. A. (1997). High-Velocity Flows in an Active Region Loop System Observed with the Coronal Diagnostic Spectrometer (Cds) on SOHO. *Solar Physics*, 175:511–521.

Bruzek, A. (1964). On the Association Between Loop Prominences and Flares. *ApJ*, 140:746–+.

Bruzek, A. (1967). On Arch-Filament Systems in Spotgroups. *Solar Physics*, 2:451–+.

Bruzek, A. (1969). Motions in Arch Filament Systems. *Solar Physics*, 8:29–+.

Caligari, P., Moreno-Insertis, F., and Schussler, M. (1995). Emerging flux tubes in the solar convection zone. 1: Asymmetry, tilt, and emergence latitude. *ApJ*, 441:886–902.

Canfield, R. C., Reardon, K. P., Leka, K. D., Shibata, K., Yokoyama, T., and Shimojo, M. (1996). H alpha Surges and X-Ray Jets in AR 7260. *ApJ*, 464:1016–+.

Chae, J., Wang, H., Qiu, J., Goode, P. R., and Wilhelm, K. (2000). Active Region Loops Observed with SUMER on Board the SOHO. *ApJ*, 533:535–545.

Cheung, M. C. M., Moreno-Insertis, F., and Schuessler, M. (2006). Moving magnetic tubes: fragmentation, vortex streets and the limit of the approximation of thin flux tubes. *A&A*, 451:303–317.

Cheung, M. C. M., Schüssler, M., and Moreno-Insertis, F. (2007). Magnetic flux emergence in granular convection: radiative MHD simulations and observational signatures. *A&A*, 467:703–719.

Chou, D.-Y. and Zirin, H. (1988). The vertical structure of arch filament systems in solar emerging flux regions. *ApJ*, 333:420–426.

Courant, R., Friedrichs, K. O., and Lewy, H. (1928). Uber die partiellen differenzengleichungen der mathematischen physik. *Math. Ann.*, 100:32–74.

Dahlburg, R. B., Antiochos, S. K., and Norton, D. (1997). Magnetic flux tube tunneling. *Physical Review E (Statistical Physics, Plasmas, Fluids, and Related Interdisciplinary Topics)*, 56:2094–2103.

Dorch, S. B. F. (2003). Buoyant Magnetic Flux Ropes and Convection: Evolution Prior to Emergence. In Brown, A., Harper, G. M., and Ayres, T. R., editors, *The Future of Cool-Star Astrophysics: 12th Cambridge Workshop on Cool Stars , Stellar Systems, and the Sun (2001 July 30 - August 3), eds. A. Brown, G.M. Harper, and T.R. Ayres, (University of Colorado), 2003, p. 186-195.*, pages 186–195.

Dorch, S. B. F. (2007). Buoyant Magnetic Flux Ropes in a Magnetised Stellar Envelope. *A&A*, 461:325–330.

Dorch, S. B. F., Archontis, V., and Nordlund, Å. (1999). 3D simulations of twisted magnetic flux ropes. *A&A*, 352:L79–L82.

Dorch, S. B. F., Gudiksen, B. V., Abbett, W. P., and Nordlund, Å. (2001). Flux-loss of buoyant ropes interacting with convective flows. *A&A*, 380:734–738.

Dorch, S. B. F. and Nordlund, A. (1998). Numerical 3D simulations of buoyant magnetic flux tubes. *A&A*, 338:329–339.

D'Silva, S. and Choudhuri, A. R. (1993). A theoretical model for tilts of bipolar magnetic regions. *A&A*, 272:621–+.

Emonet, T. and Moreno-Insertis, F. (1996). Equilibrium of twisted horizontal magnetic flux tubes. *ApJ*, 458:783 – 801.

Emonet, T. and Moreno-Insertis, F. (1998). The Physics of Twisted Magnetic Tubes Rising in a Stratified Medium: Two-dimensional Results. *ApJ*, 492:804–+.

Fan, Y. (2001). The Emergence of a Twisted Ω-Tube into the Solar Atmosphere. *ApJ*, 554:L111–L114.

Fan, Y. (2004). Magnetic Fields in the Solar Convection Zone. *Living Reviews of Solar Physics*, 1:1–+.

Fan, Y. (2005). Coronal Mass Ejections as Loss of Confinement of Kinked Magnetic Flux Ropes. *ApJ*, 630:543–551.

Fan, Y., Abbett, W. P., and Fisher, G. H. (2003). The Dynamic Evolution of Twisted Magnetic Flux Tubes in a Three-dimensional Convecting Flow. I. Uniformly Buoyant Horizontal Tubes. *ApJ*, 582:1206–1219.

Fan, Y. and Fisher, G. H. (1996). Radiative Heating and the Buoyant Rise of Magnetic Flux Tubes in the Solar interior. *Solar Physics*, 166:17–+.

Fan, Y. and Gibson, S. E. (2003). The Emergence of a Twisted Magnetic Flux Tube into a Preexisting Coronal Arcade. *ApJ*, 589:L105–L108.

Fan, Y. and Gibson, S. E. (2004). Numerical Simulations of Three-dimensional Coronal Magnetic Fields Resulting from the Emergence of Twisted Magnetic Flux Tubes. *ApJ*, 609:1123–1133.

Fan, Y., Zweibel, E. G., and Lantz, S. R. (1998a). Two-dimensional Simulations of Buoyantly Rising, Interacting Magnetic Flux Tubes. *ApJ*, 493:480–+.

Fan, Y., Zweibel, E. G., Linton, M. G., and Fisher, G. H. (1998b). The Rise of Kink-Unstable Magnetic Flux Tubes in the Solar Convection Zone. *ApJ*, 505:L59+.

Frazier, E. N. (1972). The Magnetic Structure of Arch Filament Systems. *Solar Physics*, 26:130–+.

Galsgaard, K., Archontis, V., Moreno-Insertis, F., and Hood, A. (2007). The effect of the relative orientation between the coronal field and new emerging flux: I Global Properties. *ApJ*, (submitted).

Galsgaard, K., Moreno-Insertis, F., Archontis, V., and Hood, A. (2005). A Three-dimensional Study of Reconnection, Current Sheets, and Jets Resulting from Magnetic Flux Emergence in the Sun. *ApJ*, 618:L153–L156.

Georgoulis, M. K. and Labonte, B. J. (2004). Forecasting and Real-Time Diagnostics of Solar Coronal Mass Ejections. *AGU Fall Meeting Abstracts*, pages B2+.

Gibson, S. E. and Fan, Y. (2006). The Partial Expulsion of a Magnetic Flux Rope. *ApJ*, 637:L65–L68.

Gibson, S. E., Fan, Y., Mandrini, C., Fisher, G., and Demoulin, P. (2004). Observational Consequences of a Magnetic Flux Rope Emerging into the Corona. *ApJ*, 617:600–613.

Glackin, D. L. (1975). Emerging Flux Regions. *Solar Physics*, 43:317–326.

Gold, T. and Hoyle, F. (1960). On the origin of solar flares. *Monthly Notices of the Royal Astronomical Society*, 120:89–+.

Hood, A. W. and Priest, E. R. (1981). Critical conditions for magnetic instabilities in force-free coronal loops. *Geophysical & Astrophysical Fluid Dynamics*, 17:297–318.

Hughes, D. W., Falle, S. A. E. G., and Joarder, P. (1998). The rise of twisted magnetic flux tubes. *Monthly Notices of the Royal Astronomical Society*, 298:433–444.

Hyman, J. (1979). A method of lines approach to the numerical solution of conservation laws. In Vichnevetshi, R. and Stepleman, R. S., editors, *Advances in Computer Methods for Partial Differential Equations – III*, number 313–321. IMACS.

Isobe, H., Miyagoshi, T., Shibata, K., and Yokoyama, T. (2005). Filamentary structure on the Sun from the magnetic Rayleigh-Taylor instability. *Nature*, 434:478–481.

Isobe, H., Miyagoshi, T., Shibata, K., and Yokoyama, T. (2006). Three-Dimensional Simulation of Solar Emerging Flux Using the Earth Simulator I. Magnetic Rayleigh-Taylor Instability at the Top of the Emerging Flux as the Origin of Filamentary Structure. *PASJ*, 58:423–438.

Isobe, H., Tripathi, D., and Archontis, V. (2007). Ellerman Bombs and Jets Associated with Resistive Flux Emergence. *ApJL*, 657:L53–L56.

Kaisig, M., Tajima, T., Shibata, K., Nozawa, S., and Matsumoto, R. (1990). Nonlinear excitation of magnetic undular instability by convective motion. *ApJ*, 358:698–709.

Kawaguchi, I. and Kitai, R. (1976). The velocity field associated with the birth of sunspots. *Solar Physics*, 46:125–135.

Krall, J., Chen, J., Santoro, R., Spicer, D. S., Zalesak, S. T., and Cargill, P. J. (1998). Simulation of Buoyant Flux Ropes in a Magetized Solar Atmosphere. *ApJ*, 500:992–+.

Kurokawa, H. (1987). Two distinct morphological types of magnetic shear development and their relation to flares. *Solar Physics*, 113:259–263.

Kurokawa, H. and Kawai, G. (1993). H alpha Surge Activity at the First Stage of Magnetic Flux Emergence. In Zirin, H., Ai, G., and Wang, H., editors, *IAU Colloq. 141: The Magnetic and Velocity Fields of Solar Active Regions*, volume 46 of *Astronomical Society of the Pacific Conference Series*, pages 507–+.

Leake, J. E. and Arber, T. D. (2006). The emergence of magnetic flux through a partially ionised solar atmosphere. *A&A*, 450:805–818.

Leka, K. D., Canfield, R. C., McClymont, A. N., and van Driel-Gesztelyi, L. (1996). Evidence for Current-carrying Emerging Flux. *ApJ*, 462:547–+.

Linton, M. G. (2006). Reconnection of nonidentical flux tubes. *Journal of Geophysical Research (Space Physics)*, 111(A10):12–+.

Linton, M. G. and Antiochos, S. K. (2005). Magnetic Flux Tube Reconnection: Tunneling Versus Slingshot. *ApJ*, 625:506–521.

Linton, M. G., Dahlburg, R. B., and Antiochos, S. K. (2001). Reconnection of Twisted Flux Tubes as a Function of Contact Angle. *ApJ*, 553:905–921.

Linton, M. G. and Priest, E. R. (2003). Three-dimensional Reconnection of Untwisted Magnetic Flux Tubes. *ApJ*, 595:1259–1276.

Lites, B. W., Low, B. C., Martinez Pillet, V., Seagraves, P., Skumanich, A., Frank, Z. A., Shine, R. A., and Tsuneta, S. (1995). The Possible Ascent of a Closed Magnetic System through the Photosphere. *ApJ*, 446:877–+.

Longcope, D. W. and Klapper, I. (1997). Dynamics of a Thin Twisted Flux Tube. *ApJ*, 488:443–+.

Longcope, D. W., McKenzie, D. E., Cirtain, J., and Scott, J. (2005). Observations of Separator Reconnection to an Emerging Active Region. *ApJ*, 630:596–614.

Magara, T. (2001). Dynamics of Emerging Flux Tubes in the Sun. *ApJ*, 549:608–628.

Magara, T. (2004). A model for dynamic evolution of emerging magnetic fields in the sun. *ApJ*, 605:480 – 492.

Magara, T. (2006). Dynamic and Topological Features of Photospheric and Coronal Activities Produced by Flux Emergence in the Sun. *ApJ*, 653:1499–1509.

Magara, T. and Longcope, D. W. (2001). Sigmoid Structure of an Emerging Flux Tube. *ApJ*, 559:L55–L59.

Magara, T. and Longcope, D. W. (2003). Injection of Magnetic Energy and Magnetic Helicity into the Solar Atmosphere by an Emerging Magnetic Flux Tube. *ApJ*, 586:630–649.

Manchester, W., Gombosi, T., DeZeeuw, D., and Fan, Y. (2004). Eruption of a Buoyantly Emerging Magnetic Flux Rope. *ApJ*, 610:588–596.

Matsumoto, R., Tajima, T., Shibata, K., and Kaisig, M. (1993). Three-dimensional magnetohydrodynamics of the emerging magnetic flux in the solar atmosphere. *ApJ*, 414:357–371.

Metcalf, T. R., Jiao, L., McClymont, A. N., Canfield, R. C., and Uitenbroek, H. (1995). Is the solar chromospheric magnetic field force-free? *ApJ*, 439:474–481.

Meyer, F., Schmidt, H. U., Wilson, P. R., and Weiss, N. O. (1974). The growth and decay of sunspots. *Monthly Notices of the Royal Astronomical Society*, 169:35–57.

Miyagoshi, T. and Yokoyama, T. (2003). Magnetohydrodynamic Numerical Simulations of Solar X-Ray Jets Based on the Magnetic Reconnection Model That Includes Chromospheric Evaporation. *ApJ*, 593:L133–L136.

Miyagoshi, T. and Yokoyama, T. (2004). Magnetohydrodynamic Simulation of Solar Coronal Chromospheric Evaporation Jets Caused by Magnetic Reconnection Associated with Magnetic Flux Emergence. *ApJ*, 614:1042–1053.

Moreno-Insertis, F. (2005). The Double-Lined Spectroscopic Binary Haro 1-14c. In Leibacher, J., Uitenbroek, H., and Stein, R., editors, *ASP Conf. Ser.: Solar MHD: Theory and Observations - a High Resolution Perspective*.

Moreno-Insertis, F. (2006). Magnetic flux emergence into the atmosphere. In Bothmer, V. and

Hady, A. A., editors, *IAU Symposium*, pages 33–40.

Moreno-Insertis, F. and Emonet, T. (1996). The Rise of Twisted Magnetic Tubes in a Stratified Medium. *ApJ*, 472:L53+.

Newcomb, W. A. (1961). Convective Instability Induced by Gravity in a Plasma with a Frozen-In Magnetic Field. *Physics of Fluids*, 4:391.

Nordlund, A. and Galsgaard, K. (1997). A 3D MHD Code for Parallel Computers. Technical report, Astronomical Observatory, Copenhagen University.

Parker, E. N. (1955). The Formation of Sunspots from the Solar Toroidal Field. *ApJ*, 121:491–+.

Parker, E. N. (1979a). *Cosmical magnetic fields: Their origin and their activity*. Oxford, Clarendon Press; New York, Oxford University Press, 1979, 858 p.

Parker, E. N. (1979b). Sunspots and the physics of magnetic flux tubes. I - The general nature of the sunspot. II - Aerodynamic drag. *ApJ*, 230:905–923.

Parnell, C. E. and Galsgaard, K. (2004). Elementary heating events - magnetic interactions between two flux sources. II. Rates of flux reconnection. *A&A*, 428:595–612.

Pevtsov, A. A., Canfield, R. C., and Metcalf, T. R. (1995). Latitudinal variation of helicity of photospheric magnetic fields. *ApJL*, 440:L109–L112.

Piddington, J. H. (1975). Solar magnetic fields and convection. I - Active regions and sunspots. *Ap&SS*, 34:347–362.

Piddington, J. H. (1981). Twists and rotations of solar magnetic fields. *Ap&SS*, 75:273–287.

Priest, E. R. (1982). *Solar magneto-hydrodynamics*. Dordrecht, Holland ; Boston : D. Reidel Pub. Co. ; Hingham,.

Roberts, B. (1991). Magnetohydrodynamic Waves in the Sun. In Priest, E. R. and Hood, A. W., editors, *Advances in Solar System Magnetohydrodynamics*, pages 105–+.

Rust, D. M. and Kumar, A. (1996). Evidence for Helically Kinked Magnetic Flux Ropes in Solar Eruptions. *ApJL*, 464:L199+.

Ryutova, M. and Shine, R. (2006). Coupling effects throughout the solar atmosphere: Emerging magnetic flux and structure formation. *Journal of Geophysical Research (Space Physics)*, 111:3101–+.

Schmieder, B., Demoulin, P., Aulanier, G., and Golub, L. (1996). Differential Magnetic Field Shear in an Active Region. *ApJ*, 467:881–+.

Shibata, K., Nozawa, S., and Matsumoto, R. (1992). Magnetic reconnection associated with emerging magnetic flux. *PASJ*, 44:265–272.

Shibata, K., Nozawa, S., Matsumoto, R., Sterling, A. C., and Tajima, T. (1990). Emergence of solar magnetic flux from the convection zone into the photosphere and chromosphere. *ApJ*, 351:L25–L28.

Shibata, K., Tajima, T., Matsumoto, R., Horiuchi, T., Hanawa, T., Rosner, R., and Uchida, Y. (1989a). Nonlinear Parker instability of isolated magnetic flux in a plasma. *ApJ*, 338:471–492.

Shibata, K., Tajima, T., Steinolfson, R. S., and Matsumoto, R. (1989b). Two-dimensional magnetohydrodynamic model of emerging magnetic-flux in the solar atmosphere. *ApJ*, 345:584 – 596.

Shimojo, M., Hashimoto, S., Shibata, K., Hirayama, T., Hudson, H. S., and Acton, L. W. (1996). Statistical Study of Solar X-Ray Jets Observed with the YOHKOH Soft X-Ray Telescope. *PASJ*, 48:123–136.

Solanki, S. K. (2003). Sunspots: An overview. *Astronomy and Astrophysics Review*, 11:153 – 286.

Spruit, H. C. (1981). Motion of magnetic flux tubes in the solar convection zone and chromosphere. *A&A*, 98:155–160.

Sterling, A. C. and Hudson, H. S. (1997). YOHKOH SXT Observations of X-Ray "Dimming" Associated with a Halo Coronal Mass Ejection. *ApJL*, 491:L55+.

Strous, L. H., Scharmer, G., Tarbell, T. D., Title, A. M., and Zwaan, C. (1996). Phenomena in an emerging active region. I. Horizontal dynamics. *Solar Physics*, 306:947–+.

Strous, L. H. and Zwaan, C. (1999). Phenomena in an Emerging Active Region. II. Properties of the Dynamic Small-Scale Structure. *ApJ*, 527:435–444.

Thomas, J. H. and Nye, A. H. (1975). Convective instability in the presence of a nonuniform horizontal magnetic field. *Physics of Fluids*, 18:490–+.

Titov, V. S. and Démoulin, P. (1999). Basic topology of twisted magnetic configurations in solar flares. *A&A*, 351:707–720.

Tortosa, A. (2007). Numerical experiments of magnetic flux emergence in the solar atmosphere: MHD and radiation transfere. Master's thesis, University of La Laguna, Tenerife, Spain.

Vernazza, J. E., Avrett, E. H., and Loeser, R. (1981). Structure of the solar chromosphere. III - Models of the EUV brightness components of the quiet-sun. *Astrophysical Journal Supplement Series*, 45:635–725.

Williams, D. R., Török, T., Démoulin, P., van Driel-Gesztelyi, L., and Kliem, B. (2005). Eruption of a Kink-unstable Filament in NOAA Active Region 10696. *ApJ*, 628:L163–L166.

Yokoyama, T. and Shibata, K. (1995). Magnetic Reconnection as the Origin of X-Ray Jets and Hα Surges on the Sun. *Nature*, 375:42–+.

Yokoyama, T. and Shibata, K. (1996). Numerical Simulation of Solar Coronal X-Ray Jets Based on the Magnetic Reconnection Model. *PASJ*, 48:353–376.

Yu, C. P. (1965). Magneto-Atmospheric Waves in a Horizontally Stratified Conducting Medium. *Physics of Fluids*, 8:650.

Zwaan, C. (1985). The emergence of magnetic flux. *Solar Physics*, 100:397–414.